Professur für Biochemie und Molekularbiologie

Oxidative posttranslational modifications in *Plasmodium falciparum* and coronaviruses

INAUGURALDISSERTATION

zur Erlangung des akademischen Grades

Doktor der Naturwissenschaften

- Dr. rer. nat. -

im Fachbereich Biologie und Chemie

der Justus-Liebig-Universität Gießen

vorgelegt von

Melissa Dillenberger

Juli 2022

Erstgutachterin:	**Prof. Dr. med. Katja Becker** Professur für Biochemie und Molekularbiologie Institut für Ernährungswissenschaften Justus-Liebig-Universität Gießen Interdisziplinäres Forschungszentrum Heinrich-Buff-Ring 26-32 35392 Gießen
Zweitgutachterin:	**Prof. Dr. rer. nat. Katja Sträßer** Institut für Biochemie Justus-Liebig-Universität Gießen Heinrich-Buff-Ring 17 35392 Gießen
Weitere Mitglieder der Prüfungskommission:	**Prof. Dr. med. John Ziebuhr** Institut für Medizinische Virologie Biomedizinisches Forschungszentrum Seltersberg (BFS) Justus-Liebig-Universität Gießen Schubertstraße 81 35392 Gießen
	Prof. Dr. rer. nat. Elena Evguenieva-Hackenberg Institut für Mikrobiologie und Molekularbiologie Justus-Liebig-Universität Gießen Interdisziplinäres Forschungszentrum Heinrich-Buff-Ring 26-32 35392 Gießen

Die vorliegende Arbeit wurde im Interdisziplinären Forschungszentrum der Justus-Liebig-Universität Gießen an der Professur für Biochemie und Molekularbiologie unter Leitung von Frau Prof. Dr. med. Katja Becker angefertigt.

SUMMARY

The protozoan parasite *Plasmodium falciparum* (*P. falciparum*) is the causative pathogen of the most severe form of malaria. For its survival and replication in human erythrocytes, *P. falciparum* depends on ATP as energy supply, which is almost entirely provided by the glycolytic pathway. Besides this strong dependence on glycolysis, the glycolytic enzymes of *P. falciparum* differ significantly from their human counterparts and are therefore considered promising drug targets. Moreover, many of those enzymes are shown to be targeted and potentially regulated by oxidative posttranslational modifications (oxPTMs). OxPTMs can occur at protein's cysteine residues under both basal conditions and conditions that are associated with increased oxidative and/or nitrosative stress.

Within this thesis, two glycolytic enzymes were enzymatically and structurally characterized: *P. falciparum* hexokinase (PfHK) and pyruvate kinase (PfPK). PfHK was confirmed to be a target for both S-glutathionylation and S-nitrosation. While both oxPTMs can inhibit the protein's enzymatic activity, incubations with thioredoxin (PfTrx), glutaredoxin (PfGrx), and plasmoredoxin (PfPlrx) were shown to restore the activity after the modification. In addition, the first three-dimensional protein structure of PfHK was solved. The crystal structure reveals a *Plasmodium*-specific insertion in the small domain and confirms the tetrameric assembly already described for *Plasmodium vivax* hexokinase. This oligomerization is unique compared to hexokinases from other organisms. For PfPK, C49 and C343 were identified as important contributors to the functional and structural integrity of the enzyme. Respective cysteine-to-alanine mutants showed lowered enzymatic activities and substrate affinities. Furthermore, structural analysis revealed conformational changes within the mutant structures that are in accordance with the previous data. Overall, the present findings are an important contribution to understand the complex redox regulation of *P. falciparum* glycolytic enzymes and provide novel findings about their three-dimensional structure that will be advantageous for future structure-based drug design.

Upon viral infections, both host cell and viral proteins are exposed to high levels of oxidative stress. However, viruses lack oxidative defense systems, and, in contrast to *P. falciparum* and many other organisms, there is a paucity of data about the effects of oxPTMs on viral proteins. The few studies available have shown conflicting effects: depending on the virus and protein studied, oxPTMs can induce either inhibitory or beneficial effects on the protein's function or the whole replication. Coronaviruses are positive-stranded, enveloped RNA viruses causing various diseases in different mammals and birds. In humans, coronaviruses commonly cause mild respiratory tract infections.

In this thesis, the methodological knowledge gained while studying oxPTMs of *P. falciparum* proteins was transferred to coronavirus nonstructural proteins (nsps). Among ~30 different

nsps, several targets for S-glutathionylation could be identified. It was shown that the protease activity of nsp5 from two viral strains is inhibited upon S-glutathionylation. Cysteine-to-alanine mutants of severe acute respiratory syndrome coronavirus (SARS-CoV) nsp9 further identified single cysteines that may be more susceptible for modifications. In summary, the present data provides new insights into potential redox regulation of CoV proteins via oxPTMs.
Finally, this thesis briefly summarizes results of a collaboration project in an excursus section. Using different experimental approaches, it could be confirmed that human spectrin is a target of S-glutathionylation.

ZUSAMMENFASSUNG

Die schwerste Form der Malaria wird verursacht durch den Parasiten *Plasmodium falciparum* (*P. falciparum*). Dabei sind das Überleben und die Vermehrung in menschlichen Erythrozyten stark abhängig von dem Energielieferanten ATP, welches fast vollständig mittels Glykolyse bereitgestellt wird. Zusätzlich zu dieser starken Abhängigkeit von der Glykolyse unterscheiden sich die glykolytischen Enzyme von *P. falciparum* erheblich von ihren menschlichen Pendants und werden daher als vielversprechende Angriffspunkte für mögliche Medikamente angesehen. Darüber hinaus hat sich gezeigt, dass viele dieser Enzyme Ziel von oxidativen posttranslationalen Modifikationen (oxPTMs) sind und so potenziell reguliert werden. OxPTMs können an Cysteinen von Proteinen sowohl unter basalen Bedingungen als auch unter Bedingungen auftreten, die mit erhöhtem oxidativem und/oder nitrosativem Stress einhergehen.

Im Rahmen dieser Arbeit wurden zwei glykolytische Enzyme enzymatisch und strukturell charakterisiert: *P. falciparum* Hexokinase (PfHK) und Pyruvatkinase (PfPK). Es wurde bestätigt, dass PfHK ein Ziel sowohl für S-Glutathionylierung als auch für S-Nitrosierung ist. Während beide oxPTMs die enzymatische Aktivität hemmen können, wurde gezeigt, dass Inkubationen mit Thioredoxin (PfTrx), Glutaredoxin (PfGrx) und Plasmoredoxin (PfPlrx) die Aktivität nach erfolgter Modifikation wiederherstellen. Darüber hinaus wurde die erste dreidimensionale Proteinstruktur von PfHK gelöst. Die Kristallstruktur offenbart eine *Plasmodium*-spezifische Insertion in der kleinen Domäne und bestätigt den bereits für die *Plasmodium vivax* Hexokinase beschriebenen Tetramer. Diese Oligomerisierung ist im Vergleich zu Hexokinasen anderer Organismen einzigartig. Für PfPK wurden C49 und C343 als wichtige Aminosäuren für die funktionelle und strukturelle Integrität des Enzyms identifiziert. Entsprechende Cystein-zu-Alanin-Mutanten zeigten verminderte enzymatische Aktivitäten und Substrataffinitäten. Darüber hinaus ergab die Strukturanalyse Konformationsänderungen innerhalb der Mutantenstrukturen, die mit den zuvor gezeigten Kinetikdaten übereinstimmen. Insgesamt sind die vorliegenden Ergebnisse ein wichtiger Beitrag zum Verständnis der komplexen Redox-Regulierung der glykolytischen Enzyme von *P. falciparum* und liefern, ergänzt durch die dreidimensionale Struktur, neue Erkenntnisse, die für das zukünftige strukturbasierte Wirkstoffdesign von Vorteil sein werden.

Bei Virusinfektionen sind sowohl die Wirtszelle als auch die viralen Proteine einem hohen Maß an oxidativem Stress ausgesetzt. Viren fehlt jedoch ein oxidatives Abwehrsystem, und im Gegensatz zu *P. falciparum* und vielen anderen Organismen ist kaum etwas über die Auswirkungen von oxPTMs auf virale Proteine bekannt. Die wenigen verfügbaren Studien zeigen gegensätzliche Ergebnisse: Je nach untersuchtem Virus und Protein können oxPTMs entweder hemmende oder verstärkende Auswirkungen auf die Funktion des Proteins oder die

gesamte Replikation haben. Coronaviren sind positiv-strängige, umhüllte RNA-Viren, die bei verschiedenen Säugetieren und Vögeln unterschiedliche Krankheiten verursachen. Beim Menschen verursachen Coronaviren in der Regel leichte Atemwegsinfektionen.

In dieser Arbeit wurden die bei der Untersuchung der oxPTMs von Proteinen aus *P. falciparum* gewonnenen methodischen Erkenntnisse auf die Nichtstrukturproteine (nsps) von Coronaviren übertragen. Unter ~30 verschiedenen nsps konnten mehrere Zielproteine für die S-Glutathionylierung identifiziert werden. Es wurde gezeigt, dass die Proteaseaktivität von nsp5 aus zwei Virusstämmen durch S-Glutathionylierung gehemmt wird. Durch Cystein-zu-Alanin-Mutanten von nsp9 des Virus, das als Auslöser des schweren akuten respiratorischen Syndroms (SARS-CoV) gilt, konnten außerdem einzelne Cysteine identifiziert werden, die möglicherweise anfälliger für Modifikationen sind. Zusammenfassend bieten die vorliegenden Daten neue Einblicke in die potenzielle Redox-Regulation von CoV-Proteinen durch oxPTMs. Abschließend fasst die vorliegende Arbeit die Ergebnisse eines Kooperationsprojektes kurz in einem Exkurs zusammen. Durch verschiedene experimentelle Ansätze konnte bestätigt werden, dass humanes Spektrin S-glutathionyliert wird.

LIST OF PUBLICATIONS

I. Henok Asfaw Sahile, Maria Santos Martínez-Martínez, **Melissa Dillenberger**, Katja Becker, Peter Imming **(2020)**: Synthesis and evaluation of antimycobacterial and antiplasmodial activities of hirsutellide A and its analogues. *ACS Omega,* 5(24): 14451-14460

II. Frederik Barbarino, Lucas Wäschenbach, Virginia Cavalho-Lemos, **Melissa Dillenberger**, Katja Becker, Holger Gohlke, Miriam M. Cortese-Krott **(2020)**: Targeting spectrin redox switches to regulate the mechanoproperties of red blood cells. *Biol Chem,* 402(3):317-331

III. Alice Legru, Federica Verdirosa, Jean-François Hernandez, Giusy Tassone, Filomena Sannio, Manuela Benvenuti, Pierre-Alexis Conde, Guillaume Bossis, Caitlyn A. Thomas, Michael W. Crowder, **Melissa Dillenberger**, Katja Becker, Cecilia Pozzi, Stefano Mangani, Jean-Denis Docquier, Laurent Gavara **(2021)**: 1,2,4-Triazole-3-thione compounds with a 4-ethyl alkyl/aryl sufide substituent are broad-spectrum metallo-β-lactamase inhibitors with re-sensitization activity. *Eur J Med Chem*, 226:113873

IV. Viktor A. Zapol'skii, Katja Becker, Ursula Bilitewski, Isabell Berneburg, **Melissa Dillenberger**, Stefan Jungwirth, Aditya Shekhar, Bastian Krueger, and Dieter E. Kaufmann **(2022)**: Chemistry of polyhalogenated nitrobutadienes, 17: Efficient synthesis of persubstituted chloroquinolyl-1*H*-pyrazoles and evaluation of their antimalarial, anti-SARS-CoV-2, antibacterial, and cytotoxic activities. *Beilstein J Org Chem*, 18:524-532

V. **Melissa Dillenberger**, Stefan Rahlfs, Katja Becker, Karin Fritz-Wolf: Prominent role of cysteine residues C49 and C343 in regulating *Plasmodium falciparum* pyruvate kinase activity. *Structure* - under review

VI. **Melissa Dillenberger**, Anke-Dorothee Werner, Ann-Sophie Velten, Stefan Rahlfs, Katja Becker, Karin Fritz-Wolf: Structural analysis of *Plasmodium falciparum* hexokinase provides novel information about the small domain containing a *Plasmodium*-specific insertion, *JBC* - under review

---

VII. Anke-Dorothee Werner, Martin Schauflinger, Michael Norris, Michael Klüver, Anna Trodler, **Melissa Dillenberger**, Astrid Herwig, Gerhard Klebe, Andreas Heine, Erica Ollmann Saphire, Stephan Becker**:** Butterflies reaching out - the previously unresolved C-terminus of Sudan Ebolavirus VP40 reveals functionally important posttranslational redox modifications - in preparation

VIII. Parviz Ghezellou, **Melissa Dillenberger**, Seyed Mahdi Kazemi, Daniel Jestrzemski Bernhard Hellmann, and Bernhard Spengler: Comparative venom proteomics of Iranian, *Macrovipera lebetina cernovi* and Cypriot, *Macrovipera lebetina lebetina*, giant vipers. *Toxins* - in preparation

CONTRIBUTION TO CONFERENCES

September 2018	**11th Annual GGL Conference 2018, Giessen, Germany** **Poster**: Posttranslational modifications of glycolytic enzymes of *Plasmodium falciparum*
November 2018	**1st Retreat of the LOEWE Center DRUID, "Novel Drug Targets against Poverty-Related and Neglected Tropical Infectious Diseases", Rauischholzhausen Castle, Germany** **Talk**: Posttranslational redox modifications as potential nanoswitches in apicomplexan parasites and viruses
March 2019	**8th Symposion of the DFG Priority Program 1710 „Dynamics of Thiol-based Redox Switches in Cellular Physiology", Rauischholzhausen Castle, Germany** **Talk**: Posttranslational redox modifications as potential nanoswitches in viral proteins
September 2019	**12th Annual GGL Conference 2019, Giessen, Germany** **Poster**: Posttranslational modifications of glycolytic enzymes of *Plasmodium falciparum*
February 2020	**Molecular Approaches to Malaria, Lorne, Australia** **Poster**: Posttranslational redox modifications as regulators of *Plasmodium falciparum* glycolysis
September 2020	**First Digital GGL Annual Conference 2020** **Talk**: Posttranslational redox modifications as regulators of *Plasmodium falciparum* glycolysis
March 2021	**International Symposium of the DFG Priority Program 1710 Dynamics of Thiol-based Redox Switches in Cellular Physiology** **Talk**: Posttranslational redox modifications as regulators of *Plasmodium falciparum* glycolysis

CONTENT

LIST OF FIGURES

LIST OF TABLES

LIST OF ABBREVIATIONS

ADP	adenosine diphosphate
ADRP	ADP-ribose-1''-phosphatase
AMP-PNP	adenylyl-imidodiphosphate
ATP	adenosine triphosphate
CgHK	*Cryptosporidium parvum* hexokinase
CoV	coronavirus
CTP	cytidine triphosphate
Cys-NO	S-nitroso cysteine
DTT	dithiothreitol
E protein	envelope protein
EAV	equine arteritis virus
eNOS	endothelial nitric oxide synthases
ER	endoplasmic reticulum
ERGIC	ER-Golgi intermediate compartment
ESI-MS	electrospray ionization mass spectrometry
FCoV	feline coronavirus
FDA	U.S. Food and Drug Administration
G6P	glucose-6-phosphate
G6PD	glucose-6-phosphate dehydrogenase
GAPDH	glyceraldehyde-3-phosphate dehydrogenase
Gpx	glutathione peroxidase
GR	glutathione reductase
Grx	glutaredoxin
GS	glutathione synthetase
GSH	reduced glutathione
GSNO	S-nitrosoglutathione
GSNOR	S-nitrosoglutathione reductase
GSSG	oxidized glutathione/glutathione disulfide
GST	glutathione S-transferase
GTP	guanosine triphosphate
HCoV-229E	human coronavirus 229E
HCoV-NL63	human coronavirus NL63
HDX-MS	hydrogen-deuterium exchange mass spectrometry
HE	hemagglutinin-esterase
HKIV	mammalian hexokinase IV

HTS	high-throughput screening
iNOS	inducible nitric oxide synthases
ITP	inosine triphosphate
kDa	kilodalton
M protein	membrane protein
MACS	magnet activated cell sorting
MERS	Middle-East respiratory syndrome
M^{pro}	main protease
MS	mass spectrometry
MWCO	molecular weight cut off
N protein	nucleocapsid protein
NAD/H	nicotinamide adenine dinucleotide
NADP/H	nicotinamide adenine dinucleotide phosphate
NendoU	endoribonuclease (nsp15)
NiRAN	nidovirus RdRp-associated nucleotidyltransferase
NMP	nucleoside monophosphate
NMR	nuclear magnetic resonance
nNOS	neuronal nitric oxide synthases
NO	nitric oxide
NOS	nitric oxide synthases
nsp	nonstructural protein
ORF	open reading frame
PEDV	porcine epidemic diarrhea virus
PEG	polyethylenglycol
PEP	phosphoenolpyruvate
PfGAPDH	*P. falciparum* glyceraldehyde-3-phosphate dehydrogenase
PfGrx	*P. falciparum* glutaredoxin
PfHK	*P. falciparum* hexokinase
PfOAT	*P. falciparum* ornithine aminotransferase
PfPFK	*P. falciparum* phosphofructokinase
PfPK	*P. falciparum* pyruvate kinase
PfPlrx	*P. falciparum* plasmoredoxin
PfTrx	*P. falciparum* thioredoxin
PKM2	human pyruvate kinase M2
PL^{pro}	papain-like protease
PP_i	inorganic pyrophosphate
Prx	peroxidredoxin

PvHK	*P. vivax* hexokinase
RBC	red blood cell
RBD	receptor binding domain
RCS	reactive carbonyl species
RdRp	RNA-dependent RNA polymerase
RNA	ribonucleic acid
RNS	reactive nitrosative species
ROS	reactive oxidative species
RSS	reactive sulfur species
RTC	replication and transcription complex
S protein	spike protein
SARS	severe acute respiratory syndrome
SARS-CoV	severe acute respiratory syndrom coronavirus
SDS-PAGE	sodium dodecyl sulfate polyacrylamide gel electrophoresis
SEC	size exclusion chromatography
ssRNA	single-stranded RNA
t-BOOH	*tert*-butyl hydroperoxide
TbHK	*Trypanosoma brucei* hexokinase
TGEV	transmissible gastroenteritis virus
TgHK	*Toxoplasma gondii* hexokinase
TM	transmembrane
TRS	transcriptional regulatory sequence
Trx	thioredoxin
TrxR	thioredoxin reductase
TTP	thymidine triphosphate
UTP	uridine triphosphate
WHO	World Health Organization
γGCS	γ-glutamylcysteine synthetase

1 Introduction

1.1 Oxidative posttranslational modifications

Oxidative posttranslational modifications (oxPTMs) are caused, *inter alia*, by reactive oxygen species (ROS) and reactive nitrogen species (RNS). These species are addressed in many important research fields in both health and disease, but also in aging. Besides ROS and RNS, also reactive sulfur (RSS), reactive carbonyl species (RCS) and many more can disrupt the intracellular redox equilibrium (Mock and Dietz, 2016). RNS comprise nitric oxide (NO) and peroxynitrite ($ONOO^-$), whereas singlet oxygen ($^1O_2$), superoxide ($O_2^{\bullet}$), hydrogen peroxide (H_2O_2), hydroxyl radical ($OH^{\bullet}$) and hydroperoxides (ROOH) belong to ROS (Mock and Dietz, 2016). Increased levels of ROS and/or RNS are known as so-called oxidative or nitrosative stress and associated with molecular damage and cytotoxicity (Sies and Jones, 2020; Winterbourn and Hampton, 2008). ROS and RNS can be either produced endogenously or are evoked by environmental factors, the latter can be supplied on purpose – by smoking, for instance – or are released endogenously (Hawkins and Davies, 2019). Physiological redox signaling with low levels of ROS or RNS is also called “oxidative eustress” and can contribute to intracellular redox regulation, for example increasing the expression of redox-active enzymes (Sies and Jones, 2020; Winterbourn and Hampton, 2008). These redox-active enzymes, but also non-enzymatic systems can prevent oxidative damage by rapidly responding to disruptions of the intracellular redox equilibrium (Groitl and Jakob, 2014).

There are a variety of intracellular systems to maintain a proper redox state. The most important contributor is glutathione (GSH). The ratio between its reduced state (GSH) and its oxidized state (GSSG) is an important indicator of the intracellular redox equilibrium (Dalle-Donne et al., 2007). Furthermore, many proteins and enzymes participate in maintaining physiological levels by detoxifying excess ROS and RNS. Glutathione peroxidases, for example, are glutathione-dependent and reduce hydroxyperoxides via a disulfide/dithiol exchange mechanism (Brigelius-Flohé and Flohé, 2020). Peroxiredoxins (Prx) can effectively detoxify ROS and $ONOO^-$, superoxide dismutases contribute to scavenging $O_2^{\bullet}$ and H_2O_2 is degraded by catalases (Alfonso-Prieto et al., 2009; Gretes et al., 2012; Rhee et al., 2018).

The reduction of oxidated thiols is often mediated by oxidoreductases, including the thioredoxin (Trx) and the glutaredoxin (Grx) systems. Both Trx and Grx possess a conserved Trx fold, the Cys-X-Y-Cys motif, to reduce target proteins and thus prevent them from overoxidation. After reducing the target protein, Trx is oxidized and needs to be reduced by thioredoxin reductase (TrxR) utilizing protonated nicotinamide adenine dinucleotide phosphate (NADPH). Grx catalyzes the reduction of S-glutathionylated thiols, yielding S-glutathionylated Grx. Further reaction of Grx with GSH reduces the Grx thiols, in turn, and releases GSSG. The glutathione

reductase (GR) subsequently catalyzes the reduction of the GSSG molecule yielding GSH, which is also dependent on NADPH (Groitl and Jakob, 2014).

OxPTMs can be categorized into spontaneous reactions and those catalyzed by enzymes (Mock and Dietz, 2016). Spontaneous reactions can either be the formation of an intra- and intermolecular disulfide or the addition of a glutathione or nitric oxide to a protein's cysteine (Rahbari et al., 2015). Cysteines are semi-essential amino acids and are highly conserved within protein sequences of different species, while also being "the least abundant amino acid in proteins" (Matsui et al., 2020). From an evolutionary perspective, higher cysteine levels are associated with higher biological complexity (Grek et al., 2013). Due their core sulfur atom, which contains sixteen electrons, cysteines allow various oxidation states (Chung et al., 2013). This leads to different redox potentials and, in consequence, to different susceptibilities to redox modifications. The lower the pK_a value of a cysteine's thiol group, the more likely it is to react with an oxidant (Winterbourn and Hampton, 2008; Zhang et al., 2018). Reversible oxPTMs include disulfide formation, S-nitrosation, S-glutathionylation, S-sulfhydration and S-sulfenylation (Figure 1). S-sulfenylated thiols are often stated as "intermediates" due to their high reactivity and rapid reactions with other proteins or non-protein thiols. S-sulfinylation and S-sulfonylation instead, are more stable and often irreversible (Groitl and Jakob, 2014; Shi and Carroll, 2020). S-nitrosation and S-glutathionylation are described in more detail in the following chapters. All those modifications can target single proteins under both physiological and pathological conditions, can either activate or inhibit target proteins and, therefore, can affect function, structure, or localization of proteins. Furthermore, redox regulation via posttranslational modifications (PTM) of cysteines can influence metabolism and signaling pathways (Groitl and Jakob, 2014; Jortzik et al., 2012).

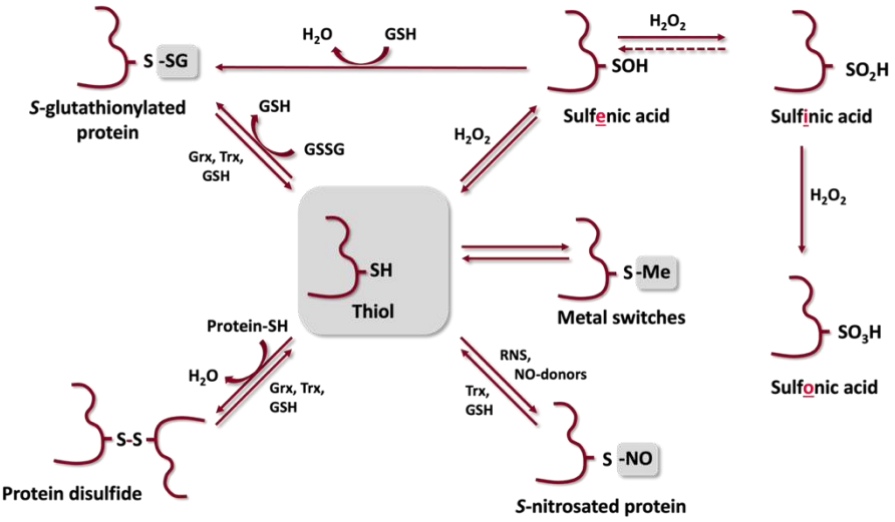

Figure 1 - Dynamic thiol switches.
Due to their core sulfur atom, thiols can have various redox potentials with different susceptibilities to oxidative posttranslational modifications (oxPTMs). They can be categorized into spontaneous reactions and enzymatically catalyzed reactions, resulting in different oxPTMs. Adapted from Rahbari et al., 2015.

During the last decade, not only the detection of modified cysteines via proteomic approaches has improved, mainly due to advances in mass spectrometry analysis, but also different kinds of redox probes have been developed to determine very sensitively the redox states of whole cells or single compartments. These methodological advances allow to detect and quantify redox modifications on amino acid level and also cluster their occurrence in different pathways (Gould et al., 2015; Hawkins and Davies, 2019; Schipper et al., 2021; Schuh et al., 2018). Nevertheless, a major challenge remains that especially S-sulfenylation, but also S-nitrosation, are transient intermediates that can quickly react to other oxidative states (Dalle-Donne et al., 2007; Matsui et al., 2020; Schipper et al., 2021).

1.1.1 S-Glutathionylation

With concentrations of ~1-10 mM in tissues, reduced glutathione is the most abundant intracellular thiol and therefore, as stated previously, an important contributor to intracellular redox homeostasis (Barbarino et al., 2021; Checconi et al., 2019). Under basal conditions, the GSH/GSSG ratio is often reported to be approximately 100:1 and therefore reducing (Kalinina et al., 2014; Matsui et al., 2020). However, in blood samples this ratio can be even higher and reaches almost 700:1 (Giustarini et al., 2013). In the context of many pathological processes, a disbalance of the intracellular GSH/GSSG ratio is reported. This disbalance can enhance protein oxidation and potentially lead to irreversible cell damage. Already small shifts of this ratio can promote S-glutathionylation (Dalle-Donne et al., 2007). Upon protein S-glutathionylation, glutathione forms a reversible mixed disulfide with protein cysteines. This reaction occurs either spontaneously or via enzymatic catalysis (Checconi et al., 2019). Upon all oxPTMs targeting thiols, S-glutathionylation is observed most frequently and occurs under both physiological and pathophysiological conditions (Jortzik et al., 2012; Kehr et al., 2011).
Spontaneous S-glutathionylation reactions include the disulfide exchange between the oxidized form GSSG and a reduced thiol or, in the presence of oxidants, a reaction between the reduced form GSH and the sulfenic acid of a cysteine residue or a S-nitrosothiol (Checconi et al., 2019; Dalle-Donne et al., 2007). S-nitrosoglutathione represents a more reactive oxidized form of glutathione and can induce not only S-glutathionylation of protein cysteines, but also S-nitrosation (Dalle-Donne et al., 2007; Kehr et al., 2011). Glutathione S-transferase (GST) and less often also Grx can catalyze S-glutathionylation (Grek et al., 2013; Matsui et al., 2020; Ye et al., 2017). Besides the prevention from overoxidation of protein thiols via S-glutathionylation, it can also provide an intracellular “storage mechanism for glutathione”, reaching levels of 20-50% S-glutathionylated protein thiols. S-glutathionylation can result in a temporary loss of the protein’s function or activity but is usually reversible. Upon severe oxidative stress and irreversible oxidation of protein thiols, proteins can no longer be regulated by S-glutathionylation and lose their function or activity (Figure 2) (Dalle-Donne et al., 2007).

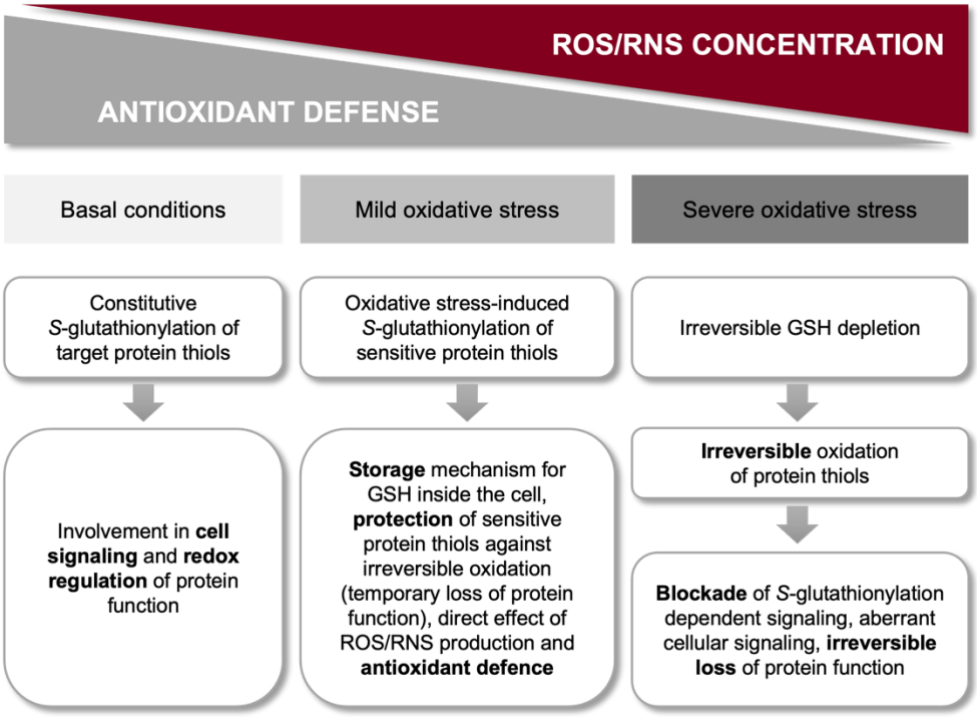

Figure 2 - Protein S-glutathionylation under different oxidative stress levels.
Under mild oxidative stress, S-glutathionylation is involved in cell signaling and redox regulation of numerous proteins. When ROS and RNS levels increase, S-glutathionylation can protect protein thiols and serve as intracellular GSH storage mechanism. Severe oxidative stress leads to irreversible oxidation of protein thiols and blocks S-glutathionylation dependent signaling. Adapted from Dalle-Donne et al., 2007.

The stability and reversibility of this modification is dependent on the oxidative state of the cell. Under oxidizing conditions, protein thiols usually remain S-glutathionylated. As soon as the intracellular redox state changes to reducing conditions, S-glutathionylation can be easily reversed (Dalle-Donne et al., 2007). The removal of a glutathione molecule from a protein's cysteine is known as deglutathionylation and restores the cysteine. The oxidoreductases Grx and Trx catalyze deglutathionylation via a dithiol exchange mechanism (Kehr et al., 2011). Sulfiredoxin, another member of the oxidoreductase family, is also known to reverse S-glutathionylation (Findlay et al., 2006; Grek et al., 2013). A prerequisite for proper deglutathionylation is a reducing environment which is represented by an adequate GSH/GSSG ratio (Dalle-Donne et al., 2007).

There are different techniques to detect and/or quantify S-glutathionylation and the methods used are under continuous improvement. The glutathione moiety can be detected and quantified directly via radiolabeled GSH and subsequent radiography (Grek et al., 2013). Indirect methods are either using biotinylated GSH or remove the GSH enzymatically and add, for example, biotin-maleimide. Avidin resins are used to separate biotinylated (originally S-glutathionylated) proteins. To identify the modified site(s) of a protein, samples can be objected to mass spectrometry. Besides labeled proteins, mass spectrometry is also providing reliable results for label-free quantification of S-glutathionylated protein sites. Compared to the whole proteome, modified proteins are less abundant. This is why affinity enrichment is often

used to enhance signal intensities (Matsui et al., 2020). Furthermore, commercially available GSH antibodies combined with immunoprecipitation and immunoblotting can detect modified proteins (Grek et al., 2013; Kehr et al., 2011).

1.1.2 S-Nitrosation

NO can be endogenously produced by nitric oxide synthases (NOS) and has a complex biological chemistry (Heinrich et al., 2013; Wynia-Smith and Smith, 2017). Biological signaling of NO can be achieved through S-nitrosation and influences a variety of cellular processes in health and disease. By targeting susceptibly cysteine residues, S-nitrosation can specifically regulate protein function and activity (Stomberski et al., 2019). The main source of NO production are NOS. In mammals, three distinct isoforms of NOS exist: endothelial NOS (eNOS), inducible NOS (iNOS) and neuronal NOS (nNOS) (Alderton et al., 2001). Determination of intracellular NO levels is challenging since NO diffusion happens rapidly and in various ways after its synthesis. Additionally, the definition of physiological concentrations is quite divers. A reasonable range of NO operation seems to be 100 pM to 5 nM, although also concentrations in the micromolar range were measured, depending on the respective tissue (Hall and Garthwaite, 2009).

In literature, S-nitrosation and S-nitrosylation are often used within the same context, but chemically, these terms must be differentiated. Nitrosation is defined as the addition of a nitroso group (nitrosonium ion, NO^+), whereas nitrosylation is defined as the addition of a nitrosyl group (NO radical, $NO^\bullet$) (Heinrich et al., 2013; Martínez-Ruiz and Lamas, 2004). Since the lifetime of NO^+ is very short under basal intracellular conditions on the one hand and a direct reaction between nitric oxide and a protein thiol is much too slow to operate physiologically on the other hand, a direct reaction of NO^+ is not considered to be biologically relevant. Instead, protein S-nitrosothiols are formed by the transfer of a NO^+ group from a NO^+ donor to the sulfur atom of a protein thiol and is, for above-mentioned reasons, properly called S-nitrosation. NO^+ donors for the formation of S-nitrosothiols can be for example dinitrogen trioxide: $N_2O_3 + R^- \rightarrow RSNO + NO_{2^-}$ (Heinrich et al., 2013). However, the most abundant physiological mechanism for S-nitrosation is trans-S-nitrosation, transferring the NO group between donor and acceptor thiol (Stomberski et al., 2019; Wynia-Smith and Smith, 2017). Also low molecular weight thiols like glutathione can be targeted by S-nitrosation, yielding S-nitrosoglutathione (GSNO) (Benhar et al., 2009). GSNO, in turn, can serve as a donor for trans-S-nitrosation of protein thiols (Broniowska et al., 2013). S-nitrosation is considered to occur with high specificity on target cysteine residues, commonly targeting only regulatory relevant thiols (Derakhshan et al., 2007; Kovacs and Lindermayr, 2013). The modification can be promoted by several enzymes, although scarcely is known about enzymes primarily catalyzing protein S-nitrosation (Hess et al., 2005). Anand and Stamler gave interesting

insights into the role of ‘nitrosylases’ and ‘denitrosylases’. Nitrosylases transfer the NO group either in the “Metal-to-Cys” or the “Cys-to-Cys” way, correctly referred to as trans-nitrosylase. Denitrosylases catalyze the removal of the NO group from thiols (Anand and Stamler, 2012). The Trx system is involved in S-nitrosation via trans-nitrosation and denitrosation. Upon both reactions, Trx is oxidized and needs the TrxR-mediated NAPDH-dependent reduction for recovery (Jedelská et al., 2020; Sengupta and Holmgren, 2013). The NADH-dependent GSNO reductase (GSNOR) catalyzes the denitrosation of GSNO (Barnett and Buxton, 2017; Benhar et al., 2009). This, in turn, provides GSH, which can rapidly reduce S-nitrosated protein thiols (Kalinina and Novichkova, 2021). A recent study describes mammalian Grx as a sufficient denitrosylase of low and high molecular weight thiols (Ren et al., 2019). Although the undisputed existence of potent ‘denitrosylases’, it has to be stated S-nitrosated thiols are considered to be intermediates, comparable to sulfenic acids, very labile and therefore, denitrosation does not necessarily require enzymes (Martínez-Ruiz and Lamas, 2004; Matsui et al., 2020).

The detection of S-nitrosated protein thiols is difficult for two major reasons: Firstly, intracellular levels of modified proteins are limited to a very low percentage and secondly, the modification is often an intermediate state due to its poor stability. S-nitrosation can be directly detected spectrophotometrically at 340 nm, via electrospray ionization mass spectrometry (ESI-MS) or nuclear magnetic resonance (NMR) with ^{15}N. Indirect detection methods are more commonly used and include the cleavage of the S-NO bond either to detect the released species (ozon chemiluminescence, Griess assay) or to replace the S-nitrosogroup with, for example, a biotinylated maleimide, using the biotin-switch method (Devarie-Baez et al., 2013; Forrester et al., 2009; Martínez-Ruiz and Lamas, 2004).

1.2 Malaria

Malaria is a serious infectious disease affecting global health by threatening people’s health and life. In 2020, the World Health Organization (WHO) reported a total of 241 million cases, leading to 627,000 deaths in 85 malaria endemic countries. Compared to the number of cases and deaths of the previous years, the burden of malaria has increased again. The annual WHO Malaria Report outlines disruptions in malaria services due to the COVID-19 pandemic as one of the reasons for this negative trend (World Health Organization, 2021). Malaria is caused by the protozoan parasite *Plasmodium* and transmitted by the bite of the female *Anopheles* ssp. mosquito. *Plasmodium* ssp. are eukaryotic single-celled microorganisms and belong to the phylum Apicomplexa. Parasites belonging to this phylum possess a unique structure, the apical complex, that is involved in cell invasion within the host (Phillips et al., 2017).

There are more than 100 *Plasmodium* species that can infect a variety of host species, but only five of them are known to cause malaria in humans: *P. falciparum*, *P. vivax*, *P. malariae*, *P. ovale* and *P. knowlesi*. The human pathogen species differ on their geographical distribution, the severity of infection and their incidences (Phillips et al., 2017; Tuteja, 2007). Among those, *P. vivax* is the most widespread species leading to severe infections. Due to its ability to enter hypnozoite stages, *P. vivax* can survive in climates that are more temperate and can lead to several malaria episodes. Infections with *P. falciparum* often cause more fatal cases and are responsible for the majority of reported deaths (Dayanand et al., 2018; Moxon et al., 2020). In total, more than 95% of all malaria infections are caused by *P. vivax* and *P. falciparum* (Loy et al., 2017). Pathogenesis and treatment of the disease, as well as the life cycle of the parasite, will be exemplified in the following section on *P. falciparum*.

1.2.1 *Plasmodium falciparum*

The origin of *P. falciparum* is controversial: the widespread hypothesis was that *P. falciparum* has co-evolved in both humans and chimpanzees, but novel findings suggest that the parasite was originally transmitted by gorillas (Loy et al., 2017). *P. falciparum* is found worldwide in tropical areas but reported predominantly in sub-Saharan Africa. It causes severe anemia and is responsible for the majority of fatal cases in children under the age of five (Moxon et al., 2020; Phillips et al., 2017).

Life cycle

P. falciparum has a complex life cycle, which can be separated into an asexual and a sexual state of reproduction. The asexual state is predominantly responsible for the clinical symptoms of the infection and comprises the mitotic replication of the parasites within human erythrocytes. The sexual state takes place within its second host, the female *Anopheles* mosquito.

The malaria infection starts with the bite of the female *Anopheles* mosquito, which injects the infective stage of *Plasmodium*, the sporozoites, into the skin of the human host (Figure 3). Being very motile, sporozoites can migrate into the lymph vessels and spread into the liver aiming for hepatocytes (Figure 3 B). Via asexual fissions, they develop into merozoites. One sporozoit can multiply to tens of thousands merozoites that are subsequently released into the blood, evading erythrocytes (Figure 3 C). The intraerythrocytic stage endures ~48 hours, while the parasite passes distinct asexual stages. Finally, the erythrocyte is hemolysed and releases merozoites back into the blood stream, evoking the clinical symptoms of malaria including fever and anemia. While most merozoites enter other erythrocytes, some of them develop into male or female gametocytes prior to the release into the blood (Figure 3 D). Through blood meals, these gametocytes can be taken up and infect further *Anopheles* mosquitos while fulfilling the sexual state of the life cycle. Within the mosquito's gut, male gametocytes produce

microgametes, while female gametocytes develop into macrogametes (Figure 3 E). Both stages fuse and form a diploid zygote, which transforms over 24 hours into a motile ookinete. During the migration of the gut's epithelium, the ookinete develops into an oocyst that, in turn, produces sporozoites upon replication (Figure 3 F). These sporozoites are released by ruptures of the oocysts and move towards the salivary glands of the mosquito, from where they can be transferred to another human host to start another life cycle (Cowman et al., 2016; Meibalan and Marti, 2017; Phillips et al., 2017; Wahlgren et al., 2017).

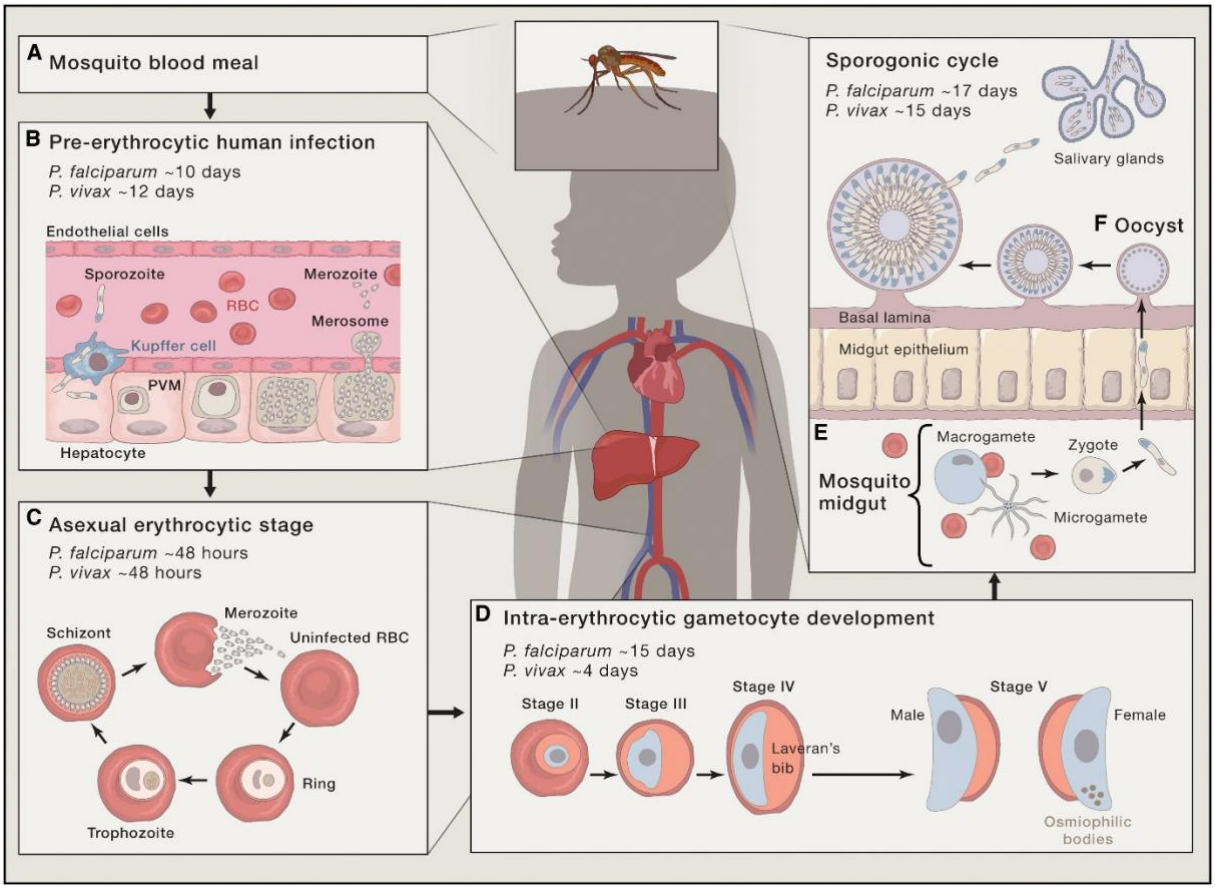

Figure 3 - Life cycle of *P. falciparum*.
P. falciparum life cycle is comprised of an asexual and a sexual state of reproduction. It starts with the bite of a female *Anopheles* mosquito, several asexual replication cycles in the human host. The subsequent transfer of gametocytes enables the completion of the sexual state (Cowman et al., 2016). For more details refer to the text.

Pathogenesis

The release of merozoites during the asexual erythrocytic stage causes periodic fever recurring every ~48 hours and is responsible for the clinical manifestation of a malaria infection. Besides these symptoms upon acute infection, intraerythrocytic stages are also responsible for further pathologies caused by *P. falciparum*: infected erythrocytes have an increased binding capacity and can therefore cause not only vascular obstruction but also activation of other blood cells which produce pro-inflammatory cytokines and serum glycoproteins. As a result, inflammation triggers the development of severe malaria and death (Haldar et al., 2018; Wahlgren et al., 2017). *P. falciparum* is responsible for severe malaria in most cases. Clinical symptoms of an infection can be divers, depending on various host and parasite factors and

are therefore difficult to confirm in diagnosis. Upon prostation, convulsions, jaundice, shock and coma, laboratory criteria like anemia and hyperparasitemia need to be assessed (Beeson and Brown, 2002; Plewes et al., 2019). Besides severe and mild malaria, there are also asymptomatic cases. Nevertheless asymptomatic malaria can, if untreated, cause anemia and lead to other serious health consequences (Chen et al., 2016).

Therapy and prevention

Essential for the survival of the patient is the early diagnosis and the prompt administration of effective antimalarials, otherwise mortality of severe malaria can reach up to 100%. Initial treatment usually starts with intravenous artesunate and is followed by an oral artemisinin-based combination therapy. Although treatment with these and other antimalarials were very efficient in the past, success of treatment decreases due to increasing resistances of *Plasmodium* against those drugs. For this reason, it is important not only to understand the mechanisms of how the parasites acquire resistance, but also to find novel strategies to develop effective antimalarials (Haldar et al., 2018; Plewes et al., 2019; Ross and Fidock, 2019). In 2021, the WHO recommended the RTS,S malaria vaccine to prevent *P. falciparum* malaria in children living in moderate to high transmission regions. The vaccination can reduce severe malaria up to 30% in children, but does not have any effects on infectivity or transmission (Duffy, 2022; Zavala, 2022). To minimize the risk of infection, the WHO further recommends the use of insecticide-treated mosquito nets or to kill mosquitos by using insecticide sprays inside the house. During pregnancy, women should be treated with preventive therapy (Thu et al., 2017; World Health Organization, 2021).

1.2.2 Redox regulation in *P. falciparum*

During its life cycle, *P. falciparum* must adopt to two different hosts, comprising different cell types and thus very divers environmental conditions each. In the mosquito host, the parasite faces an immune response associated with high levels of ROS and RNS (Clayton et al., 2014; Molina-Cruz et al., 2008). When entering hepatocytes of the human host, *Plasmodium* induces the generation of $OH^{\bullet}$ (Guha et al., 2006). The replication is located in erythrocytes, where the parasite is protected from the human immune system. During this stage, *P. falciparum* is exposed to extremely high levels of oxidative and nitrosative stress while getting in contact with host immune cells and molecules (Tran and Crompton, 2020). Moreover, erythrocytes contain ion and oxygen which can, when combined, lead to a pro-oxidant environment by forming ROS via the Fenton reaction (Müller, 2004).

The parasite itself produces high levels of toxic by-products that are redox active and increase during its rapid replication (Becker et al., 2004). As a source of amino acids, *Plasmodium* degrades human hemoglobin in its acidic food vacuole, whereby ion is oxidized, and superoxide anions are formed (Figure 4). This consequently promotes (i) the formation of H_2O_2

and OH• and (ii) the release of toxic free hem (ferri/ferroprotoporphyrin IX; FP IX), which can negatively affect both the host and the parasite, if not adequately neutralized. Nevertheless, most of the FP IX crystallizes and forms non-toxic hemozoin, referred to as malaria pigment (Becker et al., 2004; Tilley et al., 2001).

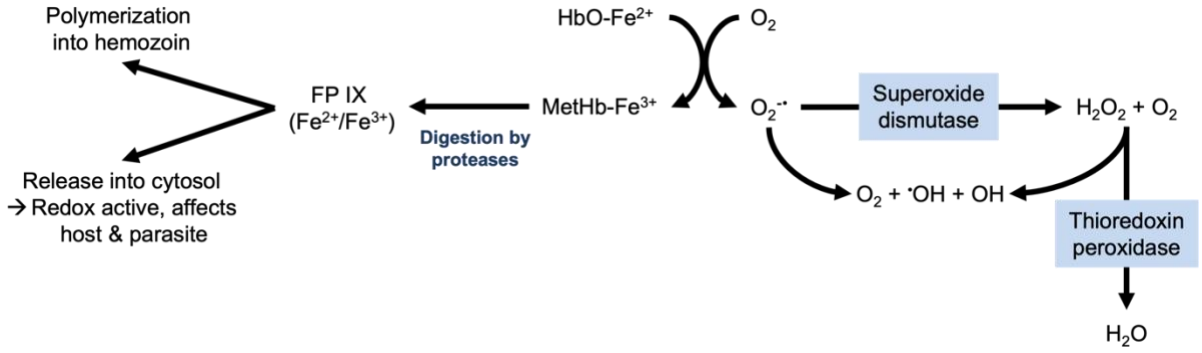

Figure 4 - Sources of reactive oxygen species in *P. falciparum.*
FP IX, ferri/ferroprotoporphyrin IX; HbO-Fe^{2+}, oxy-hemoglobin containing ferriprotoporphyrin IX; MetHb-Fe^{3+}, methemoglobin containing ferroprotoporphyrin IX. Adapted from Müller, 2004.

Unlike many other organisms, the parasite does not possess a catalase or a classical glutathione peroxidase (GPx). However, it is equipped with numerous very efficient low molecular weight antioxidants and antioxidative enzymes to ensure a redox balance that is sufficient for its survival. Among the low molecular weight antioxidants GSH is the most abundant one, and thus the central molecule of the glutathione redox system (Becker et al., 2004). The GSH/GSSG ratio is predominantly maintained by the reduction of GSSG to GSH, catalyzed by the NADPH-dependent disulfide oxidoreductase GR, which contains FAD as prosthetic group (Figure 5). Several studies have investigated the role of GR by solving its three-dimensional structure, gene knockouts and testing various inhibitors (Tiwari et al., 2021). Further contribution to an adequate GSH/GSSG ratio is ensured by GSSG-efflux pumps, protein S-glutathionylation and *de novo* synthesis of GSH by the γ-glutamylcysteine synthetase (γGCS) and the glutathione synthetase (GS) (Müller, 2004; Patzewitz et al., 2012). In addition, GSH acts as co-factor for redox-active proteins, for example glyoxalase, GPx-like thioredoxin peroxidase, GST or Grx. Glyoxylases detoxify (glycolysis-derived) methylglyoxal, whereas the GPx-like thioredoxin peroxidase only shows low reaction rates with GSH and is reduced by Trx (Sztajer et al., 2001). GST detoxifies electrophilic compounds by conjugation of GSH (Hiller et al., 2006). Grx, originally belonging to the Trx family, catalyzes the reduction of thiol-disulfides as well as deglutathionylation of proteins. In *P. falciparum*, there are three known Grxs (PfGrx1-3) that are non-enzymatically reduced by GSH (Tiwari et al., 2021).

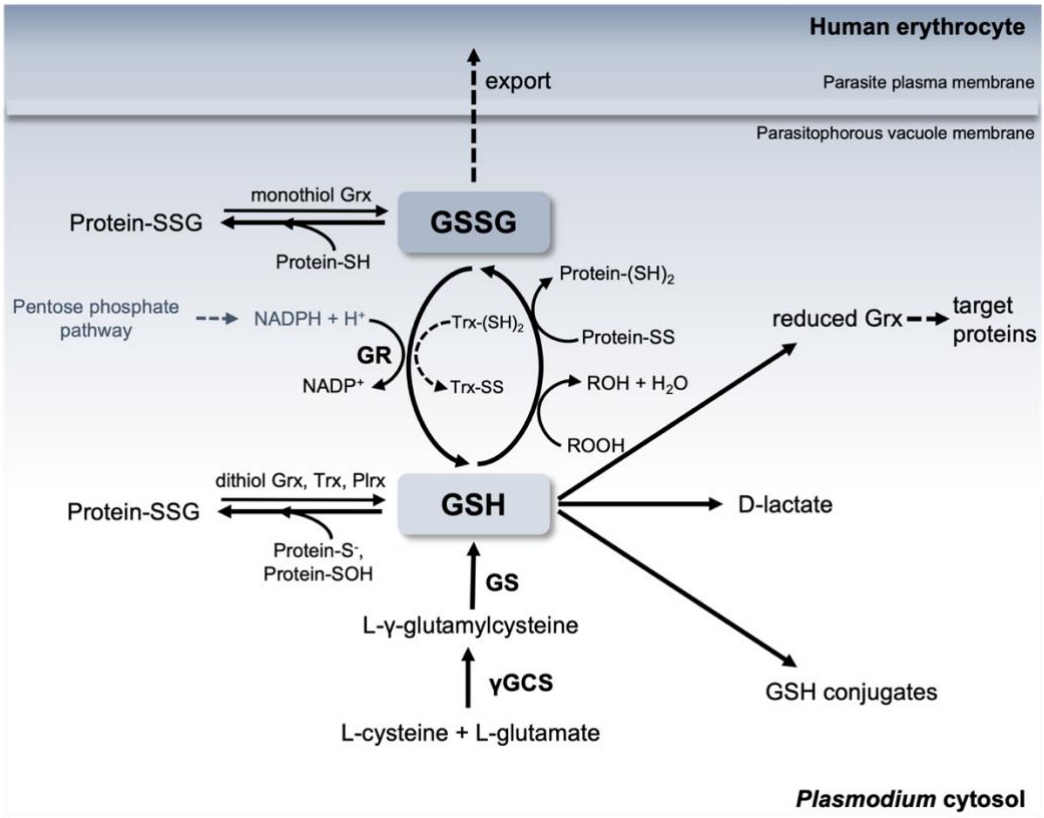

Figure 5 - The glutathione redox system in *P. falciparum*.
An adequate GSH/GSSG ratio is predominantly maintained by the GR. γGCS and GS catalyze *de novo* synthesis of GSH. Both GSH and GSSG can induce S-glutathionylation of protein thiols, involving different enzymes and non-enzymatic reactions. Moreover, GSSG can be exported into the human erythrocyte. Adapted from Jortzik and Becker, 2012.

Besides the glutathione redox system, the Trx redox system ensures proper redox homeostasis (Figure 6). Within this system, the NADPH-dependent TrxR, which was already validated as a drug target, reduces Trx. Two isoforms with similar kinetic parameters are expressed by the *trxr* gene and are located in the mitochondria and the cytosol. Like the GR, TrxR contains FAD as prosthetic group (Fritz-Wolf et al., 2013; Kehr et al., 2010). In *P. falciparum*, three classic Trxs have been identified. Their main function is to reduce target proteins, while depending on TrxR and NADPH that reduce Trx in turn. Trx1 is located in the cytosol and can reduce GSSG, detoxify hydrogene peroxide, and S-nitrosoglutathione. Furthermore, Trx1 contributes to the regulation via oxPTMs by restoring the activity of proteins through deglutathionylation of modified cysteines (Jortzik and Becker, 2012). Trx2 and Trx3 are located in the mitochondria and the endoplasmic reticulum, respectively, and are less intensively studied. Both can be reduced by TrxR, too (Kehr et al., 2010; Nickel et al., 2006). There are two Trx-like proteins expressed by the parasite that, in contrast to Trx, cannot be reduced by TrxR (Jortzik and Becker, 2012). Furthermore, *P. falciparum* possesses five Prxs that are capable of reducing H_2O_2, $ONOO^-$ and ROOH. Prx ist reduced by both Trx and Grx (Brandstaedter et al., 2019). A unique protein in *Plasmodium* sp. is plasmoredoxin (PfPlrx). Its function overlaps with those reported for Grx and Trx. Simultaneously, PfPlrx is reduced by

both proteins (Tiwari et al., 2021). *P. falciparum* has two genes encoding for superoxide dismutase, one of them ion-, the other manganese-dependent (Becker et al., 2004). Both catalyze the formation of hydrogen peroxide and oxygen by dismutation of $O_2^{\bullet}$ (Müller, 2004).

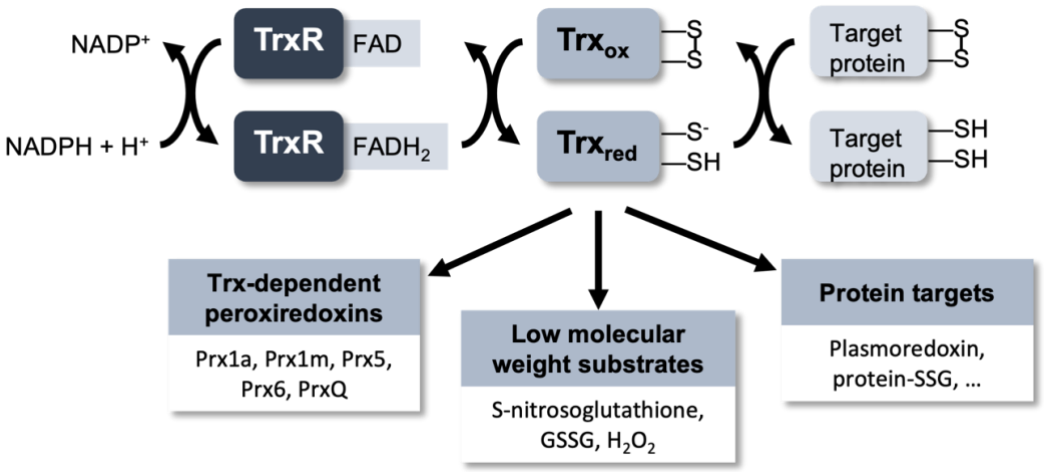

Figure 6 - The thioredoxin system of *P. falciparum*.
The TrxR is the central enzyme of the thioredoxin system by maintaining Trx in a reduced state to ensure its proper function. Trx reduces not only disulfides, but also Trx-dependent peroxiredoxins, low molecular weight substrates and other target proteins like plasmoredoxin or S-glutathionylated protein thiols. Adapted from Jortzik and Becker, 2014.

In the past decades, the interest in nitrosative and oxidative stress and the associated redox systems of *Plasmodium* has increased. Many drugs currently used within the artemisinin-based combination therapy in clinical practice are known to increase oxidative stress through their mechanism of action, while their exact cellular target remains unknown so far. Emerging resistances do not only emphasize the need to elucidate the mechanism of action, but also the importance of finding potent novel antimalaria drugs (Kavishe et al., 2017). The parasite's survival is highly dependent on its effective redox system, which makes the involved proteins and enzymes very promising drug targets and could provide novel strategies for antimalaria treatment (Tiwari et al., 2021).

1.2.3 *P. falciparum* glycolysis

Especially during its intraerythrocytic stage, *Plasmodium* is highly dependent on different energy supplies. In addition to amino acids yielding from hemoglobin degradation, metabolization of glucose via glycolysis serves as major adenosine triphosphate (ATP) supply. Infected erythrocytes have a more than 100-fold utilization of glucose compared with uninfected cells. During intra-erythrocytic stages, the parasite lacks active mitochondria and a citric acid cycle, which is why the majority of glucose passing the glycolytic pathway is metabolized to lactic acid (Mehta et al., 2006; Roth et al., 1988). Upon infection, many glycolytic enzymes within the erythrocyte are increased in their activity proportionally to parasitemia, particularly hexokinase (PfHK) and pyruvate kinase (PfPK) (Roth et al., 1988).

Several *Plasmodium* enzymes of the glycolytic pathway have been intensively studied to elucidate their role as potential drug targets, mainly due to their distinct three-dimensional structure or low sequence identity compared to their human counterparts. Besides structural differences, also the contribution of the respective enzyme to the glycolytic flux is highly relevant in the context of drug design (van Niekerk et al., 2016). Thus, targeting the regulatory enzymes PfHK, phosphofructokinase (PfPFK) and PfPK seems to be obvious. Those enzymes were already kinetically characterized and screened with regard to potential drug candidates. Nevertheless, there is scarcely any information about the three-dimensional structure of the three enzymes (Chan et al., 2007; Chan and Sim, 2005; Davis et al., 2016; Fisher et al., 2020; Harris et al., 2013; Mony et al., 2009; Tjhin et al., 2013; Zhong et al., 2020). Furthermore, all three of them seem to be massively redox regulated by oxPTMs (Figure 7), which was already shown in proteomic approaches as well as in enzymatic assays with recombinant enzymes (Kehr et al., 2010; Schipper et al., 2021; Wang et al., 2014).

In summary, targeting regulatory enzymes of the major energy supply while additionally focusing on their redox regulation, which is in accordance with current strategies of drug design, seems to be a very promising approach for novel antimalaria therapeutics. Both PfHK and PfPK contain fifteen cysteines each (3.05% and 2.98%, respectively) and are therefore considered to be exceptionally cysteine rich (Miseta and Csutora, 2000). This overrepresentation of cysteines provides a perfect basis for enzymatic regulation via oxPTMs.

PfHK

PfHK catalyzes the first reaction of glycolysis. In *P. falciparum* PfHK exists as single copy gene on chromosome 6. Among *Plasmodium* sp., hexokinases are well conserved, but show limited sequence identity with their human counterpart (< 32%). PfHK from infected erythrocytes was characterized for the first time in 1987 by Roth et al., while the recombinant enzyme was kinetically characterized more than two decades later (Harris et al., 2013; Roth, 1987). Within the latter study, PfHK was expressed in a codon optimized form with a molecular mass of 55.3 kDa. The enzyme catalyzes the phosphorylation of glucose to glucose-6-phosphate (G6P), while the phosphoryl group is provided by ATP. G6P is not only important for maintaining the glycolytic flux, but also crucial and rate-limiting for the pentose phosphate pathway ensuring the supply of NADPH for the maintenance of a reduced environment by G6P dehydrogenase (Roth, 1987). PfHK is only active in the presence of Mg^{2+} or other divalent cations, for example Mn^{2+}. The enzyme was shown to be inhibited by its substrate ATP and by its products adenosine diphosphate (ADP) and G6P. Alternative phosphoryl donors like UTP, GTP, CTP, TTP, ITP (uridine, guanosine, cytidine, thymidine, and inosine triphosphate) and inorganic pyrophosphate (PP_i) were tested without any measurable enzymatic activity of PfHK. Since the kinetic characteristics of PfHK were comparable for those measured for *Trypanosoma brucei* hexokinase (TbHK), small-molecule inhibitors originally identified for

TbHK were tested against PfHK and *P. falciparum* cell culture, revealing potent inhibitors (Harris et al., 2013). These results were followed by a high-throughput screening (HTS) assay, which identified further compounds to be active against the parasite and to have low toxicity toward human cell lines (Davis et al., 2016). Despite all these promising results, a three-dimensional structure of PfHK is not solved so far.

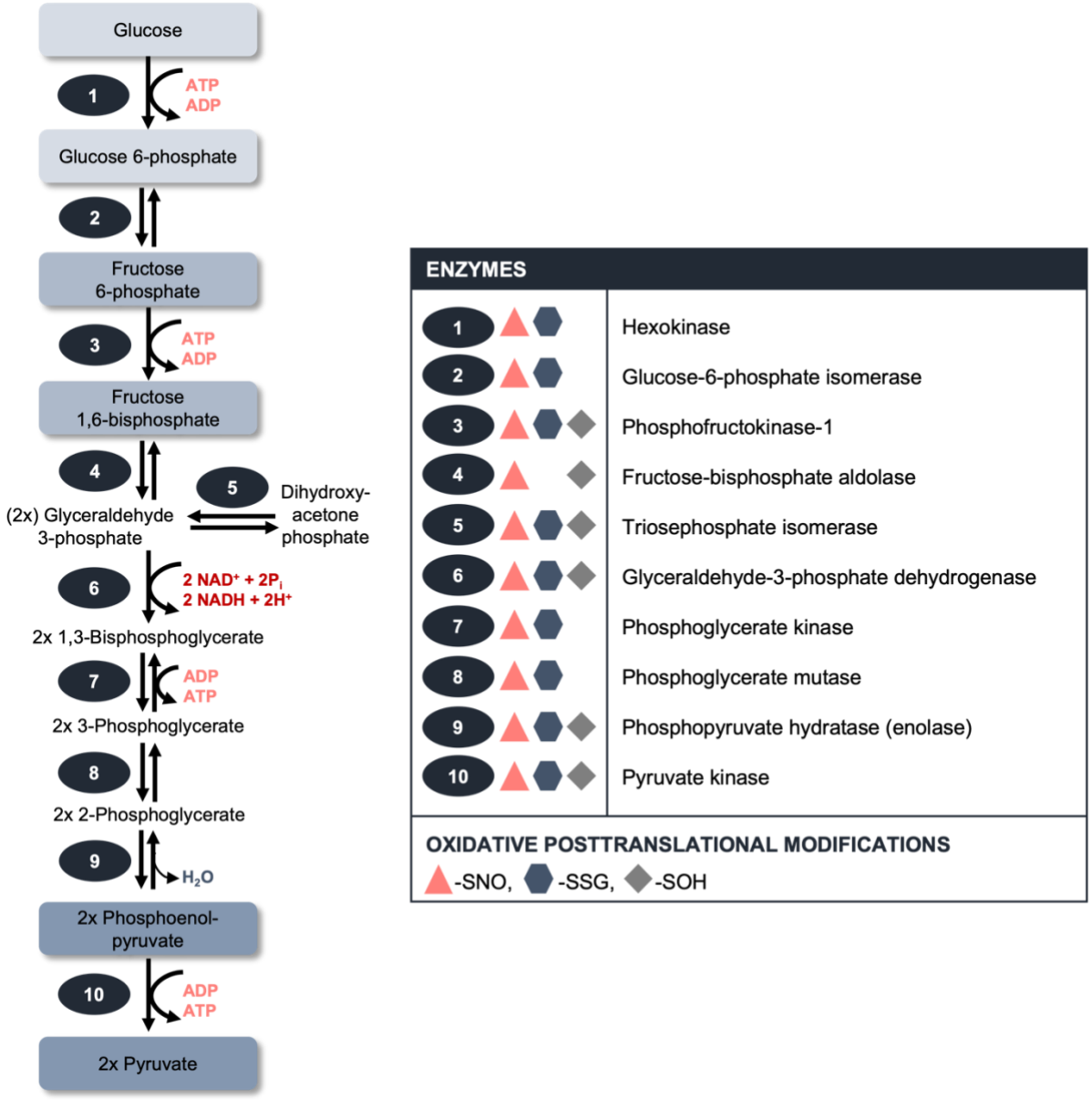

Figure 7 - Oxidative posttranslational modifications of *P. falciparum* glycolytic enzymes.
P. falciparum glycolytic enzymes were found to be massively redox regulated by oxPTMs. Proteomic analyses revealed targets for -SNO (S-nitrosation), -SSG (S-glutathionylation) and -SOH (S-sulfenylation) (Kehr et al., 2011; Schipper et al., 2021; Wang et al., 2014). Adapted from Schipper, 2021.

PfPFK

In *Plasmodium*, there are two genes encoding an ATP-dependent PfPFK, one on chromosome 9 and the other on chromosome 11. While the PfPFK encoded by chromosome 11 seems to be non-essential for the parasite, the other one is indispensable and leads to the expression of an enzyme with a size of 160 kDa. In previous studies, PfPFK was

characterized by expressing two subunits of the enzyme that are homologous to the α and β subunits, revealing the β subunit to be catalytically relevant and ATP-dependent. Furthermore, PfPFK is considered to be involved in mechanisms of drug resistance. PfPFK catalyzes the conversion of fructose-6-phosphate to fructose-1,6-bisphosphate, which is the rate-limiting step of glycolysis (Fisher et al., 2020; Mony et al., 2009).

PfPK

The last step of glycolysis is catalyzed by PfPK, an enzyme with a molecular mass of 55.6 kDa. During catalysis, phosphoenolpyruvate (PEP) is converted into the highly versatile metabolite pyruvate, while its phosphate group is transferred to ADP yielding ATP. As already observed for PfHK, the reaction requires divalent cations like Mg^{2+} and, additionally, monovalent cations like K^{+}. In intraerythrocytic stages, two isoenzymes of PfPK are expressed that share a low sequence identity (~20%). PfPK1 (chromosome 6) is localized in the cytosol and involved in glycolysis, whereas PfPK2 (chromosome 10) is predicted to be localized in the apicoplast and involved in the lipid metabolism. Furthermore, PfPK2 has been reported to have lower transcription levels (Chan et al., 2007; Maeda et al., 2009). Within this study, only PfPK1 is considered and therefore referred to as PfPK. The enzyme exists as homotetramer and its activity seems not to be affected by known activators of the enzyme like fructose-1,6-bisphosphate or G6P. ATP, citrate and pyridoxal-5'-phosphate were shown to inhibit the enzyme (Chan and Sim, 2005). A recent study presented the first crystal structure of PfPK complexed with oxalate and ATP. The authors describe both an active (R-state) and an inactive (T-state) conformation of the enzyme evoked by a rotation of the B-domain. Furthermore, they suggest G6P to bind on the effector binding site with a stabilizing effect on the enzyme and thereby opposing the results of previous studies (Zhong et al., 2020).

1.3 Coronaviruses

Coronaviruses (CoV) are enveloped, positive-stranded RNA viruses that can cause upper respiratory, gastrointestinal, and central nervous system diseases in various mammalian and avian species (Fenouillet et al., 2007; te Velthuis et al., 2012). Human coronaviruses usually cause mild respiratory tract infections and were first identified in the 1960s (Hamre and Procknow, 1966). Currently known species are HCoV-229E, HCoV-OC43, HCoV-NL63 and HCoV-HKU1 (V'kovski et al., 2020). Coronaviruses belong to the subfamily *Coronovirinae* in the family *Coronaviridae* and the order *Nidovirales* (International Committee on Taxonomy of Viruses). The subfamily consists of four genera: *Alphacoronavirus*, *Betacoronavirus*, *Gammacoronavirus*, and *Deltacoronavirus*, from which the first two solely infect mammals, whereas the other two predominantly infect avian species (Cui et al., 2019).

During the twenty-first century, three novel human pathogen coronaviruses have emerged, all leading to severe acute respiratory distress syndrome and high levels of mortality. In 2002, a previously unrecognized animal coronavirus caused the severe acute respiratory syndrome (SARS) with a mortality rate of more than 10% (Graham et al., 2013). More than 8,000 people in almost 30 countries across five continents were infected within a few weeks (Peiris et al., 2004). Nearly a decade later, the Middle East respiratory syndrome (MERS) occurred in Saudi Arabia (Cunha and Opal, 2014). In contrast to SARS-CoV, MERS-CoV caused 36% mortality in infected individuals (Davis et al., 2016). The pandemic potential as well as the global impact of emerging infectious diseases was already recognized, but no efficacious drugs or vaccines were developed at that time (Peiris et al., 2004; V'kovski et al., 2020). In 2019, a third highly pathogenic coronavirus was detected in Wuhan, China, referred to as SARS-CoV-2. It rapidly spread all over the world leading to ~400 million reported cases after about two years. Compared to SARS-CoV, the mortality rate was remarkably low (~1.5%) ("WHO Coronavirus (COVID-19) Dashboard," 2022). Although very potent vaccines have been developed, emerging mutations of the virus have challenged the world several times by overcoming the protection by the vaccine (Wratil et al., 2022).

Morphology

Coronaviruses are described as spheric and pleomorphic particles with an average diameter of 80-120 nm. There are four major structural proteins within the lipid bilayer (Figure 8): the envelope (E) protein, the spike (S) protein, the membrane (M) protein and the nucleocapsid (N) protein (Schoeman and Fielding, 2019).

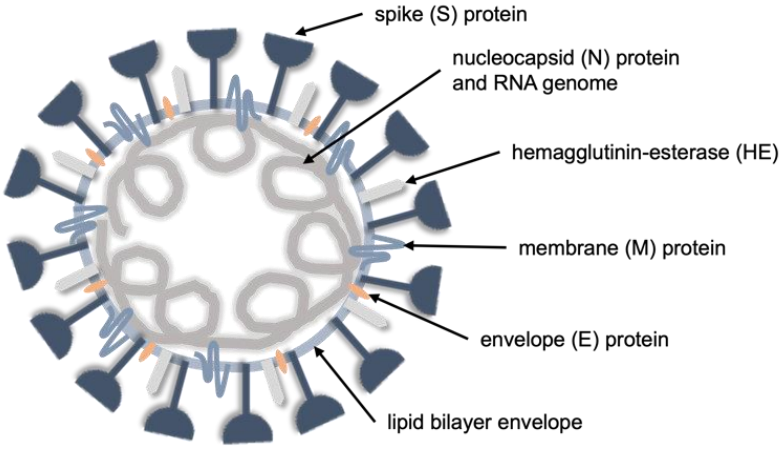

Figure 8 - Coronavirus virion, schematic representation.
Adapted from Masters, 2006.

The E protein is a small viroporin important for viral assembly and egress (Venkatagopalan et al., 2015). The club-shaped surface spike proteins are responsible for the typical crown-like appearance and protrude 17-20 nm from the viral envelope (Masters, 2006). Within this envelope, the M protein is most abundant and shapes the envelope. It is involved in the formation of virion envelopes and interacts with the N protein (Neuman et al., 2011). The main

function of the N protein is to bind to the RNA genome forming the nucleocapsid (de Haan and Rottier, 2005). Some coronaviruses have another type of surface projection in addition to the S protein, which are 8 nm projections of homodimeric hemagglutinin-esterase (HE), contributing to virion attachment (Lang et al., 2020).

1.3.1 Genome organization and replication

With a range of 27 to 32 kb in length, coronaviruses have the largest currently known viral RNA genome. About two-third of the genome encodes the viral replicase, the other third encodes for structural and accessory proteins (Fehr and Perlman, 2015). For the viral entry into the host cell, the virus is highly dependent on its homotrimeric S protein. The protein contains a receptor-binding domain (RBD) to interact with the host receptor and induces membrane fusion. Subsequently, the N-coated RNA genome is released into the host's cytoplasm (Hartenian et al., 2020). The RNA has a 3' poly(A) tail and is protected by a cap structure at the 5' end, which allows it to act like mRNA. The coronavirus replicase gene is comprised of two large open reading frames (ORF): ORF1a and ORF1b that are both located at the 5' end of the genome (Figure 9).

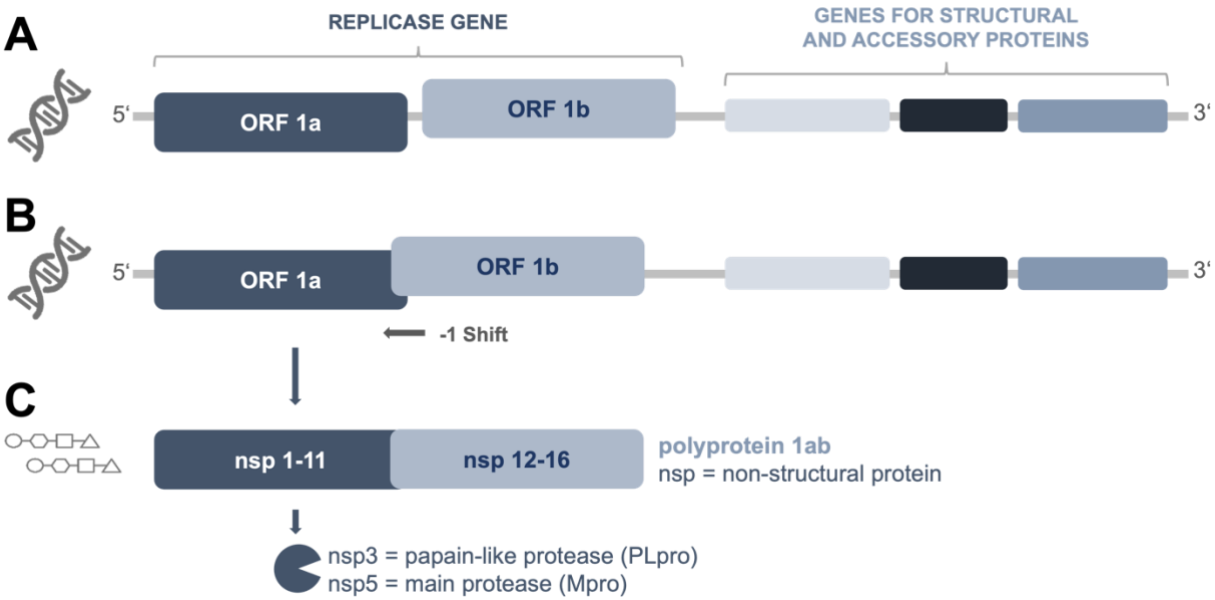

Figure 9 - Genome organization of coronaviruses.
Two thirds of the viral genome are occupied by genes encoding for coronavirus replicase proteins (open reading frame (ORF) 1a and 1b, encoding nonstructural proteins (nsps)). Expression of the polyprotein 1ab requires a ribosomal frameshift into the -1 reading frame. The polyprotein is processed by viral proteases, liberating the single nsps.

Expression of both ORF1a and ORF1b requires a ribosomal frameshift into the -1 reading frame. This frameshift promotes the expression of a ~800 kDa replicase polyprotein that is subsequently processed by viral proteases, resulting in 16 nonstructural proteins (nsps). The viral proteases are the papain-like proteases (PL^{pro}) and a serine type protease which is the main protease (M^{pro}), encoded by nsp3 and nsp5, respectively. Depending on the virus, one

or even two PL^{pro} are expressed (Ziebuhr, 2005). Many of these proteins are indispensable for the virus replication and its life cycle. Consequently, they are considered to be important targets for novel antiviral treatments (Tomar et al., 2015).

Some of the liberated nsps form the replication and transcription complexes (RTC). Most important within this complex is nsp12, the RNA-dependent RNA polymerase (RdRp), being assisted by other nonstructural proteins. Starting point of the genome replication is the synthesis of a full-length negative-strand RNA, serving as a template for positive-stranded genomic RNA, which is packaged into virions, and sub-genomic RNA. All sub-genomic RNAs contain a 5' leader sequence and have identical 3' and 5' terminal ends. The 5' leader sequence and the 3' body sequence are connected by numerous transcriptional regulatory sequences (TRS). One TRS is located at the 3' end of the leader sequence (TRS-leader) while the other TRS are located 5' of every ORF along the body sequence expect ORF1a and -1b (TRS-body). During the discontinuous extension of the negative-strand RNA, the RdRp complex passes those TRS, that either evoke a termination or a pause. The RTC can translocate from TRS-body to TRS-leader to complete transcription by adding the 5' leader sequence to the sub-genomic RNA. These sub-genomic RNAs encode for structural and accessory proteins.

The synthesis of sub-genomic RNA and full-length replication is followed by the insertion of the S, E and M protein into the endoplasmic reticulum (ER). Final virion assembly takes place in the ER-Golgi intermediate compartment (ERGIC). There, the nucleocapsid, which contains N protein and the full-length RNA genome, is budded into ERGIC membrane already assembled with the structural proteins (S, E and M). Mature virions are transported in vesicles and leave the cell through exocytosis (Fehr and Perlman, 2015; Hartenian et al., 2020).

1.3.2 Redox regulation upon coronavirus infections

Like many other viruses, coronaviruses promote high levels of oxidative stress during the infection of the host. The redox status of mammalian cells is disrupted, causing, *inter alia*, a change in thiol redox status. Simultaneously, this change of redox status can affect the fusion with the host cell or the replication of many viruses (Mitkevich et al., 2016; Ruggieri et al., 2013). For example, a temperature-dependent inhibition of the membrane fusion of murine hepatitis virus was observed while treating the cysteine-rich spike proteins with Ellmann's reagent (Gallagher, 1996). The presence of free thiols and the formation of disulfides in hepatitis C virus, on the contrary, seems to be important for infectivity, entry, fusion and budding (Hundt et al., 2013). Influenza viruses can enhance ROS production and decrease GSH levels, which provides a very favorable environment for viral replication (Checconi et al., 2020). Elevated levels of ROS can often be traced back to the induction of NADPH and xanthine oxidases, which was already shown for different respiratory viruses. This change in

redox homeostasis induces inflammation and thus tissue damage in the human host (Khomich et al., 2018). During SARS-CoV infections, for example, it was suggested that patients already having maladies associated with elevated ROS and RNS levels are at higher risk of developing a severe infection. This increased severity is potentially due to a more favorable thiol content in the receptor-binding domain of their S proteins facilitating fusion and entry into the host cell (Suhail et al., 2020). For this reason, it is obvious that protein disulfide isomerases have already been considered as potential targets for therapeutic strategies against viral infections (Chamberlain et al., 2019; Kim and Chang, 2018). Moreover, a potential correlation between low endogenous GSH levels and fatal cases of COVID-19 patients was recently reported, which is why supplementation of GSH was considered to be probably beneficial for patients (Guloyan et al., 2020; Polonikov, 2020). Also other antioxidants including thiol-based agents, polyphenols, vitamins, and selenium could provide promising therapeutic interventions and were already thoroughly reviewed (Checconi et al., 2020).

Since viruses lack own oxidative defense systems and, in many cases, even favor pro-oxidative environments, responding to oxidative and nitrosative stress is limited. OxPTMs of viral protein could be a potential response to these stressors. Nevertheless, effects of those potential modifications on viral proteins have not been intensively studied during the last decade. Saisawang and colleagues could not only show an inhibitory effect for S-glutathionylation of the chikungunya nsP2 protease, but also for the guanylyltransferase and RdRp activity of dengue and Zika NS5 protein (Saisawang et al., 2018, 2017). S-glutathionylation of hepatitis C virus RNA-dependent RNA polymerase also evoked an inhibitory effect on its activity and seems to target numerous cysteines (Kukhanova et al., 2019). It is known that both SARS-CoV and SARS-CoV-2 proteins can be posttranslationally modified, but scarcely is known about the effects on their structure and function (Stukalov et al., 2021). Recently, the regulatory impact of S-glutathionylation on the activity and dimerization of SARS-CoV-2 Mpro was reported (Davis et al., 2021).

In summary, viral infections are accompanied by an increase of oxidative and nitrosative stress that is induced by numerous intracellular pathways regulating redox balance. This stress response promotes inflammation and thus case severity in patients, while it was simultaneously shown to be beneficial for viral entry in the host cells, replication, and budding. Nevertheless, oxPTMs can lead to decreased activities of central viral proteins like its protease or RNA-polymerase. Therefore, investigations on the complex redox network of virus-host interactions could be a promising novel approach to develop antiviral therapeutics.

1.3.3 Coronavirus replicative proteins (nonstructural proteins)

As already described in subsection 1.3.1, ORF1a and -1b encode for an ~800 kDa large replicase polyprotein containing 16 nsps. This polyprotein is processed by the nsp5 protease

which has a chymotrypsin-like fold (3C-like protease, $3CL^{pro}$) and is the main protease, which is why it is also referred to as M^{pro}. It cleaves the polyprotein at the nsp4-nsp16 part at eleven conserved cleavage sites. The nsp1-nsp4 part is cleaved by one or two PL^{pro}, depending on the coronavirus. Most of the nsps assembled in the RTC are contributing to viral genome replication and transcription (Snijder et al., 2016). Table 1 gives an overview about the different nsps and their respective feature(s) and/or function(s).

Table 1 - Characteristics of coronavirus replicase gene-encoded nsps.
Adapted from Ziebuhr 2008.

Protein	Protein size (kDa)	Feature(s) / function(s)
Nsp1	12-27	Regulatory function in the host cell: binds to 40S ribosomal subunit, cleaves host mRNA (Kamitani et al., 2009)
Nsp2	65-87	Potentially involved in the disruption of intracellular host signaling (Cornillez-Ty et al., 2009)
Nsp3	177-222	Acidic domain, ubiquitin-like domain 1, macro domain with ADP-ribose-1''-phosphatase (ADRP) and poly(ADP-ribose)-binding activities, papain-like protease domain, Y-domain (Arya et al., 2021); ADP-ribosyl hydrolase (Li et al., 2016)
Nsp4	54-56	Transmembrane protein 2 (TM2)
Nsp5	33-34	3C-like protease ($3CL^{pro}$, M^{pro})
Nsp6	32-34	Transmembrane protein 3 (TM3)
Nsp7	9-10	Interacts with nsp8 to form a hexadecameric complex
Nsp8	22-23	Noncanonical RNA-polymerase, interacts with nsp7 to form a hexadecameric complex (Imbert et al., 2006)
Nsp9	12	Single-stranded RNA-binding protein (Egloff et al., 2004)
Nsp10	14-15	RNA-binding protein (Arya et al., 2021)
Nsp11	1-2	Unknown, becomes nsp12 by extension of pp1a into pp1b (Fehr and Perlman, 2015)
Nsp12	105-108	RdRp, nucleotidyltransferase (NiRAN) (Slanina et al., 2021)
Nsp13	66-67	Helicase with duplex RNA/DNA unwinding activity (Arya et al., 2021); RNA 5' triphosphatase (Ivanov and Ziebuhr, 2004)
Nsp14	58-60	Bifunctional, 3'-to-5' exoribonuclease, guanine-N7 methyl transferase (N7-MTase) (Arya et al., 2021)
Nsp15	38-42	Endoribonuclease, cleaves RNA specifically at the 3'-end of uridylates (NendoU)
Nsp16	33-34	Contains 2'-O-methyl transferase domain (Snijder et al., 2016)

Nsp5 ($3CL^{pro}$, M^{pro})

Due to its central role during virus replication after its own autoproteolysis, namely the liberation of nsps from the polyprotein to form the RTC, $3CL^{pro}$ is considered to be a promising target for

inhibitors against coronavirus infections. Viral replication can be completely blocked by the inhibition of its main protease. $3CL^{pro}$ is a cysteine protease with a size of approximately 30 kb and consists of three domains. Domains 1 and 2 consist of beta-barrels adapting a chymotrypsin-like fold and are located at the N-terminus. Domain 3 consists of five helices and is required for dimerization and stabilization of domains 1 and 2 (Anand et al., 2003; Roe et al., 2021; Stobart et al., 2013). Dimerization of $3CL^{pro}$ seems to be biologically relevant, since its protease activity can only be fulfilled as tightly associated dimer (Tomar et al., 2015). Different mutations have shown to decrease dimerization and, in consequence, the protease activity. Furthermore, the protease activity can be affected by mutations in nsp3 and nsp10 (Stobart et al., 2013). Analysis of the crystal structures from HCoV-229E and the porcine coronavirus (transmissible gastroenteritis virus, TGEV), as well as a SARS-CoV homology model, revealed strongly conserved substrate-binding sites among different species, including a Cys-His catalytic dyad (Anand et al., 2003). These sequence and structural homologies are promising prerequisites for the development of potent wide-spectrum compounds against coronavirus infections (Banerjee et al., 2021). Vuong and colleagues could already prove a drug initially used for the treatment of feline coronavirus (FCoV) to block virus replication of SARS-CoV-2 by inhibition of $3CL^{pro}$ via its catalytic Cys145 (Vuong et al., 2020).

Nsp8

As shown for nsp5, most nsp8 residues are well conserved among different coronaviruses. This suggests biological significance on the one hand and provides potential for pan-viral drugs on the other hand. During viral replication, the ~22 kDa nsp8 forms a hexadecameric complex with nsp7. Within this complex, eight copies of each nsp7 and nsp8 assemble to a cylinder-like structure, which can encircle double-stranded RNA. Nsp8 adopts two different conformations: nsp8I and nsp8II. The first one is referred to as ‘golf club’-like structure formed by a very long α-helix. This α-helix is bent in the second conformation, stated as nsp8II. While nsp8 forms the framework, nsp7 stabilizes the complex by filling remaining spaces. The binding of nucleic acids is fostered by the positive potential within the inner channel of the complex (Imbert et al., 2006; Zhai et al., 2005). The complex exhibits RdRp activity catalyzed by nsp8 and is capable of *de novo* initiation. Furthermore, nsp8 acts as primase synthesizing short oligonucleotide primers for the second RdRp (nsp12). Important for its catalytic activity is a central D/ExD/E motif and the presence of Mn^{2+} or Mg^{2+} (Imbert et al., 2006; te Velthuis et al., 2012; Ziebuhr, 2008). Heterodimers of nsp7 and nsp8 can bind to nsp12, enhancing its affinity to RNA and its polymerase activity (Arya et al., 2021). Nsp8 can further interact with other nsps, emphasizing its central role within the replication complex of coronaviruses (von Brunn et al. 2007). Nucleotide/nucleoside analogues, including Remdesivir, are RdRp inhibitors leading to nonviable viral genomes, which is why the FDA (U.S. Food and Drug Administration)

authorized “emergency use” of this broad-spectrum antiviral during the current SARS-CoV-2 pandemic (Arya et al., 2021).

Nsp9

In the viral replication complex, nsp9 binds to single-stranded RNA (ssRNA) and is therefore considered to be another potential target for antiviral compounds (Egloff et al., 2004). A recent crystal structure of SARS-CoV-2 nsp9 suggests the positively charged and glycine-rich loops β2-3 and β3-4 to participate in RNA-binding (Littler et al., 2020). It is hypothesized that nsp9 has evolved from a protease, since it shows structural homologies with subdomains of serine proteases. Interestingly, both N- and C-terminus of nsp9 are more conserved than its central core region, when comparing sequences of different coronaviruses. The protein is biologically active as a dimer with a molecular mass of 12 kDa (Sutton et al., 2004). Comparison of different coronavirus nsp9 crystal structures reveal diversity upon the formation of dimers (Zeng et al., 2018). The crystal structure of HCoV-229E, for example, revealed the ability of nsp9 to form homodimers through disulfide-linkage, which is associated with the induction of oxidative stress during the viral infection of the host cell. Cysteine-to-alanine mutants showed the same dimerization as observed for SARS-CoV nsp9 and were not able to bind ssRNA (Ponnusamy et al., 2008). Nsp9 can be nucleotidylated by the nidovirus RdRp-associated nucleotidyltransferase (NiRAN) activity. This NMPylation requires Mn^{2+} and transfers a nucleoside monophosphate (NMP) to a conserved N-terminal region of nsp9, resulting in a covalent bond. Mass spectrometry analysis indicates that nsp9 and nsp12 do not form a complex during NMPylation (Lehmann et al., 2015; Slanina et al., 2021).

1.4 *Excursus*: Human spectrin

Red blood cells (RBCs) have two important functions: transport of O_2 and CO_2 between the lung and the tissues and maintenance of a physiological acid/base balance. As stated previously, erythrocytes contain an iron atom that can induce, together with O_2, a pro-oxidant environment. Therefore, RCBs possess powerful oxidative defense systems. To ensure efficient gas transport and maintain their flexible biconcave shape, it is highly important to keep their mechanical and biophysical properties, which are mainly defined by their cytoskeleton (Barbarino et al., 2021; Kuhn et al., 2017; Mohandas and Gallagher, 2008). Spectrin fibrils are arranged as hexagonal units beneath the plasma membrane and are the most abundant component to the cytoskeleton (Figure 10). Spectrin physiologically occurs as tetramer, with ~250 kDa per subunit (Goodman et al., 2019).

OxPTMs of RBC cytoskeletal proteins, like spectrin, and/or a disruption of the cellular redox homeostasis can affect those vital properties and are associated with various pathologies (Barbarino et al., 2021; Kuhn et al., 2017). Spectrin was already proposed to be a target of

S-glutathionylation, but so far, the effect(s) on structure and/or function remains unknown (Giustarini et al., 2019; Rossi et al., 2006).

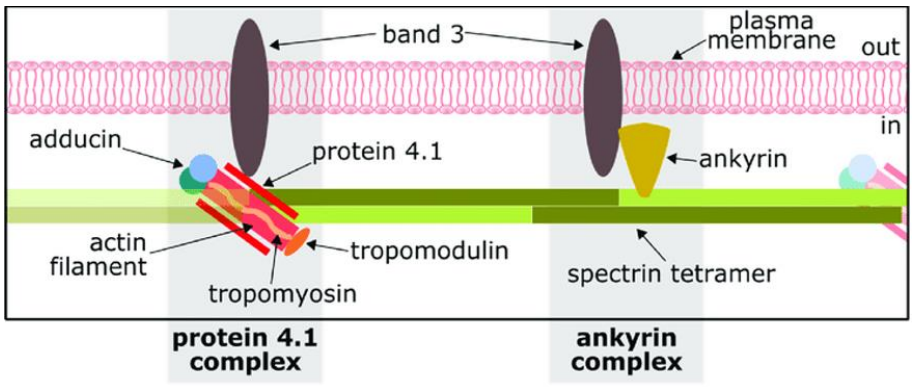

Figure 10 - Overview of the RBC cytoskeleton.
Schematic representation of the RBC cytoskeleton with its principal components and its attachment to the plasma membrane, adapted from (Unsain et al., 2018).

1.5 Objectives of the study

The present study was conducted within the DFG Priority Program SPP1710 “Dynamics of thiol-based redox switches in cellular physiology” and the LOEWE Center DRUID (Novel Drug Targets against Poverty-Related and Neglected Tropical Infectious Diseases). For this reason, it was possible to transfer methodological knowledge established on *P. falciparum* enzymes to other pathogens within the DRUID consortium, resulting in two subprojects addressed within this thesis: The influence of oxPTMs on (i) *P. falciparum* glycolytic enzymes PfHK and PfPK and (ii) coronavirus nonstructural proteins. At this point it shall be stated that both subprojects started in 2018, wherefore this thesis does not include studies on SARS-CoV-2 proteins.
Maintaining a proper redox equilibrium is essential for hosts, parasites, and viruses. To ensure an adequate redox state, organisms are equipped with several antioxidant systems, including, for instance, the Trx or the glutathione system. Besides these systems, further proteins, low molecular weight antioxidants and oxPTMs can contribute to the maintenance of redox states. In *P. falciparum*, glycolytic enzymes were already found to be targeted, and sometimes also regulated, by oxPTMs. Nevertheless, there is scarcely anything known about the effects of oxPTMs on the three-dimensional structure of those enzymes. Therefore, this thesis focused on expanding the knowledge of oxPTMs on regulatory enzymes of glycolysis and the role of single cysteines by addressing the following topics:

I. Kinetic characterization of PfHK with and without oxPTMs, mass spectrometry analyses of S-glutathionylated and S-nitrosated PfHK and protein crystallization.

II. Kinetic characterization of three different cysteine-to-alanine mutants of PfPK, mass spectrometry analyses of S-glutathionylated and S-nitrosated wild type enzyme, and protein crystallization of wild type enzyme and corresponding mutants.

As already stated previously, coronaviruses lack oxidative defense systems. Nevertheless, redox regulation via oxPTMs was already observed for several viral proteins. These modifications occurring upon increased ROS and RNS levels either foster beneficial events like infectivity, entry, fusion and budding, or can lead to inhibition of protein functions during replication. To assess S-glutathionylation patterns of coronavirus proteins and investigate potential effects on their function, this thesis further includes:

III. The screening of ~30 different coronavirus nsps for their susceptibility to S-glutathionylation.
IV. Analysis of the effect of S-glutathionylation on the activity/function of targeted proteins using available assay systems and validating this data with cysteine-to-alanine mutants and protein crystallization.

This doctoral thesis was further enriched by two side projects which will only be presented partially in this thesis. The first one comprised three very diverse subprojects of our surface plasmon resonance (SPR) facility, which were assisted and later independently conducted during my doctorate. Within those projects, we collaborated with Prof. Thomas Linn (Justus Liebig University Giessen), Prof. Arnold Grünweller (Philipps University Marburg) and Prof. Stephan Becker (Philipps University Marburg). A second project, which will be presented in brief in an excursus results section, was conducted in close collaboration with Prof. Miriam Cortese-Krott (Heinrich Heine University Düsseldorf). This project aimed at investigating the occurrence and the effect of S-glutathionylation in human spectrin and, so far, resulted in a review article (Barbarino et al., 2021).

2 Materials

2.1 Instruments

Instrument	Company
Äkta FPLC System	GE Healthcare, Freiburg
Autoclave	Webeco, Bad Schwartau
Autoclave VX-95	Systec, Wettenberg
BioSpectrometer® basic	Eppendorf, Hamburg
Centrifuge 5415R	Eppendorf, Hamburg
Centrifuge Megafuge 1.0R	Heraeus Instruments, Hanau
Centrifuge MiniSpin	Eppendorf, Hamburg
Centrifuge Sorvall RC 6+ (Rotor SS-34 and F9S-4x1000y)	Thermo Scientific, Dreieich
Crystallization robot Honeybee 961	Digilab, Marlborough, MA, USA
Electrophoresis Chamber (Mini-PROTEAN 3 cell)	Bio-Rad, Munich
Evolution™ 300 UV-Vis-Spectrophotometer	Thermo Scientific, Dreieich
Heating block neoBlock II	neoLab, Heidelberg
Heating block Thermomixer comfort	Eppendorf, Hamburg
High-purity water system OPTILAB-Plus	MembraPure, Henningsdorf
Icemaker F80C	Icematic Deutschland, Meerbusch
Incubation shaker KS 500	Junke & Kunkel, IKA-Werke, Staufen
Incubation shaker SM25	Edmund Bühler GmbH, Tübingen
Incubation system (incubator: CERTOMAT® H, shaker: CERTOMAT® R)	B. Braun, Melsungen
Incubation system	Thermo Scientific, Dreieich
Incubation shaker Innova® 44	Eppendorf, Hamburg
Intas ECL ChemoStar	Intas Science Imaging Instruments GmbH, Göttingen
Magnetic stirrer CAT M15	MAGV Laborbedarf, Rabenau-Londorf
Magnetic stirrer color squid	IKA Werke, Staufen
Magnetic stirrer HI 300N	Hanna Instruments, Kehl am Rhein
Magnetic stirrer RCTbasic	IKA Werke, Staufen
Microprocessor pH Meter	Knick, Berlin
OptiMax X-ray Processor	M&S Laborgeräte, Wiesloch
Peltier Cryobath System TPS 1500 W	Thermo Scientific, Dreieich

Pipette Eppendorf Research plus	Eppendorf, Hamburg
Pipette Gilson Pipetman (P10, P20, P100, P200, P1000)	Gilson, Middleton
Pipetting robot Lissy	Zinsser Analytic, Frankfurt
Power Pac 300	Bio-Rad, Munich
Precision scale ABT 120-5 DM	Kern & Sohn, Balingen
Quadro MACS™ separating system	Miltenyi Biotec, Bergisch Gladbach
Rotilabo®-X-ray-cassette	Roth, Karlsruhe
Scale 440-47N	Kern & Sohn, Balingen
Scale 474-32	Kern & Sohn, Balingen
Stereomicroscope SMZ1000	Nikon GmbH, Dusseldorf
Stereomicroscope system (M165 C, KL 1500 LED, camera EC 3)	Leica Microsystems, Wetzlar
TPS 1500W Peltier Cryobath System Recirculator	Thermo Scientific, Dreieich
Trans-Blot® Turbo™ Transfer System	Bio-Rad, Munich
Typhoon Phosphorimager 9200	GE Healthcare
Ultrasound Homogenizer Sonoplus HD 2070	Bandelin Electronic, Berlin
Ultrasound Waterbath Sonorex RK100	Bandelin Electronic, Berlin
Vacuum Pump Vacubrand CVC 3000	VWR, Darmstadt
Vortex mixer MS2 Minishaker	IKA®-Werke, Staufen im Breisgau
Western blot Trans-Blot® SD semi-dry transfer cell	Bio-Rad, Munich

2.2 Chemicals

All chemicals used were of the highest purity available.

Chemical	Company
1,4-Dithiothreitol (DTT)	Roth, Karlsruhe
Acetic acid	Roth, Karlsruhe
Acetone	Roth, Karlsruhe
Acrylamide/Bisacrylamide (Rotiphorese Gel 30 (37.5:1))	Roth, Karlsruhe
Adenosine diphosphate (ADP)	Roth, Karlsruhe
Adenosine triphosphate (ATP)	Merck, Darmstadt
Adenosine-5'-[(β,γ)-imido]triphosphate (AMP-PNP)	Jena Bioscience, Jena
Agarose	Roth, Karlsruhe
Ammonium persulfate (APS)	Roth, Karlsruhe

Anhydrotetracycline	IBA Lifesciences, Göttingen
Bovine serum albumin (BSA)	Roth, Karlsruhe
Carbenicillin	Roth, Karlsruhe
Chloramphenicol	Roth, Karlsruhe
Citric acid	Sigma, Steinheim
Coomassie Brilliant Blue R250	Sigma, Steinheim
Coumaric acid	Sigma, Steinheim
Cystatin	Sigma, Steinheim
Dimethyl sulfoxide (DMSO)	Roth, Karlsruhe
Di-Sodium hydrogen phosphate dihydrate	Roth, Karlsruhe
DNase I	Roche, Mannheim
DTT	Roth, Karlsruhe
Ethylenediaminetetraacetic acid (EDTA)	Roth, Karlsruhe
Glucose	Merck, Darmstadt
GSH	Sigma, Steinheim
GSSG	Sigma, Steinheim
Hepes	Roth, Karlsruhe
Hydrochloric acid (fuming, 37%, 1 M)	Roth, Karlsruhe
Imidazole	Roth, Karlsruhe
Iodoacetamid (IAA)	Sigma, Steinheim
Iodoacetyl-PEG2-Biotin	Thermo Scientific, Dreieich
Isopropanol	Roth, Karlsruhe
Isopropyl-β-D-thiogalactopyranosid (IPTG)	Roth, Karlsruhe
Kanamycin sulfate	Roth, Karlsruhe
L-Cysteine-Hydrochloride-Monohydrate	Sigma, Steinheim
Luminol	Sigma, Steinheim
Magnesium acetate	Sigma, Steinheim
Magnesium chloride ($MgCl_2$)	Sigma, Steinheim
MES (2-(N-morpholino)ethanesulfonic acid)	Roth, Karlsruhe
Methanol	Roth, Karlsruhe
Milk powder	Roth, Karlsruhe
N,N,N',N'-Tetramethylethylenediamine (TEMED)	Sigma, Steinheim
NADH	Biomol, Hamburg
$NADP^+$	Biomol, Hamburg
Neocuproine	Sigma, Steinheim
Nickle nitrilotriacetic acid (Ni-NTA)	Thermo Scientific, Dreieich
Phenylmethanesulfonyl fluoride (PMSF)	Roth, Karlsruhe

Phophoenol pyruvate	AppliChem, Darmstadt
Tween® 20	Roth, Karlsruhe
Ponceau S	Sigma, Steinheim
Potassium chloride	Roth, Karlsruhe
Potassium citrate	Roth, Karlsruhe
Sodium acetate	Roth, Karlsruhe
Sodium ascorbate (NaAsc)	Sigma, Steinheim
Sodium dihydrogen phosphate monohydrat	Roth, Karlsruhe
Sodium dodecyl sulfate (SDS)	Sigma, Steinheim
Sodium hydroxide	Roth, Karlsruhe
Sodium nitrite	Roth, Karlsruhe
Sodium oxamate	Sigma, Steinheim
Talon Metal Affinity Resin	Thermo Scientific, Dreieich
Trichloracetic acid (TCA)	Roth, Karlsruhe
Triethanolamine hydrochloride (TEA-HCl)	Sigma, Steinheim
Tris-(hydroxymethyl)-aminomethan (Tris)	Roth, Karlsruhe
Tris-HCl	Roth, Karlsruhe
Triton X-100	Roth, Karlsruhe
Tryptone/Peptone	Roth, Karlsruhe
Urea	Roth, Karlsruhe
Yeast extract	Thermo Scientific, Dreieich

2.3 Consumables

Consumable	Company
Crystallization plate, 24 well, VDX plate	Hampton Research, Jena
Crystallization plate, 96 well, MRC 2 well	Jena Bioscience, Jena
Cuvettes, polystyrol	Sarstedt, Nümbrecht
Cuvettes, micro, UV	Brand GmbH, Wertheim
Discofix® 3-way stopcock	B. Braun, Melsungen
Halfmicro cuvettes 10x4x45 mm, polystyrol	Sarstedt, Nümbrecht
Falcon tube 15 ml, 50 ml	Greiner Bio-One, Frickenhausen
High performance chemiluminescence film Amersham hyperfilmTMECL	GE Healthcare, Freiburg
Glas capillaries 5 µL	Brand GmbH, Wertheim
Membrane filter ME 25, 0.45 µm	Whatman GmbH, Dassel
Micro pipettes	Brand, Wertheim

Microscope lens paper	Glaswarenfabrik Karl Hecht, Sondheim
Nitrocellulose blotting membrane, 0.45 µm	GE Healthcare, Freiburg
Parafilm 'M' laboratory film	Pechiney Plastic Packaging, Menasha USA
Pasteur pipette 150 mm	Hirschmann Laborgeräte, Eberstadt
Petri dish, 15 cm Ø	Sarstedt, Nümbrecht
Pipette tips and tubes, disposable	Eppendorf, Hamburg
Pipette tips Omnitip FastRack 10 µL, 200 µL	Ulplast, Warschau
Plastic Vials	GE Healthcare, Munich
Protein ladder unstained protein MW marker	Fermentas, St. Leon-Rot
Protein ladder 6xHis	Qiagen, Hilden
PVDF membrane	Roth, Karlsruhe
Rubber Caps	GE Healthcare, Munich
Series S Sensor Chip CM5	GE Healthcare, Munich
Silicone oil 550	Merck, Darmstadt
STERICAN disposable hypodermic needle	Braun, Sempach
Sterile filters 0.2 µm FP030	Schleicher & Schüll, Kassel
Syringe 1 ml Plastipak	Becton Dickson, Madrid
Syringe 10 ml	B. Braun, Melsungen
24 Bottom Wells 1.7x1.6 cm MP	Biochemicals Inc., USA
Vivaspin 20, 3,000 MWCO, 10,000 MWCO and 30,000 MWCO	Sartorius Stedim Biotech, Göttingen
X-ray film Processore, Optimax	Protec, Oberstenfeld
ZebaTM Desalt Spin Columns	Thermo Scientific, Rockford, USA

2.4 Biological materials

2.4.1 Cloning and expression vectors

Vector	Properties	Source
pET-28a(+)	5369 bp, T7 promoter, T7 transcription start, His-Tag coding sequence, T7-Tag coding sequence, multiple cloning sites (*Bam*H I – *Xho* I), T7 terminator, *lacI* coding sequence, pBR322 origin, Kan coding sequence, f1 origin	Novagen
pET-30a(+)	5422 bp, T7 promoter, T7 transcription start, His-Tag coding sequence, S-Tag coding sequence, multiple cloning sites (*Nco* I – *Xho* I), T7 terminator, *lacI* coding sequence, pBR322 origin, Kan coding sequence, f1 origin	Novagen

pQE30	Carbenicillin resistance, T5 promotor, His-tag coding sequence, lac operator	Qiagen, Hilden
pCG1	Encodes for a ubiquitin-specific, carboxy-terminal protease (Ubp1) (Gohara et al. 1999)	
pASK3-Ub-Chis$_6$	Expression vector	

2.4.2 *E. coli* strains

E. coli strain	Genotype	Source
XL1 Blue	*rec*A1 *end*A1 *gyr*A96 *thi*-1 *hsd*R17 *sup*E44 *rel*A1 *lac* [F' *pro*AB *lac*Iq *ZΔM*15 Tn*10* (Tetr)]	Stratagene, Amsterdam, The Netherlands
C41 (DE3)	F – ompT hsdSB (rB- mB-) gal dcm (DE3)	Avidis SA, St. Beauzire, France
M15	F-, Φ80ΔlacM15, thi, lac-, mtl-, recA+, KmR	Qiagen, Hilden
Top10 F'	F- mcrA Δ(mrr-hsdRMS-mcrBC) φ80lacZΔM15 ΔlacX74 recA1 araD139 Δ(araleu)7697 galU galK rpsL (StrR) endA1 nupG	Fisher Scientific, Dreieich
K12 Tb1	F$^-$ *ara* Δ*(lac-proAB)* *[Φ80dlac* Δ*(lacZ)M15]* *rpsL*(Str^R) *thi hsdR*	New England Biolabs

2.4.3 Antibodies

Antibody	Solved in	Company
Anti-glutathione monoclonal antibody	TBST	Virogen, Watertown, MA, USA
Anti-6xHis-tag monoclonal antibody	3% BSA in TBST	Dianova, Hamburg
Monoclonal biotin antibody (33): sc-101339	5% milk in TBST	Santa Cruz Biotechnology, Dallas, TX, USA
Horseradish peroxidase (HRP) anti-mouse antibody	5% milk in TBST	Thermo Scientific, Dreieich
Anti-spectrin antibody	TBST	Sigma Aldrich, Steinheim

2.4.4 Enzymes

Enzymes for enzymatic assays	Company
Glucose-6-phosphate dehydrogenase, baker's yeast	Roche, Mannheim
Hexokinase, *Leuconostoc mesenteroides*	Roche, Mannheim
Lactate dehydrogenase, rabbit muscle	Roche, Mannheim

2.5 Buffers and solutions

2.5.1 Stock solutions

Solution	Concentration	Solved in	Storage
Anhydrotetracycline	2 mg/ml	100% Ethanol	-20 °C
APS	10% (w/v)	$_{dd}H_2O$	-20 °C
Carbenicillin	50 mg/ml	50% (v/v) Ethanol	-20 °C
Chloramphenicol	35 mg/ml	100% Ethanol	-20 °C
Cystatin	40 µM	$_{dd}H_2O$	-20 °C
IPTG	1 M	$_{dd}H_2O$, sterile filtrated	-20 °C
Kanamycin	25 mg/ml	$_{dd}H_2O$, sterile filtrated	-20 °C
Pepstatin A	300 µM	DMSO	-20 °C
Phenylmethylsulfonyl fluoride (PMSF)	100 mM	DMSO	-20 °C
Sodium dodecyl sulfate (SDS)	10% (w/v)	$_{dd}H_2O$	-20 °C

2.5.2 Buffers for chemically competent *E. coli* cells

Buffer	Composition	
$CaCl_2$ buffer	10 mM	Pipes
(K12 Tb1)	15%	Glycerol
	60 mM	$CaCl_2$
	pH 7.0	
$CaCl_2$ buffer	100 mM	$CaCl_2$
(Other cells)	(30%	Glycerol)
	pH 8.0	

2.5.3 Media and stock solutions for protein expression

Medium	Composition	
Lysogeny broth	10 g	Tryptone
(LB)	5 g	Yeast extract
	10 g	NaCl
	Adjusted to 1 L with dH_2O and autoclaved before use	
Terrific broth	12 g	Tryptone
(TB)	24 g	Yeast extract
	9.4 g	Di-potassium phosphate
	2.2 g	Mono-potassium phosphate
	4 ml	Glycerol
	Adjusted to 1 L with dH_2O and autoclaved before use	
Agar plates	10 g	Tryptone
	5 g	Yeast extract
	10 g	NaCl
	15 g	Agar
	Adjusted to 1 L with dH_2O and autoclaved before use;	
	Respective antibiotics are added after autoclaving at 50-60 °C	

2.5.4 Buffers and solutions for gel electrophoresis

Buffer	Composition	
Electrophoresis buffer	192 mM	Glycine
	25 mM	Tris
	0.1% (w/v)	SDS
	pH 8.3	adjusted with HCl
SDS sample buffer (4x)	250 mM	Tris-HCl, pH 6.8
	8% (w/v)	SDS
	40% (v/v)	Glycerol
	0.03% (w/v)	Bromophenol blue
	(200 mM	DTT)
SDS sample buffer (1x)	62.5 mM	Tris-HCl, pH 6.8
	2% (w/v)	SDS
	25% (v/v)	Glycerol
	0.01% (w/v)	Bromophenol blue
	(50 mM	DTT)

Coomassie staining solution	160 mg	Coomassie Brilliant Blue R 250
	ad 1 L	$_{dd}H_2O$, 2 h stirring
	3 ml	HCl, fuming, 37%
Separating gel buffer	1.5 M	Tris
	pH 8.8	
Sample gel buffer	0.5 M	Tris
	pH 6.8	

Gel	Composition	
SDS-PAGE separating gel (12%)	0.51 ml	$_{dd}H_2O$
	3.75 ml	Separating gel buffer
	6 ml	Acrylamide/bisacrylamide (30%)
	0.15 ml	SDS (10%)
	75 µl	APS (10%)
	7.5 µl	TEMED
SDS-PAGE sample gel (4%)	3.05 ml	$_{dd}H_2O$
	1.25 ml	Separating gel buffer
	0.65 ml	Acrylamide/bisacrylamide (30%)
	0.05 ml	SDS (10%)
	25 µl	APS (10%)
	5 µl	TEMED

2.5.5 Buffers and solutions for semi-dry Western blotting

Buffer	Composition	
Western blot transfer buffer	250 mM	Tris
	1.92 M	Glycine
	10% (v/v)	Ethanol
	pH 8.3	
Tris-buffered saline (TBS)	10 mM	Tris
	0.9% (w/v)	NaCl
	pH 7.4	adjusted with HCl
TBS with Tween 20 (TBST)	0.05 % (v/v)	Tween 20 in TBS buffer
Ponceau S solution	2%	Ponceau S
	3%	TCA
Ponceau S destaining solution	1%	Acetic acid
Blocking buffer	5% (w/v)	Milk powder in TBST buffer

Luminol mixture	1.25 mM	Luminol
	0.0093% (v/v)	Hydrogen peroxide
	100 mM	Tris-HCl
	pH 8.6	
Coumaric acid	0.11%	Coumaric acid in DMSO
Chemiluminescence mixture	1 ml	Luminol mixture
	10 µl	Coumaric acid

2.5.6 Buffers for protein purification, dialysis, and storage

Buffer	Composition	
Pyruvate kinase	50 mM	Sodium phosphate
	300 mM	NaCl
	pH 8.0	
Hexokinase	50 mM	Hepes
	300 mM	NaCl
	20 mM	Imidazole
	10%	Glycerol
	pH 8.0	
Glutaredoxin, Plasmoredoxin, Thioredoxin (purification)	50 mM	Na_2HPO_4
	300 mM	NaCl
	pH 8.0	
Glutaredoxin (dialysis)	50 mM	Hepes
	50 mM	KCl
	pH 7.2	
Nsps		
Lysis	20 mM	Tris-HCl
	300 mM	NaCl
	5%	Glycerol
	0.1%	Triton X-100
	2 mM	DTT
	10 mM	Imidazole
	pH 8.0	
Purification	30 mM	Imidazole
Elution	200 mM	Imidazole

Dialysis	50 mM	Hepes-KOH
	150 mM	KCl
	2 mM	DTT
	pH 8.0	

2.5.7 Assay buffers

Buffer	Composition	
biotin-Switch Assay		
Nitrosation buffer	50 mM	Tris
	1 mM	EDTA
	0.2 mM	Neocuproine
	pH 7.4	
Blocking buffer	50 mM	Tris
	8 M	Urea
	1 mM	EDTA
	mM	Neocuproine
	pH 8.0	
Labeling buffer	50 mM	Tris
	4 M	Urea
	1 mM	EDTA
	0.01 mM	Neocuproine
	pH 8.0	
Pyruvate kinase	10 mM	Hepes
enzymatic assay	10 mM	$MgCl_2$
	50 mM	KCl
	pH 7.5	
Hexokinase	100 mM	Triethanolamine
enzymatic assay	10 mM	$MgCl_2$
	pH 7.5	
Ellman’s assay	150 mM	K_2HPO_4
	pH 8.0	

2.5.8 Solutions for ghost preparation

Solution	Composition	
Hank's buffered salt solution	140 mM	NaCl
	5 mM	KCl
	1 mM	$CaCl_2$
	400 µM	$MgSO_4$-$7H_2O$
	500 µM	$MgCl_2$-$6H_2O$
	300 µM	Na_2HPO_4
	400 µM	KH_2PO_4
	6 mM	Glucose
	4 mM	$NaHCO_3$
Isotonic KCl	148 mM	KCl
Hemolysis medium A	4 mM	$MgSO_4$
pH 3.6-3.8	3.8 mM	CH_3OOH
Washing medium B	4 mM	$MgSO_4$
pH 7.0	1.4 mM	CH_3OONa
	2 mM	NaH_2PO_4
Solution C	2 M	KCl
Solution D	2 M	KCl
pH 7.2	25 mM	Tris-HCl

2.5.9 *P. falciparum* cell culture buffer

For washing and elution during enrichment of trophozoite stages, modified RPMI medium was used. The medium contained RPMI 1640 supplemented with 0.5% (w/v) AlbuMAX, 9 mM glucose, 0.2 mM hypoxanthine, 2.1 mM L-glutamine, 25 mM HEPES and 22 µg/ml gentamycin.

2.6 Crystallization buffers and screens

For crystallization, purification buffers of the respective proteins were exchange either via size exclusion chromatography (SEC) or dialysis (see subsection 3.2.2) with the buffers stated below.

Buffer	Composition	
Pyruvate kinase crystallization	10 mM	Hepes
	10 mM	$MgCl_2$
	50 mM	KCl

	pH 7.5	
Hexokinase crystallization	50 mM	Hepes
	300 mM	NaCl
	pH 8.0	
McIlvaine buffer (5x)	1 M (4 ml)	Na_2HPO_4
	0.5 M (15 ml)	Citrate
	pH 3.0	no need to adjust

Screen	Company
JBScreen Classic I & II	Jena Bioscience, Jena
JBScreen Classic III & IV	Jena Bioscience, Jena
JBScreen Wizard I & II	Jena Bioscience, Jena
JBScreen Wizard III & IV	Jena Bioscience, Jena
JCSG Core I Suite	Qiagen, Hilden
JCSG Core II Suite	Qiagen, Hilden
JCSG Core III Suite	Qiagen, Hilden
JCSG Core IV Suite	Qiagen, Hilden
MPD Suite	Qiagen, Hilden
XP Screen	Jena Bioscience, Jena
JBScreen Basic HTS	Jena Bioscience, Jena
JBScreen PEG/Salt HTS	Jena Bioscience, Jena
JBScreen PACT++ HTS	Jena Bioscience, Jena
JBScreen Classic HTS I	Jena Bioscience, Jena
JBScreen Classic HTS II	Jena Bioscience, Jena
JBScreen Plus HTS	Jena Bioscience, Jena
JBScreen JCSG++ HTS	Jena Bioscience, Jena
PEG Screen I*	In-house production
PEG Screen II*	In-house production
PEG Screen III*	In-house production
Ammonium Sulfate Screen*	In-house production
Wizard pH Buffer Screen	Rigaku, Bainbridge Island, WA USA
Morpheus I	Molecular Dimensions, Sheffield, UK
Morpheus II	Molecular Dimensions, Sheffield, UK

**In-house production screens are shown in the supplementary.*

3 Methods

3.1 Heterologous protein production and purification

3.1.1 Plasmid preparation and determination of DNA concentration

3 ml LB medium plus 50 µg/ml kanamycin was inoculated with one colony XL1 Blue cells containing the desired plasmid and incubated over night at 37 °C with vigorous shaking. For plasmid preparation, the *Fast Gene Plasmid mini kit*® standard protocol was followed. To determine the DNA concentration, 2 µl of purified plasmid are applied onto the BioSpectrometer® Basic. The desired nucleic acid concentration was 50-100 ng/µl. Plasmids were stored at -20 °C until used again.

3.1.2 Transformation

PfHK & PfPK

For heterologous overexpression, plasmids containing the sequence of the protein of interest need to be transformed into chemo-competent *E. coli* cells. The cells were stored at -80 °C and carefully thawed on ice. Then, 1-2 µl plasmid were added to a 125 µl *E. coli* aliquot (C41 cells for both PfPK and PfHK) and left on ice for 30 min. To ensure proper plasmid transformation, cells were heat-shocked for 90 s at 42 °C, cooled-down on ice for another 1-2 min and mixed with 300 µl LB medium. After 1 h incubation in the shaker at 37 °C, the cells were plated onto agar plates containing 50 µg/ml kanamycin for cell selection. The agar plates were incubated at 37 °C overnight.

PfGrx, PfPlrx & PfTrx

pQE-30 plasmids containing the sequence of PfGrx, PfPlrx and PfTrx, respectively, were transformed into M15 *E. coli* cells. For cell selection, agar plates contained 50 µg/ml kanamycin and 100 µg/ml carbenicillin. Apart from that, transformation was performed as described above for PfPK and PfHK.

Coronavirus nsp8 & nsp9

Transformation of coronavirus protein sequences was performed similarly to the transformation of PfPK and PfHK plasmids. 1 µl plasmid is added to 100 µl *E. coli* cells (K12 Tb1-pCG1; pCG1 encodes for a ubiquitin protease) and left on ice for 30 min. Cells were heat-shocked for 45 s at 42 °C, cooled-down on ice for 3-5 min. Afterwards, 300 µl LB medium was added. After 1 h incubation at 37 °C, as performed for the other transformations, cells were plated onto agar plates containing 100 µg/ml carbenicillin and 35 µg/ml chloramphenicol. The agar plates were incubated at 37 °C overnight.

3.1.3 Heterologous overexpression

PfHK & PfPK

For overexpression in *E. coli* cells, transformed cells (C41) containing the desired protein were used to inoculate 3 ml LB medium. To ensure cell selection, kanamycin was added (50 µl/ml). After 6-8 h, the culture was diluted 1:50-100 with TB-medium, the kanamycin concentration was maintained during the whole expression. Cells were again incubated shaking at 37 °C overnight before using the pre-culture to inoculate 1 L TB medium (aiming for an optical density [OD_{600}] of 0.08). To achieve adequate expression, cells were grown until an OD_{600} of 0.5-0.6 and followed by protein production induced by IPTG (0.2 mM for PfPK, 0.5 mM for PfHK). After 18 h shaking at room temperature, cells were harvested by centrifugation at 10.000 g and 4 °C for 15 min. The pellet was resuspended with storage buffer (see subsection 2.5.6) whereas the supernatant was discarded. A protease inhibitor cocktail was added to the pellet to avoid unintentional protein degradation during storage at -20 °C.

PfGrx, PfPlrx & PfTrx

Proteins were expressed for 4 h at 37 °C in M15 E. coli cells, using LB medium containing 50 µg/ml kanamycin and 100 µg/ml carbenicillin. The protocol as described above (PfHK and PfPK) was followed with slight modifications:

PfGrx	1 mM IPTG at OD_{600} = 0.8-0.9
PfPlrx	1 mM IPTG at OD_{600} = 0.6
PfTrx	0.5 mM IPTG at OD_{600} = 0.5-0.6

After cell harvest, the cell pellets were resuspended in US-buffer and stored at -20 °C until lysis.

Coronavirus nsp8 & nsp9

For overexpression in *E. coli* cells, transformed cells (K12 TB1-pCG1) containing the desired protein were used to inoculate 3 ml LB medium. To ensure cell selection, carbenicillin and chloramphenicol were added (50 µl/ml and 35 µl/ml, respectively). After 6-8 h, the culture was diluted 1:25 with LB medium, the concentration of antibiotics was maintained during the whole expression. Cells were again incubated shaking at 37 °C overnight before using the pre-culture to inoculate 1 L LB medium (aiming for an OD_{600} of 0.08). To achieve adequate expression, cells were grown until an OD_{600} of 0.6 and followed by protein production induced by anhydrotetracycline (0.2 mM). After 16 h shaking at 18 °C, cells were harvested by centrifugation at 10.000 g and 4 °C for 15 min. The pellet was resuspended with lysis buffer (see subsection 2.5.6) whereas the supernatant was discarded. A protease inhibitor cocktail was added to the pellet to avoid unintentional protein degradation during storage at -20 °C.

3.1.4 Ni-NTA and Talon affinity chromatography

PfHK & PfPK

For cell lysis, *E. coli* cells were thawed at room temperature with 16 mg lysozyme/L culture and DNase. The lysis was stirred at 4 °C (45 min for PfPK, overnight for PfHK), followed by sonication for 3x 30 s at 70% power. Lysed cells were centrifuged for 30 min at 38.000 g at 4 °C. The supernatant containing the desired protein was applied to Ni-NTA or Talon affinity chromatography. 1 ml Ni-NTA/Talon column material (= column volume, CV) was used for 1 L *E. coli* culture to ensure sufficient binding capacity. To ensure proper binding, the drop rate was adjusted to 1 drop every 4-7 s. Before eluting the protein, columns were washed with buffer to avoid contamination of the final protein samples with unspecifically bound proteins. After washing the columns, the protein was eluted with increasing concentrations of imidazole.

PfHK		**PfPK**	
Wash	20 CV buffer	**Wash**	10 CV buffer
Elution	3x 2 CV 50 mM imidazole	**Elution**	4x 2 CV 50 mM imidazole
	3x 2 CV 100 mM imidazole		2x 2 CV 75 mM imidazole
			2x 2 CV 100 mM imidazole
			2x 2 CV 200 mM imidazole
			2x 2 CV 500 mM imidazole

To check protein purity, SDS-PAGE followed by Coomassie Blue staining was performed (see subsection 3.2.1). Only pure fractions were pooled and concentrated with Vivaspins 30,000 molecular weight cut off (MWCO). To remove imidazole prior to storage of the protein, dialysis (see subsection 3.2.2) was performed.

PfGrx, PfTrx & PfPlrx

The protocol as described above (PfHK and PfPK) was followed with slight modifications. Cells were lysed for 30 min at 4 °C, centrifuged and applied to Ni-NTA affinity chromatography. The proteins were eluted with increasing concentrations of imidazole in US-buffer:

PfGrx	10, 20, 150, 200 mM imidazole
PfPlrx	30, 50, 75, 100, 500 mM imidazole
PfTrx	5, 10, 100, 200, 500 mM imidazole

Suitable fractions were pooled and concentrated with Vivaspins 5,000 or 10,000 MWCO. PfGrx was dialyzed against 50 mM Hepes, pH 7.2, and 50 mM KCl to remove the imidazole and ensure stable protein upon storage. All proteins were stored at 4 °C.

Coronavirus nsp8 & nsp9

For cell lysis, *E. coli* cells were thawed at room temperature and added by 16 mg lysozyme/L culture and DNase. The lysis was stirred for 30 min at 4 °C, followed by sonication for 3x 30 s at 70% power. Lysed cells were centrifuged for 30 min at 38.000 g at 4 °C. The supernatant containing the desired protein was applied to Ni-NTA affinity chromatography. 1 ml Ni-NTA/Talon column material was used for 1 L *E. coli* culture to ensure sufficient binding capacity. To ensure proper binding, the drop rate was adjusted to 1 drop every 4-7 s. The columns were washed with 20 CV washing buffer (see subsection 2.5.6) and eluted with 16 CV elution buffer. To check protein purity, SDS-PAGE followed by Coomassie Blue staining was performed (see subsection 3.2.1). Only pure fractions were pooled and concentrated with Vivaspins 10.000 MWCO. To remove imidazole prior to storage of the protein, dialysis (see subsection 3.2.2) was performed. Protein samples were stored at -20 °C and cryoprotected with 40% glycerol.

3.2 Protein biochemical methods

3.2.1 SDS-PAGE & Coomassie staining

Sodium dodecyl sulfate polyacrylamide gel electrophoresis (SDS-PAGE) was performed to separate proteins according to their molecular weight. By mixing the protein samples with SDS sample buffer containing 0.4% dithiothreitol (DTT) and boiling them for 5 minutes at 95 °C, proteins were reduced, and protein-protein-interactions were resolved. For the detection of posttranslational redox modifications sample buffer without DTT was used. The samples were loaded onto gels containing 10-15% acrylamide, depending on the protein size. The gels were run for 30-45 min at 200 V with a Bio-Rad Mini PROTEAN® II electrophoresis apparatus.

To visualize the proteins within the polyacrylamide matrix, Coomassie Blue staining was performed. The gels were put into a petri dish with deionized water and were heated for 40 s at 700 W with a microwave. By heating the gels with Coomassie Blue in a subsequent step, proteins became visible. Afterwards, the gels were again washed by heating them with deionized water. If SDS-PAGE was followed by Western blot analysis, staining was not required.

3.2.2 Dialysis

Protein dialysis was used to remove imidazole after purification to improve protein stability upon storage. To increase flexibility of the dialysis membrane, it was soaked in water or dialysis buffer for 5-10 min. The enzyme was pipetted into a small vessel (0.1-2 ml), sealed with the dialysis membrane using a rubber ring and placed into a beaker with dialysis/storage buffer. Buffer was used in a 100:1 ratio to the total protein solution. Dialysis was performed three times for 30 min each at 4 °C and gentle stirring. Every 30 min, the buffer was discarded and

exchanged by fresh buffer. Due to potential protein loss during dialysis, the concentration was checked before and after dialysis.

3.2.3 Size exclusion chromatography

Size exclusion chromatography (SEC) was used to achieve a higher purity of protein samples and check the oligomeric state in parallel. For this purpose, a fast protein liquid chromatography (FPLC) system was used in combination with a HiLoad 16/60 superdex 75 or 200 column, depending on the protein size. Proteins were detected photometrically with an UV-detector at 280 nm.

3.2.4 Determination of protein concentration

The concentration of protein samples was measured at 280 nm with a BioSpectrometer® basic. Storage buffer was used as blank sample. As a control or in the presence of ATP, which absorbs at 260 nm and therefore disturbs the measurements at 280 nm, protein concentration was determined with the Bradford assay at 595 nm. For this purpose, bovine serum albumin was used to create a standard curve. 500 µl water (blank) or diluted protein (sample) was mixed with 125 µl Coomassie Brilliant Blue and measured after 15 min. The protein concentration was calculated according to the following formula:

$$\mathrm{C}\ \left[\frac{\mathrm{mg}}{\mathrm{ml}}\right] = \frac{\Delta \mathrm{A}_{595\ \mathrm{nm}}}{\text{gradient of the standart curve } [\frac{\mathrm{mg}}{\mathrm{ml}}]} * \text{dilution}$$

3.2.5 Gel filtration for desalting protein samples

Gel filtration chromatography using a G6 gel powder solved in the respective storage or assay buffer was used to remove residual molecules from protein samples, for example after incubations with oxidizing or reducing reagents. The gel contains medium poly-acrylamide beads for size exclusion chromatography, which has a fractionation range from 1-6 kDa, absorbing reagents and removing them from the protein solution. The gel powder was soaked in buffer for at least 1 h and loaded onto columns. Centrifugation at 1,000 g and 4 °C for 2 min was used to remove excess buffer. After discarding the flow-through, the protein sample was loaded onto the gel and centrifuged again. Due to a potential loss of protein or unintentional dilutions during desalting, the protein samples (flow-through) should be determined afterwards. Soaked gel powder can be prepared as a stock solution and stored for 4-6 weeks at 4 °C.

3.2.6 Western blot analysis

After separating proteins with SDS-PAGE, they can be transferred to either a polyvinyl difluoride (PVDF) or a nitrocellulose membrane via semidry blotting. With Western blot analysis, proteins can be detected and identified by treating the membrane with two different antibodies (1st and 2nd antibody), the second one is coupled to a chemiluminescence signal

which can be visualized with either X-ray films or a specific soft- and hardware. Most of the blots shown in this work were developed with a Chemostar ECL Imager.

To transfer the proteins onto the membrane, six filter papers per gel, the gel itself and the membrane were soaked in transfer buffer (see subsection 2.5.5). When using a PVDF membrane, a brief incubation of the membrane with methanol was required. For the protein transfer, a Trans-Blot® Turbo™ Transfer System from Bio-Rad was used. Therefore, three filter papers were placed into the cassette, followed by the membrane, the gel and three more filter papers on top. After removing air bubbles, the cassette was closed, and blotting was performed for 30 min at 13 V. To check whether proteins were transferred successfully, the membrane was stained with Ponceau staining solution for 30 s followed by treating the membrane with 1% acetic acid to visualize the protein bands. Staining was removed by washing the membrane with TBST. By incubating the membrane with 5% milk powder in TBST for 1 h at room temperature or overnight at 4 °C, free binding sites of the membrane where blocked to prevent possible unspecific interactions with antibodies. This incubation was followed by washing the membrane three times for 5-10 min with TBST before adding the first antibody for 1 h at room temperature. Before and after incubation of the membrane with the second antibody, the membrane was washed again as described above. To visualize the protein bands of interest, chemiluminescence detection was used. The chemiluminescence mixture contained luminol and coumaric acid. After applying the mixture onto the membrane, it needed to be kept away from daylight. In case of the usage of X-ray films, they were placed onto the membrane and sealed in a dark cassette until developed with an X-ray developing machine. The other Western blots were developed with a Chemostar ECL Imager using the Chemostar Software. Depending on the antibodies used, the exposure time varied from several seconds to minutes.

3.3 Posttranslational redox modifications

For posttranslational redox modifications of proteins (S-glutathionylation and S-nitrosation), protein samples were reduced with 5 mM DTT for 30 min at 4 °C. DTT resolves disulfide bonds and makes accessible cysteines susceptible to oxidation. To remove excess DTT, protein samples were desalted (see subsection 3.2.5) For further incubations steps with agents inducing either S-glutathionylation or S-nitrosation were performed as previously described with slight modifications (Forrester et al., 2009; Kehr et al., 2011; Wang et al., 2014).

3.3.1 S-Glutathionylation

To achieve S-glutathionylation, pre-reduced samples were incubated with 0-10 mM GSSG at 37 °C for 10 min. A desalting step removed excess GSSG that could putatively interfere with the following assay. S-glutathionylated proteins could be detected via Western blot analysis using an anti-glutathione antibody (Virogen).

3.3.2 S-Nitrosation (biotin-switch assay)

S-Nitrosation was induced by incubations of proteins samples with 0 – 1,000 µM S-nitrosocysteine (Cys-NO). Cys-NO was prepared separately for each experiment. All solutions were solved freshly, kept on ice and in the dark to avoid loss of concentration due to decreased stability. For the synthesis of 95.24 mM Cys-NO, 250 mM sodium nitrite was incubated with 250 mM L-cysteine-hydrochloride-monohydrate and 1 M HCl in a 4:4:1 ratio for at least 5 min. Before starting the nitrosation, the Cys-NO solution must be neutralized with 1 M NaOH (ratio 6:1) to a final pH of 7.5. The final Cys-NO solution has an orange-red color. S-nitrosation inducing incubations were performed at 25 °C in the dark for 1 h, excess Cys-NO was removed via gel filtration. Due to a lack of an antibody directly detecting nitrosated proteins, a biotin-switch assay was performed that allows an indirect detection of nitrosated proteins by using an anti-biotin antibody (Santa Cruz) (Figure 11).

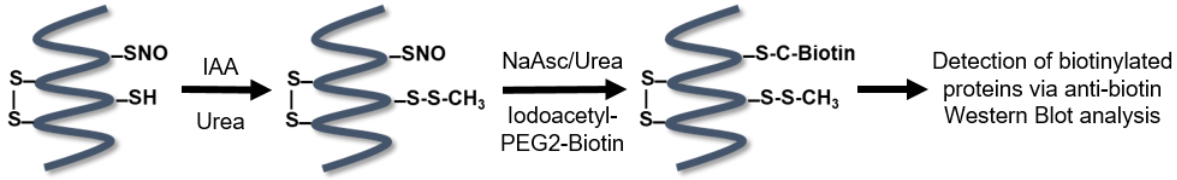

Figure 11 - Principal of the biotin-switch assay.
(Wang et al., 2014)

Nitrosation - First, the protein samples (0.4 – 0.8 mg/ml, final volume of 250 µl) were nitrosated as described above. Each Cys-NO concentration is prepared as a duplicate with regard to a negative control during the following steps. The reaction was stopped by adding 750 µl of ice-cold acetone (100%). After that, protein precipitation was performed for 30 minutes at -20 °C. The mixtures were centrifuged at 8,000 g for 5 min and the supernatant was discarded. The protein pellets were washed three times with 70% ice-cold acetone by centrifugation at 5,000 g for 5 min.

Blocking of free thiols - The protein pellets were resuspended in blocking buffer containing 100 mM iodoacetamide (IAA) to a final volume of 250 µl. After incubation for 45 min at 50 °C in the dark with constant shaking, the reaction was stopped with 100% acetone, followed by protein precipitation and three washing steps as described above.

Denitrosation and biotinylation (labeling) - The protein pellets were resuspended in labeling buffer containing 20 mM NaAsc and 0.2 mM iodoacteyl-PEG2-biotin to a final volume of 250 µl. The negative controls were prepared without NaAsc. During incubation for 1 h at 25 °C in the dark, NaAsc reduced nitrosothiols to enable the labeling with biotin. Again, adding 100% acetone stopped the reaction and pellets were washed three times with 70% acetone.

For consecutive SDS-PAGE and Western Blot analysis with an anti-biotin antibody, pellets were resuspended in blocking buffer. The Bradford assay was used to determine protein

concentrations of the respective samples. 2 µg protein was loaded per lane to get proper signals in Western Blot analysis.

3.4 Assays

3.4.1 Determination of kinetic parameters

Enzymatic activities were measured at 25 °C using either a HITACHI U-2001 spectrophotometer or an Evolution 300 UV/VIS spectrophotometer (Thermo Scientific) with a total assay volume of 500 µl. Both assays were coupled to another enzyme to measure either the increase of NADPH or the decrease of NADH. Final activities were calculated by using Lambert-Beer's law:

$$U/ml = \frac{\Delta A/\min * 0.5\ ml}{6.22\ \mu mol^{-1} min^{-1} ml^{-1} * 1\ cm * X\ ml\ enzyme} * dilution$$

$$U/mg = \frac{U/ml}{mg/ml\ enzyme}$$

For evaluations and calculation of K_M-values, GraphPad Prism 8 was used whereby only linear decreases in absorbance were considered.

3.4.1.1 PfPK enzymatic activity assay

PfPK converts PEP into pyruvate while transferring a phosphate group from PEP to ADP yielding ATP. To detect the enzymatic activity, this reaction was coupled with lactate-dehydrogenase (LDH). LDH reduces pyruvate to lactate while NADH oxidizes to NAD^+.

Phosphoenolpyruvate + ADP $\xrightarrow{PfPK}$ pyruvate + ATP

Pyruvate + NADH $\xrightarrow{LDH}$ lactate + NAD^+

The assay mixture contained 10 mM Hepes, pH 7.5, 10 mM $MgCl_2$, 50 mM KCl, 0.1 mM NADH, 10 U/ml LDH (from rabbit muscle), PEP and ADP, both ranging from 0.025 to 3 mM. To start the reaction, ~100 ng/ml PfPK was added supplemented by 2 mg/ml bovine serum albumin for increased stability of the enzyme.

3.4.1.2 PfHK enzymatic activity assay

PfHK converts D-glucose into D-G6P under the release of ADP. G6P is catalyzed by glucose-6-phosphate dehydrogenase (G6PD) to 6-phospho-gluconate while forming NADPH.

D-glucose + ATP $\xrightarrow{PfHK}$ D-glucose-6-phosphate + ADP

D-glucose-6-phosphate + $NADP^+$ $\xrightarrow{G6PD}$ 6-phospho-gluconate + NADPH

The standard assay contained 15 mM D glucose, 4 mM ATP, 1 mM $NADP^+$, 5 U/ml G6PD (from baker's yeast) in 100 mM triethanolamine, pH 7.5 and 10 mM $MgCl_2$. For determining Michaelis-Menten constants (K_M), ATP was used in concentrations ranging from 0.1 to 5 mM, D-glucose was used 0.02 to 30 mM.

3.4.2 Ellman's assay

Ellman's reagent was used to quantify the amount of free sulfhydryl groups by reference to the extinction coefficient of TNB (14,150 $M^{-1} \cdot cm^{-1}$). Ellman's reagent (5,5′-dithiobis-(2-nitrobenzoic acid) = DTNB) reacts stoichiometrically with thiols releasing 2-nitro-5-thiobenzoate (TNB^-). In water with alkaline and neutral pH, TNB^- ionizes to TNB^{2-}, which has a yellow color and can be spectrophotometrically quantified at 412 nm. The assay contained 150 mM potassium phosphate, pH 8.0, 200 µM DTNB and different concentrations of reduced protein in the micromolar range. The assay volume comprised 500 µl and was incubated for at least 15 min at 25 °C. Final concentrations were calculated by using Lambert-Beer's law:

$$mM\ [TNB^-] = \frac{\Delta A * mM * cm * v_0}{14.15 * v_i * d[cm]}$$

3.4.3 Nsp5 cleavage assay

To perform a qualitative analysis of the nsp5 protease activity, 2 µM polyprotein intermediate (nsp7-11-His_6) was incubated with 4 µM nsp5 at 4 °C for 24 h. The reaction was stopped by adding SDS-PAGE loading dye. The protease activity results in the cleavage of the polyprotein and can be detected via SDS-PAGE.

3.4.4 Nsp9 NMPylation assay

The assay for nsp12-mediated NMPylation of nsp9 contained 4 µM nsp9, 0.5 µM nsp12, 1 mM $MnCl_2$, 25 µM NTP, and 0.17 µM of the matching [α^{32}-P]NTP (UPT, GTP, ATP, CTP). Samples were incubated at 30 °C for 10 min and the reaction was stopped by adding SDS-PAGE loading dye. Proteins were separated by SDS-PAGE and fixed by Coomassie staining. After destaining, the gels were exposed to phosphorimager screens for 2 h and scanned with a Typhoon 9200 imager to assess nsp9 NMPylation.

3.5 Mass spectrometry

To identify cysteine residues modified by either S-glutathionylation or S-nitrosation, matrix-assisted laser desorption/ionization time-of-flight-mass spectrometry (MALDI-TOF MS) was used. Those analyses were performed in two different facilities (Protein Analytics, Justus Liebig University Giessen and Core Facility of Mass Spectrometry and Elemental Analysis, Philipps University Marburg). Samples were provided either by single bands of SDS-PAGE or stored at -20 °C and prepared via proteolytic digestion using trypsin without reduction.

3.6 Protein crystallization and data collection

Prior to protein crystallization, the protein was purified and as described above (see subsection 3.1.4) and, if necessary, agents potentially disturbing the crystallization process (for example imidazole), were removed. Substrate(s) or product(s) were added to the protein solution to

stabilize it during the crystallization process. Reducing agents like DTT were also shown to increase the chance of successful crystallization.

Initial screenings were performed with commercially available screens spanning 96 different conditions each, using the vapor diffusion technique. For this purpose, a Honeybee 961 crystallization robot was used. Promising crystallization conditions were optimized via in-house produced screens. For further analysis, crystals were transferred into buffer containing a cryoprotectant (DL-threitol, ethylene glycol, glycerol) and the crystallization buffer. Crystals of appropriate size and quality were stored in liquid nitrogen until analyzed via X-ray diffraction. Diffraction data was collected at X10SA (detector: Pilatus) of the Swiss Light Source in Switzerland, at 100 K. Procession of the obtained data sets was performed with XDS (Kabsch, 2010), which includes routines for space group determination. Structures were solved via molecular replacement methods. The search models were generate via homology modeling with SWISS-MODEL (Waterhouse et al., 2018). As templates for modeling, the following structures from PDB were used: 3KHD for PfPK, 6VYF and 6VYG for PfHK. Molecular replacement and structure refinement were performed with the PHENIX program (Adams et al., 2010; Moriarty et al., 2016). For modeling, the interactive graphics program Coot was used (Emsley and Cowtan, 2004). THE UCSF Chimera package was used for the production of molecular graphic images (Pettersen et al., 2004).

3.7 Human erythrocyte ghost preparation

To isolate high concentrations of spectrin, human erythrocyte ghosts were prepared. 2 ml erythrocyte concentrate, obtained from the blood bank of the University Hospital Giessen, was washed up to three times with 25 ml isotonic KCl (for buffer compositions, (see subsection 2.5.8) for 10 min at 1.600 rpm (without break). All centrifugation steps were performed at 4 °C with a Sorvall RC 5 centrifuge using the SS-34 rotor. Cells were diluted with 0.5 ml isotonic KCl and lysed for 60 s by adding 10 ml hemolysing medium A, followed by centrifugation at 13.000 rpm for 15 min. After discarding the supernatant, the pellet was incubated with 1.25 ml MilliQ-water and 125 µl of solution C for 2 min. To remove hemoglobin from the open ghosts, they were washed with 11 ml washing medium B at 13.000 rpm for 15 min. The washing step was repeated until the ghosts have a greyish white color. To reseal the ghosts and reverse tonicity, the pellet was resuspended with 1.25 ml MilliQ-water and 112.5 µl of solution D. After incubation for 45 min at 38 °C and another centrifugation step, pellets were prepared for Western Blot analysis by resuspension in 100 µl Hank's buffered salt solution. To achieve proper protein separation, 3-8% Tris-acetate gradient gels were used.

3.8 Enrichment of trophozoite-stage *P. falciparum* parasites

During the trophozoite stage, the parasites produce hemozoin which is magnetic. This magnetism can be used to separate trophozoites from non-infected RBCs and ring-stage parasites (magnetic activated cell sorting, MACS). MACS columns were connected to disposable hypodermic needles via a 3-way stopcock and attached to the Quadro MACS™ separating system. Before *P. falciparum* cell suspensions were added, the columns were equilibrated with complete medium. To separate non-infected RBCs and ring-stage parasites from the columns, they were washed with complete medium until the flow-through was clear. Afterwards, the columns were detached from the magnet and trophozoite-stage parasites were eluted with complete medium. Columns were cleaned with 1 column volume sterile H_2O, 3 ml 70% ethanol and 3 ml 100% ethanol.

4 Results

4.1 *P. falciparum* hexokinase (PfHK)

4.1.1 Heterologous overexpression, purification, and kinetic parameters

Protocols for heterologous overexpression and purification of PfHK were previously established in our working group but could not be reproduced for further analyses of the enzyme (Zhang, 2013). For this reason, one goal of this thesis was to ensure reproducible protocols for the recombinant production of soluble and stable PfHK. The coding sequence for PfHK was ordered as codon-optimized synthetic gene from General Biosystems (PlasmoDB ID: PF3D7_0624000). The sequence was cloned into pET30a-c(+), using the restriction sites NdeI and XhoII, and transformed into chemically competent *E. coli* C41(DE3) cells. DNA synthesis was induced by adding 0.5 mM IPTG and protein expression was performed overnight at room temperature. To increase the solubility of PfHK, 30% glycerol and 1% Triton-X100 were added during cell lysis. The protein was purified via Talon® Metal Affinity Resin, yielding ~0.8-1 mg soluble and active enzyme per liter *E. coli* culture. Size exclusion chromatography (SEC) confirmed PfHK exists as a tetramer (Figure 12 A+B).

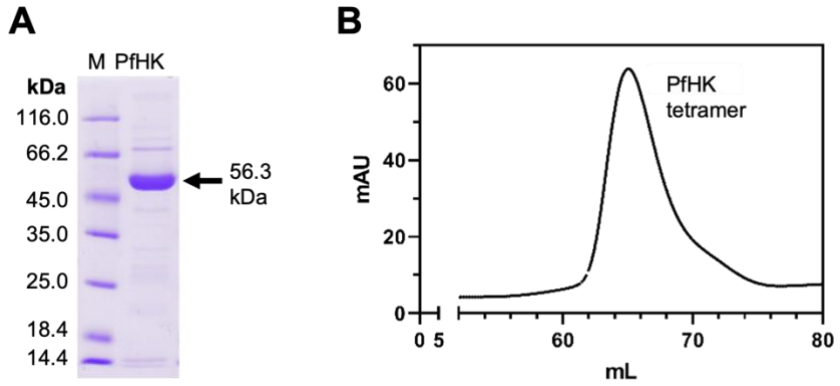

Figure 12 - Purification and size exclusion chromatography of PfHK.
(A) Coomassie staining of a 12% SDS-PAGE gel after purification of PfHK via affinity (Talon® Metal Affinity Resin) and size exclusion chromatography (Äkta FPLC System, Superdex 200 column). To control final purity, ~6 µg protein was applied to SDS-PAGE. M = unstained protein molecular weight marker. **(B)** After affinity chromatography, eluted protein fractions were applied to an ÄKTA FPLC system. PfHK eluted at 62 ml corresponding to ~225 kDa (PfHK tetramer).

Kinetic parameters of PfHK were determined spectrophotometrically in a coupled assay measuring the increase of NADPH at 340 nm. The specific activity varied from 27.0 U·mg^{-1} to 30.7 U·mg^{-1}. When stored at 4 °C, the enzymatic activity was stable for several days with the tendency to be lowered after one week (data not shown). For this reason, kinetic measurements were performed with freshly purified, biological independent batches of enzyme. At least three independent experiments were performed to determine Michaelis Menten constants. K_M values were calculated with GraphPad Prism and were 830.5 ± 78.1 µM for ATP and 126.0 ± 8.2 µM for glucose (Figure 13 A+B).

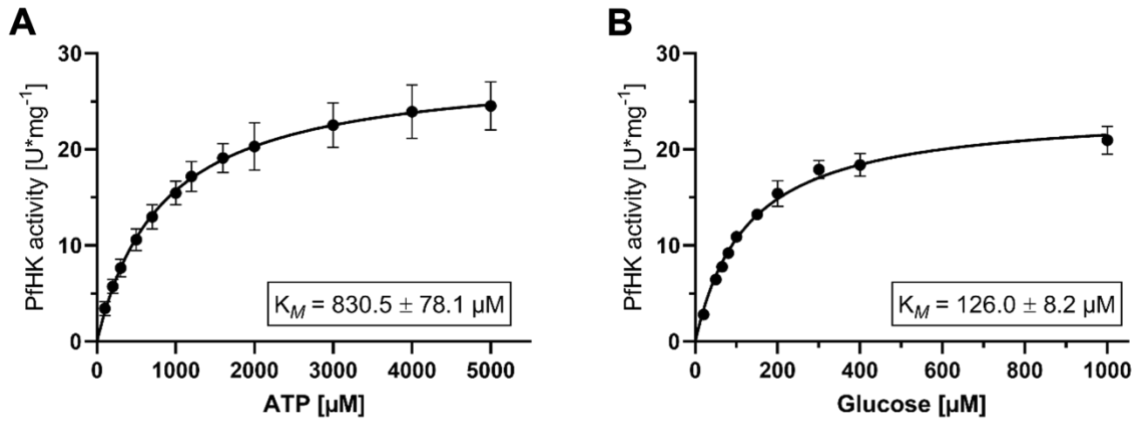

Figure 13 - PfHK K_M values for ATP and glucose.
(A) K_M for ATP (0-5 mM) in PfHK in the presence of 15 mM glucose. **(B)** K_M for glucose (0-10 mM) in PfHK in the presence of 4 mM ATP. Measurements were performed in at least three biologically independent triplicates.

4.1.2 Oxidative posttranslational modifications

4.1.2.1 S-Glutathionylation

PfHK was incubated with different concentrations of GSH and GSSG to investigate the effect of S-glutathionylation on its enzymatic activity. While GSH did not alter the enzymatic activity, incubations with GSSG decreased its activity in a concentration-dependent manner (Figure 14 A). GSSG was used in concentrations ranging from 0-10 mM. Besides this concentration-dependent inhibition also a time-dependent inhibition of PfHK enzymatic activity was shown. This decrease could already be observed after 5 min incubation time. After 30 min, its enzymatic activity was reduced by more than 70% (Figure 14 B). Western blot analysis of the modified enzyme using an anti-glutathione antibody confirmed the kinetic data and revealed increasing signal intensity with increasing concentrations of GSSG. Adding DTT to the sample that was incubated with 10 mM GSSG did not lead to any signal in the Western blot suggesting that DTT removes the modification (Figure 14 C).

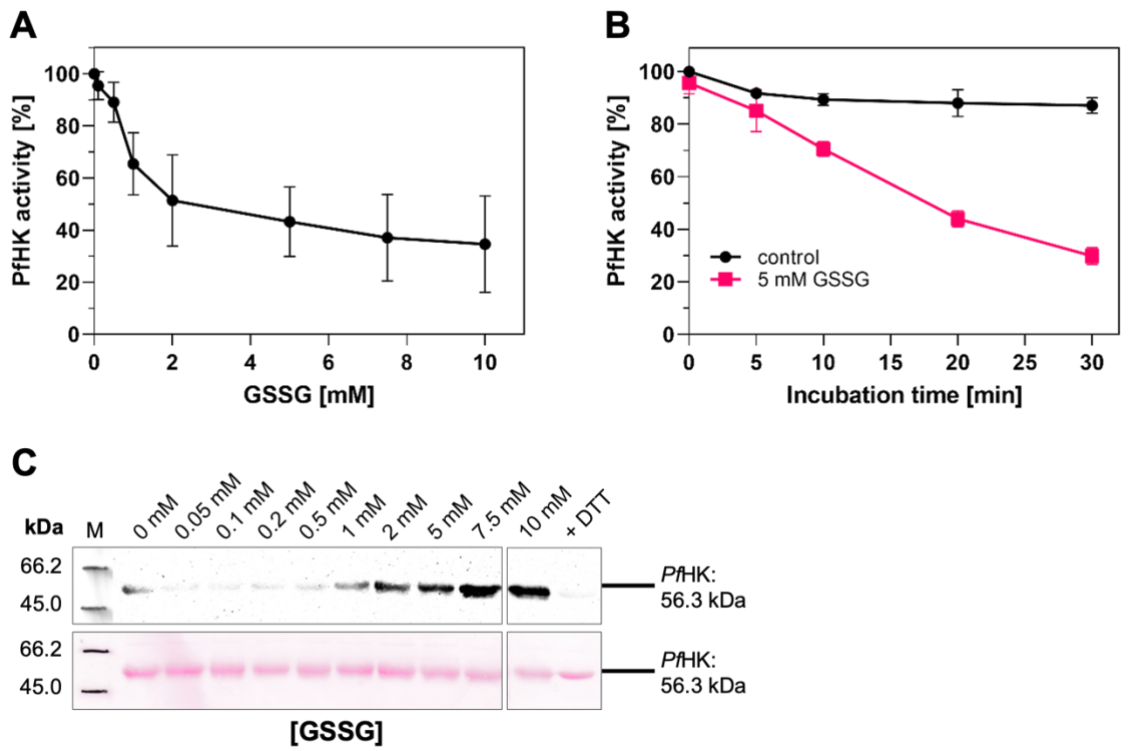

Figure 14 - Enzymatic activity and Western blot analysis of S-glutathionylated PfHK.
(A) Reduced PfHK was incubated with 0-10 mM GSSG for 10 min at 37 °C. The activity of the sample incubated with 0 mM GSSG (control) was defined as 100%. Values are shown as mean values ± SD. Measurements were performed in at least three biologically independent triplicates. **(B)** Reduced PfHK was incubated with 0 mM (control) or 5 mM GSSG for 0-30 min at 37 °C. The enzymatic activity of the control sample at 0 min was defined as 100%. Values are shown as mean values ± SD. Measurements were performed in at least three biologically independent triplicates. **(C)** S-glutathionylated samples from (A) were analyzed via Western blot analysis, using 2 µg protein per lane. S-glutathionylated PfHK was detected with an anti-glutathione antibody. SDS-PAGE loading buffer with DTT served as a chemical negative control. Ponceau staining served as a loading control.

4.1.2.2 S-Nitrosation

As previously described for S-glutathionylation, PfHK was incubated with different concentrations of Cys-NO (0-2 mM) to investigate how S-nitrosation affects its enzymatic activity. Under physiological conditions, concentrations of nitrosative species are lower compared to concentrations of GSSG which is why lower concentrations of Cys-NO were chosen for the experiments. Already 500 µM Cys-NO inhibited PfHK to a residual activity of ~50% (Figure 15 A). In a time-course experiment the effect of S-nitrosation was monitored over 120 min. After 30 min, PfHK activity was already lowered by ~40% (Figure 15 B). To check whether the concentration-dependent inhibition is evoked by S-nitrosation, a biotin-switch assay was performed. In brief, this assay is used to label S-nitrosated cysteines with a biotin-tag, which can subsequently be detected via anti-biotin Western blot analysis (for more details see ‘3 Methods’). Here it was shown that already very low concentrations (100 µM) of Cys-NO induced S-nitrosation (Figure 15 C).

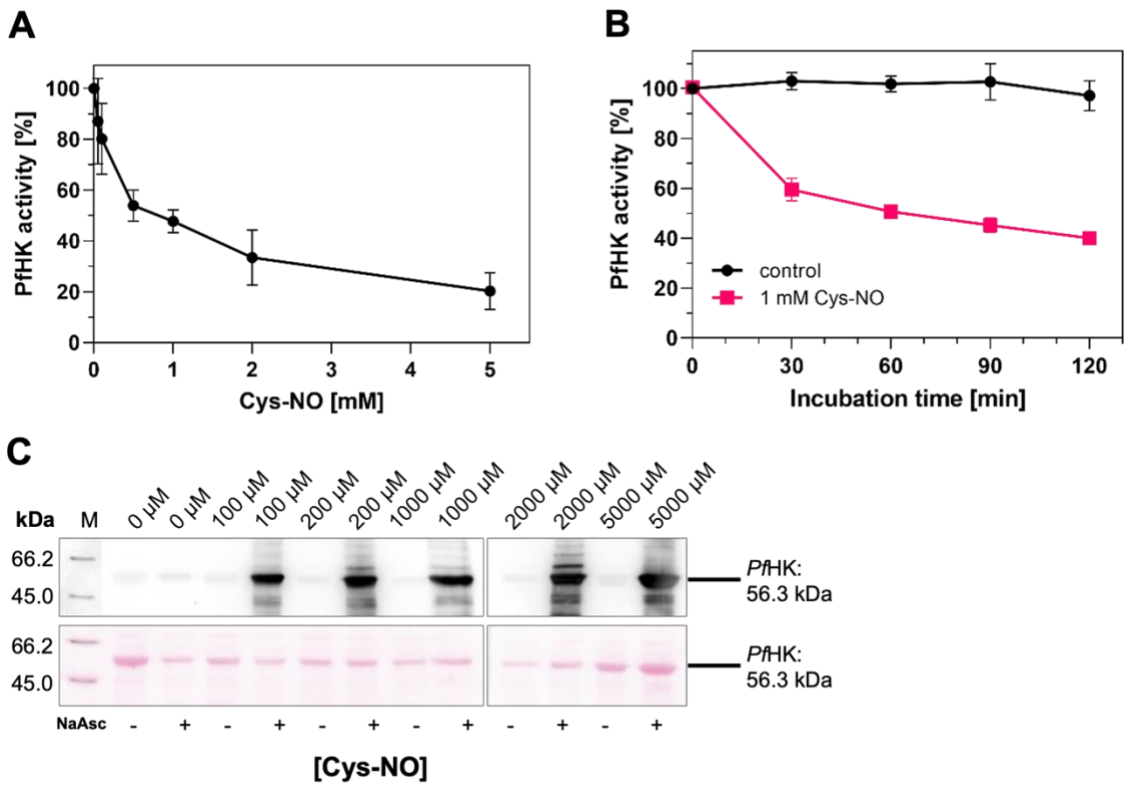

Figure 15 - Enzymatic activity and Western blot analysis of S-nitrosated PfHK.
(A) Reduced PfHK was incubated with 0-5 mM Cys-NO for 60 min at 25 °C. The activity of the sample incubated with 0 mM Cys-NO (control) was defined as 100%. Values are shown as mean values ± SD. Measurements were performed in at least three biologically independent triplicates. **(B)** Reduced PfHK was incubated with 0 mM (control) or 1 mM Cys-NO for 0-120 min at 25 °C. The enzymatic activity of the control sample at 0 min was defined as 100%. Values are shown as mean values ± SD. Measurements were performed in at least three biologically independent triplicates. **(C)** S-nitrosated samples from (A) were analyzed via anti-biotin Western blot analysis, using ~2 µg protein per lane. S-nitrosated PfHK was detected with an anti-glutathione antibody. Samples incubated without NaAsc served as a chemical negative control. Ponceau staining served as a loading control.

4.1.2.3 Susceptibility of cysteines to oxidative posttranslational modifications

In order to investigate how many cysteines out of PfHK's fifteen cysteines are potentially susceptible to oxPTMs, Ellman's reagent was used. For this purpose, different concentrations of reduced PfHK (0.5-4 µM) were incubated with 200 µM DTNB for ~15 min. Free thiols were quantified by using Lambert-Beer's law (see 3.4.2 Ellman's assay). From a total of fifteen cysteines within PfHK, ten to eleven cysteines responded to the oxidation of their sulfur group induced by Ellman's reagent.

Mass spectrometry

Both S-glutathionylated and S-nitrosated samples of PfHK were send to mass spectrometry analysis to assess the modification pattern and the susceptibility of single cysteines. To further identify cysteines that are putatively more sensitive than others, different concentrations of glutathione and Cys-NO were chosen. Three biologically independent samples were used per concentration. Nitrosated samples were objected to a biotin-switch assay prior to analyses to avoid unwanted degradation of the modification. Afterwards, biotinylated thiols were detected.

Six out of fifteen cysteines could not be detected in mass spectrometry analyses, six cysteines were found to be S-glutathionylated and nine cysteines were found to be biotinylated (originally nitrosated, Table 2). The analyses of S-glutathionylated protein revealed increasing S-glutathionylation with increasing concentrations of GSSG. At 0.1 mM GSSG 17% of the peptides were S-glutathionylated whereas 42% of the peptides were S-glutathionylated at 10 mM GSSG. Out of the nine cysteines found to be nitrosated, five were detected most often: C77, C85, C219, C346 and C399. Summarizing all data, C346 seems to be most susceptible to both kinds of modifications.

Table 2 - Oxidative posttranslational modification of PfHK cysteines.
Abbreviations: -SSG = S-glutathionylated cysteine, -SNO = S-nitrosated cysteine.
*PDB ID: 7ZZI (publication on hold)

Cysteine position	Found with both modifications	-SSG	-SNO	Not found in MS	Accessible in structure*	
					Dimer	Tetramer
21	X	X	X		(X)	(X)
77	X	X	X		X	-
85	X	X	X		X	X
186				X	-	-
193				X	X	X
219			X		X	X
236				X	X	X
237				X	(X)	(X)
249			X		X	X
260				X	X	X
273			X		-	-
346	X	X	X		(X)	(X)
399	X	X	X		X	X
431	X	X	X		-	-
445				X	X	X
∑	**6**	**6**	**9**	**6**	**9 (12)**	**8(11)**

4.1.2.4 Reversibility of oxidative posttranslational modifications

Previous studies found hexokinases to putatively interact with redox-active proteins. These data include the interaction of PfHK with PfGrx, PfPlrx and PfTrx. To validate these findings and to further investigate the efficiency of those proteins to reduce cysteines targeted by oxidative posttranslational modifications, different samples of PfHK (reduced, S-glutathionylated or S-nitrosated) were prepared. To induce deglutathionylation or denitrosation, modified PfHK was incubated with either 5 mM DTT as a chemical control or with one of the following redox-active proteins: PfGrx, PfPlrx and PfTrx. All three proteins were

reduced prior to the incubations and used in a 10-fold molar excess to the molar concentration of PfHK cysteines. PfHK was added to a final concentration of 0.1 mg·ml^{-1} (= 26.6 µM cysteines). Incubations were conducted at 25 °C for 30 min. Samples of PfHK without any addition of reducing agents or proteins served as controls. For denitrosation studies, the incubations were kept away from light to avoid misleading results by light-induced denitrosation. As already indicated by Western blot analysis, adding DTT can not only remove S-glutathionylation (as indicated by a decrease of signal intensity in Figure 14 C) but also completely restores PfHK enzymatic activity (Figure 16 A). Adding DTT to S-nitrosated PfHK seems to be less efficient, only restoring its activity back to ~90% compared to its initial activity. Incubations of modified PfHK with PfTrx, PfGrx and PfPlrx can also restore its enzymatic activity, but less effective than DTT. Among the three proteins, PfPlrx seems to have the most effective interaction with PfHK: After deglutathionylation PfHK was ~99% active, after denitrosation ~84% compared to its initial activity (100%, Figure 16 B). In general, PfHK seems to recover better from the inhibitory effect of S-glutathionylation than from the inhibition mediated by S-nitrosation. Furthermore, DTT, PfTrx, PfGrx and PfPlrx increase the enzymatic activity of unmodified PfHK by ~20-35%.

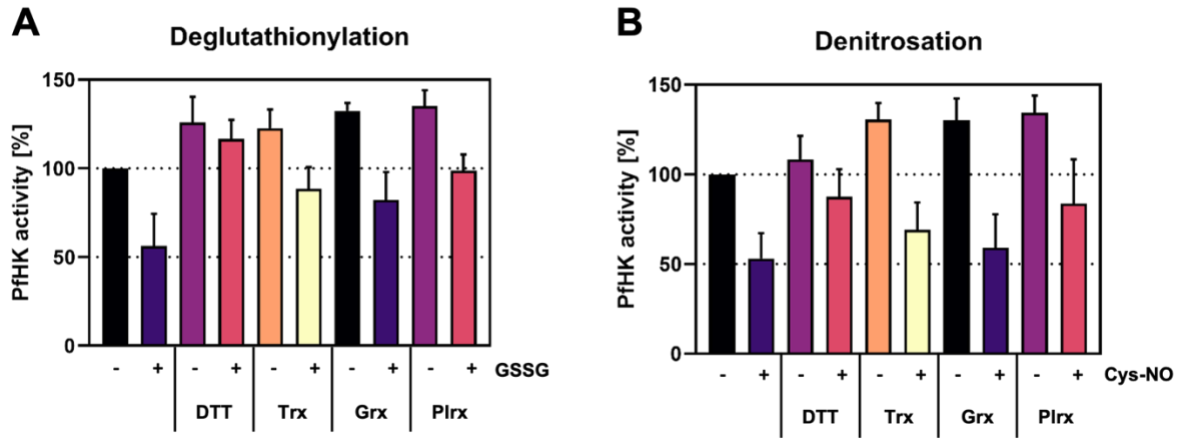

Figure 16 - Interaction of PfHK with PfTrx, PfGrx and PfPlrx.
(A) PfHK was incubated with 5 mM GSSG for 10 min at 37 °C. Excess GSSG was removed via gel filtration. **(B)** PfHK was incubated with 1 mM Cys-NO for 60 min at 25 °C. Excess Cys-NO was removed via gel filtration. S-glutathionylated/S-nitrosated PfHK was incubated with DTT or reduced PfTrx, PfGrx and PfPlrx for 30 min at 25 °C. Each value represents a mean value from at least three independently measured triplicates. Data are represented as mean ± SD.

4.1.2.5 Co-incubation with substrates

Inhibitory effects of S-glutathionylation and S-nitrosation are often mediated by modifications of cysteines near or even within the substrate binding site contributing to catalysis. To assess whether the PfHK substrates ATP and/or glucose protect from the inhibitory effect of oxPTMs, either ATP, glucose or both substrates at the same time were added to the standard S-glutathionylation and S-nitrosation mixtures. Unmodified PfHK without any additional substrate incubation served as control and was defined as 100%. The substrates were used with an at least 5-fold molar excess compared to their K_M value, respectively. After removing

excess substrates by gel filtration, PfHK enzymatic activity was determined with the standard photometric assay (see subsection 3.4.1.2).

Incubations with ATP alone did not reverse the inhibitory effect of both S-glutathionylation and S-nitrosation, it even decreases the enzymatic activity of unmodified PfHK up to 28% residual activity (Figure 17 A+B). Preincubations with glucose could slightly restore the inhibitory effect of both modifications, but the most effective were incubations with ATP and glucose in parallel. The enzymatic activity of PfHK incubated with GSSG and both substrates was 81.3%, whereas PfHK incubated with Cys-NO showed a hardly changed activity of 94.6%, compared to 100% activity of the control sample. Western blot analysis with an anti-glutathione antibody showed slightly different signal intensities for the S-glutathionylated samples incubated with either ATP, glucose, both, or none of the substrates. Adding ATP seems to increase the signal intensity for S-glutathionylation, whereas the other S-glutathionylated samples, including the control without substrate added, showed similar signal intensities (Figure 17 C).

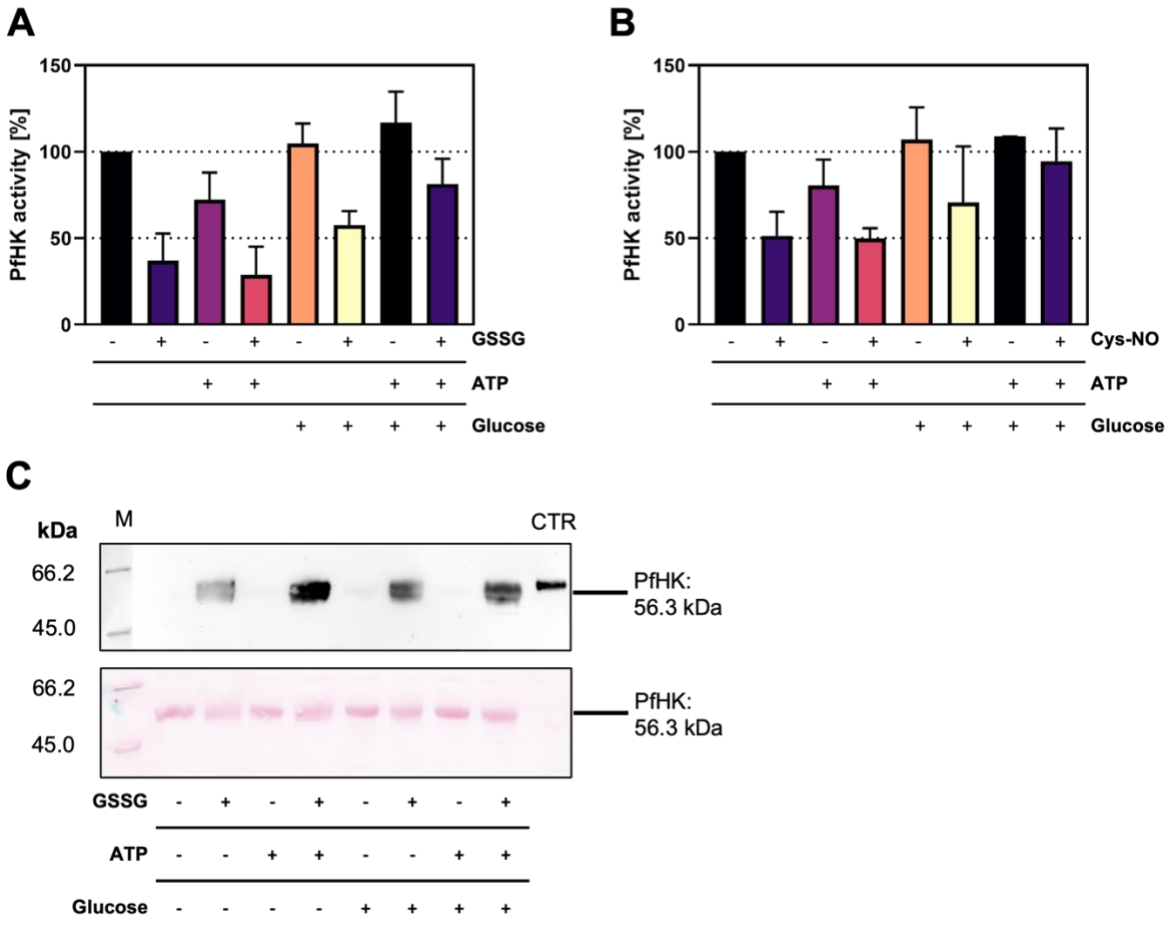

Figure 17 - Incubation of posttranslationally modified PfHK with ATP and glucose.
(A + B) PfHK was incubated with a 5-fold molar excess of either one or both substrates together with 5 mM GSSG 37 °C for 10 min or with 1 mM Cys-NO at 25 °C for 60 min. Each value represents a mean value from at least three independently measured triplicates. Data are represented as mean ± SD. **(C)** S-Glutathionylated samples, ~3 µg protein per lane, were analyzed via Western blot with an anti-glutathione antibody. M, marker; CTR, positive control.

4.1.3 Protein crystallization

Initial screenings for optimal crystallization conditions were performed with a Honey Bee crystallization robot. 5-10 mg·ml^{-1} PfHK were used with and without different mixtures of potentially stabilizing agents, for example DTT, glycerol, ADP, ATP, AMP-PNP, glucose or G6P. Various conditions lead to phase separation or the formation of spherulites. Finally, first crystals were obtained from JBScreen PEG/Salt, PACT++ HTS (20% w/v polyethylene glycol (PEG) 3,350; 200 mM tri-sodium citrate) and JCSG+ HTS (10% w/v PEG 8,000; 100 mM Tris, pH 7.0; 200 mM $MgCl_2$). Crystallization conditions were strategically varied using different percentages of PEG 3,350 and 8,000, respectively, different salts ($MgCl_2$, magnesium acetate, lithium sulfate, sodium citrate, potassium citrate) and buffers (MES, pH 6.5, Hepes, pH 7.0, Tris, pH 7.5). For more details see Tables S4-S6 in the Supplementary Information. To further optimize the crystallization conditions, different buffers with a pH ranging from pH 3.6 to 4.8 were tested in combination with 20% PEG 3,350 and 200 mM sodium citrate. Finally, crystals diffracted to a resolution of 2.8 Å, grown in 20% PEG 3,350, 200 mM sodium citrate and 0.1 M sodium citrate buffer with a pH ranging from 3.4 to 4.0 (Figure 18). The protein solution contained 5 mg·ml^{-1} PfHK, 10 mM glucose, 10 mM ATP and 5 mM DTT. As a cryoprotectant, either 25% ethylene glycol or 1 M threitol were used.

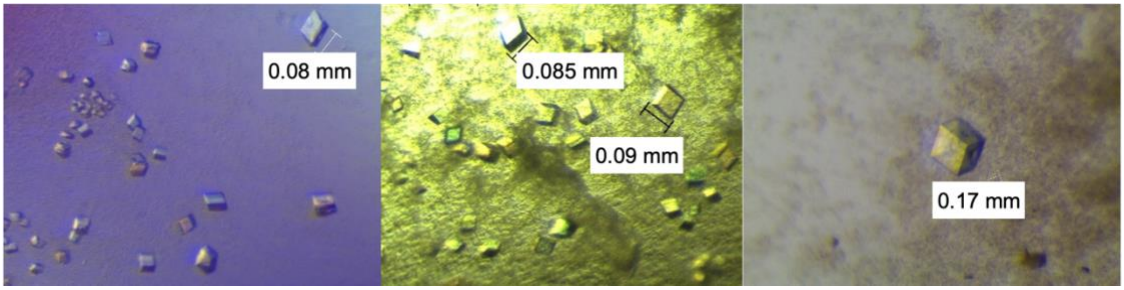

Figure 18 - Protein crystals of PfHK.
Exemplary pictures of PfHK protein crystals obtained with crystallization conditions containing 20% PEG 3,350, 200 mM sodium citrate and 0.1 M sodium citrate buffer with a pH ranging from 3.4 to 4.0. Protein solution contained 5 mg·ml^{-1} PfHK, 10 mM glucose, 10 mM ATP and 5 mM DTT.

Overall structure of PfHK

The data was assessed by Dr. Karin Fritz-Wolf at the Max Planck Institute for Medical Research in Heidelberg. The structure was solved via molecular replacement and deposited to PDB (ID: 7ZZI, on hold until publication of the primary citation). The crystals contain two monomers within the asymmetric unit and belong to the space group $P3_121$. PfHK consists of two domains: a small domain (E94-L239) and a large domain (S1-Q93; N240-P490). Within the active site of both monomers, which is located between the two domains, glucose was bound. An additional citrate molecule was detected in monomer A (Figure 19).

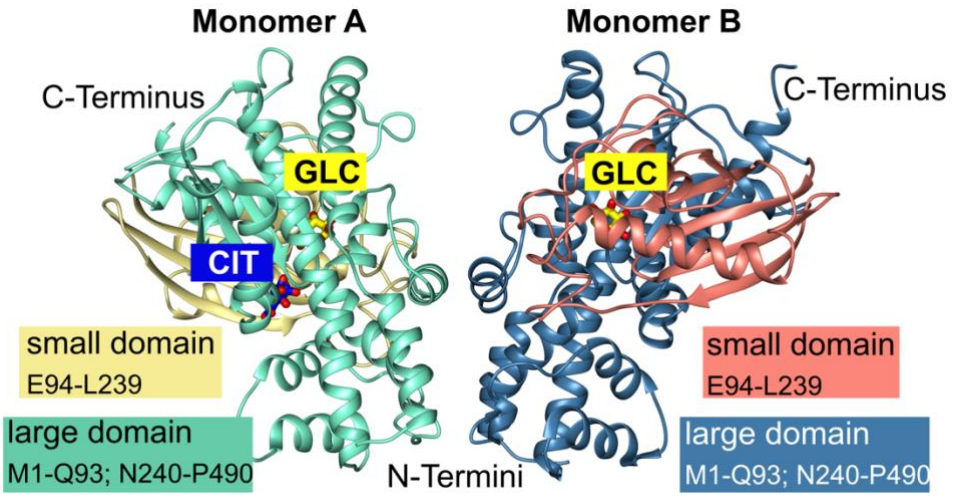

Figure 19 - The asymmetric unit of PfHK crystals consists of two subunits.
Each PfHK monomer contains two domains: a small domain (E94-L239) and a large domain (M1-Q93; N240-P490). In both monomers, glucose (GLC) was bound, whereas monomer A was complexed with an additional citrate molecule (CIT).

Tetrameric interfaces

The dimer within the asymmetric unit (AB) forms together with the symmetry-equivalent dimer (A'B') a tetramer, which is in accordance with the results of SEC (Figure 20 A). Between the four subunits of the tetramer, there are six different interfaces. However, due to the crystallographic symmetry, two interfaces are identical, respectively: AB (≙ A'B'), AA' (≙ BB') and AB' (≙ BA'). These interfaces are highlighted in Figure 20 B and were further analyzed with PISA (https://www.ebi.ac.uk/pdbe/pisa/) to identify hydrogen bonds and hydrophobic interactions.

Subunits A and B' are mainly connected by hydrophobic interactions among residues of a long helix (E49-R66) from both monomers and a hydrogen bond between $N53^{A}$ and $Y56^{B}$ (Figure 20 C). Various residues from monomer A (K281-Y282, D299 and I423) interact with residues from monomer B' (S45-K67 and K298-D299). Interestingly, H75 from all four monomers, assembling within the tetrameric center, is part of the interfaces. In Figure 20 D, residues mainly from the small domains form the interface BB': K67-E76, K80, T187-D198, R207-K220 and R316-R318. Furthermore, N70 from both monomers is hydrogen bonded to I197, D198 and E214 from the other monomer. Interaction between monomers A and B is mainly mediated via residues from the respective large domains (Figure 20 E). Seven hydrogen bonds and one salt bridge between $E28^{A}$ and $K348^{B}$ strongly connect both subunits. Additional interactions were observed among residues T302-Y312, R336-K348 and W351.

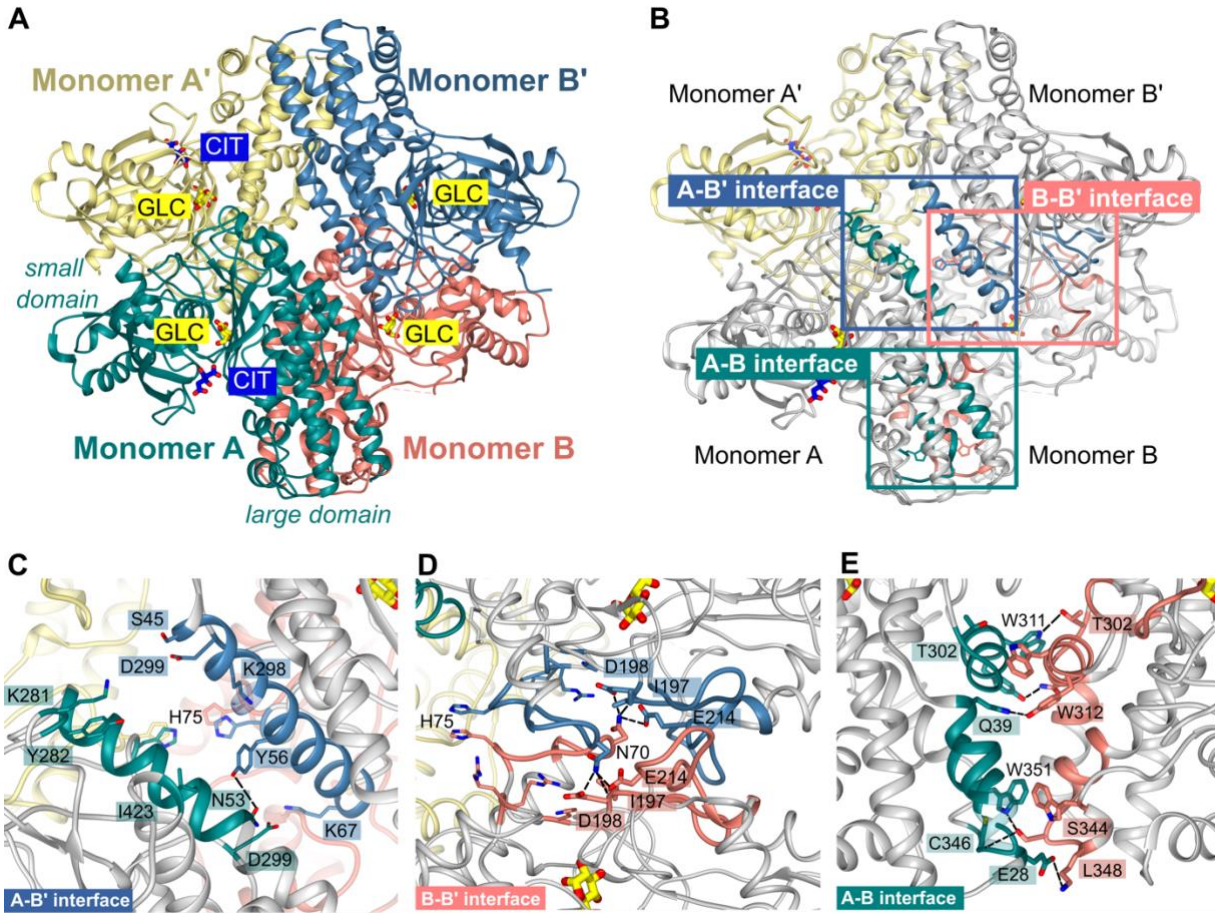

Figure 20 - PfHK tetrameric assembly and interface regions.
(A) PfHK crystallographic symmetry tetramer. **(B)** The interface regions of the tetrameric assembly are highlighted with a blue (A-B'), salmon (B-B') and green square (A-B), respectively. **(C)** The A-B' interface is formed via hydrophobic interactions between two helices and a hydrogen bond between N53 and Y56. **(D)** Mainly residues from the small domains connect monomers B-B'. N70 from each monomer can be hydrogen-bonded to I197, D198 and E214. **(E)** The A-B interface is strongly connected via seven hydrogen bonds and one additional salt bridge between E28 and K348. Besides, mainly residues from the large domains form the interface.

PfHK active site and ligand binding

Superimposition of both monomers showed that the citrate molecule causes a movement of two loops of the small domain, which broadens the cleft of the active site: G104-F108 and L130-G141 (Figure 21 A). The superimposition further revealed the citrate would clash with loop residues G104-F108 from monomer B, while in monomer A, these residues are point out of the active site. Nevertheless, except for these two loops, both monomers are considerably similar (0.7 Å with 463 residues). Although a conformational change induced by the binding of citrate was observed in the present structure, superimposition with both *P. vivax* hexokinase (PvHK) open and closed form revealed that both monomers adopt the closed conformation: 1.1 Å with 413 residues (closed state PvHK) and 1.4 Å with 378 residues (open state PvHK). Residues K131-K140 are a *Plasmodium*-specific insertion that could be shown for the first time in the present structure. Upon the binding of citrate, the loop adopts a completely different conformation, impairing the interaction of D354 to residues T133-S135 via hydrogen bonds.

Furthermore, residue S135 is shifted by up to 20 Å which makes interactions with residues of the large domain (M309, Y312, S313 and D354) impossible (Figure 21 B).

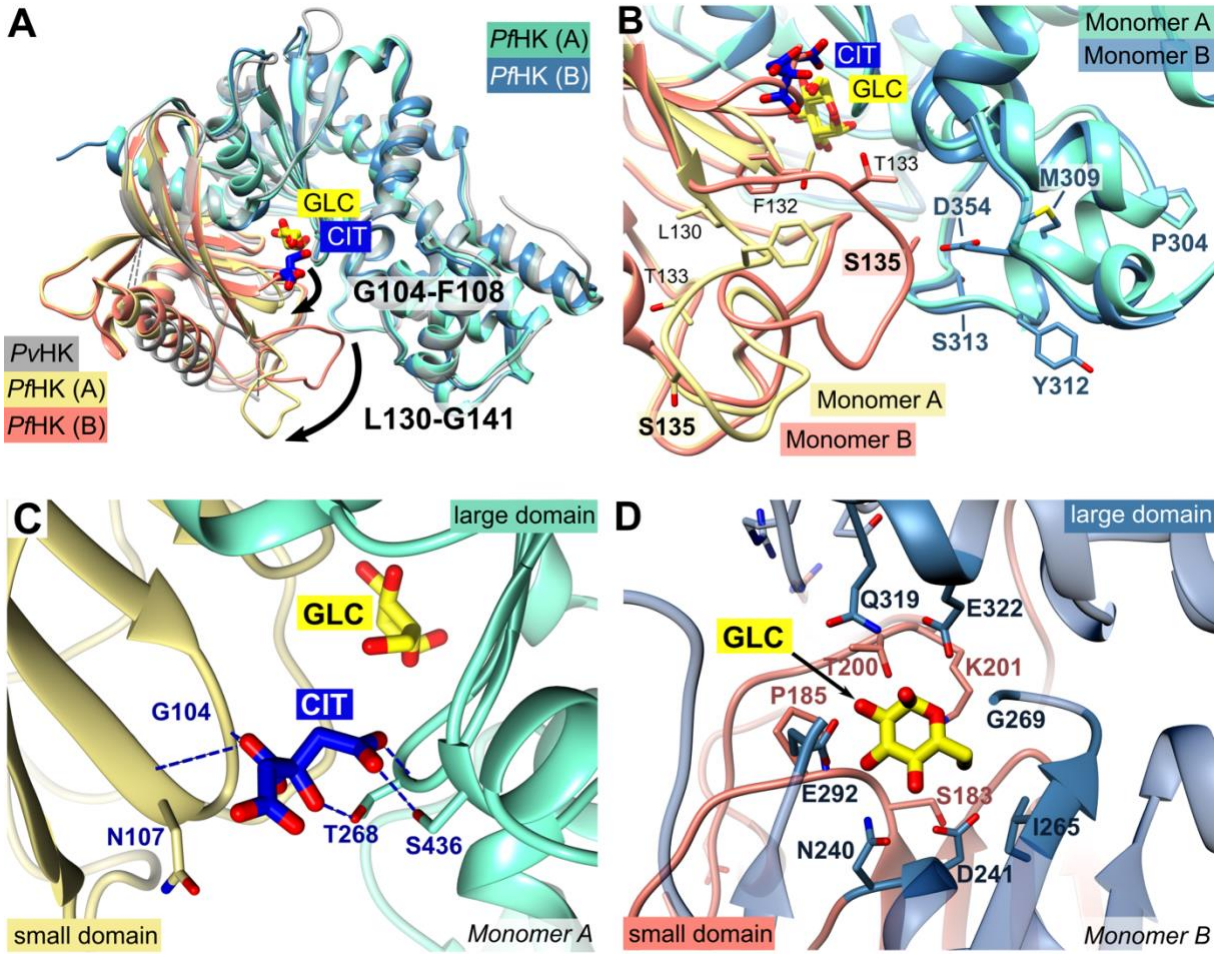

Figure 21 - The active site conformation of PfHK depends on the binding of different ligands.
(A) Superimposition of monomers A and B reveals a shift of two loops (G104-F108; L130-G141), most likely due to the citrate molecule in monomer A. **(B)** Detailed view of the superimposed monomers shows the conformational changes induced by citrate. In monomer B, S135 interacts with residues of the large domain. Due to a massive shift of the loop L130-G141, this interaction is not possibly in monomer A. **(C)** Citrate is hydrogen bonded by residues from both domains: G104, N107, T268 and S436. **(D)** Glucose is coordinated by the highlighted residues of both domains (small domain = salmon; large domain = steel blue).

The citrate molecule is in van der Waals distance to residues N107 and R109 and forms hydrogen bonds with residues G104, N107, T268 and S436 (Figure 21 C). Comparisons with other hexokinase structures from different species (PDB IDs: 1HKB, 1BG3, 6JJ9, 1DGK) showed that these residues are part of a conserved phosphate binding site and usually interact with the phosphate of G6P or ADP. Therefore, the bound citrate blocks the site where phosphate is transferred from ATP to glucose, yielding G6P. Residues G104-F108 and β–turn residues G267-T268 are both part of the corresponding PfHK ADP binding site, interacting with the α– and β–phosphate of ADP. Similar to homologous structures, the adenine ring would be enclosed by residues N357-S362 and L437-W443. As stated previously, 10 mM ATP was present in the protein solution used for crystallization, but no electron density for its binding could be observed.

Glucose, on the contrary, which was also present in the protein solution, was found to be bound within the active site of both monomers. The molecule is coordinated by residues from both domains, which are also highly conserved: S183, P185, T200, K201, N240, D241, I265, G269, E292, Q319 and E322 (Figure 21 D). The induced-fit closure of the cleft between the small and the large domain ensures that the glucose is enveloped except for the hydroxyl group on the C6 atom, to which a phosphoryl group is subsequently transferred from ATP. This closure is associated with massive conformational changes. Former X-ray crystallographic studies have shown both closed and open states of hexokinases.

Accessibility of cysteines for oxPTMs

As already indicated by the results of the Ellman assay and the mass spectrometry data, the present three-dimensional protein structure supports that out of the 15 potentially susceptible cysteines, only probably 10-11 cysteines are accessible for oxPTMs (Table 2). To have an impact on the enzymatic activity of PfHK, cysteines within or at least near the active site need to be modified. According to the present protein structure, C77, C85, C186, and C273 are located near the active site. Although the distance between the glucose binding site and C186 and C273 is relatively short (7.5 and 9 Å, respectively), their accessibility cannot be certainly confirmed. C77 and C85 could indirectly affect the enzymatic activity if modified by inducing conformational changes of surrounding beta sheets. C249 and C260, also relatively close to the active site, are reduced due to DTT in the present structure, but their orientation allows the formation of a disulfide. This disulfide bridge would be an ideal prerequisite for other modifications. Besides cysteines that are located near the active site, also those being part of the tetramer interfaces (C193, C346) could impair catalysis by conformational changes induced by modification.

4.2 *P. falciparum* pyruvate kinase (PfPK)

In previous studies, PfPK was validated to be a target of S-glutathionylation and S-nitrosation. S-glutathionylation inhibits PfPK enzymatic activity in a concentration- and time-dependent manner, whereas S-nitrosation does not affect its activity. Nevertheless, nothing is known so far about possible crosstalk among those modifications or which cysteines are targeted by them. This thesis aimed to identify the susceptibility of PfPK cysteines and their role within the three-dimensional protein structure and upon catalysis. Protocols for heterologous expression, purification, and an assay for determining the enzymatic activity were already available (Kehr et al., 2011), though purification and the activity assay were slightly optimized in this work.

4.2.1 Susceptibility of cysteines to oxidative posttranslational modifications

In order to investigate how many cysteines out of the fifteen cysteines in PfPK are potentially susceptible to oxidative posttranslational modifications, Ellman's reagent was used as already described for PfHK (see subsection 4.1.2.3). From a total of 15 cysteines within PfPK, 10-11 cysteines responded to the oxidation of their sulfur group induced by Ellman's reagent.

To identify single cysteines that are susceptible to either S-glutathionylation or S-nitrosation, mass spectrometry analysis was conducted in a former experiment already described in detail in previous studies (Dillenberger, 2017). In this former thesis, reduced PfPK was incubated with 5 mM GSSG or 400 µM nitrosoglutathione, or both to induce the respective modifications and subsequently analyzed via mass spectrometry. Here, those results are summarized and supplemented with structural information about the putative accessibility of cysteines within the three-dimensional structure (Table 3). According to its structure, nine cysteine residues (C49, C66, C94, C140, C143, C222, C433, C447 and C456), among the twelve residues found to be modified in mass spectrometry analysis, would be accessible for S-glutathionylation or S-nitrosation.

Table 3 - Oxidative posttranslational modification of PfPK cysteines.
Abbreviations: -SSG = S-glutathionylated cysteine, -SNO = S-nitrosated cysteine.
*PDB IDs: 7Z4M / 7Z4N (publication on hold)

Cysteine position	Found with both modifications	-SSG	-SNO	No modification	Accessible in structure*
43				X	
49	X	X	X		**X**
66	X	X	X		**(X)**
95		X			X
140			X		X
143			X		X
167	X	X	X		
222	X	X	X		**(X)**
302	X	X	X		
343		X			
367				X	
373				X	X
433	X	X	X		**X**
447			X		**X**
456	X	X	X		**X**
∑	**7**	**9**	**10**	**3**	**8 (10)**

4.2.2 Kinetic parameters of PfPK^{WT}, PfPK^{C49A}, PfPK^{C66A} and PfPK^{C343A}

Based on the previously presented data and to characterize cysteine-deficient mutants enzymatically and structurally, three different cysteines-to-alanine mutants were produced that possibly mime local oxPTMs. The cysteines were chosen due to their susceptibility to oxPTMs and their proximity to the catalytic site. Cloning, expression and purification of three different PfPK mutants (C49A, C66A and C343A) were already established in the master thesis prior this doctoral thesis (Dillenberger, 2017). Within this thesis, the enzymatic activity of PfPK and its mutants was measured in coupled assay monitoring the decrease of NADH at 340 nm. To ensure a stable protein and thus constant enzymatic activities, the final assay mixture was supplemented with 2 mg·ml^{-1} BSA. Michaelis-Menten constants were determined using both PEP and ADP in concentrations ranging from 0.025 to 3 mM in the final assay. For the wild type of PfPK, a V_{max} of 128.0 ± 5.6 U·mg^{-1} was measured, the K_M values were 88.6 ± 12.3 µM for ADP and 124.3 ± 18.5 µM for PEP. For the three cysteine-deficient mutants, kinetic analyses were performed in the same manner, revealing differences among the wild type and the mutants in V_{max} and K_M values (Table 4; Figure 22).

Table 4 - Comparison of kinetic characteristics of PfPK wild type and cysteine-to-alanine mutants.

	PfPK wild type	PfPK^{C49A}	PfPK^{C66A}	PfPK^{C343A}
Specific activity (U·mg^{-1})	128.0 ± 5.6	55.8 ± 4.2**	106.4 ± 6.2	105.2 ± 5.0
K_M ADP (µM)	88.6 ± 12.3	69.7 ± 19.4	103.9 ± 19.4	72.5 ± 10.3
K_M PEP (µM)	124.3 ± 18.5	283.3 ± 62.9	138.4 ± 24.2	216.8 ± 31.7

Each value is a mean ± SE from at least three independent determinations using different biological batches of enzyme. Specific activity of PfPK^{C49A} differs significantly from PfPK wild type (p=0.0059, unpaired t-test).

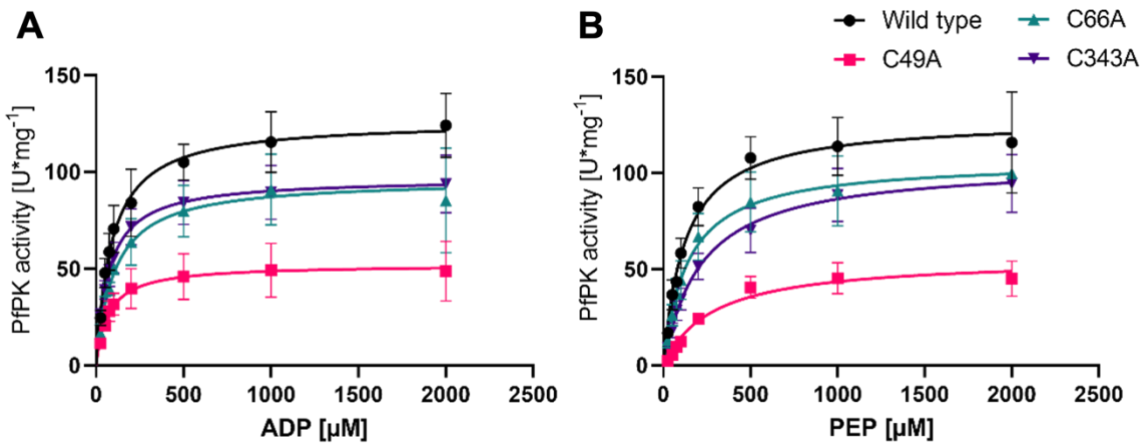

Figure 22 - K_M for ADP and PEP in PfPK wild type and mutants C49A, C66A and C343A.
(A) K_M for ADP in PfPK wild type and mutants C49A, C66A and C343A in the presence of 1 mM PEP. **(B)** K_M for PEP in PfPK wild type and mutants C49A, C66A and C343A in the presence of 1 mM ADP. Each value represents a mean value from at least three independently measured triplicates. Data are represented as mean ± SD.

Compared to the wild type ($PfPK^{WT}$), the specific activity of mutant C49A ($PfPK^{C49A}$) was significantly lowered by ~56%. Furthermore, the substrate affinity to PEP is decreased, shown by an increased K_M value of 283.3 ± 62.9 µM, which is more than two times higher than the one measured for the wild type. For mutant C343A ($PfPK^{C343A}$), the affinity to PEP is decreased, too, and for mutant C66A ($PfPK^{C66A}$) the decrease is only marginal. Compared to the wild type enzyme, V_{max} of both $PfPK^{C343A}$ and $PfPK^{C66A}$ are slightly lower (~18% less active). Interestingly, the affinities of $PfPK^{C49A}$ and $PfPK^{C343A}$ to ADP are marginally higher compared to the wild type enzyme, whereas the affinity of $PfPK^{C66A}$ is lower.

4.2.3 Protein crystallization of $PfPK^{WT}$, $PfPK^{C49A}$ and $PfPK^{C343A}$

For a better understanding of the mechanisms upon substrate binding and thus substrate affinities of PfPK, protein crystallization was performed. For protein crystallization and subsequent determination of the three-dimensional structure, it is essential to identify buffers and solutions which do not disturb the crystallization process and yield protein crystals (McPherson and Cudney, 2014). For this purpose, the available purification protocol of PfPK was slightly changed. The modified purification buffer contained 10 mM Hepes, pH 7.5, and 50 mM KCl. The protocol was further changed by adding more elution steps to achieve a higher purity of the enzyme (Figure 23 A). For dialysis, this buffer was supplemented with 10 mM $MgCl_2$ to ensure protein stability during the crystallization process. Further purification by SEC did not show any benefits for crystallization which is why this additional purification step was not included in the following experiments. Nevertheless, it confirmed PfPK to be a tetramer (Figure 23 B).

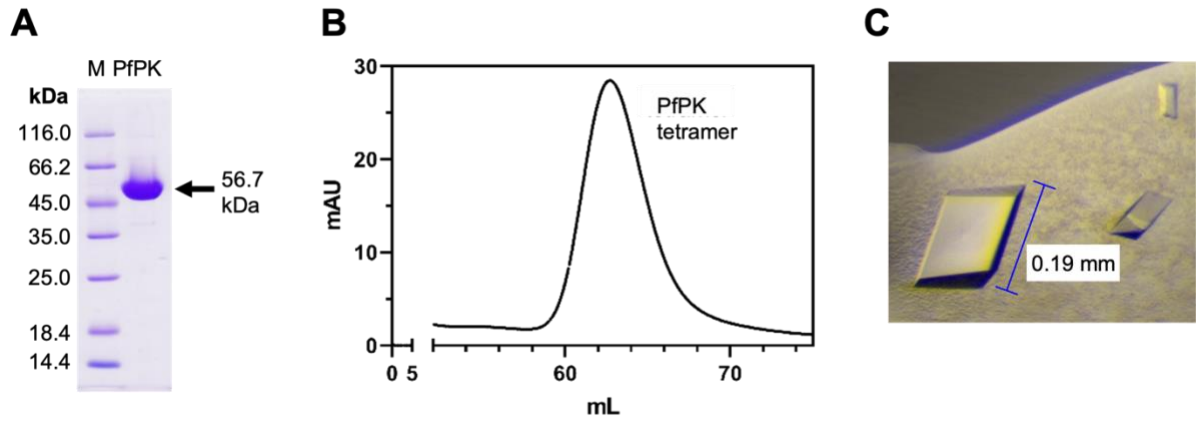

Figure 23 - Purification and initial protein crystals of PfPK wild type.
(A) Coomassie staining of a 12% SDS-PAGE gel after purification of PfPK via affinity (Ni-NTA agarose) and size exclusion chromatography (Äkta FPLC System, Superdex 200 column). To control final purity, ~6 µg protein was applied to SDS-PAGE. M = unstained protein molecular weight marker. **(B)** After affinity chromatography, eluted protein fractions were applied to an ÄKTA FPLC system. PfPK eluted at 62 ml corresponding to ~225 kDa (PfPK tetramer). **(C)** Exemplary picture of protein crystals of $PfPK^{WT}$ obtained from initial screenings.

A first approach to establish a suitable crystallization protocol for $PfPK^{WT}$ was to reproduce the experimental setup of a so far unpublished PfPK structure from Wernimont and colleagues that

was deposited in 2009 on PDB (ID: 3KHD). The original experiment and additional, slightly modified conditions were not successful. Therefore, as a second approach, different commercially available screens covering a variety of precipitants, additives and pH values, were performed with a Honey Bee crystallization robot. First hits could be achieved with PEG 600 and 6,000 as precipitant using protein concentrations of 20 $mg \cdot ml^{-1}$ (Figure 23 C). Conditions were optimized and finally, $PfPK^{WT}$ crystals diffracted to a resolution of 1.8 Å. The crystallization conditions contained 100 mM MES, pH 6.5, 50 mM KCl, 10 mM $MgCl_2$ and 14-24% PEG 600 and therefore differed completely from the ones used by the group of Wernimont et al. (not published).

4.2.3.1 Overall structure and conformational changes upon ligand binding

The orthorhombic PfPK crystals belong to the space group I222. The tetrameric conformation already shown by SEC could also be observed within the unit cell, with one monomer per asymmetric unit. Each monomer consists of four different domains, shown in Figure 24 A: N-domain (M1-E28), A-domain (P29-G105; I204-D375), B-domain (P106-P203) and C-domain (Y376-E511). Within the active site of the apo form, which is located in a cleft between the A- and the B-domain, the metals Mg^{2+} and K^+ were bound. Mg^{2+} is coordinated by residues E257 and D281, whereas K^+ is coordinated by residues N69, S71, D102 and T103 (PDB ID: 7Z4M, publication on hold).

Besides the apo structure of PfPK, we also obtained a structure with pyruvate bound to the substrate binding site (1.9 Å, WT^{Pyr}, PDB ID: 7Z4N, publication on hold). Superimposition of those two structures revealed a rigid rotation of the B-domain of ~20° (Figure 24 A). Pyruvate is bound by Mg^{2+} and residues K255, E257, A278, G280, D281 and T313. Upon pyruvate binding, the Mg^{2+} ion was shifted by about 2.5 Å, while the position of K^+ was changed only marginally (Figure 24 B). Furthermore, the rotation of the B-domain leads to a more closed conformation of PfPK, which is confirmed by the cell parameters of the crystals. The cell axis of the WT^{Pyr} crystals is 10 Å shorter than the one of the crystals without pyruvate. The movement of the B-domain induced by the ligand pyruvate is a known mechanism that serves as conformational changes between two different states: the inactive T-state and the active R-state. Comparing both structures with previously solved pyruvate kinase structures revealed that the structure with pyruvate adopts a half-closed R-state, whereas the other structure clearly adopts the open T-state (Larsen et al., 1994; Mattevi et al., 1996; Rigden et al., 1999). Besides pyruvate, also the non-hydrolyzable ATP analogue adenylyl-imidodiphosphate (AMP-PNP) was included in the solutions used for crystallization. However, it was not bound in any of the analyzed data sets. To identify the ATP binding site, the WT^{Pyr} structure was superimposed with a PfPK structure complexed with oxalate, ATP, Mg^{2+} and K^+ (PDB ID: 6KSH). This structure from Zhong et al. revealed ATP to interact with Mg^{2+} and K^+.

The superimposition further revealed that the binding of ATP apparently results in a shift of oxalate, Mg^{2+} and K^+ of 1 Å, 0.8 Å and 1.8 Å, respectively (Figure 24 C).

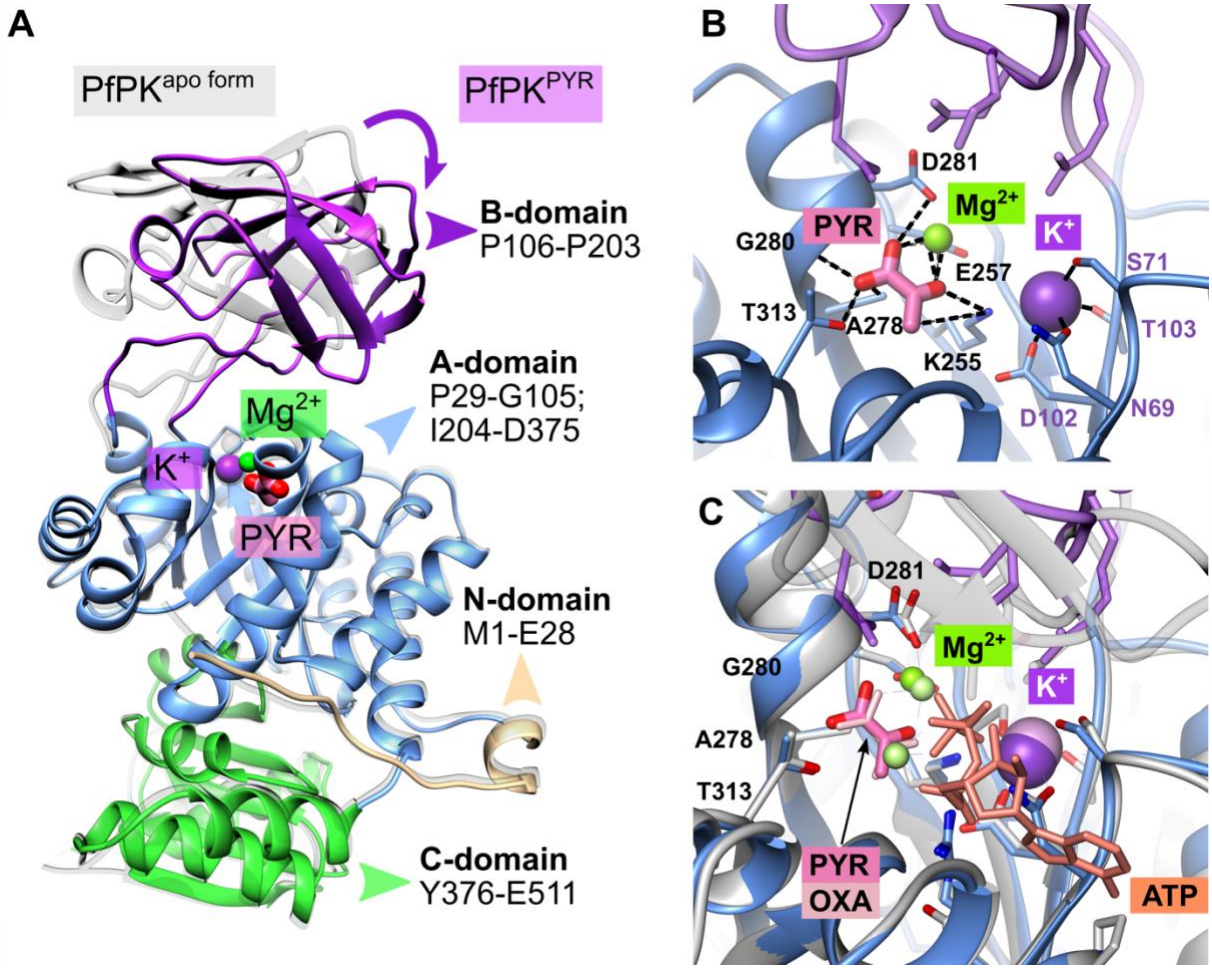

Figure 24 - Three-dimensional structure of PfPK wild type.
(A) PfPK wild type bound with Mg^{2+} and K^+. Each monomer consists of four conserved domains: N-domain (M1-E28), A-domain (P29-G105; I204-D375), B-domain (P106-P203) and C-domain (Y376-E511). Superimposition of T- and R-state of PfPK wild type shows the movement of the B-domain upon pyruvate binding. The open-conformation structure without substrate (apo form) is represented in grey, the closed conformation colored according to its domain-organization (N-, A-, B- and C-domain). **(B)** Close-up into the active site with bound pyruvate, Mg^{2+} and K^+. Pyruvate is coordinated by residues K255, E257, A278, G280, D281 and T313. **(C)** Superimposition of WT^{Pyr} with a PfPK structure complexed with oxalate, ATP, Mg^{2+} and K^+ (PDB ID: 6KSH).

To identify posttranslationally modified cysteine residues within the three-dimensional structure that could confirm mass spectrometry data, crystallization of modified PfPK was performed. First, PfPK was S-glutathionylated and S-nitrosated as described previously for PfHK (see subsections 4.1.2.1 and 4.1.2.2). Protein solutions were prepared equally to the ones used for crystallization of native PfPK with and without additional ligands. While crystals of S-nitrosated PfPK grew and resembled in shape and size the ones obtained for unmodified PfPK (Figure 25), S-glutathionylated PfPK did only show marginal phase separation. Although the resolution of S-nitrosated PfPK reached ~2.3 Å, this resolution was not sufficient for the definite detection of the small nitroso groups potentially bound to the cysteine residues. To obtain crystals with S-glutathionylated PfPK, further strategies included (i) adding GSSG to the unmodified protein

solution without prior incubation time at 37 °C and (ii) soaking trials of fully grown crystals of native PfPK. The first strategy did not yield crystals either and soaking trials crashed the crystals.

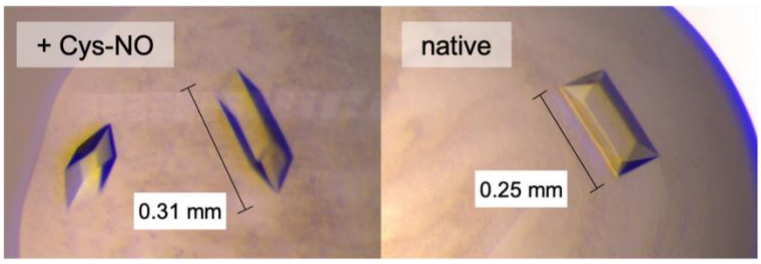

Figure 25 - PfPK wild type protein crystals +/- Cys-NO.
Exemplary pictures of PfPK protein crystals obtained with crystallization conditions containing 20-24% PEG 600, 100 mM MES, pH 6.5, 50 mM KCl and 10 mM $MgCl_2$. The protein solution contained 20 mg·ml^{-1} native or S-nitrosated PfPK.

4.2.3.2 Structural comparison of PfPK^{WT} and mutants PfPK^{C49A} and PfPK^{C343A}

After establishing the protocols for PfPK^{WT}, crystallization for mutants PfPK^{C49A} and PfPK^{C343A} was performed. The crystals diffracted to a resolution of 2.1 Å (PfPK^{C49A}, PDB ID: 7Z4Q, publication on hold) and 2.0 Å (PfPK^{C343A}, PDB ID: 7Z4R, publication on hold) and adopted the canonical fold and domain organization of pyruvate kinase. Both structures were solved in an open conformation, comparable to the PfPK^{WT} structure without pyruvate. Although pyruvate and AMP-PNP were included in the crystallization process, no electron densities for successful binding could be observed. Indeed, both mutants disclosed several conformational changes in the A-domain, adjacent to the substrate binding site. The structure of PfPK^{C49A} revealed structural changes in the following regions: R67-F82, M276-M284 and T311-R324 and L346-K354. These changes are caused by the loss of two hydrogen bonds upon mutation, involving residue T44 and T350 as well as residue A48 and A351 (Figure 26 A). In consequence, the loop region M346-K354 adopts a partially more relaxed conformation, leading to further conformational changes of region T311-R324 and subsequently region M276-M284. Rearrangement of the latter one leads to a conflict of the pyruvate binding site and a disruption of the precise alignment of the phosphates, which is required for catalysis. Moreover, T313 is relocated and therefore considered not to be able to bind pyruvate properly anymore. By the conformational change of residues S347-T359, that are part of the ADP/ATP binding pocket, adequate phosphate transfer is impaired.

In both mutant structures, Mg^{2+} was bound, although shifted by 1.7 Å in the PfPK^{C49A} structure compared to the one obtained for PfPK^{WT}. K^+ was only bound in PfPK^{C343A}, but not in PfPK^{C49A}. This can be explained by the rearrangement of residues N69 and S71 in PfPK^{C49A}, which interact with K^+ in PfPK^{WT} and PfPK^{C343A}, and prevent binding due to conformational changes. The structural changes of PfPK^{C343A} were less drastic and did not affect the position or binding of Mg^{2+} and K^+. However, minor shifts of the regions L45-V52, A312-K321, and S347-V357 could be observed. These conformational changes affect the binding of both pyruvate and

ADP, which is in accordance with the kinetic data. As already observed in the PfPK^{C49A} structure, T313 and Q314 are displaced in PfPK^{C343A}. The regions K321-P323 and T350-G353 are probably more flexible compared to the wild type structure, which is indicated by not clearly defined electron densities.

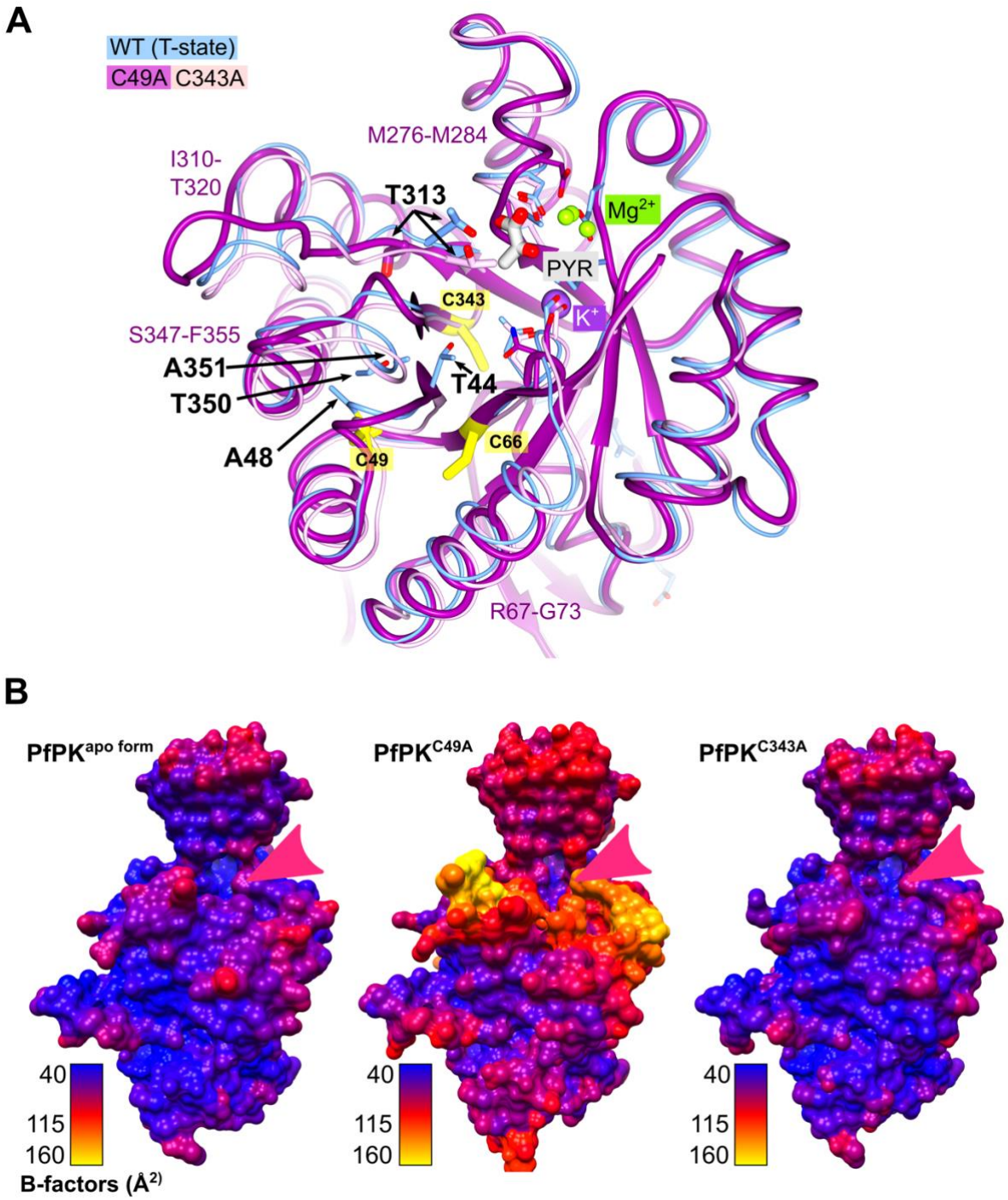

Figure 26 – Superimposition and surface representation of PfPK wild type and mutants C49A and C343A. (A) Superimposition of PfPK^{PYR} (light blue), mutant C49A (purple) and C343A (tan). Cysteines are highlighted in yellow. Massively changed residues of C49A are associated with strong contribution to catalysis (R67-G73, M276-M284, I310-T320 and S347-F355). In the wild type structure, T44-T350 and A48-A351 and are connected via hydrogen bonds. This connection is altered in mutant C343A and lost in mutant C49A causing elevated flexibility and high B-factors. (B) Surface representation of PfPK wild type (apo form) and mutants C49A and C343A. B-factors are shown in a color scheme ranging from blue to yellow (low B-factors to high B-factors) and reveal a massive increase in B-factors for mutant C49A in general, but especially in proximity to the active site. Active sites are marked with pink arrows, respectively.

Besides these residue-specific alterations, also a general increase of the atomic B-factors (Å²) could be observed for both mutants upon surface representation. For PfPK^{C343A}, the increase was only marginal compared to the wild type enzyme, but PfPK^{C49A} revealed massive increases, especially near the active site (Figure 26 B). This data is in accordance with the increased flexibility and rearrangements observed for several residues within the A-domain and also with the kinetic data obtained for both mutants (PfPK^{C49A}: ~47% residual activity; PfPK^{C343A}: ~82% residual activity).

Consistent with the results from SEC, in all structures the PfPK tetramer could be constructed via crystallographic symmetry operations (Figure 27 A). By superimposing the PfPK^{WT} and the PfPK^{C49A} tetramers, further differences could be revealed: Residues A312-E329 from PfPK^{C49A} approach the substrate binding site of the adjacent monomer and therefore leads to an altered interface. Superimposition of the WT^{Pyr} structure revealed that those residues of PfPK^{C49A} probably impede the movement of the B-domain and, in consequence, the closure of the active site upon catalysis (Figure 27 B).

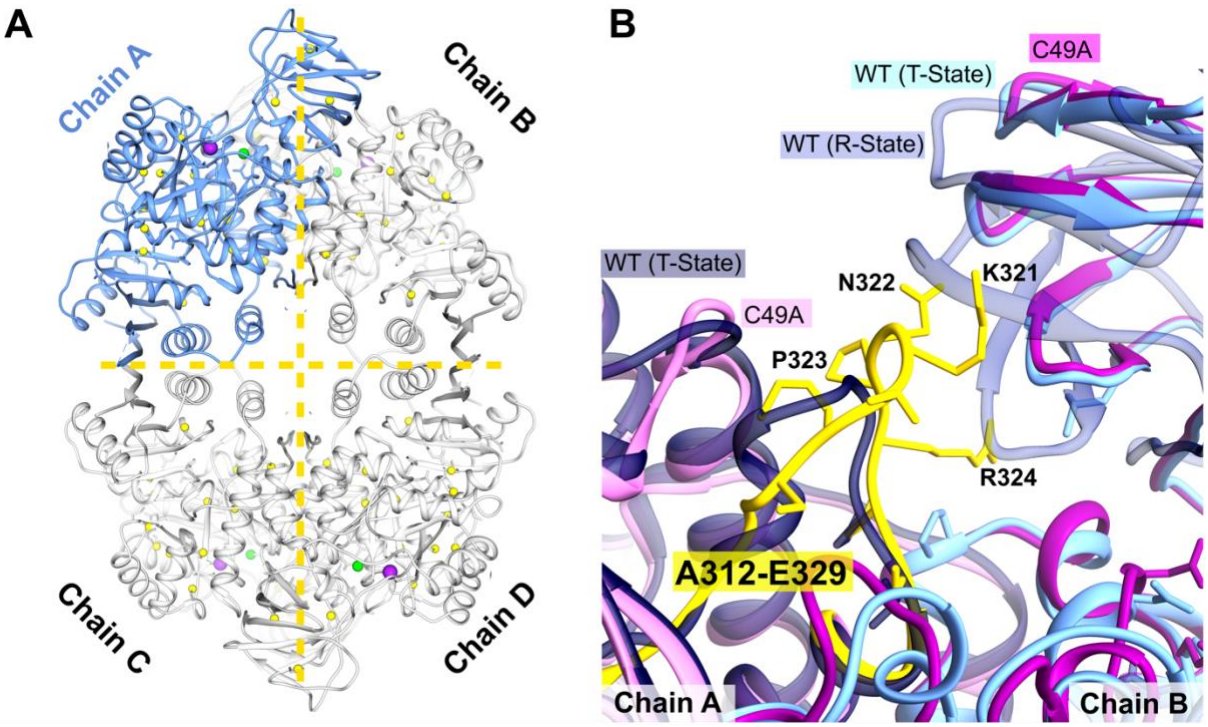

Figure 27 - Mutation of C49 affects the tetrameric assembly of PfPK.
(A) Tetrameric assembly of PfPK wild type. Cysteines are highlighted in yellow, active sites are indicated by Mg^{2+} (green) and K^{+} (purple). **(B)** Tetrameric assembly of PfPK wild type (Chain A: dark blue; Chain B: light blue/grey blue) vs. C49A (Chain A: pink/yellow; Chain B: purple). Focus onto disassembled residues A312-E329 (yellow, C49A) affecting the adjacent monomer by intruding the space required for the catalysis-associated movement of the B-domain (PfPK wild type R-state shown in grey blue).

4.3 Coronavirus nonstructural proteins

4.3.1 Susceptibility of coronavirus nonstructural proteins to S-glutathionylation

In contrast to a variety of organisms, scarcely is known about the occurrence nor the effects of posttranslational redox modifications like S-glutathionylation in viruses. Within this project, the susceptibility of coronavirus nsps for S-glutathionylation was investigated. For this purpose, 22 different recombinant wild type nsps from different viral strains including SARS-CoV, HCoV-229E, FCoV causing feline infectious peritonitis, TGEV, HCoV-NL63 and porcine epidemic diarrhea virus (PEDV; compare Table 5) were screened. Equine arteritis virus (EAV), which is no coronavirus indeed, but a member of the *Arteriviridae* family, was also included within this first screening. Later in this project, four cysteine to alanine mutants of SARS-CoV nsp9 were included in the analyses. In an initial screening with at least three independent samples for each protein, 5 mM GSSG was used to identify target proteins. Out of the 22 wild type proteins initially screened, eleven were susceptible to S-glutathionylation. For six proteins, no S-glutathionylation could be observed, whereby two out of those six proteins do not possess any cysteine and served as an internal negative control. For five proteins S-glutathionylation is putatively possible but could not finally be detected due to contradictory results in several independent experiments. Nsps among different species differ not only by the amount of their cysteines, but also in their susceptibility to S-glutathionylation. Nsp9, for example, has one cysteine in HCoV-229E and was found not to be S-glutathionylated, whereas SARS-CoV nsp9 has three cysteines susceptible to S-glutathionylation and FCoV nsp9 does not possess any cysteine. Nsp5, on the other hand, has different amounts of cysteines among these three strains, too, but all of them are targeted by S-glutathionylation.

Table 5 - Coronavirus proteins screened for their susceptibility to S-glutathionylation.
Proteins were reduced, incubated with 5 mM GSSG and applied to Western blot analysis using an anti-glutathione antibody. Unmodified protein samples served as negative control.

Virus	Protein	Cysteine(s)	Glutathionylation
HCov-229E	nsp5	8	Yes
	nsp(7+8)	4	?
	nsp7-8-9	5	No
	nsp8	1	Yes
	nsp9	1	No
SARS-CoV	nsp5	12	Yes
	nsp7	3	No
	nsp(7+8)	5	Yes
	nsp8	2	Yes

	nsp9	3	Yes
	nsp9$^{C14/23A}$	1	Yes
	nsp9$^{C14/73A}$	1	Yes
	nsp9$^{C23/73A}$	1	Yes
	nsp9$^{C14/23/73A}$	0	No
FCoV	nsp5	7	Yes
	nsp(7+8)	6	?
	nsp7-8-9	6	Yes
	nsp8	2	Yes
	nsp9	0	No
EAV*	nsp4	2	Yes
	nsp7	3	No
	nsp9	21	Yes
TGEV	nsp7-8-9-10-11	17	No
	nsp7-8 (precursor)	?	?
HCoV-NL63	nsp7-8 (precursor)	?	?
PEDV	nsp7-8 (precursor)	?	?

**Member of the* Arteriviridae *family*

4.3.2 S-Glutathionylation of nsp5

The coronavirus main protease, nsp5, has a key role during replication by cleaving the large polyprotein into single nsps and is S-glutathionylated in a concentration-dependent manner (Figure 28 A-C). By using an anti-glutathione antibody in Western blot analysis, we could show increasing signal intensities by increasing concentrations of GSSG. FCoV nsp5 already is S-glutathionylated at 1-2.5 mM GSSG, whereas SARS-CoV and HCoV-229E both show weaker signals at higher concentrations. The addition of DTT confirmed the modification to be reversible.

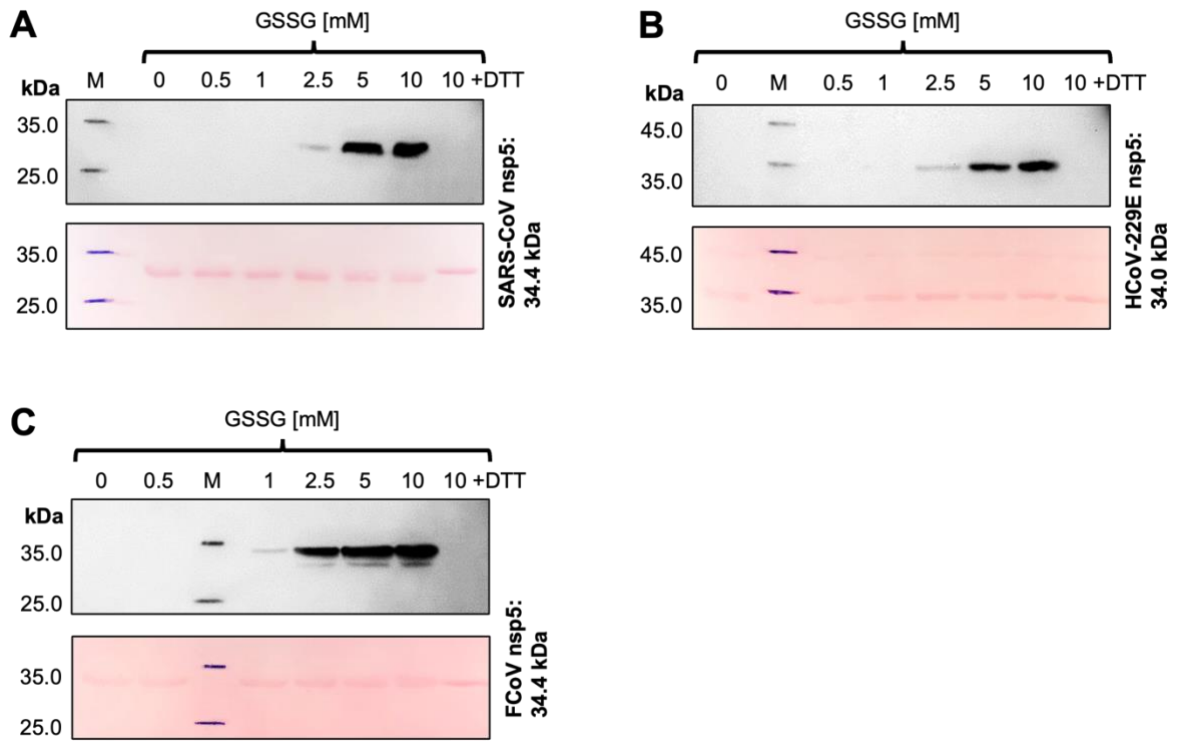

Figure 28 – S-Glutathionylation of SARS-CoV, HCoV-229E and FcoV nsp5.
Reduced nsp5 was incubated with 0-10 mM GSSG for 10 min at 37 °C. Samples were applied to Western blot analysis, using 2 µg protein per lane. S-Glutathionylated protein was detected with an anti-glutathione antibody. SDS-PAGE loading buffer with DTT served as a chemical negative control. Ponceau staining served as a loading control. **(A)** SARS-CoV; **(B)** HCoV-229E; **(C)** FcoV.

To investigate whether the modification has any impact on the efficiency of nsp5-mediated cleavage, nsp5 (HCoV-229E and FcoV) was incubated with 0-5 mM GSSG at 37 °C for 10 min. Afterwards, S-glutathionylated nsp was added to the standard nsp5 cleavage assay. Within the standard cleavage assay, 2 µM polyprotein intermediates, nsp7-11-His_6 (HCoV-229E and SARS-CoV), were incubated with 4 µM of nsp5 at 4 °C for 24 h. It was already shown that nsp5s from different species can properly cleave polyproteins from other species, so they were combined in four different ways: (i) HCoV-229E nsp5 + HCoV-229E polyprotein, (ii) FcoV nsp5 + HCoV-229E polyprotein, (iii) HCoV-229E nsp5 + SARS-CoV polyprotein, and (iv) FcoV nsp5 + SARS-CoV polyprotein. The reaction was stopped by adding SDS-PAGE loading dye. As shown in Figure 29 A, 229E nsp5 seems to be less sensitive for glutathionylation-induced loss of function compared to FcoV nsp5. HCoV-229E nsp5 loses its protease activity when facing GSSG concentrations of 5 mM, FcoV nsp5 is already inhibited by concentrations higher than 0.5 mM GSSG. Although nsp7 and nsp11 are both part of the polyprotein, they are too small to be identified in the present gels. Proper S-glutathionylation of both nsp5s was validated by subsequent Western blot analysis, using an anti-glutathione antibody (Figure 29 B). S-Glutathionylated PfPK served as a positive control.

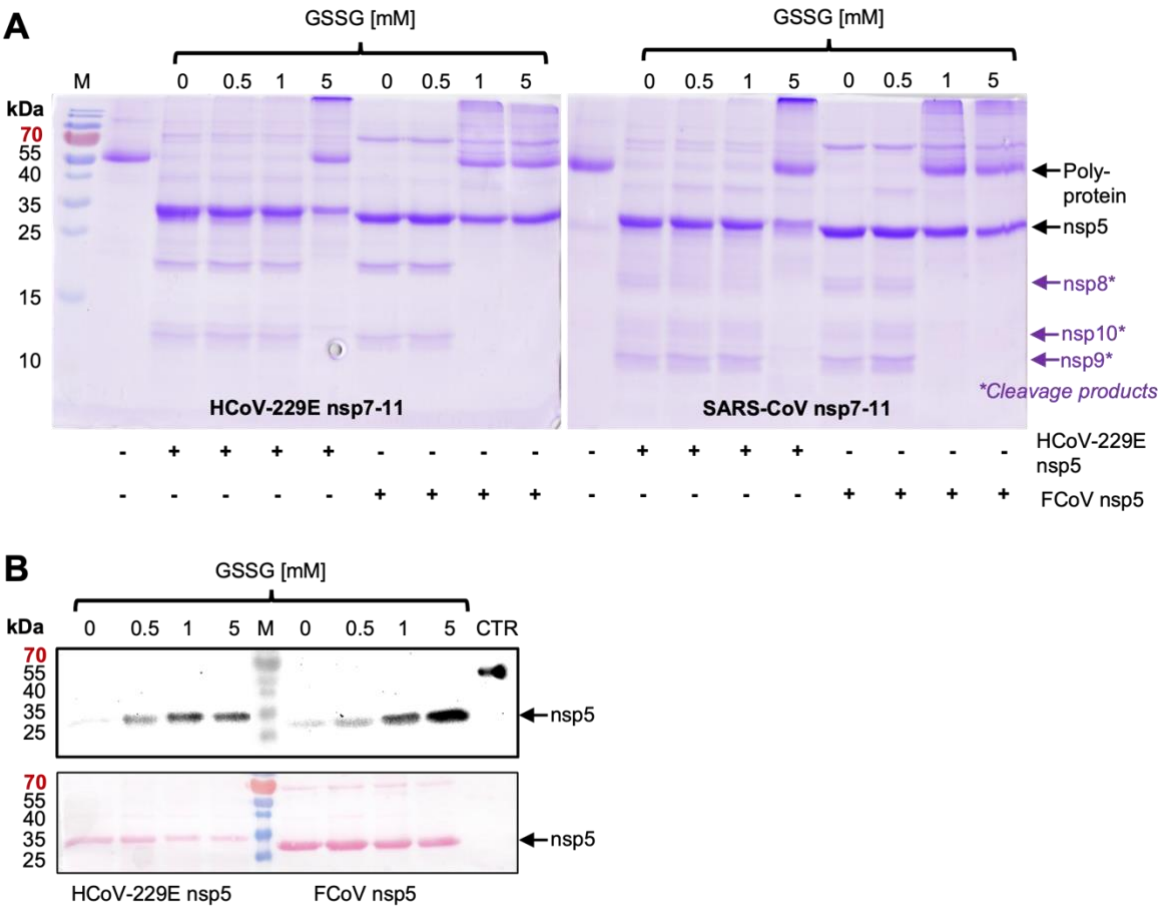

Figure 29 – Nsp5 cleavage activity is affected by S-glutathionylation.
Reduced nsp5 (HCoV-229E and FCoV) was incubated with 0-5 mM GSSG for 10 min at 37 °C. Afterwards, 4 µM nsp5 was mixed with 2 µM nsp7-11 polyprotein (HCoV-229E and SARS-CoV) and incubated at 4 °C for 24 h. The reaction was stopped by adding SDS-PAGE loading dye. **(A)** Proteins were separated by SDS-PAGE, using 15% gels, and polyprotein cleavage was shown by Coomassie Blue staining. **(B)** Nsp5 samples were applied to Western blot analysis, using 2 µg protein per lane. S-Glutathionylated protein was detected with an anti-glutathione antibody. S-Glutathionylated PfPK served as positive control. Ponceau staining served as a loading control.

4.3.3 S-Glutathionylation of nsp8

All nsp8 seem to respond to S-glutathionylation in a concentration-dependent manner already starting at GSSG concentrations of 0.1 mM (Figure 30 A-C). In contrast to other nsps included in the screening, treatment with 10 mM GSSG lead to protein precipitation. The corresponding anti-glutathione Western blot does show a decrease in signal intensity at 10 mM GSSG, suggesting S-glutathionylation is not efficient any more due to protein instability. Although nsp8 seems to be very sensitive for modifications by GSSG, a functional analysis could not be conducted. The available assay in the Ziebuhr lab consists of nsp8, nsp7 and nsp12 and requires reducing agents like DTT to guarantee protein stability and detectable activities. However, DTT induces deglutathionylation and would therefore lead to unreliable data within the assay.

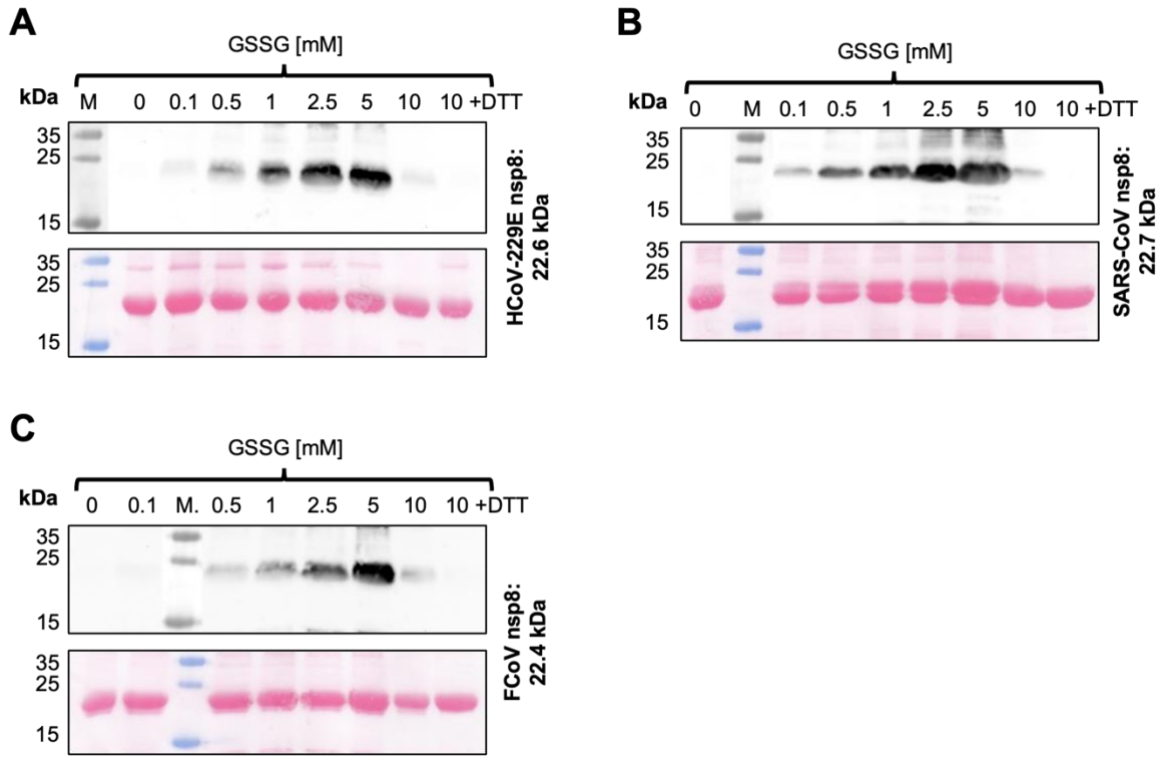

Figure 30 - S-Glutathionylation of HCoV-229E, SARS-CoV and FCoV nsp8.
Reduced nsp8 was incubated with 0-10 mM GSSG for 10 min at 37 °C. Samples were applied to Western blot analysis, using 2 µg protein per lane. S-Glutathionylated protein was detected with an anti-glutathione antibody. SDS-PAGE loading buffer with DTT served as a chemical negative control. Ponceau staining served as a loading control. **(A)** HCoV-229E; **(B)** SARS-CoV; **(C)** FCoV.

4.3.4 S-Glutathionylation of nsp9

As already stated previously, not all coronavirus proteins respond to S-glutathionylation. Nsp9 is S-glutathionylated in SARS-CoV (Figure 31), whereas HCoV-229E is putatively not susceptible to S-glutathionylation. FCoV does not possess any cysteines and was thus used as a negative control in the initial screening (data not shown).

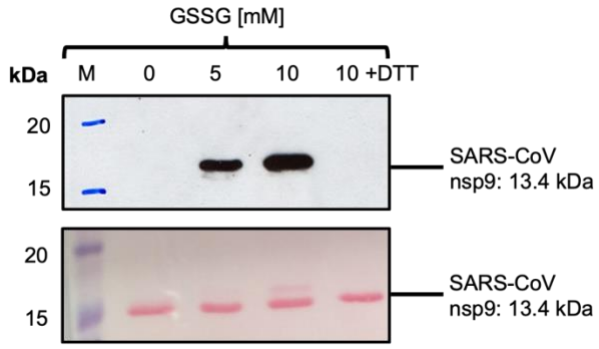

Figure 31 - S-Glutathionylation of SARS-CoV nsp9.
Reduced nsp9 was incubated with 0-10 mM GSSG for 10 min at 37 °C. Samples were applied to Western blot analysis, using 2 µg protein per lane. S-Glutathionylated protein was detected with an anti-glutathione antibody. SDS-PAGE loading buffer with DTT served as a chemical negative control. Ponceau staining served as a loading control.

To assess whether the protein is also stable without DTT, with regard to future NMPylation assays, nsp9 was purified with and without DTT via affinity chromatography followed by SEC

(Figure 32 A-D). The elution profile changed and revealed a higher dimer:monomer ratio. This was further supported by SDS-PAGE, showing an extra band that coincides with the molecular weight of the nsp9 dimer.

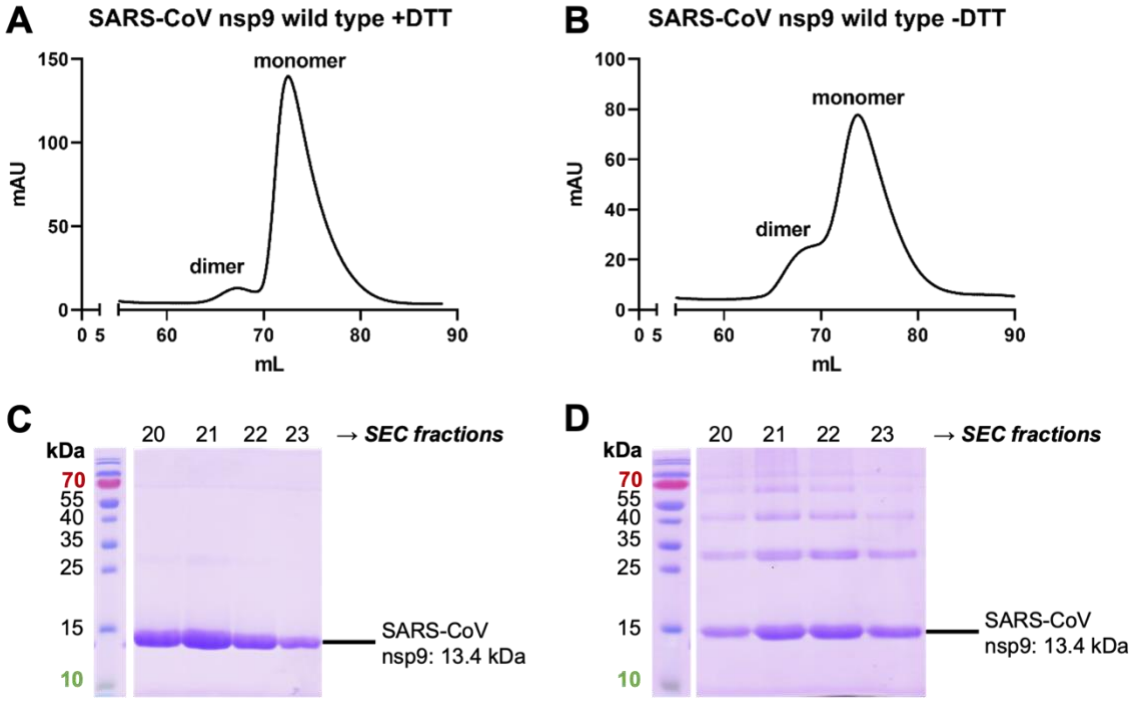

Figure 32 - Size exclusion chromatography of SARS-CoV nsp9 wild type +/- DTT.
After affinity chromatography, eluted protein was further purified via size exclusion chromatography (Äkta FPLC System, Superdex 75 column). **(A)** SARS-CoV nsp9 wild type with DTT; **(B)** SARS-CoV nsp9 wild type without DTT; **(C)** Samples from (A) on a 15% gel after SDS-PAGE and Coomassie staining; **(D)** Samples from (B) on a 15% gel after SDS-PAGE and Coomassie staining.

4.3.4.1 Susceptibility of single cysteines: cysteine-to-alanine mutants

To determine which of the three cysteines of SARS-CoV nsp9 are susceptible to the modification, four different cysteine-deficient mutants were created via site-directed mutagenesis: nsp9$^{C14/23A}$, nsp9$^{C14/73A}$, nsp9$^{C23/73A}$, nsp$^{C14/23/73A}$. Mutagenesis was performed by the Ziebuhr lab in Giessen. Three of the produced mutants had a single remaining cysteine; one of them had no remaining cysteine and served as negative control. Before subjecting the mutants to glutathionylation, they were investigated concerning differences upon expression, purification, or oligomerization behavior. All the mutants expressed very well, and purification yielded similar amounts of protein compared to the wild type: >20 mg/L *E. coli* culture (Figure 33 A-E).

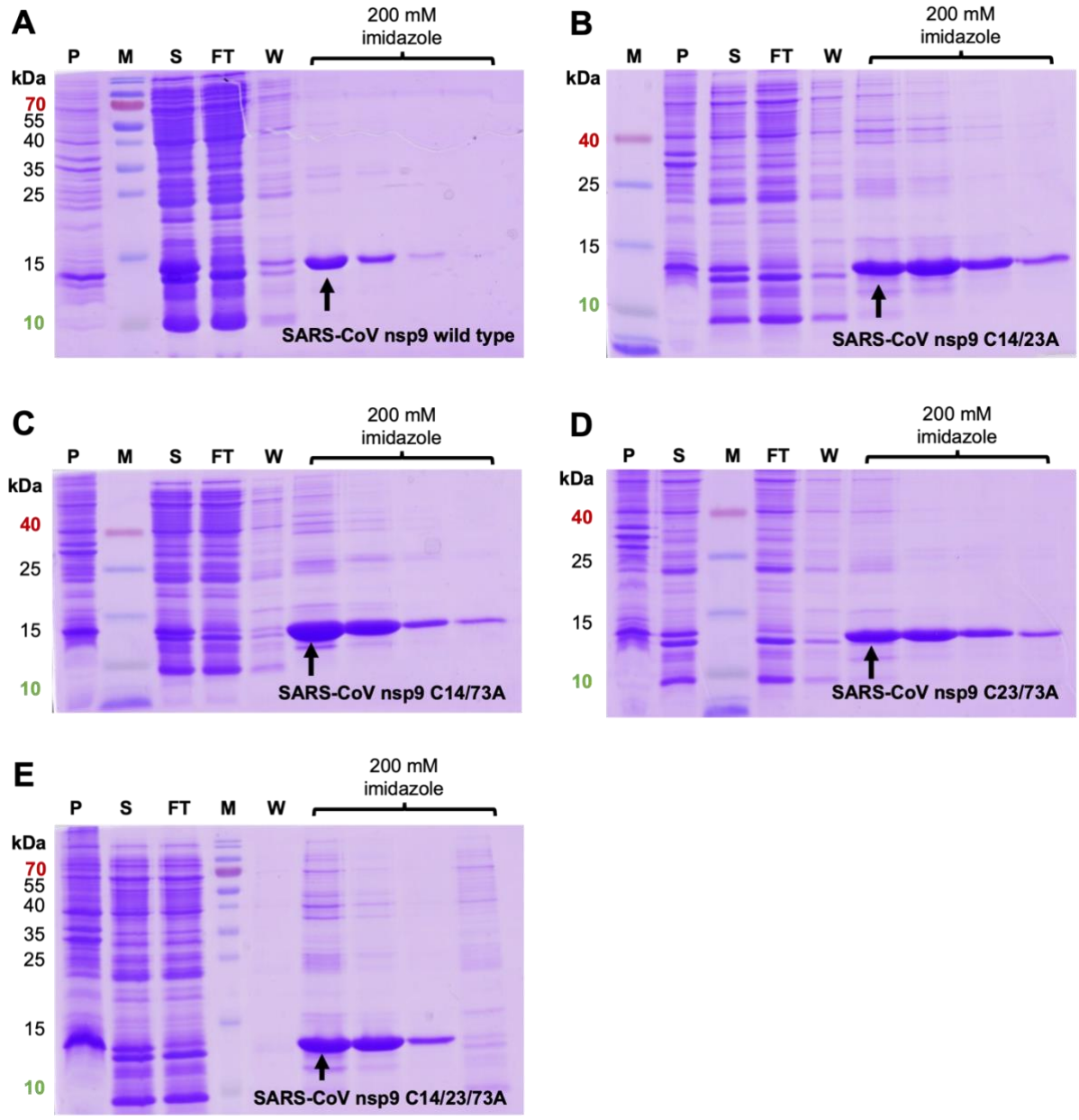

Figure 33 - SDS gels of purified SARS-CoV nsp9 wild type and nsp9 cysteine-to-alanine mutants.
SARS-CoV nsp9 wild type and mutants were purified by using affinity chromatography (Ni-NTA affinity resin). Protein samples were applied to SDS-PAGE (15% gels) and stained with Coomassie Blue. **(A)** SARS-CoV nsp9 wild type; **(B)** SARS-CoV nsp9$^{C14/23A}$; **(C)** SARS-CoV nsp9$^{C14/73A}$; **(D)** SARS-CoV nsp9$^{C23/73A}$; **(E)** SARS-CoV nsp9$^{C14/23/73A}$. M = marker, P = pellet, S = supernatant, FT = flow-through, W = wash.

The elution profiles of the nsp9 mutants differed slightly due to different amounts of protein applied to SEC, but SDS-PAGE showed no differences compared to the wild type protein purified with DTT (Figure 34 A-D). For inducing S-glutathionylation, all mutants were incubated with different concentrations of GSSG (0-10 mM). Mutants C14/73A and C23/73A did show a clear signal in anti-glutathione Western blot analysis. The signals for mutant C14/23A were less intense, suggesting that cysteine C73 is less sensitive for S-glutathionylation compared to C14 and C23. Mutant C14/23/73A, which lacks all cysteines, served as negative control and did not show any signal in anti-glutathione Western blot analysis (Figure 34 E-H).

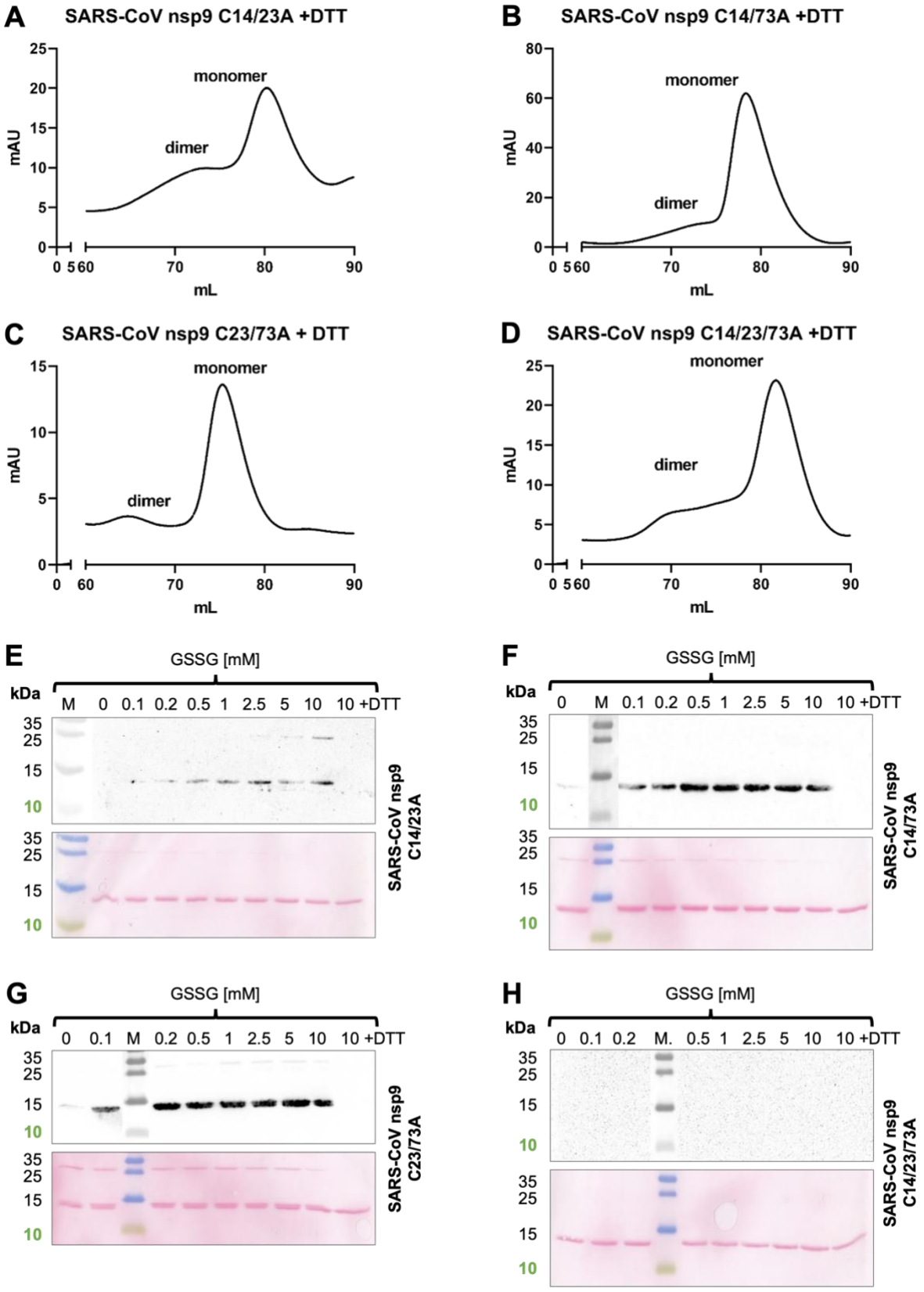

Figure 34 - Size exclusion chromatography and S-glutathionylation of SARS-CoV nsp9 cysteine-to-alanine mutants.
(A-D) After affinity chromatography, eluted protein was further purified via size exclusion chromatography (Äkta FPLC System, Superdex 75 column). **(E-H)** Reduced nsp9 was incubated with 0-10 mM GSSG for 10 min at 37 °C. Samples were applied to Western blot analysis, using 2 µg protein per lane. S-Glutathionylated protein was detected with an anti-glutathione antibody. SDS-PAGE loading buffer with DTT served as a chemical negative control. Ponceau staining served as a loading control.

4.3.4.2 NMPylation assay

To investigate proper folding and function of nsp9, the protein can be subjected to a nucleotidyl transferase (NMPylation) assay. Within this assay, nsp12 transfers a nucleotide either from ATP, UTP, GTP or CTP to the N-terminus of nsp9 in the presence of $MnCl_2$. The nucleotides are radioactively labeled and can be detected afterwards.

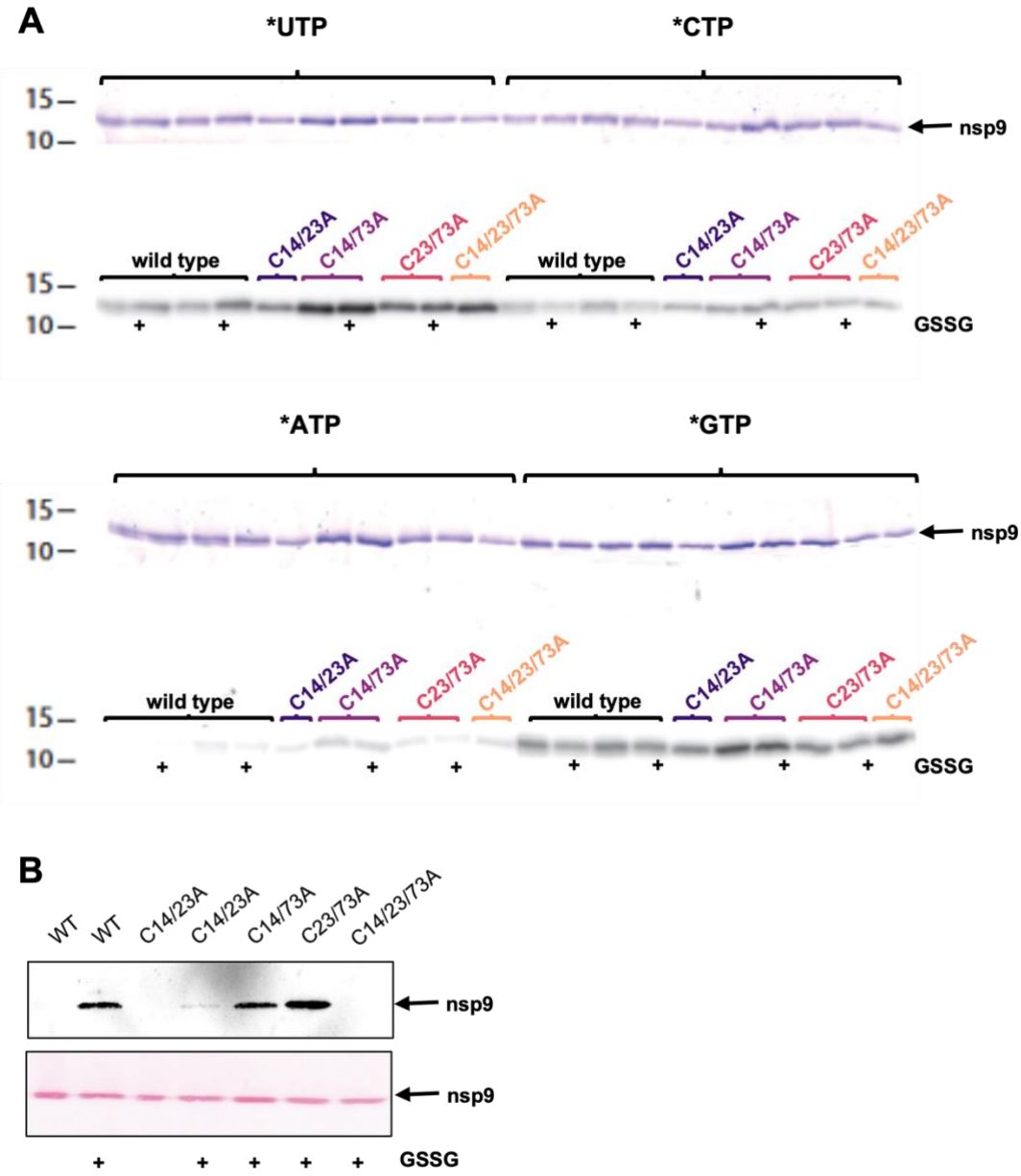

Figure 35 - NMPylation of SARS-CoV nsp9 wild type and cysteine-to-alanine mutants.
Reduced nsp9 was incubated with 0 or 5 mM GSSG for 10 min at 37 °C. **(A)** Protein samples were incubated with radioactively labeled nucleotides for 10 min at 30 °C and separated by SDS-PAGE. After fixing the proteins with Coomassie staining, the gels were exposed to phosphorimager screens. To finally assess NMPylation, gels were scanned with a Typhoon 9200 imager. **(B)** To validate proper S-glutathionylation, samples were applied to Western blot analysis, using 2 µg protein per lane. S-Glutathionylated protein was detected with an anti-glutathione antibody. SDS-PAGE loading buffer with DTT served as a chemical negative control. Ponceau staining served as a loading control.

The aim of this assay was to investigate whether (i) the cysteine-deficient mutants are NMPylated in the same manner as the wild type protein, and (ii), if there are any effects of

nsp9 S-glutathionylation on the assay efficiency. For this purpose, two different batches of nsp9 wild type and its four cysteine mutants (only one batch each) were incubated either with or without 5 mM GSSG and desalted prior to the NMPylation assay. Proper S-glutathionylation of the proteins was confirmed via anti-glutathione Western blot analysis in parallel. Although the wild type protein as well as the susceptible mutants were clearly S-glutathionylated, no effects on the efficiency of NMPylation could be observed (Figure 35 A+B). In accordance with these findings, also the mutation of cysteines did not seem to alter the NMPylation pattern compared to the wild type.

4.3.4.3 Protein crystallization of S-glutathionylated SARS-CoV nsp9

To further confirm the localization of S-glutathionylation within the structure of nsp9, protein crystallization with modified protein was tested. The three-dimensional structure of nsp9 was already solved and protocols were available (Egloff et al., 2004; Sutton et al., 2004), so these protocols were used with slight modifications. Crystals grew in 2 M $(NH_4)_2SO_4$ and 0.3 M phosphate-citrate buffer, pH 3.0. The protein solution contained 20 mg·ml^{-1} nsp9, 2 mM DTT in nsp9 storage buffer without glycerol (50 mM Hepes-KOH, pH 8.0, and 150 mM KCl). Crystals grew over night at room temperature. To identify S-glutathionylated cysteines, different concentrations of GSSG were used for cocrystallization. With increasing concentrations of GSSG, the crystals became smaller and fewer crystals grew (Figure 36). However, they only diffracted to a resolution of ~9 Å. Since the data was of poor quality, molecular replacement was not applicable to identify electron densities for bound glutathione.

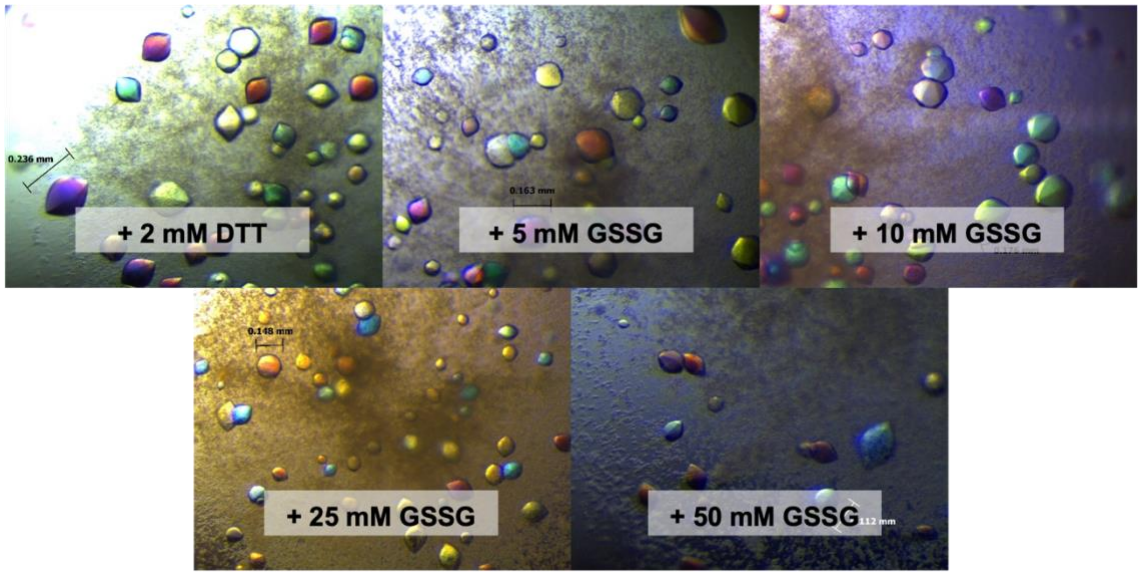

Figure 36 - Protein crystals of SARS-CoV nsp9 wild type +/- GSSG.
Exemplary pictures of SARS-CoV nsp9 protein crystals obtained with crystallization conditions containing 2 M ammonium sulfate and 0.3 M McIlvaine buffer, pH 3.0. Protein solution contained 20 mg/ml^{-1} nsp9 (+/- GSSG), 2 mM DTT, 50 mM Hepes, pH 8.0, 150 mM KCl and 5% glycerol.

4.4 *Excursus*: S-glutathionylation of human spectrin

Within this side project, we wanted to confirm human spectrin to be a target for S-glutathionylation in the context of hypertension and whether this modification also occurs during malaria infections. This project was conducted in close cooperation with the Cortese-Krott lab, who provided many of the samples and protocols.

First, purified spectrin from human erythrocytes was incubated with varying concentrations of GSSG (0-10 mM). Western blot analysis could show that spectrin is S-glutathionylated in a concentration-dependent manner, although GSSG concentrations higher than 3 mM revealed decreased signal intensity. In addition, the modification is reversible by adding DTT (Figure 37 A). Interestingly, both subunits of the protein (α and β; 279.7 and 245.6 kDa, respectively) could be detected with the glutathione antibody, whereas the anti-spectrin antibody only detects the smaller β-subunit.

An additional approach was the isolation of high concentrations of spectrin via RBC ghost preparation, which is described in more detail in Methods. RBC ghosts are well suited for membrane biochemistry studies and have similar properties to intact RBCs (Bjerrum, 1979). During preparation, the RBC membrane is opened via isotonic lysis to remove the hemoglobin. Prior to resealing the ghosts, they were incubated with relatively low concentrations of GSSG to roughly approximate physiological concentrations. S-glutathionylation of spectrin could be shown by Western blot analysis (Figure 37 B).

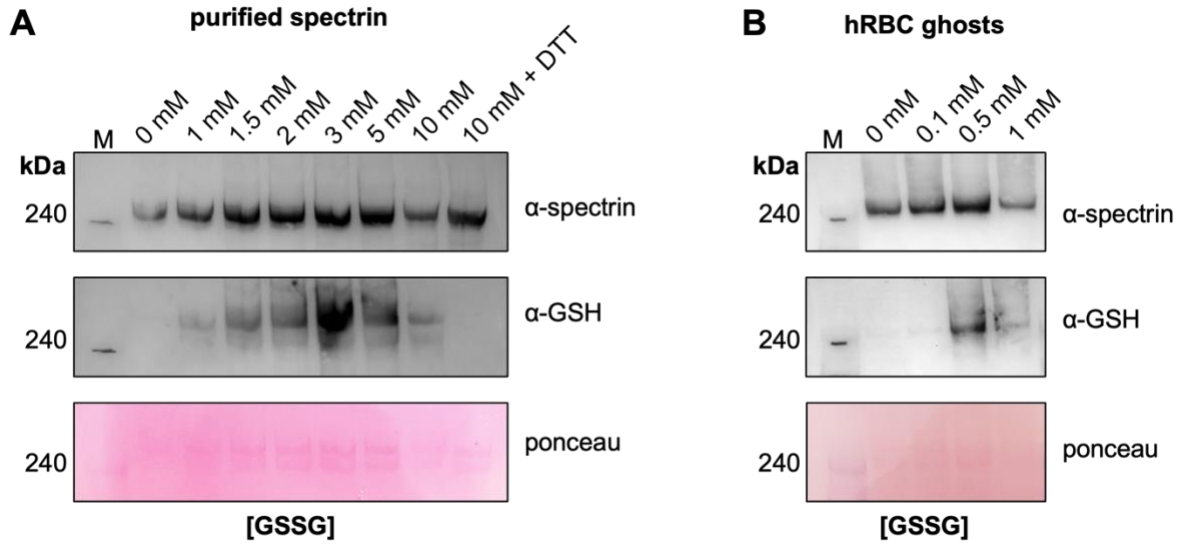

Figure 37 - Human spectrin can be S-glutathionylated by incubations with GSSG.
Samples from A + B were analyzed via Western blot analysis, using ~2 µg spectrin per lane. S-Glutathionylated spectrin was detected with an anti-glutathione antibody (α-GSH). SDS-PAGE loading buffer with DTT served as a chemical negative control. Ponceau staining and, in addition, a second antibody treatment after stripping with an anti-spectrin antibody (α-spectrin) served as loading controls. **(A)** Purified spectrin from human erythrocytes was incubated with 0-10 mM GSSG for 10 min at 37 °C. **(B)** Unsealed human erythrocyte (RBC) ghosts were incubated with 0-1 mM GSSG for 10 min at 37 °C. M = dual color protein marker, hRBC = human red blood cells.

Due to very low concentrations of spectrin within the samples used, it was difficult to achieve equal loading of the analyzed blots. The Ponceau staining was quite weak, which is why an

additional loading control was performed. The anti-spectrin antibody revealed slightly unequal loading, which must be considered when the interpretation of the signals for S-glutathionylation is made.

To investigate which cysteines are targeted by S-glutathionylation, samples of both experiments were sent to mass spectrometry analysis. Summarizing the results for both subunits, 27 from 36 cysteines were found to be S-glutathionylated. Depending on the sample analyzed, also less cysteines were found to be modified. However, 14 cysteines were found the most often and are highlighted with asterisks in Table 6.

Table 6 - Spectrin cysteines targeted by S-glutathionylation.
Abbreviations: -SSG = S-glutathionylated cysteine. / *Were detected more often than other cysteines.

α-subunit, 279.7 kDa			*β-subunit, 245.6 kDa*		
No.	**Position**	**-SSG**	**No.**	**Position**	**-SSG**
1	**167***	X	1	73	
2	224	X	2	112	
3	324	X	3	183	X
4	475	X	4	**603***	X
5	773		5	**618***	X
6	799		6	735	X
7	**965***	X	7	860	X
8	**1203***	X	8	960	
9	1394	X	9	963	
10	1404	X	10	**1167***	X
11	1524	X	11	1283	X
12	1568		12	**1552***	X
13	1571	X	13	**1892***	X
14	1847	X	14	**1962***	X
15	**1879***	X	15	**2012***	X
16	**2059***				
17	**2072***	X			
18	**2101***	X			
19	2159	X			
20	2299				
21	2388	X			
	Σ	16		**Σ**	11

S-glutathionylation of human spectrin upon P. falciparum *infection*

To confirm the occurrence of S-glutathionylation without adding any inducing agents during infection of RBCs with *P. falciparum*, we enriched trophozoites using MACS (described in

Methods, section 3.8). During its trophozoite stage, hemozoin (malaria pigment) is produced by the parasite, which is magnetic and can therefore be used to enrich trophozoites. The *P. falciparum* culture was kindly provided by the technical assistance in our laboratory. Via MACS, trophozoites (= eluate) and non-infected RBCs or ring-stage parasites (= flow-through) were separated. Efficient sorting was confirmed via blood smears (Figure 38 A). Samples were gently lysed with a single freeze-thaw cycle (-80 °C, room temperature) and subsequently analyzed via Western blot analysis, using first an anti-glutathione antibody and an anti-spectrin antibody afterwards (Figure 38 B). In all samples, an appropriate amount of spectrin could be detected. Though, no assumptions about its S-glutathionylation upon malaria infection could be made due to low signal intensities that could not be solved during replicates.

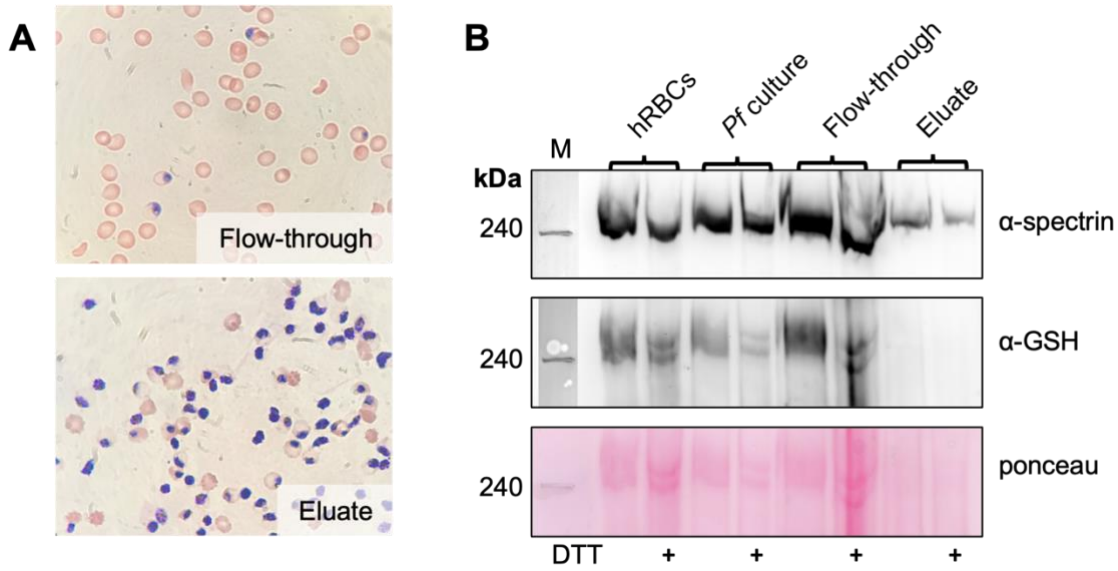

Figure 38 - Magnet assisted cell sorting to detect S-glutathionylated spectrin in *Plasmodium* cell culture. **(A**) *P. falciparum* trophozoite stages were isolated form cell culture. Efficient sorting was controlled via blood smears. **(B)** Samples were analyzed via Western blot analysis. S-glutathionylated spectrin was detected with an anti-glutathione antibody (α-GSH). SDS-PAGE loading buffer with DTT served as a chemical negative control. Ponceau staining and, in addition, a second antibody treatment after stripping with an anti-spectrin antibody (α-spectrin) served as loading control. M = dual color protein marker, hRBCs = human red blood cells, *Pf* culture = *P. falciparum* culture.

5 Discussion

5.1 *P. falciparum* hexokinase

Hexokinases catalyze phosphorylation of glucose to G6P, whereby ATP provides the phosphoryl group. G6P is important for glycolysis and the pentose phosphate pathway. In the latter one, G6P is the rate-limiting substrate for G6P dehydrogenase, which produces the reducing agent NADPH (Haeussler et al., 2019; Roth, 1987). The catalysis of hexokinases is dependent on Mg^{2+} or other divalent cations (Hurley, 1996; Nishimasu et al., 2006; Roy et al., 2019).

PfHK was enzymatically characterized in our working group in 2013, but the protocols could not be reproduced. Therefore, the aim of this thesis was to establish new protocols for expression and purification with a codon optimized synthetic gene. The usage of a codon optimized sequence was already described by Harris et al., 2013, however, they used a pQE30 vector with an N-terminal His_6-tag, whereas in this study a C-terminal His_6-tag was used. Interestingly, although the assay conditions were essentially similar, the K_M value for glucose was almost 5-fold lower compared to the Michaelis-Menten constants presented previously (Harris et al., 2013; Roth, 1987). The glucose affinities measured for *Cryptosporidium parvum* and *Toxoplasma gondii* hexokinase (CpHK, TgHK) on the other hand were similar low and therefore comparable to the present values (Table 7). High affinities to glucose are important for the survival of parasites, which have to deal with low intracellular glucose concentrations (Saito et al., 2002; Yu et al., 2014). In erythrocytes infected with *Plasmodium*, it has already been shown that hexokinase activity and glucose consumption equally are significantly increased. This increase accordingly results in a generation of NADPH, which, in turn, can increase the production of GSH via downstream redox reactions (Roth, 1987).

Table 7 - Kinetic characterization of hexokinases from different organisms.

	K_M (mM)	
	Glucose	**ATP**
PfHK *Present study*	0.13 ± 0.01	0.83 ± 0.08
PfHK Harris et al. 2013	0.62 ± 0.06	0.66 ± 0.08
PfHK (*from infected erythrocytes*) Roth et al. 1987	0.431 ± 0.021	3.1 ± 1.4
CpHK Yu et al. 2015	0.138	0.673
TgHK Saito et al. 2002	0.0080 ± 0.0008	1.05 ± 0.25

5.1.1 Effects of oxidative posttranslational modifications

The contribution of cysteines to redox regulation is mediated via oxidation and reduction of their thiols. Due to the core sulfur atom, they can adapt to several oxidation states and thereby alter the structure and/or function of proteins. As stated previously, PfHK is considered to be exceptionally cysteine rich (3.05%). Furthermore, the enzyme has been reported to be a target for S-glutathionylation, S-nitrosation and three proteins of the thioredoxin superfamily in *P. falciparum*: PfTrx, PfGrx, PfPlrx (Kehr et al., 2011; Sturm et al., 2009; Wang et al., 2014).
Within this thesis it was shown for the first time PfHK is targeted and inhibited by both S-glutathionylation and S-nitrosation. Although there are various studies providing data about S-glutathionylation of glyceraldehyde-3-phosphate dehydrogenase (GAPDH) and other glycolytic enzymes, S-glutathionylated hexokinases have not been intensively studied. This is in accordance with the findings from Kehr and colleagues, who could prove an inhibition of S-glutathionylated PfGAPDH and PfPK (Kehr et al., 2011). The effects of the modification reported by them are comparable to the level of inhibition observed in this thesis, however, both PfPK and PfHK require higher levels of GSSG to observe considerable inhibition compared to the inhibition observed for PfGAPDH. There, a modified active site cysteine was found to be responsible for the inhibitory effect both S-glutathionylation and S-nitrosation.
Many hexokinases are known to be S-nitrosated, though the effect of this modification depends on the organism that is studied. In some organisms, S-nitrosation does not affect the enzymatic activity, whereas in others, S-nitrosated proteins reveal reduced activities. The inhibitory effect can, in some cases, be prevented by the incubation with substrates prior to the modification. But, as reported for ATP, it can also increase the exposure of reactive thiols and, subsequently, enhance the inhibitory effect (Miller et al., 2007; Mongin et al., 2012; Romero and Bizzozero, 2009). Within this thesis, PfHK was shown to be S-nitrosated by 100 µM Cys-NO, though the effect of concentrations lower than 200 µM on the activity were only minimal. Overall and compared to concentrations of GSSG used for S-glutathionylation, lower concentrations were required to see either an inhibitory effect in the enzymatic assay or a signal for S-nitrosation in Western blot analysis. This proportionally corresponds to physiological levels of both oxidants *in vivo*: There, nitrosative species or other NO-donors are less abundant than glutathione (Barbarino et al., 2021; Checconi et al., 2019; Hall and Garthwaite, 2009).
Most often, changing environments evoke the posttranslational modification of numerous parasitic, mammalian, yeast, and plant hexokinases. Besides their important and most popular role in glycolysis, hexokinases are reported to perform further different functions. Proteins that perform different and independent functions are called moonlighting proteins. Hexokinases, for example, can regulate redox signaling, perform as a gene repressor, kinase functions or act as immune receptor (Heneberg, 2019; Rodríguez-Saavedra et al., 2021).

The results of the Ellman assay and the mass spectrometry analysis suggest 9-11 cysteines to be targeted by either S-glutathionylation or S-nitrosation. This is further supported by the herein solved three-dimensional structure (Figure 39 A). Modification of C77, C85, C219, C346, and C399, respectively, were detected most often via mass spectrometry and are accessible according to the crystal structure. The addition of either GSH or NO at a cysteine residue results in an increase of mass of +305 Da and +29 Da, respectively (Farley and Link, 2009; Xiong et al., 2011). Thus, the remarkably smaller NO could easily fit into smaller pockets on the protein's surface. In contrast to PfGAPDH, for example, no cysteine of PfHK is located in the catalytic site. Therefore, oxPTMs cannot directly impair catalysis. C193 was not found in mass spectrometry but is part of the tetrameric interface, probably accessible and highly conserved among *Plasmodium* species. The second cysteine participating in the tetrameric assembly of PfHK is C346, which is restricted to *P. falciparum* and six other *Plasmodium* species infecting chimpanzees and gorillas, as shown in Figure 39 B (Ngoubangoye et al., 2016). If those cysteines near the active site or within the tetrameric interface are indeed targeted *in vivo*, they could indirectly affect the enzymatic activity. However, the present data could only show them to be an *in vitro* target. As stated previously, C249 and C260 could form a disulfide and consequently allow for further modification. Moreover, these cysteines could be the target for redox-active proteins like PfTrx, PfGrx and PfPlrx, which were shown to potentially interact with PfHK (Sturm et al., 2009).

In this thesis, the interaction of PfHK with PfTrx, PfGrx and PfPlrx was kinetically confirmed. Therefore, reduced and modified PfHK were incubated with the three proteins, respectively, whereas DTT served as a chemical control. It has been shown that DTT restores the activity of PfHK after both S-glutathionylation and S-nitrosation. Although not being as efficient as DTT, all three proteins were able to restore the activity of PfHK at least partially and have a beneficial effect on the activity of unmodified PfHK. However, further experiments should demonstrate that this increase in enzymatic activity can be traced back to a decrease of S-glutathionylation and/or S-nitrosation. Although different approaches for a subsequent Western blot analyses with an glutathione antibody were performed, no specific (de)glutathionylation pattern could be determined. Kehr and colleagues could show that PfTrx can be modified by S-glutathionylation and that incubations with PfTrx, PfGrx and PfPlrx restore the enzymatic activity of PfGAPDH and PfPK. PfTrx itself is also a target for S-nitrosation and was shown to be an efficient denitrosylase for a variety of *Plasmodium* proteins and GSNO. Usually, GSNO is the substrate for the NADH-dependent GSNOR, which provides GSH for the reduction of S-nitrosated thiols via denitrosation of GSNO. Interestingly, *Plasmodium* lacks GSNOR, suggesting PfTrx to compensate sufficient denitrosation (Barnett and Buxton, 2017; Benhar et al., 2009; Kanzok et al., 2000; Wang et al., 2014). Sturm and colleagues could show that PfTrx enhances the enzymatic activity of ornithine aminotransferase (PfOAT), which is in accordance with the

present data showing an increase of activity of unmodified PfHK in the presence of PfTrx, PfGrx and PfPlrx.

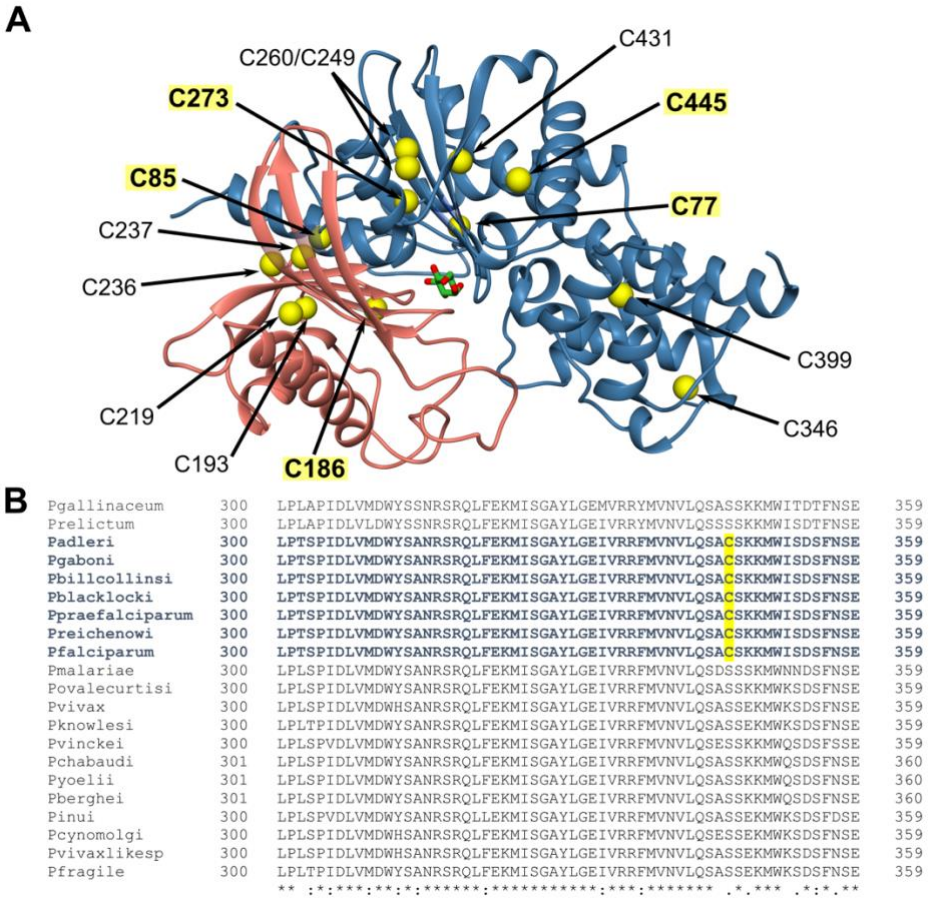

Figure 39 - Distribution of cysteines in PfHK and their conservation among different *Plasmodium* species. **(A)** Distribution of PfHK monomer B, which contains 15 cysteines. Cysteines near the active site are highlighted in yellow. **(B)** Multiple sequence alignment of different *Plasmodium* species. Sequences were analyzed using Clustal Omega Multiple Sequence Alignment. C346 is highlighted in yellow and restricted to seven *Plasmodium* species.

Besides the incubations with PfTrx, PfGrx and PfPlrx, also pre- and coincubations with substrates have been reported to prevent or reverse the inhibition caused by oxPTMs. This effect has already been shown for PfGAPDH, which has an active site cysteine (C153) that is part of the substrate binding site (Kehr et al., 2011; Wang et al., 2014). The enzymatic analysis of PfHK revealed that adding both ATP and glucose in the standard S-glutathionylation and S-nitrosation assay can partially prevent the inhibition of PfHK. Although this could not be clearly confirmed by a decreased signal intensity in Western blot analysis, the analysis showed an increased signal intensity for the sample plus ATP, which equally revealed a decreased enzymatic activity. As stated above, the binding of ATP within the active site could induce conformational changes that eases the accessibility of some cysteines. From other hexokinase structures and the herein presented structural analysis of PfHK it is known that upon binding of glucose, PfHK undergoes massive conformational changes. Moreover, occupation of the phosphate transfer binding site leads to the movement of the *Plasmodium*-specific loop, which protects the active site residues from the exposure to solvents. When ATP binds, the active

site gets even more compact to ensure the adequate transfer of the phosphoryl group to yield G6P. Together with the kinetic analysis one could hypothesis the conformational changes during catalysis protect at least some cysteines from S-glutathionylation and, consequently, the whole enzyme from an oxPTM-mediated loss of activity.

It should be mentioned that the parasite's antioxidative defense system is a proven target for drugs, since currently available therapies are already known to hamper this complex system. Nevertheless, many mechanisms remain unknown and could possibly represent novel approaches for drug development, especially when combined with vitally important enzymes like PfHK (Alam et al., 2014; Becker et al., 2004; Pereira et al., 2020; Tiwari et al., 2021).

5.1.2 The three-dimensional structure of PfHK

As stated previously, PfHK shares < 32% identity with its human counterpart, which is why PfHK is considered as a promising drug target. However, most important are differences within the active or allosteric sites and/or differences concerning the mechanism upon catalysis. An analysis with NCBI Smart BLAST revealed that among different *Plasmodium* species, hexokinases are quite conserved, covering a range from 85.5% (*P. relictum*) to 99.8% (*P. reichenowi*) sequence identity. The so far sole *Plasmodium* hexokinase structure obtained for PvHK shares 89.6% sequence identity with PfHK, therefore the data presented in this thesis confirms most of the previously shown structural analysis (Srivastava et al., 2020). Due to the higher resolution and possibly due to the binding of ligands, some additional loops could be defined within this thesis, including the *Plasmodium*-specific insertion.

In contrast to *P. falciparum*, four distinct hexokinases have been identified in mammalian tissues (type I-IV). Mammalian hexokinase type IV (HKIV) is known as 'glucokinase' and is a ~50 kDa isoenzyme, while types I-III have probably evolved from gene duplication and form a dimer with a size of ~100 kDa (Wilson, 2003). In yeast, there are two isoenzymes similar to the mammalian HKIV (Kuser et al., 2008). Despite differences in oligomerization, the domain organization of hexokinases is highly conserved among different organisms and was also observed in the present PfHK structure (Aleshin et al., 1998; Bennett and Steitz, 1978; He et al., 2019). Yeast hexokinases can be active as both monomers and dimers. Another example for the occurrence of dimeric hexokinase is the hyperthermophilic archaeon *Sulfulobus tokodaii*, which, although adapting the typical hexokinase core fold, differs from other hexokinases by several loop regions that participate in substrate binding (Hoggett and Kellett, 1992; Kuettner et al., 2010; Kuser et al., 2008; Nishimasu et al., 2007, 2006). Tetrameric hexokinases, on the contrary, are quite unique (Figure 40). So far, only PvHK and a hexokinase form the archaeon *Thermus thermophilus* have been shown to form a homotetramer, though the latter one reveals a completely different arrangement (Nakamura et al., 2012; Srivastava et al., 2020). The tetrameric interfaces among the two *Plasmodium* hexokinases are well

conserved and both datasets provide mutual confirmation. Since this oligomerization is quite unique and gives insights into unknown mechanisms of regulation, it may be postulated as new and promising approach for inhibitor design.

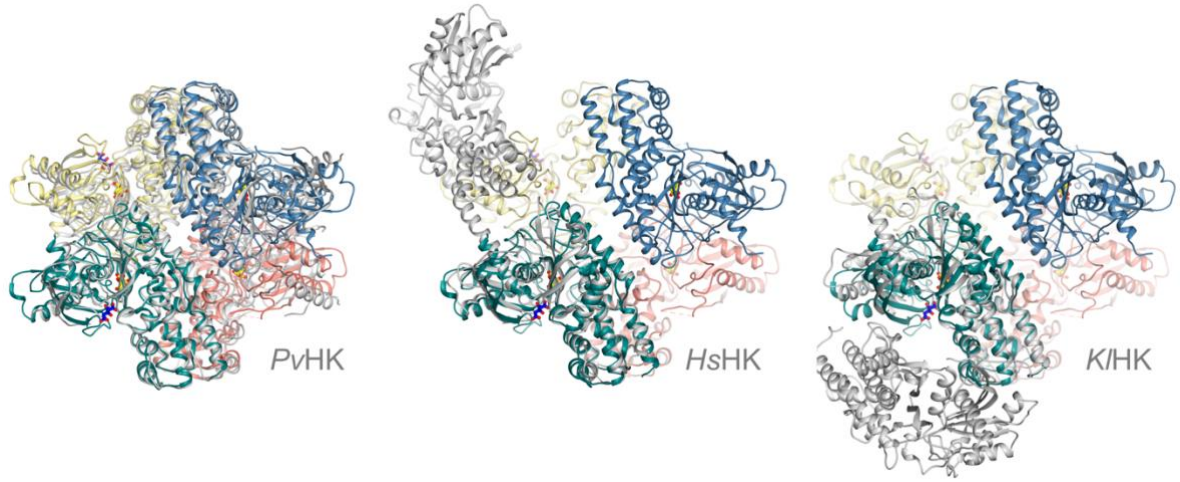

Figure 40 - Superimposition of PfHK with different hexokinase oligomers.
The present structure was superimposed with tetrameric *P. vivax*, monomeric human brain hexokinase I (HsHK) and dimeric *Kluyveromyces lactis* (KlHK) hexokinase (PDB IDs: 6VYG, 1HKB, 3O08), represented in grey, respectively.

Mammalian hexokinases I-III consist of N- and C-terminal halves that form pseudo-dimers, connected with a transition helix. They are usually active as monomers; however, crystalline dimers were used for *in vitro* analysis (Aleshin et al., 1998; Fang et al., 1998). Type I and III possess a catalytically relevant C-terminus, respectively, whereas the N-termini fulfill a regulatory role. Via ligand-induced conformational changes, the subunits of the pseudo-dimer can communicate and therefore provide allosteric regulation of the enzyme (Aleshin et al., 1998; Fang et al., 1998; Hashimoto and Wilson, 2002; Mulichak et al., 1998; Sebastian et al., 1999). A similar way of communication among the different monomers could be hypothesized for the present PfHK structure, involving residues of the *Plasmodium*-specific insertion. In monomer B with solely glucose bound to the active site, residues L130-S135 from the small domain interact with residues P304-Y312 and D354 from the large domain. The latter residues are part of the tetrameric AB interface. Upon the binding of citrate, these interface residues are displaced. Thus, the contact and the hypothesized communication among the small and the large domain residues is lost, which further could be an indication why citrate is only bound in monomer A.

The present citrate molecule occupies strictly conserved residues of the active site, that typically bind phosphate alone, or the phosphates from either G6P or ATP/ADP (Aleshin et al., 2000, 1998; Mulichak et al., 1998). Although ATP was present in the protein solution used for crystallization with a concentration of 10 mM, no electron density for its binding could be observed. Citrate, on the other hand, was used with a concentration of 300 mM, rather suggesting its random binding and/or crowding out of ATP than physiological significance.

Since the binding site is well conserved among different species and this conflicts with common criteria of promising drug targets, citrate was excluded to be a candidate for inhibitor design. Therefore, and due to the high concentrations used (300 mM), no further kinetic analysis of the regulatory impact of citrate on PfHK was included in this thesis. In general, there are only a few studies about the effect of citrate on hexokinases. While it was shown to activate mammalian and yeast HK, only a single study presented data about the inhibitory effect of citrate on the fungal hexokinase from *Aspergillus niger* with a K_I value of 0.15 mM (Colowick, 1973; Kosow et al., 1973; Kosow and Rose, 1971; Steinböck et al., 1994). However, the flexible small domain and residues L130-G141 in particular are stabilized upon citrate binding, leading to a better-defined electron density of this region, which could be shown for the first time for *Plasmodium* hexokinases.

In the present structure, the substrate glucose was bound to highly conserved residues from both monomers (Aleshin et al., 1998; He et al., 2019; Kuettner et al., 2010; Kuser et al., 2008). It is known that the binding of glucose induces massive conformational changes of the enzyme, resulting in a rotation of 12° of both domains towards each other and the movement of the polypeptide backbone of 8 Å (Bennett and Steitz, 1978). Thereby, the active site is closed, and the glucose molecule is enveloped. Only the hydroxyl group of the C6 atom remains susceptible for the transfer of the phosphoryl group that is provided by ATP (Roy et al., 2019). Besides this usually described mechanism upon substrate binding, there is also data about alternating states to ensure efficient substrate binding and product release. This study could additionally show that the binding of glucose does not only induce a closed conformation, but also promotes an active open state (Liu et al., 2012). Hexokinases prefer to bind glucose first, though the substrate binding order is random (Hurley, 1996). There is also a preferred order for product release after catalysis: First, ADP is released by a movement of the small domain, followed by the release of G6P (Aleshin et al., 1998; Kosow and Rose, 1970). This is in accordance with the data presented in this thesis that shows two different conformations of the *Plasmodium*-specific insertion in the small domain. In the presence of citrate at the phosphate binding site, the cleft between the two domains is broadened, suggesting a conformational state that promotes product release.

5.2 *P. falciparum* pyruvate kinase

Among different *Plasmodium* species, pyruvate kinase is quite conserved, ranging from ~90% (*P. malariae, P. yoelii*) to over 99% (*P. gaboni, P. reichenowi*) sequence identity. Human and various other mammalian pyruvate kinases, on the contrary, share ~45% sequence identity with the herein presented PfPK (analyzed with NCBI Smart BLAST). Although this is clearly higher than the sequence identity reported for human and PfHK, PfPK is nevertheless

considered to be a promising drug target. As stated previously, a second PfPK isoenzyme (PfPK2) with only 20% sequence identity is expressed in intraerythrocytic stages that is presumably located in the apicoplast (Chan et al., 2007). Compared to other proteins within similar species, PfPK is considered to be exceptionally cysteine-rich (Miseta and Csutora, 2000). It contains fifteen cysteine residues, which is about 3% of the total amino acid content. As shown by multiple sequence alignment, other apicomplexan parasites revealed to have a comparable ratio of cysteines to total amino acids, whereas human and rabbit pyruvate kinase only have 1.33% and 1.7% cysteines, respectively. There are six cysteines that seem to be restricted to *Plasmodium* which were all targeted by oxPTMs expect for the last one: C49, C66, C140, C143, C222 and C367. Previous studies could show that PfPK is strongly inhibited by S-glutathionylation and targeted by S-nitrosation, though without any effect on its enzymatic activity, (Kehr et al., 2011; Wang et al., 2014). Within those studies, protein targets were identified via mass spectrometry analysis and further characterized with (enzymatic) assays. Due to insufficient sensitivity of former mass spectrometric analyses the modifications could not be identified on amino acid or, to be more precise, on cysteine level.

5.2.1 Identification and mutation of cysteines susceptible to oxidative posttranslational modifications

To gain first insights into how many of the PfPK cysteines are targeted by S-glutathionylation and S-nitrosation, (i) the number of thiol groups in reduced PfPK samples were quantified using Ellman's reagent and (ii) complemented with mass spectrometry data of modified protein samples. It is noteworthy the number of modified cysteines depend on the concentrations of GSSG and nitrosoglutathione used. During this experiment, the concentrations used were relatively high (5 mM GSSG and 400 µM nitrosoglutathione), to identify as many susceptible cysteines as possible. Lower concentrations would probably have targeted fewer cysteines. Moreover, the original scope this mass spectrometry analyses was to investigate potential crosstalk among different oxPTMs. For this reason, Table 3 summarizes information about different types of samples (n = 22; +GSSG, +GSNO, +GSSG/GSNO). However, a specific modification pattern could not be determined, possibly due to low sequence coverage (mean value = 63.9 %).

Combining the mass spectrometry data with the data gained from the solved three-dimensional protein structure, nine cysteines with a high probability to be accessible for either S-glutathionylation or S-nitrosation and five for both could be identified, which is approximately in accordance with the results from Ellman's assay. Recently, PfPK was also proven to be a target of S-sulfenylation. The mass spectrometry data obtained in this work is more precise than former data sets and suggests four potential SOH sites on C222, C302, C343, and C433 (Schipper et al., 2021). In the present thesis, C222, C302, and C433 could be confirmed as

targets for both S-glutathionylation and S-nitrosation, although C222 and C302 are both located in a small pocket on the enzyme's surface and require minor conformational changes to be modified. C343 was only found to be S-glutathionylated and, according to the three-dimensional structure, is putatively not accessible for oxPTMs. To further verify these findings, another goal of this thesis was to crystallize modified PfPK. In general, there are two strategies to identify the localization and binding pose of ligands within protein structures. For cocrystallization, the protein is either incubated with the desired ligand in solution prior to the crystallization protocol or the ligand is added during the crystallization process. A second approach is to soak the fully grown protein crystals with a solution containing the ligand. While the establishment of an adequate cocrystallization protocol is rather time-consuming, soaking experiment can be misleading with regard to correct binding poses of the ligands (Müller, 2017; Wienen-Schmidt et al., 2021). Although both approaches were performed within this thesis, no binding sites for oxPTMs could be identified. The crystals obtained for S-nitrosated PfPK were of too poor quality to obtain electron densities for NO sites and S-glutathionylated protein crystals did not grow at all. This may be in accordance with the enzymatic analysis of modified PfPK: While S-nitrosated PfPK maintains its enzymatic activity, S-glutathionylated PfPK is inhibited (Kehr et al., 2011; Wang et al., 2014). One could hypothesize that S-glutathionylation induces conformational changes that impair the crystallization process. Furthermore, the number of deposited protein structures with "glutathionylated" or "nitrosylated/ nitrosated" in their title is quite low: 24 and 56 structures, respectively (searched with RCSB PDB). Searching for such structures via the option 'ligand' yields ~450 structures complexed with GSH and ~170 structures complexed with NO, though most of the proteins complexed with GSH are Grx or GST.

Based on these findings, three different cysteine-to-alanine mutants were kinetically characterized: $PfPK^{C49A}$, $PfPK^{C66A}$, and $PfPK^{C343A}$. As already described in more detail in the previous master thesis, the mutation to alanine was chosen over the also very common mutation to serine, since serine is very similar to cysteines and might prevent from observing significant structural and/or functional changes (Dillenberger, 2017; Scholl and Wells, 2000). All the mutated cysteines are located either near the ADP binding pocket or the pyruvate binding site but are not catalytic residues themselves. Still, a significantly decreased specific activity for $PfPK^{C49A}$ and massively increased K_M values for PEP for both $PfPK^{C49A}$ and $PfPK^{C343A}$ could be measured, indicating major functional and possibly also structural changes of the enzyme induced by the mutations. Although C66 is adjacent to residue R67, which usually interacts with the α- and γ-phosphates of ATP, $PfPK^{C66A}$ does not show any significant differences compared to the wild type enzyme. Massive alterations induced by the modification of a single cysteine were already observed for mammalian pyruvate kinase M2 (PKM2): There, the oxidation of only one cysteine lead to inhibition of the enzyme and subsequently a

regulation of the pentose phosphate pathway (Anastasiou et al., 2011; Irokawa et al., 2021; Mitchell et al., 2018; Yang and Lu, 2013). Since pyruvate kinases are known to be regulated by several different modifications, conformational and kinetic changes are substantially more complex to analyze. In addition, modifications can either increase, decrease, or have no effect on the enzymatic activity. If different sites of a protein are targeted by different types of modification, the regulation is even more complex (Gould et al., 2015). Not only different sites of the protein, but one single cysteine can be susceptible for more than one modification. Regulation by diverse modifications is often referred to as crosstalk (Hess and Stamler, 2012; Leonard et al., 2009; Sehrawat and Deswal, 2014). PfPK wild type has 15 cysteines in total. Although not all of them are susceptible for either S-glutathionylation or S-nitrosation, there are still multiple potential combinations of oxPTMs to occur at multiple modification sites. Moreover, the two oxPTMs studied in this thesis only provide a small insight into the complex network of oxPTMs, other modifications as well as involved low molecular weight molecules and redox active proteins.

5.2.2 Three-dimensional structure of PfPK^{WT}

While mass spectrometry data and kinetic characterizations provide important information about the cysteines targeted by oxPTMs and how the mutation or modification of a single cysteine can affect the enzymatic activity, analysis of the three-dimensional protein structures provided further insights into the mechanism upon substrate binding and thus substrate affinities of PfPK.

As stated previously, the crystallization protocol used in this thesis differs significantly from the one used for the unpublished structure of Wernimont and colleagues, which was deposited on PDB, and therefore provide independently collected data. In the course of this project, another structure was deposited and published by Zhong and colleagues, also differing from the protocol used in this thesis (Table 8).

Table 8 - Comparison of different PfPK crystallization protocols.

	Wernimont et al., 2009	**Zhong et al., 2020**	**Present structure** (Data collection in 2018/19)
Precipitant	10% PEG 8,000	12% PEG 8,000 10-20% glycerol	14-24% PEG 600
Buffer	100 mM Tris, pH 8.5	50 mM TEA, pH 7.2	100 mM MES, pH 6.5
Salt(s)	none	100 mM KCl 50 mM $MgCl_2$	50 mM KCl 10 mM $MgCl_2$
Ligand(s)	2 mM NaPyruvate 4 mM MgAcetate 2 mM AMPPNP 2 mM TCEP	5 mM oxalate 5 mM ATP 5 mM G6P	Only for WT^{Pyr}: 2 mM NaPyruvate 4 mM MgAcetate 2 mM AMPPNP 2 mM DTT

The herein presented domain organization of PfPK is conserved among mammalian, other apicomplexan and *Plasmodium* pyruvate kinases (Schormann et al., 2019; Zhong et al., 2020, 2013). Upon catalysis, both Mg^{2+} and K^+ are essential to allow the substrates to bind properly. The closure of the active site after random binding of both substrates is induced by K^+, whereas the absence of K^+ fosters PEP to bind first and ADP to bind afterwards (Jurica et al., 1998; Oria-Hernández et al., 2005). After precise substrate alignment, residues T313-T331 enable the transfer of phosphate form PEP to ADP, yielding the products pyruvate and ATP (Israelsen and Vander Heiden, 2015; Matte et al., 1998). As stated previously, comparison with other structures revealed the present wild type structures to adopt an open and a half-closed conformation. It seems that the presence of only pyruvate or oxalate promotes a half-closed state as observed in this thesis. In contrast to that, the binding of ATP forces a larger movement of the B-domain that completely closes the active site. However, also the binding of the substrate PEP can induce a fully closed conformation (Christofk et al., 2008; Larsen et al., 1997, 1994; Morgan et al., 2010; Zhong et al., 2020, 2013).

5.2.3 Structural differences among $PfPK^{WT}$ and its mutants $PfPK^{C49A}$ and $PfPK^{C343A}$

Both mutants reveal structural differences within the active site when compared to the wild type structure. All superimpositions were performed without the B-domain, since this led to a better alignment of the A-domain. The main cause for the conformational changes of $PfPK^{C49A}$, which are more severe than the changes observed for mutant $PfPK^{C343a}$, is the loss of two hydrogen bonds between T44-T350 and A48-A351 (Figure 41). Hydrogen bonds are known to stabilize not only protein secondary structures by connecting helices and beta sheets but also tertiary structures, ensuring proper protein folding (Pauling et al., 1951; Pauling and Corey, 1951). Several regions in $PfPK^{C49A}$ are displaced, leading to an increased flexibility and similarly elevated B-factors. Given the high resolution and since the B-factors for $PfPK^{C343A}$ were only slightly increased, the B-factors for $PfPK^{C49A}$ seem to be reasonable. Another approach to confirm the findings of the structural analyses could be to perform Hydrogen-Deuterium Exchange Mass Spectrometry (HDX-MS). This method complements the rather static X-ray analysis and provides information about different conformations and flexible regions of proteins (Narang et al., 2020).

The conformational changes in $PfPK^{C49A}$ affect the pyruvate binding site (M276-M284), the ADP/ATP binding site (S347-G352) and probably prevent K^+ from binding to residues N69 and S71. The ADP/ATP binding site was identified via superimposition with a human pyruvate kinase (PDB ID: 4FXF), rabbit pyruvate kinase (PDB ID: 1A49) and another PfPK structure (PDB ID: 6KSH), all complexed with ATP. The conformational changes at the ADP/ATP binding site could explain why no electron densities for either pyruvate or AMP-PNP were observed,

although both were present in the protein solutions used for crystallization. Moreover, the alterations fit well to the kinetic analysis of PfPK^{C49A}, revealing a twofold decrease of PEP affinity and support the previously reported findings that the absence of K^+ affects the substrate-binding order (Oria-Hernández et al., 2005). Superimposition of the tetramers of PfPK^{WT} and PfPK^{C49A} further revealed that the flexible regions within the A-domain impede the movement of the B-domain not only within each monomer but also among adjacent monomers within the tetrameric assembly. Even though protein engineering could show that a truncation of the B-domain does not lead to a complete loss of function of the enzyme, the domain organization is strictly conserved and critical for glycolysis (Sugrue et al., 2020). Therefore, the observed impediment of the B-domain movement is very likely to affect catalysis and probably tetramerization of PfPK. It is known that the enzymatically active form of human PKM2 exists as a tetramer. However, upon posttranslational modifications or other allosteric regulations, PKM2 forms less active dimers or monomers (Grant, 2021; Mitchell et al., 2018; Prakasam et al., 2018). In general, the tetrameric assembly of pyruvate kinases across different species is quite conserved and spans mammalian, yeast, plant and bacterial pyruvate kinases, though the individual connections among the different monomers can vary (Morgan et al., 2014).

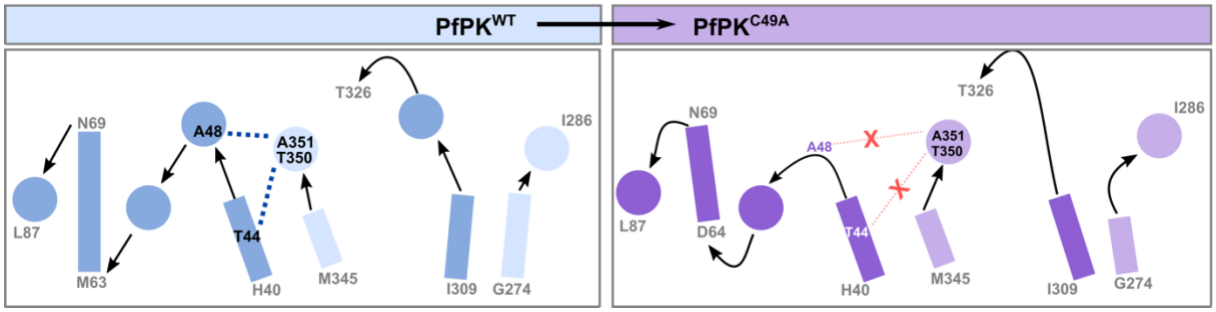

Figure 41 - Schematic representation of the conformational changes upon the loss of C49.
The mutation of C49 to alanine causes the loss of two hydrogen bonds (T44-T350; A48-A351). Thereby, residues R67-F82, M276-M284, T311-R324, and L346-K354 are rearranged. Helices are indicated by circles, beta sheets by squares.

Instead of the herein presented alanine mutants, one could also argue that the introduction of larger residues would be more reliable to mimic and represent the actual effects of oxPTMs. This may be true for S-glutathionylation, which means the addition of three amino acids to the thiol group (+305 Da). S-nitrosation, on the other hand represents a considerably smaller modification (+29 Da). Exchanging the cysteines with, for example, serine, methionine, glutamine, or asparagine puts the protein at risk to be susceptible for other (oxidative) PTMs (Figure 42). Another approach to label or mimic modified cysteines that are targeted by oxPTMs could be reactions of their sulfhydryls with maleimides, haloacetyls or pyridyl disulfides (Kim et al., 2008; Ravasco et al., 2019; Thermo Scientific, 2012). These reagents are often used in proteomics and represent a wide range for different purposes. Though, a big disadvantage of these crosslinking reagents is that they cannot target specific cysteines. Therefore, a protein like PfPK, which has so many cysteines, is difficult to study. Oxidative

derivates of C49, like sulfenic (-SOH), sulfinic (-SO(OH) or sulfonic acids (-S(=O)$_2$OH), could also easily lead to a similar collapse of hydrogen bonds that were observed in PfPK^{C49A}.

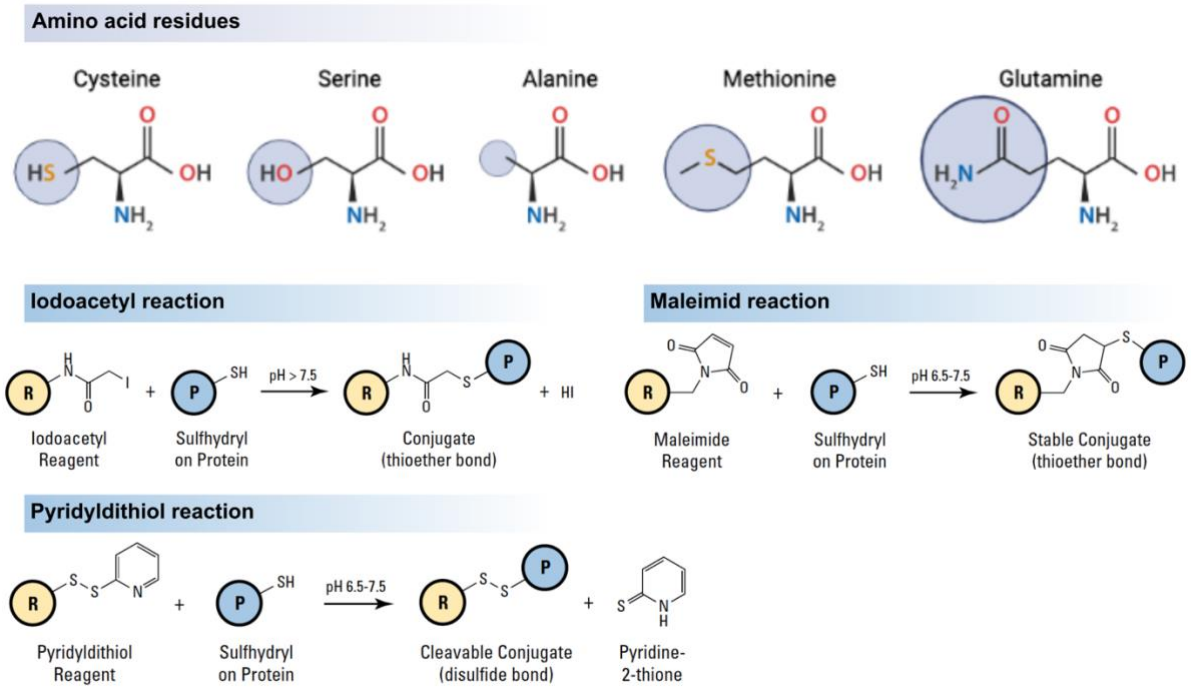

Figure 42 - Overview of amino acid residues and crosslinking chemistry.
Overview of different amino acid side chains. While cysteine and methionine both contain sulfur atoms, alanine, serine, and glutamine are characterized as aliphatic, hydroxylic, and amidic amino acids. Instead of replacing the cysteine with a different amino acid, it can also be labeled via crosslinking chemistry. Sulfhydryls are reactive towards haloacetyls, maleimides and pyridyl dithiols. Adapted from Thermo Scientific 2012 and BioRender.

5.3 S-Glutathionylation patterns in coronavirus nonstructural proteins

Upon viral infections, both viral entry and replication disrupt the redox state of the host's cells and consequently promote a pro-oxidant environment. This environment can be advantageous to viruses by facilitating different phases from infectivity to budding. However, viruses are not equipped with any antioxidants to protect their own proteins from oxidative or nitrosative stress. Both S-nitrosation and S-glutathionylation are known to protect cysteines residues from overoxidation, which could also be a protective mechanism of viral proteins. As previously shown, this modification of cysteines is most probably not random, but dependent on the cysteine's accessibility within the three-dimensional structure, its pK_a value, and the cysteine's environment, meaning vicinal amino acids. The screening of various nsps from different viruses confirmed this specificity, since not all proteins screened were found to be S-glutathionylated. For many of those proteins S-glutathionylation was shown for the first time. Though, a specific S-glutathionylation pattern could not be concluded from this screening. To validate these findings and possibly identify single cysteines that are targeted by oxPTMs, one

could additionally use proteomic approaches of cell culture samples followed by Western blot and mass spectrometry analyses. A big advantage of the coronavirus proteome is that it contains less proteins compared to *Plasmodium*, for example, which would probably facilitate the analyses and identification of single proteins. However, it is of course not known what percentage of the coronavirus proteome would be S-glutathionylated and whether this percentage is sufficient for an adequate analysis. If it would be too low, cells could be treated with diamide or *tert*-butyl hydroperoxide (*t*-BOOH) to increase oxidative stress and thus S-glutathionylation. Moreover, target proteins could be labeled via crosslinking chemistry to pull down the proteins of interest and increase the concentration of modified proteins. Another parameter that affects the outcome is when to collect the samples, which would be probably during the expression of the polyprotein after the viral entry.

5.3.1 S-glutathionylation of nsp5

SARS-CoV, HCoV-229E and FCoV nsp5 were glutathionylated in a concentration-dependent manner to find out whether their susceptibility to S-glutathionylation is similar or whether there are differences among the nsps of different viral strains. Indeed, FCoV nsp5 seems to be more susceptible to the modification, showing a weak signal in anti-glutathione Western blot analysis already after incubations with 1 mM GSSG. However, to achieve even better comparison, the samples should be applied to a single blot. Interestingly, FCoV has the lowest number of cysteines (n=7), compared to HCoV-229E (n=8) and SARS-CoV (n=12). The data obtained in this thesis could show for the first time that S-glutathionylation inhibits the protease activity of both HCoV-229E and FCoV nsp5. In accordance with the results from the former Western blot analysis, the inhibition of HCoV-229E nsp5 requires higher concentrations of GSSG compared to FCoV. It is already known that polyproteins and nsp5 from different coronavirus strains can be combined to achieve proper cleavage. Therefore, different combinations were used in the experiments performed in this thesis.

The first manuscript containing experimental data about the inhibitory effect of S-glutathionylation of nonstructural proteins was published in 2017 by Saisawang and colleagues. There, they investigated S-glutathionylation of nsp2, the protease of chikungunya virus. Comparable to the present data, they could confirm S-glutathionylation of nsp2 upon incubations with 5 mM GSSG and that incubations with low concentrations of DTT reversed the modification, both via Western blot analysis. Kinetic analyses further revealed an inhibition of its protease activity (Saisawang et al., 2017). In dengue virus cell culture, the nonstructural proteins NS1, NS3, NS4B and NS5 were identified to be targets for S-glutathionylation. NS5 has two important functions, that are both inhibited when modified by glutathione: a guanylyltransferase and an RdRp activity. These findings were also confirmed for Zika virus NS5 (Saisawang et al., 2018). A very recent study revealed the dimeric interface cysteine C300

of SARS-CoV-2 M^{pro} to be relevant for dimerization and, consequently also its protease activity (Davis et al., 2021). S-Glutathionylation of this cysteine promotes a monomeric and inactive form of nsp5 but is reversible via the addition of reducing agents. This cysteine was further validated to mainly contribute to the inhibition by the characterization of a C300S mutant of nsp5, that had an ~50% residual activity compared to the wild type protein. Although it was shown its activity was not affected by S-glutathionylation, the mutant can still be S-glutathionylated via other cysteine residues. Multiple sequence alignment showed this cysteine is conserved among SARS-CoV and SARS-CoV-2, but not among the other nsp5 that were characterized in this thesis (Figure 43). Therefore, the herein observed inhibition mediated by S-glutathionylation must be evoked by (an)other cysteine(s), like, for example, the active site C145, which was indeed not found to be S-glutathionylated by Davis and colleagues. However, another study showed the covalent modification of C145 of the SARS-CoV-2 nsp5 via an inhibitor can block the viral replication, which was previously shown for MERS-CoV as well (Tomar et al., 2015; Vuong et al., 2020).

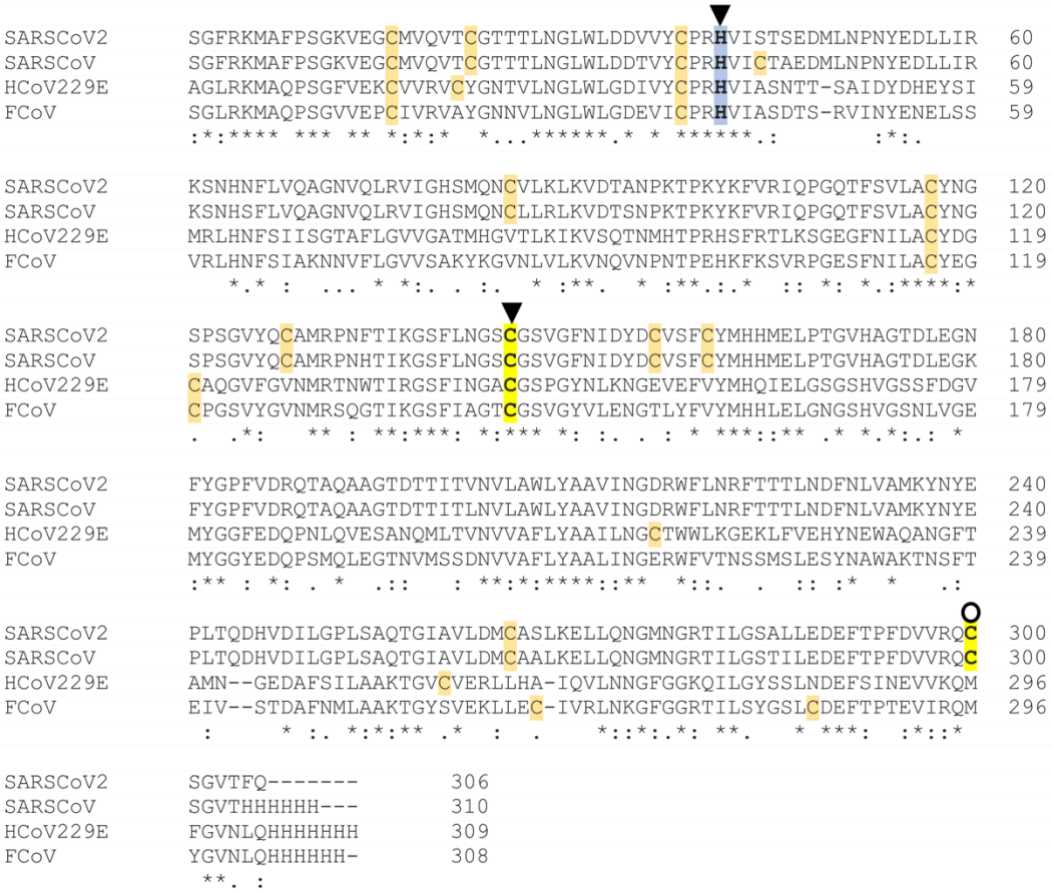

Figure 43 - Sequence alignment of SARS-CoV-2, SARS-CoV, HCoV-229E, and FCoV nsp5.
The catalytic residues H41 and C145 are marked in blue and yellow, respectively, and highlighted by triangles. C300, marked by a circle, is conserved among SARS-CoV and SARS-CoV-2 and part of their dimeric interface. All other cysteines are marked in lighter yellow. The alignment was performed with Clustal Omega.

5.3.2 S-glutathionylation of nsp8

Multiple sequence alignment of nsp(7+8) from three different coronavirus strains (SARS-CoV, HCoV-229E and FCoV) revealed a very divers distribution of cysteines within the three nsp8 analyzed (Figure 44). Interestingly, the cysteines in nsp7 seem to be more conserved and, in relation to its size, nsp7 contains more cysteines. Together, nsp7 and nsp8 form a hexadecameric complex during viral replication that binds RNA. Within this thesis, nsp8 was confirmed to be targeted by S-glutathionylation in all three analyzed strains. HCoV-229E contains only one cysteine (C188) which is also conserved in FCoV, as well as the adjacent amino acids. Therefore, C188 is probably susceptible to S-glutathionylation in both viral strains. To find out which of the other cysteines can be modified, cysteine-to-alanine mutants could be produced and analyzed. Indeed, this would only require two different mutants for SARS-CoV and FCoV, respectively, but was not performed due to the focus on nsp9. Upon incubations with > 5 mM GSSG, the protein stability decreased and no signal for S-glutathionylation was detected. Furthermore, nsp8 is highly dependent on reducing agents within the assay. Both observations suggest that the protein's activity and perhaps also its three-dimensional structure is very sensitive to oxidative stress. Due to its various functions and interactions with other nsps, like nsp12, nsp8 occupies a central role during the replication of coronaviruses (Arya et al., 2021; Imbert et al., 2006; te Velthuis et al., 2012; Zhai et al., 2005). These functions must be protected somehow, possibly through the formation of the hexadecameric complex with nsp7 that could protect nsp8 either via the oligomerization itself or via the additional cysteines provided by nsp7 from oxidative and nitrosative stress.

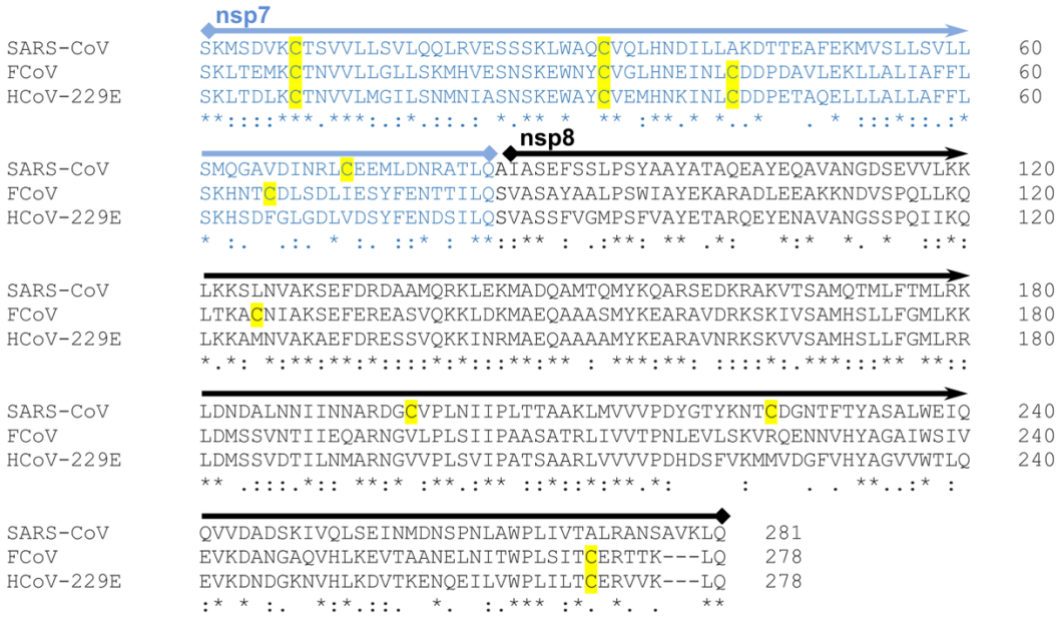

Figure 44 - Sequence alignment of SARS-CoV, FCoV and HCoV-229E nsp(7+8).
Nsp7 is shown in blue, nsp8 in black. Cysteines of both nsps are highlighted in yellow and seem to be more conserved in nsp7. The alignment was performed with Clustal Omega.

5.3.3 S-glutathionylation of nsp9

As stated previously, not all proteins respond to incubation with GSSG by getting S-glutathionylated. Indeed, HCoV-229E seems to be not susceptible for the modification. It contains only one cysteine (C69) that was reported to be part of the homodimeric interface. Interestingly, this wild type dimerization is contrary to the dimeric fold of SARS-CoV or SARS-CoV-2 nsp9, as shown in Figure 45 A (Littler et al., 2020; Sutton et al., 2004). For SARS-CoV nsp9 it was shown that dimerization is essential for the viral replication and growth (Miknis et al., 2009). Upon mutation of this C69 to alanine, the dimerization of HCoV-229E resembles the one observed for SARS-CoV (Figure 45 B). In contrast to these findings, the authors could not identify significant differences among SARS-CoV nsp9 and a mutant without the corresponding cysteine (C73). They suppose both dimers to be biologically relevant and the disulfide-linked dimer to be a protective mechanism for increased oxidative stress levels occurring in the host cells during viral infection (Ponnusamy et al., 2008).

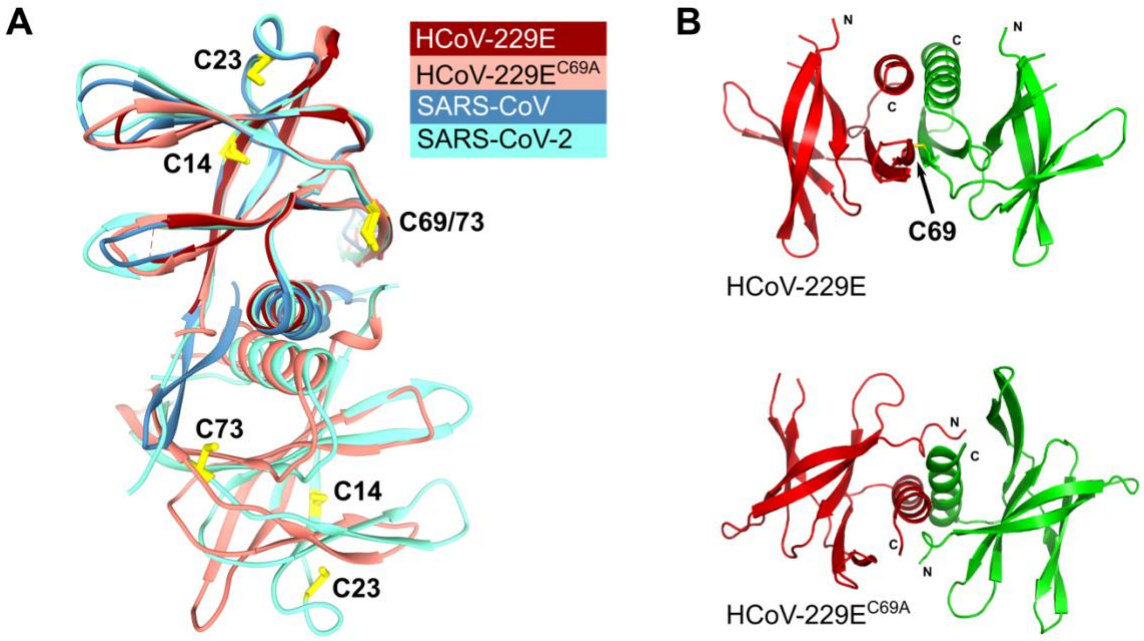

Figure 45 - Structural comparison of HCoV-229E, HCoV-229E^{C69A}, SARS-CoV and SARS-CoV-2 nsp9.
(A) Superimposition of different nsp9 shows the distribution of cysteines. HCoV-229E contains only one cysteine (C69). A C→A mutant of HCoV-229E nsp9 reveals a dimeric organization like observed for SARS-CoV(-2). PDB IDs are: HCoV-229E (2J97); HCoV-229E^{C69A} (2J98); SARS-CoV (1UW7); SARS-CoV-2 (6WXD). **(B)** Comparison of dimeric HCoV-229E wild type and its cysteine-deficient mutant dimerization. Adapted from Ponnusamy et al. 2008.

In the context of the present thesis, this form of dimerization via the disulfide bridge could explain why no S-glutathionylation was detected for nsp9 of HCoV-229E. PEDV nsp9 was also found to form disulfide-linked dimers, however, the location of the cysteine required for dimerization is not conserved. Thus, the dimer adopts a different conformation. The PEDV nsp9 C59A mutant exists as a monomer in solution and the mutation did only marginally affect the nucleic acid binding ability (Zeng et al., 2018). In contrast to that, the dimer of avian

infectious bronchitis virus nsp9 resembles the dimeric fold of SARS-CoV nsp9. Its dimeric interface is formed by hydrophobic interactions among two parallel α-helices. Mutations of single amino acids that disrupt the dimeric form of nsp9 also impaired the ability to bind nucleic acids. Although nsp9 is highly important for replication of coronaviruses, it is not strictly conserved (Hu et al., 2017).

It was shown in this thesis that purification of SARS-CoV nsp9 with and without DTT resulted in a different monomer:dimer ratio. Purification without DTT seems to promote a higher amount of dimeric protein, which could potentially be induced by the rather pro-oxidative environment. The SEC samples that were analyzed via SDS-PAGE revealed many additional bands for the non-reduced nsp9. Usually, the presence of DTT prevents from disulfide formation and can therefore either impair or improve protein folding (Cleland, 1964).

To assess which of the three cysteines of SARS-CoV nsp9 are targeted by S-glutathionylation, cysteine-to-alanine mutants were produced and subsequently S-glutathionylated. All mutants could be easily expressed and purified, suggesting robust proteins without any significant differences concerning stability compared to the wild type protein. Furthermore, no significant change in monomer:dimer ratios compared to the wild type could be observed. Differences in curve shapes are most probably due to different amounts of protein applied to the SEC column. Anti-glutathione Western blot analysis showed the least intense signals for mutant C14/23A, suggesting that cysteine C73 is less sensitive for S-glutathionylation than C14 and C23. The adjacent regions are highly conserved among SARS-CoV and HCoV-229E, further confirming no or at least only minimal susceptibility of the corresponding C69 in HCoV-229E.

The NMPylation assay did not show any alterations when performed with either S-glutathionylated wild type nsp9 or one of the four nsp9 mutants with and without S-glutathionylation. Consequently, the absence or modification of cysteines does not affect the transfer efficiency and cysteines are unlikely to be involved in the underlying mechanism. This result is not totally surprising, since NMPylation is selectively occurring at the first N-terminal asparagine, simultaneously being the very first amino acid of nsp9 (Slanina et al., 2021; Wang et al., 2021). The distances between the Cα-atoms of N1 and C14, C23, and C73, respectively, are 36.1 Å, 42.5 Å, and 34.9 Å (Figure 46). Thus, even the addition of a glutathione to one of those cysteines does probably not cause any (structural) alterations that impair the NMPylation. However, the mutation of the cysteines might have had an impact on the three-dimensional structure that is not linked to its NMPylation. To further elucidate possible alterations caused by the mutations, confirm S-glutathionylation sites, and to possibly crystallize NMPylated nsp9, protein crystallization was performed. Interestingly, the obtained crystals had different sizes, depending on the concentration of GSSG used. While the addition of 5 mM GSSG resemble the ones obtained without GSSG but with DTT, 50 mM promoted the growth of remarkably smaller and yielded less crystals. This could indicate that

S-glutathionylation disturbs the crystallization process, leading to crystals of smaller size and number.

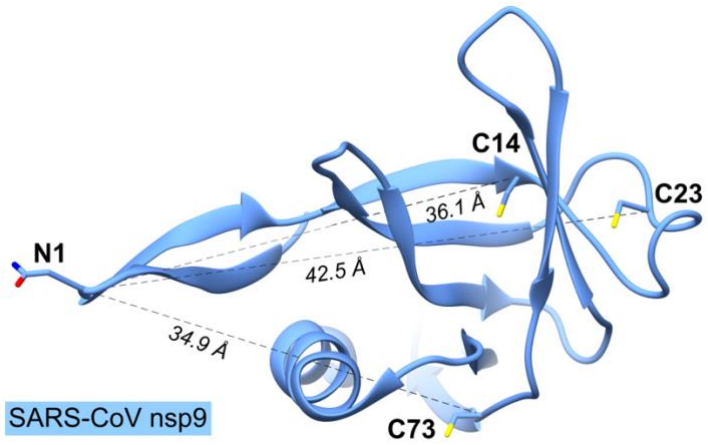

Figure 46 - Distances between the NMPylation target N1 and the three cysteines of SARS-CoV nsp9. Distances were measured between the Cα-atoms of the respective amino acids, using UCSF Chimera. Sulfor atoms are highlighted in yellow.

In general, the herein characterized SARS-CoV nsp5, nsp8 and nsp9 contain more cysteines compared to the other viral strains (Figure 47). Among the nsps that were analyzed, nsp5 seems to have the highest cysteine content. Since it is the most central protein during the expression and required for the release of the other proteins from the large polyprotein, it seems to be reasonable that it is well equipped with cysteines to react to oxidative and nitrosative stress. It was shown that there is a positive correlation between the complexity of organisms and their cysteine content, suggesting cysteines to have been augmented during evolutionary processes. Those processes are further hypothesized to have located cysteines in a way their physiochemical properties could be advantageous for the organism. The cysteine content of mammalian proteins is 2.26% on average, while bacterial proteins contain a significantly lower number of cysteines (Miseta and Csutora, 2000; Wiedemann et al., 2020). However, when predicting cysteine contents of proteins with regard to the number of triplets coding for cysteines, average proteins should contain 3.3% cysteines (Fahey et al., 1977). Consistent with the paucity of data about effects of oxPTMs on viral proteins, there has nothing been reported about cysteine contents of viral proteins. Usually in proteins, cysteines may occur as sulfhydryls or form disulfides. The latter ones are not only important for proper protein folding, but can also increase the thermal stability of proteins that are exposed to high levels of oxidative or nitrosative stress (Bhopatkar et al., 2020). The intracellular formation of disulfides is mediated by thioredoxins or protein disulfide isomerases (Wiedemann et al., 2020).

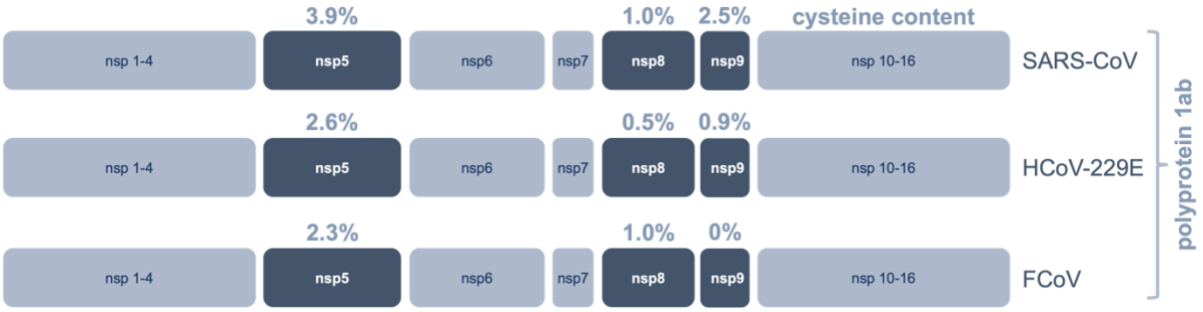

Figure 47 - Cysteine content of nsp5, nsp8 and nsp9.
Schematic representation of the polyprotein from SARS-CoV, HCoV-229E and FCoV. The cysteine content is specified in percent above the respective protein.

5.4 *Excursus:* S-glutathionylation of human spectrin

Spectrin is the most abundant cytoskeletal protein of RBCs. Therefore, the flexibility and elasticity of RBCs is highly dependent on the structural integrity of spectrin. It is known that upon the occurrence of oxPTMs, this structural integrity can be disabled and can, in consequence, lead to various pathologies (Barbarino et al., 2021). While many studies confirmed spectrin to be S-nitros(yl)ated and present data about the influence of NO, there are only a few studies proposing S-glutathionylation and the effects on proteins of the RBC cytoskeleton. Rossi et al., for example, induced S-glutathionylation of human RBCs with the thiol-oxidizing agent diamide. They could show a disruption of the GSH:GSSG ratio and S-glutathionylation of RBC cytoskeletal proteins upon the exposure with diamide. Moreover, their data suggests S-glutathionylation affects RBC membrane stability and the susceptibility of RBCs to hemolysis (Rossi et al., 2006). These findings were confirmed by another study that used *t*-BOOH to induce S-glutathionylation in human RBCs (Giustarini et al., 2019). The authors claim that RBC cytoskeletal proteins are highly susceptible towards S-glutathionylation, providing another reliable biomarker for oxidative stress in addition to the commonly measured GSH:GSSG ratio. In the present thesis, S-glutathionylation of purified spectrin induced by incubations with GSSG could be shown for the first time. To achieve a more biologically relevant confirmation of this data, RBC ghosts were prepared and S-glutathionylated in the same manner with comparable results. To get first insights into possible effects on amino acid level, samples were sent to mass spectrometry analysis, revealing that some cysteines might be more susceptible to modifications than others, though no specific modification pattern could be determined so far. These findings should be substantiated with further experimental approaches, including structural analysis or modeling approaches, ektacytometry, which determines the deformability of RBCs, or viscosimetry of blood samples. Besides S-glutathionylation, also S-nitrosation was confirmed to target spectrin and other RBC cytoskeletal proteins, though without pathological consequences for the RBC deformability (Diederich et al., 2018). It was even shown that increased S-nitrosation is

accompanied with increased RBC deformability, which potentially provides novel therapeutic approaches.

Among other pathologies, hemoglobinopathies are related to RBC membrane fragility, which can lead to loss of RBC integrity and increased hemolysis. Interestingly, these often hereditary conditions can prevent severe disease during malaria infections (Grau et al., 2013). During its complex life cycle, the parasite *Plasmodium* is exposed to very high levels of oxidative and nitrosative stress. Especially during its replication in the RBCs, the human hemoglobin promotes an extremely pro-oxidant environment. While for proteins from trophozoite stage parasites the occurrence of oxPTMs were already shown via proteomic approaches, no data is available for modifications of human RBC proteins during the infection. Therefore, infected cell culture samples were analyzed via α-glutathione Western blot analysis. In contrast to previous experiments, whole blood samples were used for analysis, including many additional proteins that are present within the erythrocyte. Although spectrin could be identified via Ponceau staining, no signal for its S-glutathionylation could be detected. This could be either due to very low levels of S-glutathionylation of spectrin upon infection or due to interference with other RBC proteins that were present in higher concentrations and therefore interfere with the lower concentration of spectrin. For further experiments, one could consider increasing S-glutathionylation by adding GSSG to the cell culture. Another approach may be to tag S-glutathionylated proteins via crosslinking chemistry and identify them with mass spectrometry analysis, as described before (Kehr et al., 2011). This could also confirm specific cysteines to be modified in cell culture.

As already assumed in the review article related to this project, disruptions of the intracellular redox balance could ‘intentionally’ label RBCs via oxPTMs of RBC cytoskeletal proteins. By decreasing their deformability and leading to eryptosis, oxPTMs may provide a “naturally occurring protective mechanism” against malaria (Barbarino et al., 2021; Cyrklaff et al., 2016; Gupta et al., 1982; Pantaleo et al., 2017).

REFERENCES

Adams, P.D., Afonine, P.V., Bunkóczi, G., Chen, V.B., Davis, I.W., Echols, N., Headd, J.J., Hung, L.-W., Kapral, G.J., Grosse-Kunstleve, R.W., McCoy, A.J., Moriarty, N.W., Oeffner, R., Read, R.J., Richardson, D.C., Richardson, J.S., Terwilliger, T.C., Zwart, P.H., 2010. PHENIX: a comprehensive Python-based system for macromolecular structure solution. Acta Crystallogr D Biol Crystallogr 66, 213–221. https://doi.org/10.1107/S0907444909052925

Alam, A., Neyaz, M.K., Ikramul Hasan, S., 2014. Exploiting unique structural and functional properties of malarial glycolytic enzymes for antimalarial drug development. Malar Res Treat. https://doi.org/10.1155/2014/451065

Alderton, W.K., Cooper, C.E., Knowles, R.G., 2001. Nitric oxide synthases: structure, function and inhibition. Biochem J 357, 593–615. https://doi.org/10.1042/0264-6021:3570593

Aleshin, A.E., Kirby, C., Liu, X., Bourenkov, G.P., Bartunik, H.D., Fromm, H.J., Honzatko, R.B., 2000. Crystal structures of mutant monomeric hexokinase I reveal multiple ADP binding sites and conformational changes relevant to allosteric regulation. J Mol Biol 296, 1001–1015. https://doi.org/10.1006/jmbi.1999.3494

Aleshin, A.E., Zeng, C., Bartunik, H.D., Fromm, H.J., Honzatko, R.B., 1998. Regulation of hexokinase I: crystal structure of recombinant human brain hexokinase complexed with glucose and phosphate. J Mol Biol 282, 345–357. https://doi.org/10.1006/jmbi.1998.2017

Alfonso-Prieto, M., Biarnés, X., Vidossich, P., Rovira, C., 2009. The molecular mechanism of the catalase reaction. J Am Chem Soc 131, 11751–11761. https://doi.org/10.1021/ja9018572

Anand, K., Ziebuhr, J., Wadhwani, P., Mesters, J.R., Hilgenfeld, R., 2003. Coronavirus main proteinase (3CLpro) structure: basis for design of anti-SARS drugs. Science 300, 1763–1767. https://doi.org/10.1126/science.1085658

Anand, P., Stamler, J.S., 2012. Enzymatic mechanisms regulating protein S-nitrosylation: implications in health and disease. J Mol Med (Berl) 90, 233–244. https://doi.org/10.1007/s00109-012-0878-z

Anastasiou, D., Poulogiannis, G., Asara, J.M., Boxer, M.B., Jiang, J., Shen, M., Bellinger, G., Sasaki, A.T., Locasale, J.W., Auld, D.S., Thomas, C.J., Vander Heiden, M.G., Cantley, L.C., 2011. Inhibition of pyruvate kinase M2 by reactive oxygen species contributes to cellular antioxidant responses. Science 334, 1278–1283. https://doi.org/10.1126/science.1211485

Arya, R., Kumari, S., Pandey, B., Mistry, H., Bihani, S.C., Das, A., Prashar, V., Gupta, G.D., Panicker, L., Kumar, M., 2021. Structural insights into SARS-CoV-2 proteins. J Mol Biol 433, 166725. https://doi.org/10.1016/j.jmb.2020.11.024

Banerjee, R., Perera, L., Tillekeratne, L.M.V., 2021. Potential SARS-CoV-2 main protease inhibitors. Drug Discov Today 26, 804–816. https://doi.org/10.1016/j.drudis.2020.12.005

Barbarino, F., Wäschenbach, L., Cavalho-Lemos, V., Dillenberger, M., Becker, K., Gohlke, H., Cortese-Krott, M.M., 2021. Targeting spectrin redox switches to regulate the mechanoproperties of red blood cells. Biol Chem 402, 317–331. https://doi.org/10.1515/hsz-2020-0293

Barnett, S.D., Buxton, I.L.O., 2017. The role of S-nitrosoglutathione reductase (GSNOR) in human disease and therapy. Crit Rev Biochem Mol Biol 52, 340–354. https://doi.org/10.1080/10409238.2017.1304353

Becker, K., Tilley, L., Vennerstrom, J.L., Roberts, D., Rogerson, S., Ginsburg, H., 2004. Oxidative stress in malaria parasite-infected erythrocytes: host-parasite interactions. Int J Parasitol 34, 163–189. https://doi.org/10.1016/j.ijpara.2003.09.011

Beeson, J.G., Brown, G.V., 2002. Pathogenesis of Plasmodium falciparum malaria: the roles of parasite adhesion and antigenic variation. CMLS, Cell. Mol. Life Sci. 59, 258–271. https://doi.org/10.1007/s00018-002-8421-y

Benhar, M., Forrester, M.T., Stamler, J.S., 2009. Protein denitrosylation: enzymatic mechanisms and cellular functions. Nat Rev Mol Cell Biol 10, 721–732. https://doi.org/10.1038/nrm2764

Bennett, W.S., Steitz, T.A., 1978. Glucose-induced conformational change in yeast hexokinase. Proc Natl Acad Sci U S A 75, 4848–4852. https://doi.org/10.1073/pnas.75.10.4848

Bhopatkar, A.A., Uversky, V.N., Rangachari, V., 2020. Disorder and cysteines in proteins: A design for orchestration of conformational see-saw and modulatory functions. Prog Mol Biol Transl Sci 174, 331–373. https://doi.org/10.1016/bs.pmbts.2020.06.001

Bjerrum, P.J., 1979. Hemoglobin-depleted human erythrocyte ghosts: characterization of morphology and transport functions. J Membr Biol 48, 43–67. https://doi.org/10.1007/BF01869256

Brandstaedter, C., Delahunty, C., Schipper, S., Rahlfs, S., Yates, J.R., Becker, K., 2019. The interactome of 2-Cys peroxiredoxins in Plasmodium falciparum. Sci Rep 9, 13542. https://doi.org/10.1038/s41598-019-49841-3

Brigelius-Flohé, R., Flohé, L., 2020. Regulatory phenomena in the glutathione peroxidase superfamily. Antioxid Redox Signal 33, 498–516. https://doi.org/10.1089/ars.2019.7905

Broniowska, K.A., Diers, A.R., Hogg, N., 2013. S-NITROSOGLUTATHIONE. Biochim Biophys Acta 1830, 3173–3181. https://doi.org/10.1016/j.bbagen.2013.02.004

Chamberlain, N., Korwin-Mihavics, B.R., Nakada, E.M., Bruno, S.R., Heppner, D.E., Chapman, D.G., Hoffman, S.M., van der Vliet, A., Suratt, B.T., Dienz, O., Alcorn, J.F., Anathy, V., 2019. Lung epithelial protein disulfide isomerase A3 (PDIA3) plays an important role in influenza infection, inflammation, and airway mechanics. Redox Biol 22, 101129. https://doi.org/10.1016/j.redox.2019.101129

Chan, M., Sim, T.-S., 2005. Functional analysis, overexpression, and kinetic characterization of pyruvate kinase from Plasmodium falciparum. Biochem Biophys Res Commun 326, 188–196. https://doi.org/10.1016/j.bbrc.2004.11.018

Chan, M., Tan, D.S.H., Sim, T.S., 2007. Plasmodium falciparum pyruvate kinase as a novel target for antimalarial drug-screening. Travel Med Infect Dis 5, 125–131. https://doi.org/10.1016/j.tmaid.2006.01.015

Checconi, P., De Angelis, M., Marcocci, M.E., Fraternale, A., Magnani, M., Palamara, A.T., Nencioni, L., 2020. Redox-modulating agents in the treatment of viral infections. Int J Mol Sci 21, 4084. https://doi.org/10.3390/ijms21114084

Checconi, P., Limongi, D., Baldelli, S., Ciriolo, M.R., Nencioni, L., Palamara, A.T., 2019. Role of glutathionylation in infection and inflammation. Nutrients 11, 1952. https://doi.org/10.3390/nu11081952

Chen, I., Clarke, S.E., Gosling, R., Hamainza, B., Killeen, G., Magill, A., O'Meara, W., Price, R.N., Riley, E.M., 2016. "Asymptomatic" malaria: a chronic and debilitating infection that should be treated. PLoS Med 13, e1001942. https://doi.org/10.1371/journal.pmed.1001942

Christofk, H.R., Vander Heiden, M.G., Wu, N., Asara, J.M., Cantley, L.C., 2008. Pyruvate kinase M2 is a phosphotyrosine-binding protein. Nature 452, 181–186. https://doi.org/10.1038/nature06667

Chung, H.S., Wang, S.-B., Venkatraman, V., Murray, C.I., Van Eyk, J.E., 2013. Cysteine oxidative post-translational modifications: emerging regulation in the cardiovascular system. Circ Res 112, 382–392. https://doi.org/10.1161/CIRCRESAHA.112.268680

Clayton, A.M., Dong, Y., Dimopoulos, G., 2014. The Anopheles Innate Immune System in the Defense against Malaria Infection. J Innate Immun 6, 169–181. https://doi.org/10.1159/000353602

Cleland, W.W., 1964. Dithiothreitol, a new protective reagent for SH groups. Biochemistry 3, 480–482. https://doi.org/10.1021/bi00892a002

Colowick, S.P., 1973. The hexokinases, in: Boyer, P.D. (Ed.), The Enzymes. Academic Press, pp. 1–48. https://doi.org/10.1016/S1874-6047(08)60113-4

Cornillez-Ty, C.T., Liao, L., Yates, J.R., Kuhn, P., Buchmeier, M.J., 2009. Severe acute respiratory syndrome coronavirus nonstructural protein 2 interacts with a host protein complex involved in mitochondrial biogenesis and intracellular signaling. J Virol 83, 10314–10318. https://doi.org/10.1128/JVI.00842-09

Cowman, A.F., Healer, J., Marapana, D., Marsh, K., 2016. Malaria: biology and disease. Cell 167, 610–624. https://doi.org/10.1016/j.cell.2016.07.055

Cui, J., Li, F., Shi, Z.-L., 2019. Origin and evolution of pathogenic coronaviruses. Nat Rev Microbiol 17, 181–192. https://doi.org/10.1038/s41579-018-0118-9

Cunha, C.B., Opal, S.M., 2014. Middle East respiratory syndrome (MERS): a new zoonotic viral pneumonia. Virulence 5, 650–654. https://doi.org/10.4161/viru.32077

Cyrklaff, M., Srismith, S., Nyboer, B., Burda, K., Hoffmann, A., Lasitschka, F., Adjalley, S., Bisseye, C., Simpore, J., Mueller, A.-K., Sanchez, C.P., Frischknecht, F., Lanzer, M., 2016. Oxidative insult can induce malaria-protective trait of sickle and fetal erythrocytes. Nat Commun 7, 13401. https://doi.org/10.1038/ncomms13401

Dalle-Donne, I., Rossi, R., Giustarini, D., Colombo, R., Milzani, A., 2007. S-glutathionylation in protein redox regulation. Free Radic Biol Med 43, 883–898. https://doi.org/10.1016/j.freeradbiomed.2007.06.014

Davis, D.A., Bulut, H., Shrestha, P., Yaparla, A., Jaeger, H.K., Hattori, S.-I., Wingfield, P.T., Mieyal, J.J., Mitsuya, H., Yarchoan, R., 2021. Regulation of the dimerization and activity of SARS-CoV-2 main protease through reversible glutathionylation of cysteine 300. mBio 12, e0209421. https://doi.org/10.1128/mBio.02094-21

Davis, M.I., Patrick, S.L., Blanding, W.M., Dwivedi, V., Suryadi, J., Golden, J.E., Coussens, N.P., Lee, O.W., Shen, M., Boxer, M.B., Hall, M.D., Sharlow, E.R., Drew, M.E., Morris, J.C., 2016. Identification of novel Plasmodium falciparum hexokinase inhibitors with antiparasitic activity. Antimicrob Agents Chemother 60, 6023–6033. https://doi.org/10.1128/AAC.00914-16

Dayanand, K.K., Achur, R.N., Gowda, D.C., 2018. Epidemiology, drug resistance, and pathophysiology of Plasmodium vivax malaria. J Vector Borne Dis 55, 1–8. https://doi.org/10.4103/0972-9062.234620

de Haan, C.A.M., Rottier, P.J.M., 2005. Molecular interactions in the assembly of coronaviruses. Adv Virus Res 64, 165–230. https://doi.org/10.1016/S0065-3527(05)64006-7

Derakhshan, B., Hao, G., Gross, S.S., 2007. Balancing reactivity against selectivity: The evolution of protein S-nitrosylation as an effector of cell signaling by nitric oxide. Cardiovasc Res 75, 210–219. https://doi.org/10.1016/j.cardiores.2007.04.023

Devarie-Baez, N.O., Zhang, D., Li, S., Whorton, A.R., Xian, M., 2013. Direct methods for detection of protein S-nitrosylation. Methods 62, 171–176. https://doi.org/10.1016/j.ymeth.2013.04.018

Diederich, L., Suvorava, T., Sansone, R., Keller, T.C.S., Barbarino, F., Sutton, T.R., Kramer, C.M., Lückstädt, W., Isakson, B.E., Gohlke, H., Feelisch, M., Kelm, M., Cortese-Krott, M.M., 2018. On the effects of reactive oxygen species and nitric oxide on red blood cell deformability. Front Physiol 9, 332. https://doi.org/10.3389/fphys.2018.00332

Dillenberger, M., 2017. Posttranslational redox-modifications in Plasmodium falciparum pyruvate kinase. Justus Liebig University, Giessen.

Duffy, P.E., 2022. Making a good malaria vaccine better. Trends Parasitol 38, 9–10. https://doi.org/10.1016/j.pt.2021.11.006

Egloff, M.-P., Ferron, F., Campanacci, V., Longhi, S., Rancurel, C., Dutartre, H., Snijder, E.J., Gorbalenya, A.E., Cambillau, C., Canard, B., 2004. The severe acute respiratory syndrome-coronavirus replicative protein nsp9 is a single-stranded RNA-binding subunit unique in the RNA virus world. Proc Natl Acad Sci U S A 101, 3792–3796. https://doi.org/10.1073/pnas.0307877101

Emsley, P., Cowtan, K., 2004. Coot: model-building tools for molecular graphics. Acta Crystallogr D Biol Crystallogr 60, 2126–2132. https://doi.org/10.1107/S0907444904019158

Fahey, R.C., Hunt, J.S., Windham, G.C., 1977. On the cysteine and cystine content of proteins. Differences between intracellular and extracellular proteins. J Mol Evol 10, 155–160. https://doi.org/10.1007/BF01751808

Fang, T.Y., Alechina, O., Aleshin, A.E., Fromm, H.J., Honzatko, R.B., 1998. Identification of a phosphate regulatory site and a low affinity binding site for glucose 6-phosphate in the N-terminal half of human brain hexokinase. J Biol Chem 273, 19548–19553. https://doi.org/10.1074/jbc.273.31.19548

Farley, A.R., Link, A.J., 2009. Identification and quantification of protein posttranslational modifications. Methods Enzymol 463, 725–763. https://doi.org/10.1016/S0076-6879(09)63040-8

Fehr, A.R., Perlman, S., 2015. Coronaviruses: an overview of their replication and pathogenesis. Methods Mol Biol 1282, 1–23. https://doi.org/10.1007/978-1-4939-2438-7_1

Fenouillet, E., Barbouche, R., Jones, I.M., 2007. Cell entry by enveloped viruses: redox considerations for HIV and SARS-coronavirus. Antioxid Redox Signal 9, 1009–1034. https://doi.org/10.1089/ars.2007.1639

Findlay, V.J., Townsend, D.M., Morris, T.E., Fraser, J.P., He, L., Tew, K.D., 2006. A novel role for human sulfiredoxin in the reversal of glutathionylation. Cancer Res 66, 6800–6806. https://doi.org/10.1158/0008-5472.CAN-06-0484

Fisher, G.M., Cobbold, S.A., Jezewski, A., Carpenter, E.F., Arnold, M., Cowell, A.N., Tjhin, E.T., Saliba, K.J., Skinner-Adams, T.S., Lee, M.C.S., Odom John, A., Winzeler, E.A., McConville, M.J., Poulsen, S.-A., Andrews, K.T., 2020. The key glycolytic enzyme phosphofructokinase is involved in resistance to antiplasmodial glycosides. mBio 11, e02842-20. https://doi.org/10.1128/mBio.02842-20

Forrester, M.T., Foster, M.W., Benhar, M., Stamler, J.S., 2009. Detection of protein S-nitrosylation with the biotin switch technique. Free Radic Biol Med 46, 119–126. https://doi.org/10.1016/j.freeradbiomed.2008.09.034

Fritz-Wolf, K., Jortzik, E., Stumpf, M., Preuss, J., Iozef, R., Rahlfs, S., Becker, K., 2013. Crystal structure of the Plasmodium falciparum thioredoxin reductase-thioredoxin complex. J Mol Biol 425, 3446–3460. https://doi.org/10.1016/j.jmb.2013.06.037

Gallagher, T.M., 1996. Murine coronavirus membrane fusion is blocked by modification of thiols buried within the spike protein. J Virol 70, 4683–4690. https://doi.org/10.1128/JVI.70.7.4683-4690.1996

Giustarini, D., Dalle-Donne, I., Milzani, A., Braconi, D., Santucci, A., Rossi, R., 2019. Membrane skeletal protein S-glutathionylation in human red blood cells as index of oxidative stress. Chem Res Toxicol 32, 1096–1102. https://doi.org/10.1021/acs.chemrestox.8b00408

Giustarini, D., Dalle-Donne, I., Milzani, A., Fanti, P., Rossi, R., 2013. Analysis of GSH and GSSG after derivatization with N-ethylmaleimide. Nat Protoc 8, 1660–1669. https://doi.org/10.1038/nprot.2013.095

Goodman, S.R., Johnson, D., Youngentob, S.L., Kakhniashvili, D., 2019. The spectrinome: the interactome of a scaffold protein creating nuclear and cytoplasmic connectivity and function. Exp Biol Med (Maywood) 244, 1273–1302. https://doi.org/10.1177/1535370219867269

Gould, N.S., Evans, P., Martínez-Acedo, P., Marino, S.M., Gladyshev, V.N., Carroll, K.S., Ischiropoulos, H., 2015. Site-specific proteomic mapping identifies selectively modified regulatory cysteine residues in functionally distinct protein networks. Chem Biol 22, 965–975. https://doi.org/10.1016/j.chembiol.2015.06.010

Graham, R.L., Donaldson, E.F., Baric, R.S., 2013. A decade after SARS: strategies for controlling emerging coronaviruses. Nat Rev Microbiol 11, 836–848. https://doi.org/10.1038/nrmicro3143

Grant, M.M., 2021. Pyruvate kinase, inflammation and periodontal disease. Pathogens 10, 784. https://doi.org/10.3390/pathogens10070784

Grau, M., Pauly, S., Ali, J., Walpurgis, K., Thevis, M., Bloch, W., Suhr, F., 2013. RBC-NOS-dependent S-nitrosylation of cytoskeletal proteins improves RBC deformability. PLoS One 8, e56759. https://doi.org/10.1371/journal.pone.0056759

Grek, C.L., Zhang, J., Manevich, Y., Townsend, D.M., Tew, K.D., 2013. Causes and consequences of cysteine S-glutathionylation. J Biol Chem 288, 26497–26504. https://doi.org/10.1074/jbc.R113.461368

Gretes, M.C., Poole, L.B., Karplus, P.A., 2012. Peroxiredoxins in parasites. Antioxid Redox Signal 17, 608–633. https://doi.org/10.1089/ars.2011.4404

Groitl, B., Jakob, U., 2014. Thiol-based redox switches. Biochim Biophys Acta 1844, 1335–1343. https://doi.org/10.1016/j.bbapap.2014.03.007

Guha, M., Kumar, S., Choubey, V., Maity, P., Bandyopadhyay, U., 2006. Apoptosis in liver during malaria: role of oxidative stress and implication of mitochondrial pathway. FASEB J 20, 1224–1226. https://doi.org/10.1096/fj.05-5338fje

Guloyan, V., Oganesian, B., Baghdasaryan, N., Yeh, C., Singh, M., Guilford, F., Ting, Y.-S., Venketaraman, V., 2020. Glutathione supplementation as an adjunctive therapy in COVID-19. Antioxidants (Basel) 9, 914. https://doi.org/10.3390/antiox9100914

Gupta, C.M., Alam, A., Mathur, P.N., Dutta, G.P., 1982. A new look at nonparasitized red cells of malaria-infected monkeys. Nature 299, 259–261. https://doi.org/10.1038/299259a0

Haeussler, K., Berneburg, I., Jortzik, E., Hahn, J., Rahbari, M., Schulz, N., Preuss, J., Zapol'skii, V.A., Bode, L., Pinkerton, A.B., Kaufmann, D.E., Rahlfs, S., Becker, K., 2019. Glucose 6-phosphate dehydrogenase 6-phosphogluconolactonase: characterization of the Plasmodium vivax enzyme and inhibitor studies. Malar J 18, 22. https://doi.org/10.1186/s12936-019-2651-z

Haldar, K., Bhattacharjee, S., Safeukui, I., 2018. Drug resistance in Plasmodium. Nat Rev Microbiol 16, 156–170. https://doi.org/10.1038/nrmicro.2017.161

Hall, C.N., Garthwaite, J., 2009. What is the real physiological NO concentration in vivo? Nitric Oxide 21, 91–103. https://doi.org/10.1016/j.niox.2009.07.002

Hamre, D., Procknow, J.J., 1966. A new virus isolated from the human respiratory tract. Proc Soc Exp Biol Med 121, 190–193. https://doi.org/10.3181/00379727-121-30734

Harris, M.T., Walker, D.M., Drew, M.E., Mitchell, W.G., Dao, K., Schroeder, C.E., Flaherty, D.P., Weiner, W.S., Golden, J.E., Morris, J.C., 2013. Interrogating a hexokinase-selected small-molecule library for inhibitors of Plasmodium falciparum hexokinase. Antimicrob Agents Chemother 57, 3731–3737. https://doi.org/10.1128/AAC.00662-13

Hartenian, E., Nandakumar, D., Lari, A., Ly, M., Tucker, J.M., Glaunsinger, B.A., 2020. The molecular virology of coronaviruses. J Biol Chem 295, 12910–12934. https://doi.org/10.1074/jbc.REV120.013930

Hashimoto, M., Wilson, J.E., 2002. Kinetic and regulatory properties of HK I(+), a modified form of the type I isozyme of mammalian hexokinase in which interactions between the N- and C-terminal halves have been disrupted. Arch Biochem Biophys 399, 109–115. https://doi.org/10.1006/abbi.2001.2744

Hawkins, C.L., Davies, M.J., 2019. Detection, identification, and quantification of oxidative protein modifications. J Biol Chem 294, 19683–19708. https://doi.org/10.1074/jbc.REV119.006217

He, C., Chen, J., Wang, H., Wan, Y., Zhou, J., Dan, Z., Zeng, Y., Xu, W., Zhu, Y., Huang, W., Yin, L., 2019. Crystal structures of rice hexokinase 6 with a series of substrates shed light on its enzymatic mechanism. Biochem Biophys Res Commun 515, 614–620. https://doi.org/10.1016/j.bbrc.2019.05.139

Heinrich, T.A., da Silva, R.S., Miranda, K.M., Switzer, C.H., Wink, D.A., Fukuto, J.M., 2013. Biological nitric oxide signalling: chemistry and terminology. Br J Pharmacol 169, 1417–1429. https://doi.org/10.1111/bph.12217

Heneberg, P., 2019. Redox regulation of hexokinases. Antioxid Redox Signal 30, 415–442. https://doi.org/10.1089/ars.2017.7255

Hess, D.T., Matsumoto, A., Kim, S.-O., Marshall, H.E., Stamler, J.S., 2005. Protein S-nitrosylation: purview and parameters. Nat Rev Mol Cell Biol 6, 150–166. https://doi.org/10.1038/nrm1569

Hess, D.T., Stamler, J.S., 2012. Regulation by S-nitrosylation of protein post-translational modification. J Biol Chem 287, 4411–4418. https://doi.org/10.1074/jbc.R111.285742

Hiller, N., Fritz-Wolf, K., Deponte, M., Wende, W., Zimmermann, H., Becker, K., 2006. Plasmodium falciparum glutathione S-transferase—Structural and mechanistic studies on ligand binding and enzyme inhibition. Protein Sci 15, 281–289. https://doi.org/10.1110/ps.051891106

Hoggett, J.G., Kellett, G.L., 1992. Kinetics of the monomer-dimer reaction of yeast hexokinase PI. Biochem J 287 (Pt 2), 567–572. https://doi.org/10.1042/bj2870567

Hu, T., Chen, C., Li, H., Dou, Y., Zhou, M., Lu, D., Zong, Q., Li, Y., Yang, C., Zhong, Z., Singh, N., Hu, H., Zhang, R., Yang, H., Su, D., 2017. Structural basis for dimerization and RNA binding of avian infectious bronchitis virus nsp9. Protein Sci 26, 1037–1048. https://doi.org/10.1002/pro.3150

Hundt, J., Li, Z., Liu, Q., 2013. Post-translational modifications of hepatitis C viral proteins and their biological significance. World J Gastroenterol 19, 8929–8939. https://doi.org/10.3748/wjg.v19.i47.8929

Hurley, J.H., 1996. The sugar kinase/heat shock protein 70/actin superfamily: implications of conserved structure for mechanism. Annu Rev Biophys Biomol Struct 25, 137–162. https://doi.org/10.1146/annurev.bb.25.060196.001033

Imbert, I., Guillemot, J.-C., Bourhis, J.-M., Bussetta, C., Coutard, B., Egloff, M.-P., Ferron, F., Gorbalenya, A.E., Canard, B., 2006. A second, non-canonical RNA-dependent RNA polymerase in SARS coronavirus. EMBO J 25, 4933–4942. https://doi.org/10.1038/sj.emboj.7601368

Irokawa, H., Numasaki, S., Kato, S., Iwai, K., Inose-Maruyama, A., Ohdate, T., Hwang, G.-W., Toyama, T., Watanabe, T., Kuge, S., 2021. Comprehensive analyses of the cysteine thiol oxidation of PKM2 reveal the effects of multiple oxidation on cellular oxidative stress response. Biochem J 478, 1453–1470. https://doi.org/10.1042/BCJ20200897

Israelsen, W.J., Vander Heiden, M.G., 2015. Pyruvate kinase: Function, regulation and role in cancer. Seminars in Cell & Developmental Biology 43, 43–51. https://doi.org/10.1016/j.semcdb.2015.08.004

Ivanov, K.A., Ziebuhr, J., 2004. Human coronavirus 229E nonstructural protein 13: characterization of duplex-unwinding, nucleoside triphosphatase, and RNA 5'-triphosphatase activities. J Virol 78, 7833–7838. https://doi.org/10.1128/JVI.78.14.7833-7838.2004

Jedelská, T., Luhová, L., Petřivalský, M., 2020. Thioredoxins: Emerging players in the regulation of protein S-nitrosation in plants. Plants (Basel) 9, 1426. https://doi.org/10.3390/plants9111426

Jortzik, E., Becker, K., 2012. Thioredoxin and glutathione systems in Plasmodium falciparum. Int J Med Microbiol 302, 187–194. https://doi.org/10.1016/j.ijmm.2012.07.007

Jortzik, E., Wang, L., Becker, K., 2012. Thiol-based posttranslational modifications in parasites. Antioxid Redox Signal 17, 657–673. https://doi.org/10.1089/ars.2011.4266

Jurica, M.S., Mesecar, A., Heath, P.J., Shi, W., Nowak, T., Stoddard, B.L., 1998. The allosteric regulation of pyruvate kinase by fructose-1,6-bisphosphate. Structure 6, 195–210. https://doi.org/10.1016/S0969-2126(98)00021-5

Kabsch, W., 2010. XDS. Acta Crystallogr D Biol Crystallogr 66, 125–132. https://doi.org/10.1107/S0907444909047337

Kalinina, E., Novichkova, M., 2021. Glutathione in protein redox modulation through S-glutathionylation and S-nitrosylation. Molecules 26, E435. https://doi.org/10.3390/molecules26020435

Kalinina, E.V., Chernov, N.N., Novichkova, M.D., 2014. Role of glutathione, glutathione transferase, and glutaredoxin in regulation of redox-dependent processes. Biochemistry (Mosc) 79, 1562–1583. https://doi.org/10.1134/S0006297914130082

Kamitani, W., Huang, C., Narayanan, K., Lokugamage, K.G., Makino, S., 2009. A two-pronged strategy to suppress host protein synthesis by SARS coronavirus Nsp1 protein. Nat Struct Mol Biol 16, 1134–1140. https://doi.org/10.1038/nsmb.1680

Kanzok, S.M., Schirmer, R.H., Turbachova, I., Iozef, R., Becker, K., 2000. The thioredoxin system of the malaria parasite Plasmodium falciparum. Glutathione reduction revisited. J Biol Chem 275, 40180–40186. https://doi.org/10.1074/jbc.M007633200

Kavishe, R.A., Koenderink, J.B., Alifrangis, M., 2017. Oxidative stress in malaria and artemisinin combination therapy: Pros and Cons. FEBS J 284, 2579–2591. https://doi.org/10.1111/febs.14097

Kehr, S., Jortzik, E., Delahunty, C., Yates, J.R., Rahlfs, S., Becker, K., 2011. Protein S-glutathionylation in malaria parasites. Antioxid Redox Signal 15, 2855–2865. https://doi.org/10.1089/ars.2011.4029

Kehr, S., Sturm, N., Rahlfs, S., Przyborski, J.M., Becker, K., 2010. Compartmentation of redox metabolism in malaria parasites. PLoS Pathog 6, e1001242. https://doi.org/10.1371/journal.ppat.1001242

Khomich, O.A., Kochetkov, S.N., Bartosch, B., Ivanov, A.V., 2018. Redox biology of respiratory viral infections. Viruses 10, 392. https://doi.org/10.3390/v10080392

Kim, Y., Chang, K.-O., 2018. Protein disulfide isomerases as potential therapeutic targets for influenza A and B viruses. Virus Res 247, 26–33. https://doi.org/10.1016/j.virusres.2018.01.010

Kim, Y., Ho, S.O., Gassman, N.R., Korlann, Y., Landorf, E.V., Collart, F.R., Weiss, S., 2008. Efficient site-specific labeling of proteins via cysteines. Bioconjug Chem 19, 786–791. https://doi.org/10.1021/bc7002499

Kosow, D.P., Oski, F.A., Warms, J.V., Rose, I.A., 1973. Regulation of mammalian hexokinase: regulatory differences between isoenzyme I and II. Arch Biochem Biophys 157, 114–124. https://doi.org/10.1016/0003-9861(73)90396-2

Kosow, D.P., Rose, I.A., 1971. Activators of yeast hexokinase. J Biol Chem 246, 2618–2625.

Kosow, D.P., Rose, I.A., 1970. Product inhibition of the hexokinases. J Biol Chem 245, 198–204.

Kovacs, I., Lindermayr, C., 2013. Nitric oxide-based protein modification: formation and site-specificity of protein S-nitrosylation. Front Plant Sci 4, 137. https://doi.org/10.3389/fpls.2013.00137

Kuettner, E.B., Kettner, K., Keim, A., Svergun, D.I., Volke, D., Singer, D., Hoffmann, R., Müller, E.-C., Otto, A., Kriegel, T.M., Sträter, N., 2010. Crystal structure of hexokinase KlHxk1 of Kluyveromyces lactis: a molecular basis for understanding the control of yeast hexokinase functions via covalent modification and oligomerization. J Biol Chem 285, 41019–41033. https://doi.org/10.1074/jbc.M110.185850

Kuhn, V., Diederich, L., Keller, T.C.S., Kramer, C.M., Lückstädt, W., Panknin, C., Suvorava, T., Isakson, B.E., Kelm, M., Cortese-Krott, M.M., 2017. Red blood cell function and dysfunction: redox regulation, nitric oxide metabolism, anemia. Antioxid Redox Signal 26, 718–742. https://doi.org/10.1089/ars.2016.6954

Kukhanova, M.K., Tunitskaya, V.L., Smirnova, O.A., Khomich, O.A., Zakirova, N.F., Ivanova, O.N., Ziganshin, R., Bartosch, B., Kochetkov, S.N., Ivanov, A.V., 2019. Hepatitis C virus RNA-dependent RNA polymerase is regulated by cysteine S-glutathionylation. Oxid Med Cell Longev 2019, 3196140. https://doi.org/10.1155/2019/3196140

Kuser, P., Cupri, F., Bleicher, L., Polikarpov, I., 2008. Crystal structure of yeast hexokinase PI in complex with glucose: A classical “induced fit” example revised. Proteins 72, 731–740. https://doi.org/10.1002/prot.21956

Lang, Y., Li, W., Li, Z., Koerhuis, D., van den Burg, A.C.S., Rozemuller, E., Bosch, B.-J., van Kuppeveld, F.J.M., Boons, G.-J., Huizinga, E.G., van der Schaar, H.M., de Groot, R.J., 2020. Coronavirus hemagglutinin-esterase and spike proteins coevolve for functional balance and optimal virion avidity. Proc Natl Acad Sci USA 117, 25759–25770. https://doi.org/10.1073/pnas.2006299117

Larsen, T.M., Benning, M.M., Wesenberg, G.E., Rayment, I., Reed, G.H., 1997. Ligand-induced domain movement in pyruvate kinase: Structure of the enzyme from rabbit muscle with Mg2+, K+, and l-phospholactate at 2.7 Å resolution. Arch Biochem Biophys 345, 199–206. https://doi.org/10.1006/abbi.1997.0257

Larsen, T.M., Laughlin, L.T., Holden, H.M., Rayment, I., Reed, G.H., 1994. Structure of rabbit muscle pyruvate kinase complexed with Mn2+, K+, and pyruvate. Biochemistry 33, 6301–6309. https://doi.org/10.1021/bi00186a033

Lehmann, K.C., Gulyaeva, A., Zevenhoven-Dobbe, J.C., Janssen, G.M.C., Ruben, M., Overkleeft, H.S., van Veelen, P.A., Samborskiy, D.V., Kravchenko, A.A., Leontovich, A.M., Sidorov, I.A., Snijder, E.J., Posthuma, C.C., Gorbalenya, A.E., 2015. Discovery of an essential nucleotidylating activity associated with a newly delineated conserved domain in the RNA polymerase-containing protein of all nidoviruses. Nucleic Acids Research 43, 8416–8434. https://doi.org/10.1093/nar/gkv838

Leonard, S.E., Reddie, K.G., Carroll, K.S., 2009. Mining the thiol proteome for sulfenic acid modifications reveals new targets for oxidation in cells. ACS Chem Biol 4, 783–799. https://doi.org/10.1021/cb900105q

Li, C., Debing, Y., Jankevicius, G., Neyts, J., Ahel, I., Coutard, B., Canard, B., 2016. Viral macro domains reverse protein ADP-ribosylation. J Virol 90, 8478–8486. https://doi.org/10.1128/JVI.00705-16

Littler, D.R., Gully, B.S., Colson, R.N., Rossjohn, J., 2020. Crystal Structure of the SARS-CoV-2 Non-structural Protein 9, Nsp9. iScience 23. https://doi.org/10.1016/j.isci.2020.101258

Liu, S., Ammirati, M.J., Song, X., Knafels, J.D., Zhang, J., Greasley, S.E., Pfefferkorn, J.A., Qiu, X., 2012. Insights into mechanism of glucokinase activation: observation of multiple distinct protein conformations. J Biol Chem 287, 13598–13610. https://doi.org/10.1074/jbc.M111.274126

Loy, D.E., Liu, W., Li, Y., Learn, G.H., Plenderleith, L.J., Sundararaman, S.A., Sharp, P.M., Hahn, B.H., 2017. Out of Africa: origins and evolution of the human malaria parasites Plasmodium falciparum and Plasmodium vivax. Int J Parasitol 47, 87–97. https://doi.org/10.1016/j.ijpara.2016.05.008

Maeda, T., Saito, T., Harb, O.S., Roos, D.S., Takeo, S., Suzuki, H., Tsuboi, T., Takeuchi, T., Asai, T., 2009. Pyruvate kinase type-II isozyme in Plasmodium falciparum localizes to the apicoplast. Parasitol Int 58, 101–105. https://doi.org/10.1016/j.parint.2008.10.005

Martínez-Ruiz, A., Lamas, S., 2004. S-nitrosylation: a potential new paradigm in signal transduction. Cardiovasc Res 62, 43–52. https://doi.org/10.1016/j.cardiores.2004.01.013

Masters, P.S., 2006. The molecular biology of coronaviruses. Adv Virus Res 66, 193–292. https://doi.org/10.1016/S0065-3527(06)66005-3

Matsui, R., Ferran, B., Oh, A., Croteau, D., Shao, D., Han, J., Pimentel, D.R., Bachschmid, M.M., 2020. Redox regulation via glutaredoxin-1 and protein S-glutathionylation. Antioxid Redox Signal 32, 677–700. https://doi.org/10.1089/ars.2019.7963

Matte, A., Tari, L.W., Delbaere, L.T., 1998. How do kinases transfer phosphoryl groups? Structure 6, 413–419. https://doi.org/10.1016/s0969-2126(98)00043-4

Mattevi, A., Bolognesi, M., Valentini, G., 1996. The allosteric regulation of pyruvate kinase. FEBS Lett 389, 15–19. https://doi.org/10.1016/0014-5793(96)00462-0

McPherson, A., Cudney, B., 2014. Optimization of crystallization conditions for biological macromolecules. Acta Crystallogr F Struct Biol Commun 70, 1445–1467. https://doi.org/10.1107/S2053230X14019670

Mehta, M., Sonawat, H.M., Sharma, S., 2006. Glycolysis in Plasmodium falciparum results in modulation of host enzyme activities. J Vector Borne Dis 43, 95–103.

Meibalan, E., Marti, M., 2017. Biology of malaria transmission. Cold Spring Harb Perspect Med 7, a025452. https://doi.org/10.1101/cshperspect.a025452

Miknis, Z.J., Donaldson, E.F., Umland, T.C., Rimmer, R.A., Baric, R.S., Schultz, L.W., 2009. Severe acute respiratory syndrome coronavirus nsp9 dimerization is essential for efficient viral growth. J Virol 83, 3007–3018. https://doi.org/10.1128/JVI.01505-08

Miller, S., Ross-Inta, C., Giulivi, C., 2007. Kinetic and proteomic analyses of S-nitrosoglutathione-treated hexokinase A: consequences for cancer energy metabolism. Amino Acids 32, 593–602. https://doi.org/10.1007/s00726-006-0424-9

Miseta, A., Csutora, P., 2000. Relationship between the occurrence of cysteine in proteins and the complexity of organisms. Mol Biol Evol 17, 1232–1239. https://doi.org/10.1093/oxfordjournals.molbev.a026406

Mitchell, A.R., Yuan, M., Morgan, H.P., McNae, I.W., Blackburn, E.A., Le Bihan, T., Homem, R.A., Yu, M., Loake, G.J., Michels, P.A., Wear, M.A., Walkinshaw, M.D., 2018. Redox regulation of pyruvate kinase M2 by cysteine oxidation and S-nitrosation. Biochem J 475, 3275–3291. https://doi.org/10.1042/BCJ20180556

Mitkevich, V.A., Petrushanko, I.Y., Poluektov, Y.M., Burnysheva, K.M., Lakunina, V.A., Anashkina, A.A., Makarov, A.A., 2016. Basal glutathionylation of Na,K-ATPase α-subunit depends on redox status of cells during the enzyme biosynthesis. Oxid Med Cell Longev 2016, 9092328. https://doi.org/10.1155/2016/9092328

Mock, H.-P., Dietz, K.-J., 2016. Redox proteomics for the assessment of redox-related posttranslational regulation in plants. Biochim Biophys Acta 1864, 967–973. https://doi.org/10.1016/j.bbapap.2016.01.005

Mohandas, N., Gallagher, P.G., 2008. Red cell membrane: past, present, and future. Blood 112, 3939–3948. https://doi.org/10.1182/blood-2008-07-161166

Molina-Cruz, A., DeJong, R.J., Charles, B., Gupta, L., Kumar, S., Jaramillo-Gutierrez, G., Barillas-Mury, C., 2008. Reactive oxygen species modulate Anopheles gambiae immunity against bacteria and Plasmodium. J Biol Chem 283, 3217–3223. https://doi.org/10.1074/jbc.M705873200

Mongin, A.A., Dohare, P., Jourd'heuil, D., 2012. Selective vulnerability of synaptic signaling and metabolism to nitrosative stress. Antioxid Redox Signal 17, 992–1012. https://doi.org/10.1089/ars.2012.4559

Mony, B.M., Mehta, M., Jarori, G.K., Sharma, S., 2009. Plant-like phosphofructokinase from Plasmodium falciparum belongs to a novel class of ATP-dependent enzymes. Int J Parasitol 39, 1441–1453. https://doi.org/10.1016/j.ijpara.2009.05.011

Morgan, H.P., McNae, I.W., Nowicki, M.W., Hannaert, V., Michels, P.A.M., Fothergill-Gilmore, L.A., Walkinshaw, M.D., 2010. Allosteric mechanism of pyruvate kinase from Leishmania mexicana uses a rock and lock model. J Biol Chem 285, 12892–12898. https://doi.org/10.1074/jbc.M109.079905

Morgan, H.P., Zhong, W., McNae, I.W., Michels, P.A.M., Fothergill-Gilmore, L.A., Walkinshaw, M.D., 2014. Structures of pyruvate kinases display evolutionarily divergent allosteric strategies. R Soc Open Sci 1, 140120. https://doi.org/10.1098/rsos.140120

Moriarty, N.W., Tronrud, D.E., Adams, P.D., Karplus, P.A., 2016. A new default restraint library for the protein backbone in Phenix: a conformation-dependent geometry goes mainstream. Acta Cryst D 72, 176–179. https://doi.org/10.1107/S2059798315022408

Moxon, C.A., Gibbins, M.P., McGuinness, D., Milner, D.A., Marti, M., 2020. New insights into malaria pathogenesis. Annu Rev Pathol 15, 315–343. https://doi.org/10.1146/annurev-pathmechdis-012419-032640

Mulichak, A.M., Wilson, J.E., Padmanabhan, K., Garavito, R.M., 1998. The structure of mammalian hexokinase-1. Nat Struct Biol 5, 555–560. https://doi.org/10.1038/811

Müller, I., 2017. Guidelines for the successful generation of protein–ligand complex crystals. Acta Cryst D 73, 79–92. https://doi.org/10.1107/S2059798316020271

Müller, S., 2004. Redox and antioxidant systems of the malaria parasite Plasmodium falciparum. Mol Microbiol 53, 1291–1305. https://doi.org/10.1111/j.1365-2958.2004.04257.x

Nakamura, T., Kashima, Y., Mine, S., Oku, T., Uegaki, K., 2012. Characterization and crystal structure of the thermophilic ROK hexokinase from Thermus thermophilus. J Biosci Bioeng 114, 150–154. https://doi.org/10.1016/j.jbiosc.2012.03.018

Narang, D., Lento, C., J Wilson, D., 2020. HDX-MS: An analytical tool to capture protein motion in action. Biomedicines 8, E224. https://doi.org/10.3390/biomedicines8070224

Neuman, B.W., Kiss, G., Kunding, A.H., Bhella, D., Baksh, M.F., Connelly, S., Droese, B., Klaus, J.P., Makino, S., Sawicki, S.G., Siddell, S.G., Stamou, D.G., Wilson, I.A., Kuhn, P., Buchmeier, M.J., 2011. A structural analysis of M protein in coronavirus assembly and morphology. J Struct Biol 174, 11–22. https://doi.org/10.1016/j.jsb.2010.11.021

Ngoubangoye, B., Boundenga, L., Arnathau, C., Mombo, I.M., Durand, P., Tsoumbou, T.-A., Otoro, B.V., Sana, R., Okouga, A.-P., Moukodoum, N., Willaume, E., Herbert, A., Fouchet, D., Rougeron, V., Bâ, C.T., Ollomo, B., Paupy, C., Leroy, E.M., Renaud, F., Pontier, D., Prugnolle, F., 2016. The host specificity of ape malaria parasites can be broken in confined environments. Int J Parasitol 46, 737–744. https://doi.org/10.1016/j.ijpara.2016.06.004

Nickel, C., Rahlfs, S., Deponte, M., Koncarevic, S., Becker, K., 2006. Thioredoxin networks in the malarial parasite Plasmodium falciparum. Antioxid Redox Signal 8, 1227–1239. https://doi.org/10.1089/ars.2006.8.1227

Nishimasu, H., Fushinobu, S., Shoun, H., Wakagi, T., 2007. Crystal structures of an ATP-dependent hexokinase with broad substrate specificity from the hyperthermophilic archaeon Sulfolobus tokodaii. J Biol Chem 282, 9923–9931. https://doi.org/10.1074/jbc.M610678200

Nishimasu, H., Fushinobu, S., Shoun, H., Wakagi, T., 2006. Identification and characterization of an ATP-dependent hexokinase with broad substrate specificity from the hyperthermophilic archaeon Sulfolobus tokodaii. J Bacteriol 188, 2014–2019. https://doi.org/10.1128/JB.188.5.2014-2019.2006

Oria-Hernández, J., Cabrera, N., Pérez-Montfort, R., Ramírez-Silva, L., 2005. Pyruvate kinase revisited: the activating effect of K+. J Biol Chem 280, 37924–37929. https://doi.org/10.1074/jbc.M508490200

Pantaleo, A., Kesely, K.R., Pau, M.C., Tsamesidis, I., Schwarzer, E., Skorokhod, O.A., Chien, H.D., Ponzi, M., Bertuccini, L., Low, P.S., Turrini, F.M., 2017. Syk inhibitors interfere with erythrocyte membrane modification during P falciparum growth and suppress parasite egress. Blood 130, 1031–1040. https://doi.org/10.1182/blood-2016-11-748053

Patzewitz, E.-M., Wong, E.H., Müller, S., 2012. Dissecting the role of glutathione biosynthesis in Plasmodium falciparum. Mol Microbiol 83, 304–318. https://doi.org/10.1111/j.1365-2958.2011.07933.x

Pauling, L., Corey, R.B., 1951. Configurations of polypeptide chains with favored orientations around single bonds: Two new pleated sheets. Proc Natl Acad Sci U S A 37, 729–740. https://doi.org/10.1073/pnas.37.11.729

Pauling, L., Corey, R.B., Branson, H.R., 1951. The structure of proteins; two hydrogen-bonded helical configurations of the polypeptide chain. Proc Natl Acad Sci U S A 37, 205–211. https://doi.org/10.1073/pnas.37.4.205

Peiris, J.S.M., Guan, Y., Yuen, K.Y., 2004. Severe acute respiratory syndrome. Nat Med 10, S88-97. https://doi.org/10.1038/nm1143

Pereira, D.M.S., Carvalho Júnior, A.R., Lacerda, E.M. da C.B., da Silva, L.C.N., Marinho, C.R.F., André, E., Fernandes, E.S., 2020. Oxidative and nitrosative stresses in cerebral malaria: can we target them to avoid a bad prognosis? J Antimicrob Chemother 1363–1373. https://doi.org/10.1093/jac/dkaa032

Pettersen, E.F., Goddard, T.D., Huang, C.C., Couch, G.S., Greenblatt, D.M., Meng, E.C., Ferrin, T.E., 2004. UCSF Chimera - a visualization system for exploratory research and analysis. J Comput Chem 25, 1605–1612. https://doi.org/10.1002/jcc.20084

Phillips, M.A., Burrows, J.N., Manyando, C., van Huijsduijnen, R.H., Van Voorhis, W.C., Wells, T.N.C., 2017. Malaria. Nat Rev Dis Primers 3, 1–24. https://doi.org/10.1038/nrdp.2017.50

Plewes, K., Leopold, S.J., Kingston, H.W.F., Dondorp, A.M., 2019. Malaria: What's new in the management of malaria? Infect Dis Clin North Am 33, 39–60. https://doi.org/10.1016/j.idc.2018.10.002

Polonikov, A., 2020. Endogenous deficiency of glutathione as the most likely cause of serious manifestations and death in COVID-19 patients. ACS Infect Dis 1558–1562. https://doi.org/10.1021/acsinfecdis.0c00288

Ponnusamy, R., Moll, R., Weimar, T., Mesters, J.R., Hilgenfeld, R., 2008. Variable oligomerization modes in coronavirus non-structural protein 9. J Mol Biol 383, 1081–1096. https://doi.org/10.1016/j.jmb.2008.07.071

Prakasam, G., Iqbal, M.A., Bamezai, R.N.K., Mazurek, S., 2018. Posttranslational modifications of pyruvate kinase M2: Tweaks that benefit cancer. Front Oncol 8, 22. https://doi.org/10.3389/fonc.2018.00022

Rahbari, M., Diederich, K., Becker, K., Krauth-Siegel, R.L., Jortzik, E., 2015. Detection of thiol-based redox switch processes in parasites - facts and future. Biol Chem 396, 445–463. https://doi.org/10.1515/hsz-2014-0279

Ravasco, J.M.J.M., Faustino, H., Trindade, A., Gois, P.M.P., 2019. Bioconjugation with maleimides: A useful tool for chemical biology. Chemistry 25, 43–59. https://doi.org/10.1002/chem.201803174

Ren, X., Sengupta, R., Lu, J., Lundberg, J.O., Holmgren, A., 2019. Characterization of mammalian glutaredoxin isoforms as S-denitrosylases. FEBS Letters 593, 1799–1806. https://doi.org/10.1002/1873-3468.13454

Rhee, S.G., Woo, H.A., Kang, D., 2018. The role of peroxiredoxins in the transduction of H2O2 signals. Antioxid Redox Signal 28, 537–557. https://doi.org/10.1089/ars.2017.7167

Rigden, D.J., Phillips, S.E.V., Michels, P.A.M., Fothergill-Gilmore, L.A., 1999. The structure of pyruvate kinase from Leishmania mexicana reveals details of the allosteric transition and unusual effector specificity. J Mol Biol 293, 615–635. https://doi.org/10.1006/jmbi.1999.3170

Rodríguez-Saavedra, C., Morgado-Martínez, L.E., Burgos-Palacios, A., King-Díaz, B., López-Coria, M., Sánchez-Nieto, S., 2021. Moonlighting proteins: The case of the hexokinases. Front Mol Biosci 8. https://doi.org/10.3389/fmolb.2021.701975

Roe, M.K., Junod, N.A., Young, A.R., Beachboard, D.C., Stobart, C.C., 2021. Targeting novel structural and functional features of coronavirus protease nsp5 (3CLpro, Mpro) in the age of COVID-19. J Gen Virol 102, 001558. https://doi.org/10.1099/jgv.0.001558

Romero, J.M., Bizzozero, O.A., 2009. Intracellular glutathione mediates the denitrosylation of protein nitrosothiols in the rat spinal cord. J Neurosci Res 87, 701–709. https://doi.org/10.1002/jnr.21897

Ross, L.S., Fidock, D.A., 2019. Elucidating mechanisms of drug-resistant Plasmodium falciparum. Cell Host Microbe 26, 35–47. https://doi.org/10.1016/j.chom.2019.06.001

Rossi, R., Giustarini, D., Milzani, A., Dalle-Donne, I., 2006. Membrane skeletal protein S-glutathionylation and hemolysis in human red blood cells. Blood Cells Mol Dis 37, 180–187. https://doi.org/10.1016/j.bcmd.2006.09.003

Roth, E.F., 1987. Malarial parasite hexokinase and hexokinase-dependent glutathione reduction in the Plasmodium falciparum-infected human erythrocyte. J Biol Chem 262, 15678–15682.

Roth, E.F., Calvin, M.C., Max-Audit, I., Rosa, J., Rosa, R., 1988. The enzymes of the glycolytic pathway in erythrocytes infected with Plasmodium falciparum malaria parasites. Blood 72, 1922–1925. https://doi.org/10.1182/blood.V72.6.1922.1922

Roy, S., Vivoli Vega, M., Harmer, N.J., 2019. Carbohydrate kinases: A conserved mechanism across differing folds. Catalysts 9, 29. https://doi.org/10.3390/catal9010029

Ruggieri, A., Anticoli, S., Nencioni, L., Sgarbanti, R., Garaci, E., Palamara, A.T., 2013. Interplay between Hepatitis C virus and redox cell signaling. Int J Mol Sci 14, 4705–4721. https://doi.org/10.3390/ijms14034705

Saisawang, C., Kuadkitkan, A., Auewarakul, P., Smith, D.R., Ketterman, A.J., 2018. Glutathionylation of dengue and Zika NS5 proteins affects guanylyltransferase and RNA dependent RNA polymerase activities. PLoS One 13, e0193133. https://doi.org/10.1371/journal.pone.0193133

Saisawang, C., Kuadkitkan, A., Smith, D.R., Ubol, S., Ketterman, A.J., 2017. Glutathionylation of chikungunya nsP2 protein affects protease activity. Biochim Biophys Acta Gen Subj 1861, 106–111. https://doi.org/10.1016/j.bbagen.2016.10.024

Saito, T., Maeda, T., Nakazawa, M., Takeuchi, T., Nozaki, T., Asai, T., 2002. Characterisation of hexokinase in Toxoplasma gondii tachyzoites. Int J Parasitol 32, 961–967. https://doi.org/10.1016/s0020-7519(02)00059-0

Schipper, S., Wu, H., Furdui, C.M., Poole, L.B., Delahunty, C.M., Park, R., Yates, J.R., Becker, K., Przyborski, J.M., 2021. Identification of sulfenylation patterns in trophozoite stage Plasmodium falciparum using a non-dimedone based probe. Mol Biochem Parasitol 242, 111362. https://doi.org/10.1016/j.molbiopara.2021.111362

Schoeman, D., Fielding, B.C., 2019. Coronavirus envelope protein: current knowledge. Virol J 16, 69. https://doi.org/10.1186/s12985-019-1182-0

Scholl, D.J., Wells, J.N., 2000. Serine and alanine mutagenesis of the nine native cysteine residues of the human A1 adenosine receptor. Biochem Pharmcol 60, 1647–1654. https://doi.org/10.1016/S0006-2952(00)00474-3

Schormann, N., Hayden, K.L., Lee, P., Banerjee, S., Chattopadhyay, D., 2019. An overview of structure, function, and regulation of pyruvate kinases. Protein Science 28, 1771–1784. https://doi.org/10.1002/pro.3691

Schuh, A.K., Rahbari, M., Heimsch, K.C., Mohring, F., Gabryszewski, S.J., Weder, S., Buchholz, K., Rahlfs, S., Fidock, D.A., Becker, K., 2018. Stable integration and comparison of hGrx1-roGFP2 and sfroGFP2 redox probes in the malaria parasite Plasmodium falciparum. ACS Infect Dis 4, 1601–1612. https://doi.org/10.1021/acsinfecdis.8b00140

Sebastian, S., Wilson, J.E., Mulichak, A., Garavito, R.M., 1999. Allosteric regulation of type I hexokinase: A site-directed mutational study indicating location of the functional glucose 6-phosphate binding site in the N-terminal half of the enzyme. Arch Biochem Biophys 362, 203–210. https://doi.org/10.1006/abbi.1998.1043

Sehrawat, A., Deswal, R., 2014. Sub-proteome S-nitrosylation analysis in Brassica juncea hints at the regulation of Brassicaceae specific as well as other vital metabolic pathway(s) by nitric oxide and suggests post-translational modifications cross-talk. Nitric Oxide 43, 97–111. https://doi.org/10.1016/j.niox.2014.08.010

Sengupta, R., Holmgren, A., 2013. Thioredoxin and thioredoxin reductase in relation to reversible S-nitrosylation. Antioxid Redox Signal 18, 259–269. https://doi.org/10.1089/ars.2012.4716

Shi, Y., Carroll, K.S., 2020. Activity-based sensing for site-specific proteomic analysis of cysteine oxidation. Acc Chem Res 53, 20–31. https://doi.org/10.1021/acs.accounts.9b00562

Sies, H., Jones, D.P., 2020. Reactive oxygen species (ROS) as pleiotropic physiological signalling agents. Nat Rev Mol Cell Biol 21, 363–383. https://doi.org/10.1038/s41580-020-0230-3

Slanina, H., Madhugiri, R., Bylapudi, G., Schultheiß, K., Karl, N., Gulyaeva, A., Gorbalenya, A.E., Linne, U., Ziebuhr, J., 2021. Coronavirus replication–transcription complex: Vital and selective NMPylation of a conserved site in nsp9 by the NiRAN-RdRp subunit. PNAS 118, e2022310118. https://doi.org/10.1073/pnas.2022310118

Snijder, E.J., Decroly, E., Ziebuhr, J., 2016. The nonstructural proteins directing coronavirus RNA synthesis and processing. Adv Virus Res 96, 59–126. https://doi.org/10.1016/bs.aivir.2016.08.008

Srivastava, S.S., Darling, J.E., Suryadi, J., Morris, J.C., Drew, M.E., Subramaniam, S., 2020. Plasmodium vivax and human hexokinases share similar active sites but display distinct quaternary architectures. IUCrJ 7, 453–461. https://doi.org/10.1107/S2052252520002456

Steinböck, F., Choojun, S., Held, I., Roehr, M., Kubicek, C.P., 1994. Characterization and regulatory properties of a single hexokinase from the citric acid accumulating fungus Aspergillus niger. Biochim Biophys Acta 1200, 215–223. https://doi.org/10.1016/0304-4165(94)90138-4

Stobart, C.C., Sexton, N.R., Munjal, H., Lu, X., Molland, K.L., Tomar, S., Mesecar, A.D., Denison, M.R., 2013. Chimeric exchange of coronavirus nsp5 proteases (3CLpro) identifies common and divergent regulatory determinants of protease activity. J Virol 87, 12611–12618. https://doi.org/10.1128/JVI.02050-13

Stomberski, C.T., Hess, D.T., Stamler, J.S., 2019. Protein S-nitrosylation: Determinants of specificity and enzymatic regulation of S-nitrosothiol-based signaling. Antioxid Redox Signal 30, 1331–1351. https://doi.org/10.1089/ars.2017.7403

Stukalov, A., Girault, V., Grass, V., Karayel, O., Bergant, V., Urban, C., Haas, D.A., Huang, Y., Oubraham, L., Wang, A., Hamad, M.S., Piras, A., Hansen, F.M., Tanzer, M.C., Paron, I., Zinzula, L., Engleitner, T., Reinecke, M., Lavacca, T.M., Ehmann, R., Wölfel, R., Jores, J., Kuster, B., Protzer, U., Rad, R., Ziebuhr, J., Thiel, V., Scaturro, P., Mann, M., Pichlmair, A., 2021. Multilevel proteomics reveals host perturbations by SARS-CoV-2 and SARS-CoV. Nature 594, 246–252. https://doi.org/10.1038/s41586-021-03493-4

Sturm, N., Jortzik, E., Mailu, B.M., Koncarevic, S., Deponte, M., Forchhammer, K., Rahlfs, S., Becker, K., 2009. Identification of proteins targeted by the thioredoxin superfamily in Plasmodium falciparum. PLOS Pathogens 5, e1000383. https://doi.org/10.1371/journal.ppat.1000383

Sugrue, E., Coombes, D., Wood, D., Zhu, T., Donovan, K.A., Dobson, R.C.J., 2020. The lid domain is important, but not essential, for catalysis of Escherichia coli pyruvate kinase. Eur Biophys J 49, 761–772. https://doi.org/10.1007/s00249-020-01466-5

Suhail, S., Zajac, J., Fossum, C., Lowater, H., McCracken, C., Severson, N., Laatsch, B., Narkiewicz-Jodko, A., Johnson, B., Liebau, J., Bhattacharyya, S., Hati, S., 2020. Role of oxidative stress on SARS-CoV (SARS) and SARS-CoV-2 (COVID-19) infection: a review. Protein J 1–13. https://doi.org/10.1007/s10930-020-09935-8

Sutton, G., Fry, E., Carter, L., Sainsbury, S., Walter, T., Nettleship, J., Berrow, N., Owens, R., Gilbert, R., Davidson, A., Siddell, S., Poon, L.L.M., Diprose, J., Alderton, D., Walsh, M., Grimes, J.M., Stuart, D.I., 2004. The nsp9 replicase protein of SARS-coronavirus, structure and functional insights. Structure 12, 341–353. https://doi.org/10.1016/j.str.2004.01.016

Sztajer, H., Gamain, B., Aumann, K.-D., Slomianny, C., Becker, K., Brigelius-Flohé, R., Flohé, L., 2001. The putative glutathione peroxidase gene of Plasmodium falciparum codes for a thioredoxin peroxidase. J Biol Chem 276, 7397–7403. https://doi.org/10.1074/jbc.M008631200

te Velthuis, A.J.W., van den Worm, S.H.E., Snijder, E.J., 2012. The SARS-coronavirus nsp7+nsp8 complex is a unique multimeric RNA polymerase capable of both de novo initiation and primer extension. Nucleic Acids Res 40, 1737–1747. https://doi.org/10.1093/nar/gkr893

Thermo Scientific, 2012. Crosslinking Technical Handbook.

Thu, A.M., Phyo, A.P., Landier, J., Parker, D.M., Nosten, F.H., 2017. Combating multidrug-resistant Plasmodium falciparum malaria. FEBS J 284, 2569–2578. https://doi.org/10.1111/febs.14127

Tilley, L., Loria, P., Foley, M., 2001. Chloroquine and other quinoline antimalarials, in: Rosenthal, P.J. (Ed.), Antimalarial Chemotherapy: Mechanisms of Action, Resistance, and New Directions in Drug Discovery, Infectious Disease. Humana Press, Totowa, NJ, pp. 87–121. https://doi.org/10.1007/978-1-59259-111-4_6

Tiwari, S., Sharma, N., Sharma, G.P., Mishra, N., 2021. Redox interactome in malaria parasite Plasmodium falciparum. Parasitol Res 120, 423–434. https://doi.org/10.1007/s00436-021-07051-9

Tjhin, E.T., Staines, H.M., van Schalkwyk, D.A., Krishna, S., Saliba, K.J., 2013. Studies with the Plasmodium falciparum hexokinase reveal that PfHT limits the rate of glucose entry into glycolysis. FEBS Lett 587, 3182–3187. https://doi.org/10.1016/j.febslet.2013.07.052

Tomar, S., Johnston, M.L., St John, S.E., Osswald, H.L., Nyalapatla, P.R., Paul, L.N., Ghosh, A.K., Denison, M.R., Mesecar, A.D., 2015. Ligand-induced dimerization of Middle East Respiratory Syndrome (MERS) Coronavirus nsp5 protease (3CLpro): implications for nsp5 regulation and the development of antivirals. J Biol Chem 290, 19403–19422. https://doi.org/10.1074/jbc.M115.651463

Tran, T.M., Crompton, P.D., 2020. Decoding the complexities of human malaria through systems immunology. Immunol Rev 293, 144–162. https://doi.org/10.1111/imr.12817

Tuteja, R., 2007. Malaria − an overview. FEBS J 274, 4670–4679. https://doi.org/10.1111/j.1742-4658.2007.05997.x

Unsain, N., Stefani, F.D., Cáceres, A., 2018. The actin/spectrin membrane-associated periodic skeleton in neurons. Front Synaptic Neurosci 10, doi: 10.3389/fnsyn.2018.00010.

van Niekerk, D.D., Penkler, G.P., du Toit, F., Snoep, J.L., 2016. Targeting glycolysis in the malaria parasite Plasmodium falciparum. FEBS J 283, 634–646. https://doi.org/10.1111/febs.13615

Venkatagopalan, P., Daskalova, S.M., Lopez, L.A., Dolezal, K.A., Hogue, B.G., 2015. Coronavirus envelope (E) protein remains at the site of assembly. Virology 478, 75–85. https://doi.org/10.1016/j.virol.2015.02.005

V'kovski, P., Kratzel, A., Steiner, S., Stalder, H., Thiel, V., 2020. Coronavirus biology and replication: implications for SARS-CoV-2. Nat Rev Microbiol 1–16. https://doi.org/10.1038/s41579-020-00468-6

Vuong, W., Khan, M.B., Fischer, C., Arutyunova, E., Lamer, T., Shields, J., Saffran, H.A., McKay, R.T., van Belkum, M.J., Joyce, M.A., Young, H.S., Tyrrell, D.L., Vederas, J.C., Lemieux, M.J., 2020. Feline coronavirus drug inhibits the main protease of SARS-CoV-2 and blocks virus replication. Nat Commun 11, 4282. https://doi.org/10.1038/s41467-020-18096-2

Wahlgren, M., Goel, S., Akhouri, R.R., 2017. Variant surface antigens of Plasmodium falciparum and their roles in severe malaria. Nat Rev Microbiol 15, 479–491. https://doi.org/10.1038/nrmicro.2017.47

Wang, B., Svetlov, D., Artsimovitch, I., 2021. NMPylation and de-NMPylation of SARS-CoV-2 nsp9 by the NiRAN domain. Nucleic Acids Research 49, 8822–8835. https://doi.org/10.1093/nar/gkab677

Wang, L., Delahunty, C., Prieto, J.H., Rahlfs, S., Jortzik, E., Yates, J.R., Becker, K., 2014. Protein S-nitrosylation in Plasmodium falciparum. Antioxid Redox Signal 20, 2923–2935. https://doi.org/10.1089/ars.2013.5553

Waterhouse, A., Bertoni, M., Bienert, S., Studer, G., Tauriello, G., Gumienny, R., Heer, F.T., de Beer, T.A.P., Rempfer, C., Bordoli, L., Lepore, R., Schwede, T., 2018. SWISS-MODEL: homology modelling of protein structures and complexes. Nucleic Acids Res 46, W296–W303. https://doi.org/10.1093/nar/gky427

WHO Coronavirus (COVID-19) Dashboard [WWW Document], 2022. URL https://covid19.who.int (accessed 1.29.22).

Wiedemann, C., Kumar, A., Lang, A., Ohlenschläger, O., 2020. Cysteines and disulfide bonds as structure-forming units: insights from different domains of life and the potential for characterization by NMR. Front. Chem. 0. https://doi.org/10.3389/fchem.2020.00280

Wienen-Schmidt, B., Oebbeke, M., Ngo, K., Heine, A., Klebe, G., 2021. Two methods, one goal: structural differences between cocrystallization and crystal soaking to discover ligand binding poses. ChemMedChem 16, 292–300. https://doi.org/10.1002/cmdc.202000565

Wilson, J.E., 2003. Isozymes of mammalian hexokinase: structure, subcellular localization and metabolic function. J Exp Biol 206, 2049–2057. https://doi.org/10.1242/jeb.00241

Winterbourn, C.C., Hampton, M.B., 2008. Thiol chemistry and specificity in redox signaling. Free Radic Biol Med 45, 549–561. https://doi.org/10.1016/j.freeradbiomed.2008.05.004

World Health Organization, 2021. World malaria report 2021.

Wratil, P.R., Stern, M., Priller, A., Willmann, A., Almanzar, G., Vogel, E., Feuerherd, M., Cheng, C.-C., Yazici, S., Christa, C., Jeske, S., Lupoli, G., Vogt, T., Albanese, M., Mejías-Pérez, E., Bauernfried, S., Graf, N., Mijocevic, H., Vu, M., Tinnefeld, K., Wettengel, J., Hoffmann, D., Muenchhoff, M., Daechert, C., Mairhofer, H., Krebs, S., Fingerle, V., Graf, A., Steininger, P., Blum, H., Hornung, V., Liebl, B., Überla, K., Prelog, M., Knolle, P., Keppler, O.T., Protzer, U., 2022. Three exposures to the spike protein of SARS-CoV-2 by either infection or vaccination elicit superior neutralizing immunity to all variants of concern. Nat Med 496–503. https://doi.org/10.1038/s41591-022-01715-4

Wynia-Smith, S.L., Smith, B.C., 2017. Nitrosothiol formation and S-nitrosation signaling through nitric oxide synthases. Nitric Oxide 63, 52–60. https://doi.org/10.1016/j.niox.2016.10.001

Xiong, Y., Uys, J.D., Tew, K.D., Townsend, D.M., 2011. S-glutathionylation: from molecular mechanisms to health outcomes. Antioxid Redox Signal 15, 233–270. https://doi.org/10.1089/ars.2010.3540

Yang, W., Lu, Z., 2013. Regulation and function of pyruvate kinase M2 in cancer. Cancer Lett 339, 153–158. https://doi.org/10.1016/j.canlet.2013.06.008

Ye, Z.-W., Zhang, J., Ancrum, T., Manevich, Y., Townsend, D.M., Tew, K.D., 2017. Glutathione S-transferase P-mediated protein S-glutathionylation of resident endoplasmic reticulum proteins influences sensitivity to drug-induced unfolded protein response. Antioxid Redox Signal 26, 247–261. https://doi.org/10.1089/ars.2015.6486

Yu, Y., Zhang, H., Guo, F., Sun, M., Zhu, G., 2014. A unique hexokinase in Cryptosporidium parvum, an apicomplexan pathogen lacking the Krebs cycle and oxidative phosphorylation. Protist 165, 701–714. https://doi.org/10.1016/j.protis.2014.08.002

Zavala, F., 2022. RTS,S: the first malaria vaccine. J Clin Invest 132, e156588. https://doi.org/10.1172/JCI156588

Zeng, Z., Deng, F., Shi, K., Ye, G., Wang, G., Fang, L., Xiao, S., Fu, Z., Peng, G., 2018. Dimerization of coronavirus nsp9 with diverse modes enhances its nucleic acid binding affinity. J Virol e00692-18. https://doi.org/10.1128/JVI.00692-18

Zhai, Y., Sun, F., Li, X., Pang, H., Xu, X., Bartlam, M., Rao, Z., 2005. Insights into SARS-CoV transcription and replication from the structure of the nsp7–nsp8 hexadecamer. Nat Struct Mol Biol 12, 980–986. https://doi.org/10.1038/nsmb999

Zhang, J., Ye, Z.-W., Singh, S., Townsend, D.M., Tew, K.D., 2018. An evolving understanding of the S-glutathionylation cycle in pathways of redox regulation. Free Radic Biol Med 120, 204–216. https://doi.org/10.1016/j.freeradbiomed.2018.03.038

Zhang, T., 2013. Characterization and S-glutathionylation of hexokinase from the malaria parasite Plasmodium falciparum. Justus Liebig University, Giessen.

Zhong, W., Li, K., Cai, Q., Guo, J., Yuan, M., Wong, Y.H., Walkinshaw, M.D., Fothergill-Gilmore, L.A., Michels, P.A.M., Dedon, P.C., Lescar, J., 2020. Pyruvate kinase from Plasmodium falciparum: Structural and kinetic insights into the allosteric mechanism. Biochem Biophys Res Commun 532, 370–376. https://doi.org/10.1016/j.bbrc.2020.08.048

Zhong, W., Morgan, H.P., McNae, I.W., Michels, P.A.M., Fothergill-Gilmore, L.A., Walkinshaw, M.D., 2013. “In crystallo” substrate binding triggers major domain movements and reveals magnesium as a co-activator of Trypanosoma brucei pyruvate kinase. Acta Crystallogr D Biol Crystallogr 69, 1768–1779. https://doi.org/10.1107/S0907444913013875

Ziebuhr, J., 2008. Coronavirus replicative proteins, in: Perlman, S., Gallagher, T., Snijder, E.J. (Eds.), Nidoviruses. ASM Press, Washington, DC, USA, pp. 65–81. https://doi.org/10.1128/9781555815790.ch5

Ziebuhr, J., 2005. The coronavirus replicase. Curr Top Microbiol Immunol 287, 57–94. https://doi.org/10.1007/3-540-26765-4_3

SUPPLEMENTARY INFORMATION

Table S 1 - PEG Screen I (96-well format).

Well	Precipitant	Buffer	Well	Precipitant	Buffer
A1	5% Ethylenglycol	0.1 M MES pH 6.5	**E1**	5% MME 550	0.1 M MES pH 6.5
A2	10% Ethylenglycol	0.1 M MES pH 6.5	**E2**	10% MME 550	0.1 M MES pH 6.5
A3	15% Ethylenglycol	0.1 M MES pH 6.5	**E3**	15% MME 550	0.1 M MES pH 6.5
A4	20% Ethylenglycol	0.1 M MES pH 6.5	**E4**	20% MME 550	0.1 M MES pH 6.5
A5	25% Ethylenglycol	0.1 M MES pH 6.5	**E5**	25% MME 550	0.1 M MES pH 6.5
A6	30% Ethylenglycol	0.1 M MES pH 6.5	**E6**	30% MME 550	0.1 M MES pH 6.5
A7	20% Ethylenglycol	0.1 M Sodium Acetate pH 4.6	**E7**	20% MME 550	0.1 M Sodium Acetate pH 4.6
A8	20% Ethylenglycol	0.1 M Sodium Citrate pH 5.5	**E8**	20% MME 550	0.1 M Sodium Citrate pH 5.5
A9	20% Ethylenglycol	0.1 M Hepes pH 7.5	**E9**	20% MME 550	0.1 M Hepes pH 7.5
A10	20% Ethylenglycol	0.1 M Imidazole pH 8	**E10**	20% MME 550	0.1 M Imidazole pH 8
A11	20% Ethylenglycol	0.1 M Tris pH 8.5	**E11**	20% MME 550	0.1 M Tris pH 8.5
A12	20% Ethylenglycol	0.1 M Bicine pH 9	**E12**	20% MME 550	0.1 M Bicine pH 9
B1	5% PEG 200	0.1 M MES pH 6.5	**F1**	5% PEG 600	0.1 M MES pH 6.5
B2	10% PEG 200	0.1 M MES pH 6.5	**F2**	10% PEG 600	0.1 M MES pH 6.5
B3	15% PEG 200	0.1 M MES pH 6.5	**F3**	15% PEG 600	0.1 M MES pH 6.5
B4	20% PEG 200	0.1 M MES pH 6.5	**F4**	20% PEG 600	0.1 M MES pH 6.5
B5	25% PEG 200	0.1 M MES pH 6.5	**F5**	25% PEG 600	0.1 M MES pH 6.5
B6	30% PEG 200	0.1 M MES pH 6.5	**F6**	30% PEG 600	0.1 M MES pH 6.5
B7	20% PEG 200	0.1 M Sodium Acetate pH 4.6	**F7**	20% PEG 600	0.1 M Sodium Acetate pH 4.6
B8	20% PEG 200	0.1 M Sodium Citrate pH 5.5	**F8**	20% PEG 600	0.1 M Sodium Citrate pH 5.5
B9	20% PEG 200	0.1 M Hepes pH 7.5	**F9**	20% PEG 600	0.1 M Hepes pH 7.5
B10	20% PEG 200	0.1 M Imidazole pH 8	**F10**	20% PEG 600	0.1 M Imidazole pH 8
B11	20% PEG 200	0.1 M Tris pH 8.5	**F11**	20% PEG 600	0.1 M Tris pH 8.5
B12	20% PEG 200	0.1 M Bicine pH 9	**F12**	20% PEG 600	0.1 M Bicine pH 9
C1	5% PEG 300	0.1 M MES pH 6.5	**G1**	5% PEG 1000	0.1 M MES pH 6.5
C2	10% PEG 300	0.1 M MES pH 6.5	**G2**	10% PEG 1000	0.1 M MES pH 6.5
C3	15% PEG 300	0.1 M MES pH 6.5	**G3**	15% PEG 1000	0.1 M MES pH 6.5
C4	20% PEG 300	0.1 M MES pH 6.5	**G4**	20% PEG 1000	0.1 M MES pH 6.5
C5	25% PEG 300	0.1 M MES pH 6.5	**G5**	25% PEG 1000	0.1 M MES pH 6.5
C6	30% PEG 300	0.1 M MES pH 6.5	**G6**	30% PEG 1000	0.1 M MES pH 6.5
C7	20% PEG 300	0.1 M Sodium Acetate pH 4.6	**G7**	20% PEG 1000	0.1 M Sodium Acetate pH 4.6
C8	20% PEG 300	0.1 M Sodium Citrate pH 5.5	**G8**	20% PEG 1000	0.1 M Sodium Citrate pH 5.5
C9	20% PEG 300	0.1 M Hepes pH 7.5	**G9**	20% PEG 1000	0.1 M Hepes pH 7.5
C10	20% PEG 300	0.1 M Imidazole pH 8	**G10**	20% PEG 1000	0.1 M Imidazole pH 8
C11	20% PEG 300	0.1 M Tris pH 8.5	**G11**	20% PEG 1000	0.1 M Tris pH 8.5
C12	20% PEG 300	0.1 M Bicine pH 9	**G12**	20% PEG 1000	0.1 M Bicine pH 9
D1	5% PEG 400	0.1 M MES pH 6.5	**H1**	5% PEG 1500	0.1 M MES pH 6.5
D2	10% PEG 400	0.1 M MES pH 6.5	**H2**	10% PEG 1500	0.1 M MES pH 6.5
D3	15% PEG 400	0.1 M MES pH 6.5	**H3**	15% PEG 1500	0.1 M MES pH 6.5
D4	20% PEG 400	0.1 M MES pH 6.5	**H4**	20% PEG 1500	0.1 M MES pH 6.5
D5	25% PEG 400	0.1 M MES pH 6.5	**H5**	25% PEG 1500	0.1 M MES pH 6.5
D6	30% PEG 400	0.1 M MES pH 6.5	**H6**	30% PEG 1500	0.1 M MES pH 6.5
D7	20% PEG 400	0.1 M Sodium Acetate pH 4.6	**H7**	20% PEG 1500	0.1 M Sodium Acetate pH 4.6
D8	20% PEG 400	0.1 M Sodium Citrate pH 5.5	**H8**	20% PEG 1500	0.1 M Sodium Citrate pH 5.5
D9	20% PEG 400	0.1 M Hepes pH 7.5	**H9**	20% PEG 1500	0.1 M Hepes pH 7.5
D10	20% PEG 400	0.1 M Imidazole pH 8	**H10**	20% PEG 1500	0.1 M Imidazole pH 8
D11	20% PEG 400	0.1 M Tris pH 8.5	**H11**	20% PEG 1500	0.1 M Tris pH 8.5
D12	20% PEG 400	0.1 M Bicine pH 9	**H12**	20% PEG 1500	0.1 M Bicine pH 9

Table S 2 - PEG Screen II (96-well format).

Well	Precipitant	Buffer	Well	Precipitant	Buffer
A1	5% MME 2000	0.1 M MES pH 6.5	**E1**	5% PEG 5000	0.1 M MES pH 6.5
A2	10% MME 2000	0.1 M MES pH 6.5	**E2**	10% PEG 5000	0.1 M MES pH 6.5
A3	15% MME 2000	0.1 M MES pH 6.5	**E3**	15% PEG 5000	0.1 M MES pH 6.5
A4	20% MME 2000	0.1 M MES pH 6.5	**E4**	20% PEG 5000	0.1 M MES pH 6.5
A5	25% MME 2000	0.1 M MES pH 6.5	**E5**	25% PEG 5000	0.1 M MES pH 6.5
A6	30% MME 2000	0.1 M MES pH 6.5	**E6**	30% PEG 5000	0.1 M MES pH 6.5
A7	20% MME 2000	0.1 M Sodium Acetate pH 4.6	**E7**	20% PEG 5000	0.1 M Sodium Acetate pH 4.6
A8	20% MME 2000	0.1 M Sodium Citrate pH 5.5	**E8**	20% PEG 5000	0.1 M Sodium Citrate pH 5.5
A9	20% MME 2000	0.1 M Hepes pH 7.5	**E9**	20% PEG 5000	0.1 M Hepes pH 7.5
A10	20% MME 2000	0.1 M Imidazole pH 8	**E10**	20% PEG 5000	0.1 M Imidazole pH 8
A11	20% MME 2000	0.1 M Tris pH 8.5	**E11**	20% PEG 5000	0.1 M Tris pH 8.5
A12	20% MME 2000	0.1 M Bicine pH 9	**E12**	20% PEG 5000	0.1 M Bicine pH 9
B1	5% PEG 3000	0.1 M MES pH 6.5	**F1**	5% PEG 6000	0.1 M MES pH 6.5
B2	10% PEG 3000	0.1 M MES pH 6.5	**F2**	10% PEG 6000	0.1 M MES pH 6.5
B3	15% PEG 3000	0.1 M MES pH 6.5	**F3**	15% PEG 6000	0.1 M MES pH 6.5
B4	20% PEG 3000	0.1 M MES pH 6.5	**F4**	20% PEG 6000	0.1 M MES pH 6.5
B5	25% PEG 3000	0.1 M MES pH 6.5	**F5**	25% PEG 6000	0.1 M MES pH 6.5
B6	30% PEG 3000	0.1 M MES pH 6.5	**F6**	30% PEG 6000	0.1 M MES pH 6.5
B7	20% PEG 3000	0.1 M Sodium Acetate pH 4.6	**F7**	20% PEG 6000	0.1 M Sodium Acetate pH 4.6
B8	20% PEG 3000	0.1 M Sodium Citrate pH 5.5	**F8**	20% PEG 6000	0.1 M Sodium Citrate pH 5.5
B9	20% PEG 3000	0.1 M Hepes pH 7.5	**F9**	20% PEG 6000	0.1 M Hepes pH 7.5
B10	20% PEG 3000	0.1 M Imidazole pH 8	**F10**	20% PEG 6000	0.1 M Imidazole pH 8
B11	20% PEG 3000	0.1 M Tris pH 8.5	**F11**	20% PEG 6000	0.1 M Tris pH 8.5
B12	20% PEG 3000	0.1 M Bicine pH 9	**F12**	20% PEG 6000	0.1 M Bicine pH 9
C1	5% PEG 3350	0.1 M MES pH 6.5	**G1**	5% PEG 8000	0.1 M MES pH 6.5
C2	10% PEG 3350	0.1 M MES pH 6.5	**G2**	10% PEG 8000	0.1 M MES pH 6.5
C3	15% PEG 3350	0.1 M MES pH 6.5	**G3**	15% PEG 8000	0.1 M MES pH 6.5
C4	20% PEG 3350	0.1 M MES pH 6.5	**G4**	20% PEG 8000	0.1 M MES pH 6.5
C5	25% PEG 3350	0.1 M MES pH 6.5	**G5**	25% PEG 8000	0.1 M MES pH 6.5
C6	30% PEG 3350	0.1 M MES pH 6.5	**G6**	30% PEG 8000	0.1 M MES pH 6.5
C7	20% PEG 3350	0.1 M Sodium Acetate pH 4.6	**G7**	20% PEG 8000	0.1 M Sodium Acetate pH 4.6
C8	20% PEG 3350	0.1 M Sodium Citrate pH 5.5	**G8**	20% PEG 8000	0.1 M Sodium Citrate pH 5.5
C9	20% PEG 3350	0.1 M Hepes pH 7.5	**G9**	20% PEG 8000	0.1 M Hepes pH 7.5
C10	20% PEG 3350	0.1 M Imidazole pH 8	**G10**	20% PEG 8000	0.1 M Imidazole pH 8
C11	20% PEG 3350	0.1 M Tris pH 8.5	**G11**	20% PEG 8000	0.1 M Tris pH 8.5
C12	20% PEG 3350	0.1 M Bicine pH 9	**G12**	20% PEG 8000	0.1 M Bicine pH 9
D1	5% PEG 4000	0.1 M MES pH 6.5	**H1**	5% PEG 10,000	0.1 M MES pH 6.5
D2	10% PEG 4000	0.1 M MES pH 6.5	**H2**	10% PEG 10000	0.1 M MES pH 6.5
D3	15% PEG 4000	0.1 M MES pH 6.5	**H3**	15% PEG 10000	0.1 M MES pH 6.5
D4	20% PEG 4000	0.1 M MES pH 6.5	**H4**	20% PEG 10000	0.1 M MES pH 6.5
D5	25% PEG 4000	0.1 M MES pH 6.5	**H5**	25% PEG 10000	0.1 M MES pH 6.5
D6	30% PEG 4000	0.1 M MES pH 6.5	**H6**	30% PEG 10000	0.1 M MES pH 6.5
D7	20% PEG 4000	0.1 M Sodium Acetate pH 4.6	**H7**	20% PEG 10000	0.1 M Sodium Acetate pH 4.6
D8	20% PEG 4000	0.1 M Sodium Citrate pH 5.5	**H8**	20% PEG 10000	0.1 M Sodium Citrate pH 5.5
D9	20% PEG 4000	0.1 M Hepes pH 7.5	**H9**	20% PEG 10000	0.1 M Hepes pH 7.5
D10	20% PEG 4000	0.1 M Imidazole pH 8	**H10**	20% PEG 10000	0.1 M Imidazole pH 8
D11	20% PEG 4000	0.1 M Tris pH 8.5	**H11**	20% PEG 10000	0.1 M Tris pH 8.5
D12	20% PEG 4000	0.1 M Bicine pH 9	**H12**	20% PEG 10000	0.1 M Bicine pH 9

Table S 3 - PEG Screen III (96-well format).

Well	Precipitant	Additive	Well	Precipitant	Additive
A1	20% PEG 400	200 mM Lithium Chlorid	**E1**	20% PEG 4000	200 mM Lithium Chlorid
A2	20% PEG 400	200 mM Calcium Chlorid	**E2**	20% PEG 4000	200 mM Calcium Chlorid
A3	20% PEG 400	200 mM Magnesium Chlorid	**E3**	20% PEG 4000	200 mM Magnesium Chlorid
A4	20% PEG 400	200 mM Sodium Jodid	**E4**	20% PEG 4000	200 mM Sodium Jodid
A5	20% PEG 400	200 mM Sodium Formiad	**E5**	20% PEG 4000	200 mM Sodium Formiad
A6	20% PEG 400	200 mM Ammonium Nitrat	**E6**	20% PEG 4000	200 mM Ammonium Nitrat
A7	20% PEG 400	200 mM Sodium Acetate	**E7**	20% PEG 4000	200 mM Sodium Acetate
A8	20% PEG 400	200 mM Magnesium Acetate	**E8**	20% PEG 4000	200 mM Magnesium Acetate
A9	20% PEG 400	200 mM Lithium Sulfat	**E9**	20% PEG 4000	200 mM Lithium Sulfat
A10	20% PEG 400	200 mM Ammonium Sulfat	**E10**	20% PEG 4000	200 mM Ammonium Sulfat
A11	20% PEG 400	200 mM Sodium Phosphat	**E11**	20% PEG 4000	200 mM Sodium Phosphat
A12	20% PEG 400	200 mM Sodium Citrat	**E12**	20% PEG 4000	200 mM Sodium Citrat
B1	30% PEG 400	200 mM Lithium Chlorid	**F1**	30% PEG 4000	200 mM Lithium Chlorid
B2	30% PEG 400	200 mM Calcium Chlorid	**F2**	30% PEG 4000	200 mM Calcium Chlorid
B3	30% PEG 400	200 mM Magnesium Chlorid	**F3**	30% PEG 4000	200 mM Magnesium Chlorid
B4	30% PEG 400	200 mM Sodium Jodid	**F4**	30% PEG 4000	200 mM Sodium Jodid
B5	30% PEG 400	200 mM Sodium Formiad	**F5**	30% PEG 4000	200 mM Sodium Formiad
B6	30% PEG 400	200 mM Ammonium Nitrat	**F6**	30% PEG 4000	200 mM Ammonium Nitrat
B7	30% PEG 400	200 mM Sodium Acetate	**F7**	30% PEG 4000	200 mM Sodium Acetate
B8	30% PEG 400	200 mM Magnesium Acetate	**F8**	30% PEG 4000	200 mM Magnesium Acetate
B9	30% PEG 400	200 mM Lithium Sulfat	**F9**	30% PEG 4000	200 mM Lithium Sulfat
B10	30% PEG 400	200 mM Ammonium Sulfat	**F10**	30% PEG 4000	200 mM Ammonium Sulfat
B11	30% PEG 400	200 mM Sodium Phosphat	**F11**	30% PEG 4000	200 mM Sodium Phosphat
B12	30% PEG 400	200 mM Sodium Citrat	**F12**	30% PEG 4000	200 mM Sodium Citrat
C1	20% PEG 3350	200 mM Lithium Chlorid	**G1**	20% PEG 6000	200 mM Lithium Chlorid
C2	20% PEG 3350	200 mM Calcium Chlorid	**G2**	20% PEG 6000	200 mM Calcium Chlorid
C3	20% PEG 3350	200 mM Magnesium Chlorid	**G3**	20% PEG 6000	200 mM Magnesium Chlorid
C4	20% PEG 3350	200 mM Sodium Jodid	**G4**	20% PEG 6000	200 mM Sodium Jodid
C5	20% PEG 3350	200 mM Sodium Formiad	**G5**	20% PEG 6000	200 mM Sodium Formiad
C6	20% PEG 3350	200 mM Ammonium Nitrat	**G6**	20% PEG 6000	200 mM Ammonium Nitrat
C7	20% PEG 3350	200 mM Sodium Acetate	**G7**	20% PEG 6000	200 mM Sodium Acetate
C8	20% PEG 3350	200 mM Magnesium Acetate	**G8**	20% PEG 6000	200 mM Magnesium Acetate
C9	20% PEG 3350	200 mM Lithium Sulfat	**G9**	20% PEG 6000	200 mM Lithium Sulfat
C10	20% PEG 3350	200 mM Ammonium Sulfat	**G10**	20% PEG 6000	200 mM Ammonium Sulfat
C11	20% PEG 3350	200 mM Sodium Phosphat	**G11**	20% PEG 6000	200 mM Sodium Phosphat
C12	20% PEG 3350	200 mM Sodium Citrat	**G12**	20% PEG 6000	200 mM Sodium Citrat
D1	30% PEG 3350	200 mM Lithium Chlorid	**H1**	30% PEG 6000	200 mM Lithium Chlorid
D2	30% PEG 3350	200 mM Calcium Chlorid	**H2**	30% PEG 6000	200 mM Calcium Chlorid

D3	30% PEG 3350	200 mM Magnesium Chlorid	**H3**	30% PEG 6000	200 mM Magnesium Chlorid
D4	30% PEG 3350	200 mM Sodium Jodid	**H4**	30% PEG 6000	200 mM Sodium Jodid
D5	30% PEG 3350	200 mM Sodium Formiad	**H5**	30% PEG 6000	200 mM Sodium Formiad
D6	30% PEG 3350	200 mM Ammonium Nitrat	**H6**	30% PEG 6000	200 mM Ammonium Nitrat
D7	30% PEG 3350	200 mM Sodium Acetate	**H7**	30% PEG 6000	200 mM Sodium Acetate
D8	30% PEG 3350	200 mM Magnesium Acetate	**H8**	30% PEG 6000	200 mM Magnesium Acetate
D9	30% PEG 3350	200 mM Lithium Sulfat	**H9**	30% PEG 6000	200 mM Lithium Sulfat
D10	30% PEG 3350	200 mM Ammonium Sulfat	**H10**	30% PEG 6000	200 mM Ammonium Sulfat
D11	30% PEG 3350	200 mM Sodium Phosphat	**H11**	30% PEG 6000	200 mM Sodium Phosphat
D12	30% PEG 3350	200 mM Sodium Citrat	**H12**	30% PEG 6000	200 mM Sodium Citrat

Table S 4 - PfHK Screen NEO (96-well format).

Well	Precipitant	Salt	Buffer
A1	6% PEG 8,000	200 mM Magnesium Chlorid	0.1 M MES pH 6.5
A2	6% PEG 8,000	200 mM Magnesium Chlorid	0.1 M Hepes pH 7.0
A3	6% PEG 8,000	200 mM Magnesium Chlorid	0.1 M Tris pH 7.5
A4	6% PEG 8,000	200 mM Magnesium Acetate	0.1 M Hepes pH 7.0
A5	6% PEG 8,000	200 mM Lithium Sulfate	0.1 M Hepes pH 7.0
A6	6% PEG 8,000	200 mM Sodium Citrate	0.1 M Hepes pH 7.0
A7	14% PEG 3,350	200 mM Sodium Citrate	
A8	14% PEG 3,350	200 mM Sodium Citrate	
A9	14% PEG 3,350	200 mM Magnesium Acetate	
A10	14% PEG 3,350	200 mM Potassium Citrate	
A11	14% PEG 3,350	200 mM Lithium Sulfate	
A12	14% PEG 3,350	200 mM Magnesium Chlorid	
B1	8% PEG 8,000	200 mM Magnesium Chlorid	0.1 M MES pH 6.5
B2	8% PEG 8,000	200 mM Magnesium Chlorid	0.1 M Hepes pH 7.0
B3	8% PEG 8,000	200 mM Magnesium Chlorid	0.1 M Tris pH 7.5
B4	8% PEG 8,000	200 mM Magnesium Acetate	0.1 M Hepes pH 7.0
B5	8% PEG 8,000	200 mM Lithium Sulfate	0.1 M Hepes pH 7.0
B6	8% PEG 8,000	200 mM Sodium Citrate	0.1 M Hepes pH 7.0
B7	16% PEG 3,350	200 mM Sodium Citrate	
B8	16% PEG 3,350	200 mM Sodium Citrate	
B9	16% PEG 3,350	200 mM Magnesium Acetate	
B10	16% PEG 3,350	200 mM Potassium Citrate	
B11	16% PEG 3,350	200 mM Lithium Sulfate	
B12	16% PEG 3,350	200 mM Magnesium Chlorid	
C1	10% PEG 8,000	200 mM Magnesium Chlorid	0.1 M MES pH 6.5
C2	10% PEG 8,000	200 mM Magnesium Chlorid	0.1 M Hepes pH 7.0
C3	10% PEG 8,000	200 mM Magnesium Chlorid	0.1 M Tris pH 7.5
C4	10% PEG 8,000	200 mM Magnesium Acetate	0.1 M Hepes pH 7.0
C5	10% PEG 8,000	200 mM Lithium Sulfate	0.1 M Hepes pH 7.0
C6	10% PEG 8,000	200 mM Sodium Citrate	0.1 M Hepes pH 7.0
C7	18% PEG 3,350	200 mM Sodium Citrate	
C8	18% PEG 3,350	200 mM Sodium Citrate	
C9	18% PEG 3,350	200 mM Magnesium Acetate	
C10	18% PEG 3,350	200 mM Potassium Citrate	
C11	18% PEG 3,350	200 mM Lithium Sulfate	
C12	18% PEG 3,350	200 mM Magnesium Chlorid	
D1	10% PEG 8,000	200 mM Magnesium Chlorid	0.1 M MES pH 6.5
D2	10% PEG 8,000	200 mM Magnesium Chlorid	0.1 M Hepes pH 7.0
D3	10% PEG 8,000	200 mM Magnesium Chlorid	0.1 M Tris pH 7.5
D4	10% PEG 8,000	200 mM Magnesium Acetate	0.1 M Hepes pH 7.0

D5	10% PEG 8,000	200 mM Lithium Sulfate	0.1 M Hepes pH 7.0
D6	10% PEG 8,000	200 mM Sodium Citrate	0.1 M Hepes pH 7.0
D7	20% PEG 3,350	200 mM Sodium Citrate	
D8	20% PEG 3,350	200 mM Sodium Citrate	
D9	20% PEG 3,350	200 mM Magnesium Acetate	
D10	20% PEG 3,350	200 mM Potassium Citrate	
D11	20% PEG 3,350	200 mM Lithium Sulfate	
D12	20% PEG 3,350	200 mM Magnesium Chlorid	
E1	12% PEG 8,000	200 mM Magnesium Chlorid	0.1 M MES pH 6.5
E2	12% PEG 8,000	200 mM Magnesium Chlorid	0.1 M Hepes pH 7.0
E3	12% PEG 8,000	200 mM Magnesium Chlorid	0.1 M Tris pH 7.5
E4	12% PEG 8,000	200 mM Magnesium Acetate	0.1 M Hepes pH 7.0
E5	12% PEG 8,000	200 mM Lithium Sulfate	0.1 M Hepes pH 7.0
E6	12% PEG 8,000	200 mM Sodium Citrate	0.1 M Hepes pH 7.0
E7	20% PEG 3,350	200 mM Sodium Citrate	
E8	20% PEG 3,350	200 mM Sodium Citrate	
E9	20% PEG 3,350	200 mM Magnesium Acetate	
E10	20% PEG 3,350	200 mM Potassium Citrate	
E11	20% PEG 3,350	200 mM Lithium Sulfate	
E12	20% PEG 3,350	200 mM Magnesium Chlorid	
F1	14% PEG 8,000	200 mM Magnesium Chlorid	0.1 M MES pH 6.5
F2	14% PEG 8,000	200 mM Magnesium Chlorid	0.1 M Hepes pH 7.0
F3	14% PEG 8,000	200 mM Magnesium Chlorid	0.1 M Tris pH 7.5
F4	14% PEG 8,000	200 mM Magnesium Acetate	0.1 M Hepes pH 7.0
F5	14% PEG 8,000	200 mM Lithium Sulfate	0.1 M Hepes pH 7.0
F6	14% PEG 8,000	200 mM Sodium Citrate	0.1 M Hepes pH 7.0
F7	22% PEG 3,350	200 mM Sodium Citrate	
F8	22% PEG 3,350	200 mM Sodium Citrate	
F9	22% PEG 3,350	200 mM Magnesium Acetate	
F10	22% PEG 3,350	200 mM Potassium Citrate	
F11	22% PEG 3,350	200 mM Lithium Sulfate	
F12	22% PEG 3,350	200 mM Magnesium Chlorid	
G1	16% PEG 8,000	200 mM Magnesium Chlorid	0.1 M MES pH 6.5
G2	16% PEG 8,000	200 mM Magnesium Chlorid	0.1 M Hepes pH 7.0
G3	16% PEG 8,000	200 mM Magnesium Chlorid	0.1 M Tris pH 7.5
G4	16% PEG 8,000	200 mM Magnesium Acetate	0.1 M Hepes pH 7.0
G5	16% PEG 8,000	200 mM Lithium Sulfate	0.1 M Hepes pH 7.0
G6	16% PEG 8,000	200 mM Sodium Citrate	0.1 M Hepes pH 7.0
G7	24% PEG 3,350	200 mM Sodium Citrate	
G8	24% PEG 3,350	200 mM Sodium Citrate	
G9	24% PEG 3,350	200 mM Magnesium Acetate	
G10	24% PEG 3,350	200 mM Potassium Citrate	
G11	24% PEG 3,350	200 mM Lithium Sulfate	
G12	24% PEG 3,350	200 mM Magnesium Chlorid	
H1	18% PEG 8,000	200 mM Magnesium Chlorid	0.1 M MES pH 6.5
H2	18% PEG 8,000	200 mM Magnesium Chlorid	0.1 M Hepes pH 7.0
H3	18% PEG 8,000	200 mM Magnesium Chlorid	0.1 M Tris pH 7.5
H4	18% PEG 8,000	200 mM Magnesium Acetate	0.1 M Hepes pH 7.0
H5	18% PEG 8,000	200 mM Lithium Sulfate	0.1 M Hepes pH 7.0
H6	18% PEG 8,000	200 mM Sodium Citrate	0.1 M Hepes pH 7.0
H7	26% PEG 3,350	200 mM Sodium Citrate	
H8	26% PEG 3,350	200 mM Sodium Citrate	
H9	26% PEG 3,350	200 mM Magnesium Acetate	
H10	26% PEG 3,350	200 mM Potassium Citrate	
H11	26% PEG 3,350	200 mM Lithium Sulfate	
H12	26% PEG 3,350	200 mM Magnesium Chlorid	

Table S 5 - PfHK Screen Dressing (96-well format).

Well	Precipitant	Salt 1	Salt 2	Buffer
A1	20% PEG 3,350			
A2	20% PEG 3,350			
A3	20% PEG 3,350			Sodium lactate pH 3.6
A4	20% PEG 3,350			Sodium lactate pH 3.6
A5	20% PEG 3,350			Citrate pH 4.0
A6	20% PEG 3,350			Citrate pH 4.0
A7	20% PEG 3,350			Sodium Acetate pH 4.4
A8	20% PEG 3,350			Sodium Acetate pH 4.4
A9	20% PEG 3,350			Sodium Acetate pH 4.6
A10	20% PEG 3,350			Sodium Acetate pH 4.6
A11	20% PEG 3,350			Sodium Acetate pH 4.8
A12	20% PEG 3,350			Sodium Acetate pH 4.8
B1	20% PEG 3,350	200 mM Sodium Citrate		
B2	20% PEG 3,350	200 mM Sodium Citrate		
B3	20% PEG 3,350	200 mM Sodium Citrate		Sodium lactate pH 3.6
B4	20% PEG 3,350	200 mM Sodium Citrate		Sodium lactate pH 3.6
B5	20% PEG 3,350	200 mM Sodium Citrate		Citrate pH 4.0
B6	20% PEG 3,350	200 mM Sodium Citrate		Citrate pH 4.0
B7	20% PEG 3,350	200 mM Sodium Citrate		Sodium Acetate pH 4.4
B8	20% PEG 3,350	200 mM Sodium Citrate		Sodium Acetate pH 4.4
B9	20% PEG 3,350	200 mM Sodium Citrate		Sodium Acetate pH 4.6
B10	20% PEG 3,350	200 mM Sodium Citrate		Sodium Acetate pH 4.6
B11	20% PEG 3,350	200 mM Sodium Citrate		Sodium Acetate pH 4.8
B12	20% PEG 3,350	200 mM Sodium Citrate		Sodium Acetate pH 4.8
C1	20% PEG 3,350	100 mM Sodium Citrate		
C2	20% PEG 3,350	100 mM Sodium Citrate		
C3	20% PEG 3,350	100 mM Sodium Citrate		Sodium lactate pH 3.6
C4	20% PEG 3,350	100 mM Sodium Citrate		Sodium lactate pH 3.6
C5	20% PEG 3,350	100 mM Sodium Citrate		Citrate pH 4.0
C6	20% PEG 3,350	100 mM Sodium Citrate		Citrate pH 4.0
C7	20% PEG 3,350	100 mM Sodium Citrate		Sodium Acetate pH 4.4
C8	20% PEG 3,350	100 mM Sodium Citrate		Sodium Acetate pH 4.4
C9	20% PEG 3,350	100 mM Sodium Citrate		Sodium Acetate pH 4.6
C10	20% PEG 3,350	100 mM Sodium Citrate		Sodium Acetate pH 4.6
C11	20% PEG 3,350	100 mM Sodium Citrate		Sodium Acetate pH 4.8
C12	20% PEG 3,350	100 mM Sodium Citrate		Sodium Acetate pH 4.8
D1	20% PEG 3,350	100 mM Sodium Citrate	100 mM Magnesium Chloride	
D2	20% PEG 3,350	100 mM Sodium Citrate	100 mM Magnesium Chloride	
D3	20% PEG 3,350	100 mM Sodium Citrate	100 mM Magnesium Chloride	Sodium lactate pH 3.6
D4	20% PEG 3,350	100 mM Sodium Citrate	100 mM Magnesium Chloride	Sodium lactate pH 3.6
D5	20% PEG 3,350	100 mM Sodium Citrate	100 mM Magnesium Chloride	Citrate pH 4.0
D6	20% PEG 3,350	100 mM Sodium Citrate	100 mM Magnesium Chloride	Citrate pH 4.0
D7	20% PEG 3,350	100 mM Sodium Citrate	100 mM Magnesium Chloride	Sodium Acetate pH 4.4
D8	20% PEG 3,350	100 mM Sodium Citrate	100 mM Magnesium Chloride	Sodium Acetate pH 4.4
D9	20% PEG 3,350	100 mM Sodium Citrate	100 mM Magnesium Chloride	Sodium Acetate pH 4.6
D10	20% PEG 3,350	100 mM Sodium Citrate	100 mM Magnesium Chloride	Sodium Acetate pH 4.6
D11	20% PEG 3,350	100 mM Sodium Citrate	100 mM Magnesium Chloride	Sodium Acetate pH 4.8
D12	20% PEG 3,350	100 mM Sodium Citrate	100 mM Magnesium Chloride	Sodium Acetate pH 4.8
E1	20% PEG 3,350	200 mM Magnesium Chloride		
E2	20% PEG 3,350	200 mM Magnesium Chloride		
E3	20% PEG 3,350	200 mM Magnesium Chloride		Sodium lactate pH 3.6
E4	20% PEG 3,350	200 mM Magnesium Chloride		Sodium lactate pH 3.6
E5	20% PEG 3,350	200 mM Magnesium Chloride		Citrate pH 4.0
E6	20% PEG 3,350	200 mM Magnesium Chloride		Citrate pH 4.0
E7	20% PEG 3,350	200 mM Magnesium Chloride		Sodium Acetate pH 4.4
E8	20% PEG 3,350	200 mM Magnesium Chloride		Sodium Acetate pH 4.4
E9	20% PEG 3,350	200 mM Magnesium Chloride		Sodium Acetate pH 4.6

E10	20% PEG 3,350	200 mM Magnesium Chloride		Sodium Acetate pH 4.6
E11	20% PEG 3,350	200 mM Magnesium Chloride		Sodium Acetate pH 4.8
E12	20% PEG 3,350	200 mM Magnesium Chloride		Sodium Acetate pH 4.8
F1	20% PEG 3,350	200 mM Sodium Acetate		
F2	20% PEG 3,350	200 mM Sodium Acetate		
F3	20% PEG 3,350	200 mM Sodium Acetate		Sodium lactate pH 3.6
F4	20% PEG 3,350	200 mM Sodium Acetate		Sodium lactate pH 3.6
F5	20% PEG 3,350	200 mM Sodium Acetate		Citrate pH 4.0
F6	20% PEG 3,350	200 mM Sodium Acetate		Citrate pH 4.0
F7	20% PEG 3,350	200 mM Sodium Acetate		Sodium Acetate pH 4.4
F8	20% PEG 3,350	200 mM Sodium Acetate		Sodium Acetate pH 4.4
F9	20% PEG 3,350	200 mM Sodium Acetate		Sodium Acetate pH 4.6
F10	20% PEG 3,350	200 mM Sodium Acetate		Sodium Acetate pH 4.6
F11	20% PEG 3,350	200 mM Sodium Acetate		Sodium Acetate pH 4.8
F12	20% PEG 3,350	200 mM Sodium Acetate		Sodium Acetate pH 4.8
G1	20% PEG 3,350	100 mM Sodium Acetate		
G2	20% PEG 3,350	100 mM Sodium Acetate		
G3	20% PEG 3,350	100 mM Sodium Acetate		Sodium lactate pH 3.6
G4	20% PEG 3,350	100 mM Sodium Acetate		Sodium lactate pH 3.6
G5	20% PEG 3,350	100 mM Sodium Acetate		Citrate pH 4.0
G6	20% PEG 3,350	100 mM Sodium Acetate		Citrate pH 4.0
G7	20% PEG 3,350	100 mM Sodium Acetate		Sodium Acetate pH 4.4
G8	20% PEG 3,350	100 mM Sodium Acetate		Sodium Acetate pH 4.4
G9	20% PEG 3,350	100 mM Sodium Acetate		Sodium Acetate pH 4.6
G10	20% PEG 3,350	100 mM Sodium Acetate		Sodium Acetate pH 4.6
G11	20% PEG 3,350	100 mM Sodium Acetate		Sodium Acetate pH 4.8
G12	20% PEG 3,350	100 mM Sodium Acetate		Sodium Acetate pH 4.8
H1	20% PEG 3,350	100 mM Sodium Acetate	100 mM Magnesium Chloride	
H2	20% PEG 3,350	100 mM Sodium Acetate	100 mM Magnesium Chloride	
H3	20% PEG 3,350	100 mM Sodium Acetate	100 mM Magnesium Chloride	Sodium lactate pH 3.6
H4	20% PEG 3,350	100 mM Sodium Acetate	100 mM Magnesium Chloride	Sodium lactate pH 3.6
H5	20% PEG 3,350	100 mM Sodium Acetate	100 mM Magnesium Chloride	Citrate pH 4.0
H6	20% PEG 3,350	100 mM Sodium Acetate	100 mM Magnesium Chloride	Citrate pH 4.0
H7	20% PEG 3,350	100 mM Sodium Acetate	100 mM Magnesium Chloride	Sodium Acetate pH 4.4
H8	20% PEG 3,350	100 mM Sodium Acetate	100 mM Magnesium Chloride	Sodium Acetate pH 4.4
H9	20% PEG 3,350	100 mM Sodium Acetate	100 mM Magnesium Chloride	Sodium Acetate pH 4.6
H10	20% PEG 3,350	100 mM Sodium Acetate	100 mM Magnesium Chloride	Sodium Acetate pH 4.6
H11	20% PEG 3,350	100 mM Sodium Acetate	100 mM Magnesium Chloride	Sodium Acetate pH 4.8
H12	20% PEG 3,350	100 mM Sodium Acetate	100 mM Magnesium Chloride	Sodium Acetate pH 4.8

Table S 6 - PfHK Screen Dressing II (24-well format).

Well	Precipitant	Salt	Buffer
A1	20% PEG 3,350	200 mM Sodium Citrate	100 mM Sodium Citrate pH 3.6
A2	20% PEG 3,350	200 mM Sodium Citrate	100 mM Sodium Citrate pH 3.8
A3	20% PEG 3,350	200 mM Sodium Citrate	100 mM Sodium Citrate pH 4.0
A4	20% PEG 3,350	200 mM Sodium Citrate	100 mM Sodium Citrate pH 4.0
A5	20% PEG 3,350	200 mM Sodium Citrate	100 mM Sodium Citrate pH 4.2
A6	20% PEG 3,350	200 mM Sodium Citrate	100 mM Sodium Citrate pH 4.4
B1	20% PEG 3,350	200 mM Sodium Citrate	100 mM Sodium Citrate pH 3.6
B2	20% PEG 3,350	200 mM Sodium Citrate	100 mM Sodium Citrate pH 3.8
B3	20% PEG 3,350	200 mM Sodium Citrate	100 mM Sodium Citrate pH 4.0
B4	20% PEG 3,350	200 mM Sodium Citrate	100 mM Sodium Citrate pH 4.0
B5	20% PEG 3,350	200 mM Sodium Citrate	100 mM Sodium Citrate pH 4.2
B6	20% PEG 3,350	200 mM Sodium Citrate	100 mM Sodium Citrate pH 4.4
C1	20% PEG 3,350	300 mM Sodium Citrate	100 mM Sodium Citrate pH 3.6
C2	20% PEG 3,350	300 mM Sodium Citrate	100 mM Sodium Citrate pH 3.8
C3	20% PEG 3,350	300 mM Sodium Citrate	100 mM Sodium Citrate pH 4.0
C4	20% PEG 3,350	300 mM Sodium Citrate	100 mM Sodium Citrate pH 4.0
C5	20% PEG 3,350	300 mM Sodium Citrate	100 mM Sodium Citrate pH 4.2

C6	20% PEG 3,350	300 mM Sodium Citrate	100 mM Sodium Citrate pH 4.4
D1	20% PEG 3,350	200 mM Sodium Citrate	100 mM Sodium Citrate pH 3.6
D2	20% PEG 3,350	200 mM Sodium Citrate	100 mM Sodium Citrate pH 3.8
D3	20% PEG 3,350	200 mM Sodium Citrate	100 mM Sodium Citrate pH 4.0
D4	20% PEG 3,350	200 mM Sodium Citrate	100 mM Sodium Citrate pH 4.0
D5	20% PEG 3,350	200 mM Sodium Citrate	100 mM Sodium Citrate pH 4.2
D6	20% PEG 3,350	200 mM Sodium Citrate	100 mM Sodium Citrate pH 4.4

Table S 7 - Summary of data collection and refinement statistics of PfPK crystals.

	PfPK^{WT}	**PfPK^{WT} with pyruvate (WT^{Pyr})**	**PfPK^{C343A}**	**PfPK^{C49A}**
Space group	I222	I222	I222	I222
Unit cell parameters				
a, b, c (Å)	89.2 109.67 134.14	79.89 112.4 131.97	89.42 109.13 134.1	89.66 109.81 133.35
α, β, γ (°)	90, 90, 90	90, 90, 90	90, 90, 90	90, 90, 90
Data collection				
Beamline	SLS beam line X10SA	SLS beam line X10SA	SLS beam line X10SA	SLS beam line X10SA
Temperature (K)	100	100	100	100
Wavelength (Å)	0.9999	0.9999	0.9999	0.9999
Resolution range	19.74 - 1.9 (1.968 - 1.9)	36.2 - 1.8 (1.864 - 1.8)	32.25 - 2.0 (2.072 - 2.0)	41.2 - 2.1 (2.175 - 2.1)
Wilson B-factor	44.90	35.23	49.89	59.32
Total reflections	271619 (27518)	176088 (16815)	162857 (16600)	153591 (15062)
Unique reflections	51642 (5122)	53978 (5355)	44287 (4443)	38216 (3757)
Multiplicity	5.3 (5.4)	3.3 (3.1)	3.7 (3.7)	4.0 (4.0)
Completeness (%)	99.12 (99.51)	97.59 (97.82)	99.18 (99.66)	98.49 (97.96)
Mean I /σ(I)	15.09 (1.10)	10.60 (1.14)	12.20 (1.08)	12.67 (1.03)
R-merge[a] (%)	0.05152 (1.382)	0.0597 (1.061)	0.04934 (1.184)	0.04602 (1.185)
R-pim[b] (%)	0.02389 (0.6384)	0.03788 (0.6847)	0.0296 (0.705)	0.02634 (0.6587)
CC1/2 (%)	0.999 (0.389)	0.999 (0.511)	0.999 (0.439)	0.999 (0.589)
Molecules per ASU	1	1	1	1
Refinement				
Reflections used for R-free	3099 (307)	3237 (320)	3541 (355)	3051 (298)
R-work	0.2040 (0.3864)	0.2053 (0.4929)	0.2145 (0.4243)	0.2508 (0.4596)
R-free	0.2418 (0.4339)	0.2450 (0.5154)	0.2482 (0.4541)	0.2787 (0.5117)
No. Of atoms/Average B (Å^2)				
Protein	3782	3782	3767	3781
Ligands	28	105	2	1
Solvent	178	161	174	55
Non-hydrogen atoms	3988	4048	3943	3837
Protein residues	497	495	494	497
Ramachandran plot (%)				
Favored (%)	97.57	97.15	97.96	96.96
Outliers (%)	0.20	0.20	0.00	0.00
RMS deviations				
Bonds (Å)	0.006	0.015	0.003	0.003
Angles (°)	0.77	1.37	0.58	0.61
PDB accession code				

Statistics for the high-resolution shell are shown in parentheses.
aR_{merge} = $\sum_{hkl}\sum_i|I_i(hkl)$ $[I(hkl)]|/\sum_{hkl}\sum_i I_i(hkl)$, where $I_i(hkl)$ is the ith measurement of reflection hkl and $[I(hkl)]$ is the weighted mean of all mea- surements.;
bR_{pim} = $\sum_{hkl}$ [1/(N 1)] 1/2 $\sum_i|I_i(hkl)$ $[I(hkl)]|/\sum_{hkl}\sum_i I_i(hkl)$, where N is the redundancy for the hkl reflection.;
cR_{work}/R_{free} = $\sum_{hkl}|$ F_o $F_c|/\sum_{hkl}|F_o|$, where F_c is the calculated and F_o is the observed structure-factor amplitude of reflection hkl for the working/free (5%) set, respectively.

ACKNOWLEDGEMENTS (DANKSAGUNG)

An erster Stelle möchte ich Prof. Dr. KATJA BECKER danken. Herzlichen Dank für die wunderbare Möglichkeit, meine Promotion zu einem äußerst spannenden Thema und in dieser so familiären Arbeitsgruppe verfolgen zu dürfen. Ich habe nicht nur sehr viele Labormethoden, das Präsentieren von Forschungsergebnissen und wissenschaftliche Soft Skills lernen dürfen, sondern auch gleichermaßen die Möglichkeit bekommen, Einblicke in das Erstellen von Gutachten und Anträgen zu erhalten. Auch boten sich viele Gelegenheiten (inter)nationale Konferenzerfahrung, sowohl als Teilnehmerin, als auch als Mitglied des Organisationsteams, zu sammeln. Ebenfalls danken möchte ich Prof. Dr. JUDE PRZYBORSKI für seine erstklassige Vertretung von Prof. Dr. Katja Becker und das damit einhergehende Engagement für uns „adoptierte“ Doktorand:innen. Prof. Dr. KATJA STRÄßER danke ich herzlich für die Übernahme der Zweitbetreuung und auch den weiteren Mitgliedern der Prüfungskommission gilt mein Dank: Prof. Dr. ELENA EVGUENIEVA-HACKENBERG für ihr Interesse an meiner Arbeit und Prof. Dr. JOHN ZIEBUHR für die spannende Einführung in die Coronavirus-Forschung, welche in eine erfolgreiche Kooperation gemündet ist. Darüber hinaus danke ich Prof. Dr. MIRIAM CORTESE-KROTT (Heinrich-Heine-Universität Düsseldorf) für die ebenfalls erfolgreiche und interessante Kooperation. Ein weiterer Dank geht an Frau Dr. KARIN FRITZ-WOLF für ihre Geduld bei den vielen detaillierten Nachfragen zur Strukturauflösung, die Einführung in Labor- und Software-Skills, die Cappuccinos in Heidelberg und für das Lösen der in dieser Arbeit dargestellten Kristallstrukturen. Im Labor zeichnete sich MICHAELA STUMPF durch ihre tatkräftige Unterstützung in der Kristallographie, viele erfahrungsträchtige Ratschläge und ihre Ruhe in scheinbar aussichtslosen Situationen aus. Danke auch für das Vertrauen mir und Isabell gegenüber, uns in die Bedienung der „Honey Bee“ einzuweisen. MARINA FISCHER möchte ich für ihre geduldige und ausführliche Einführung in die Enzymkinetik danken, mit ihrer Hilfe waren selbst komplizierte Assay-Systeme kein Problem mehr. Dr. STEFAN RAHLFS danke ich für die Unterstützung des molekularbiologischen Teils meiner Arbeit und die vielen Anekdoten, die mir das Kennenlernen der Arbeitsgruppe erleichtert haben. Ein weiterer großer Dank geht an Dr. CHRISTINA BRANDSTÄDTER und Dr. JULIA HAHN, die stets eine Antwort auf meine Fragen hatten oder zumindest beruhigende Worte bei aufkeimender Laborpanik parat hatten. Dr. SUSANNE SCHIPPER möchte ich für die Einführung in die Laborarbeit und zeitgleich die Betreuung meiner Masterarbeit danken, die mich erst zu meiner Promotion geführt hat. Hierbei sind ebenfalls die vielen kulinarischen Büro- und Feierabenderlebnisse zu erwähnen. Zu guter Letzt danke ich ISABELL BERNEBURG ganz herzlich für ihr offenes Ohr bei den vielen methodischen, mathematischen und persönlichen Problemen, die ein paar Diskussionsminuten später meist gar nicht mehr dramatisch oder unlösbar erschienen.

DECLARATION (EIDESSTATTLICHE ERKLÄRUNG)

Hiermit versichere ich, die vorgelegte Dissertation selbständig und ohne unerlaubte fremde Hilfe und nur mit den Hilfen angefertigt zu haben, die ich in der Dissertation angegeben habe. Alle Textstellen, die wörtlich oder sinngemäß aus veröffentlichten Schriften entnommen sind, und alle Angaben, die auf mündlichen Auskünften beruhen, sind als solche kenntlich gemacht. Ich stimme einer evtl. Überprüfung meiner Dissertation durch eine Antiplagiat-Software zu. Bei den von mir durchgeführten und in der Dissertation erwähnten Untersuchungen habe ich die Grundsätze guter wissenschaftlicher Praxis, wie sie in der „Satzung der Justus-Liebig-Universität Gießen zur Sicherung guter wissenschaftlicher Praxis“ niedergelegt sind, eingehalten.

Gießen, Juli 2022

Melissa Dillenberger